**Barbara Eicher**

# Investigation of Transbilayer and Intraleaflet Coupling Mechanisms in Asymmetric Lipid Membranes

## Doctoral Thesis

For obtaining the academic degree of

Doktor der technischen Wissenschaften

Doctoral Programme of Technical Sciences
Technical Physics



**Graz University of Technology**

# EIDESSTATTLICHE ERKLÄRUNG

# AFFIDAVIT

Ich erkläre an Eides statt, dass ich die vorliegende Arbeit selbstständig verfasst, andere als die angegebenen Quellen/Hilfsmittel nicht benutzt, und die den benutzten Quellen wörtlich und inhaltlich entnommenen Stellen als solche kenntlich gemacht habe. Das in TUGRAZonline hochgeladene Textdokument ist mit der vorliegenden Dissertation identisch.

I declare that I have authored this thesis independently, that I have not used other than the declared sources/resources, and that I have explicitly indicated all material which has been quoted either literally or by content from the sources used. The text document uploaded to TUGRAZonline is identical to the present doctoral dissertation.

_____ _____

Datum / Date Unterschrift / Signature

# Acknowledgment

would like to thank my husband Robert who was always my personal and mental backup during the last years.

# Abstract

Most biological membranes show an asymmetric distribution of lipids between the two leaflets. This bilayer asymmetry is expected to affect structural properties, such as area per lipid, bilayer thickness and thickness of the single leaflets. Due to the difficulty of preparing asymmetric vesicles (aLUVs), the interactions between bilayer leaflets are poorly understood. These problems were addressed by modifying a protocol to prepare tensionless and solvent free asymmetric vesicles with well defined inner and outer leaflet composition via a cyclodextrin mediated exchange process, which can be used for a wide range of biophysical studies. Additionally, tools were developed to quantify the lipid composition of the single leaflets, enabling to resolve bilayer structural features with sub-nanometer resolution. A high and low resolution model was developed to determine these structural parameters via a joint analysis of different contrasts of small angle neutron and X–ray scattering data. First we investigated a sample where dipalmitoyl phosphatidylcholine (DPPC) was partially exchanged into palmitoyl oleoyl phosphatidylcholine (POPC) vesicles. These aLUVs consisted of a gel/fluid outer- and fluid inner-leaflet. Interestingly, we have found that the disordered inner leaflet reduces the lipid packing density of the outer leaflet. Further, wide-angle X-ray scattering, differential scanning calorimetry and cryo-transmission electron microscopy were applied to study the coupling mechanism between the single leaflets of aLUVs consisting of palmitoyl oleoyl phosphatidylethanolamine (POPE) and POPC. We observed strong transbilayer coupling in the gel phase when POPE was placed on the inner leaf, while no coupling was detected for samples where POPE was placed on the outer leaflet in gel-phase. These results agree with the preferred location of POPE on the inner monolayer due to its negative intrinsic curvature, coupling the inner to the outer leaf. In general, no coupling was observed when both lipids are in fluid phase for all studied samples.

# Kurzfassung

Die meisten biologischen Membranen weisen eine asymmetrische Verteilung der Lipide zwischen den einzelnen Monolayern der Lipid-Doppelschicht auf. Es wird vermutet, dass diese asymmetrische Verteilung der Lipide die strukturellen Parameter der Membran beeinflusst. Aufgrund der Schwierigkeiten asymmetrische Lipid-Membranen zu erzeugen, werden bis jetzt die Wechselwirkungen zwischen den einzelnen Schichten kaum verstanden. In dieser Arbeit wurden Protokolle zur Herstellung asymmetrischer Membranen modifiziert, um mittels Cyclodextrin spannungs- und lösungsmittelfreie asymmetrische Vesikel (aLUVs) zu erzeugen. Diese aLUVs können für eine große Vielfalt an biophysikalischen Studien eingesetzt werden. Zusätzlich wurden Methoden entwickelt um die Lipid-Zusammensetzung der inneren und äußeren Membranschicht zu quantifizieren um in weiterer Folge die Struktur der Doppelschicht mittels Kleinwinkel-Röntgen- und Neutronenstreu-Daten (SAXS/SANS) im sub-Nanometerbereich zu bestimmen. Dafür wurde ein hoch- und nieder-auflösendes Model zur gemeinsamen Analyse von SAXS und SANS-Daten entwickelt. Zuerst wurden aLUVs hergestellt bei welchen die äußere Lipid-Schicht eines Palmitoyl Oleoyl Phosphatidylcholine (POPC) Vesikels mittels Dipalmitoyl Phosphatidylcholine (DPPC) zum Teil ausgetauscht wurde. Somit setzten sich diese aLUVs aus einer gelförmigen/fluiden äußeren und einer homogenen fluiden inneren Membranschicht zusammen. Interessanterweise haben wir festgestellt, dass der ungeordnete innere Membran Monolayer die Lipid Packungsdichte einer geordneten äußeren Membranschicht reduziert. Außerdem wurden Weitwinkel-Röntgenstreuung, dynamische Differenzkalorimetrie und Cryo-Transmissionselektronenmikroskopie eingesetzt um den Kopplungsmechanismus zwischen den einzelnen Monolayern der Lipid-Doppelschicht, zusammengesetzt aus Palmitoyl Oleoyl Phosphatidylethanolamine (POPE) und POPC zu ermitteln. Eine starke Kopplung zwischen den Monoschichten wurde gemessen wenn POPE auf der inneren Seite platziert wurde, jedoch

nicht wenn POPE auf der äußeren Seite lokalisiert ist. Diese Ergebnisse stimmen mit der bevorzugten Positionierung von POPE im inneren Monolayer, aufgrund dessen negativer intrinsischer Krümmung, überein. Im Allgemeinen wurde jedoch, für alle Proben die in der fluiden Phase gemessen wurden, keine Kopplung zwischen den Monoschichten detektiert.

# Contents

Contents

# List of Figures

List of Figures

# List of Abbreviations

$\alpha_A^T$ ...................... area expansion coefficient
$\lambda$ ........................ wavelength
$\Sigma_{as}$ ..................... degree of asymmetry
$A_C$ ........................ area per hydrocarbon
$A_L$ ........................ area per lipid
$D_B$ ........................ thickness of the bilayer
$D_C$ ........................ hydrocarbon thickness
$F_{FB}$ ..................... flat bilayer form factor
$J_0$ ......................... intrinsic/spontaneous curvature
$n_W$ ........................ number of bound water molecules
$T_M$ ........................ phase transition temperature
aLUV ................... asymmetric large unilamellar vesilce
aSDP ................... asymmetric scattering density profile
CD ....................... cyclodextrin
CG ...................... carbonyl and glycerol group
cryo-TEM ................ cryo transmission electron microscopy
D/A ..................... donor to acceptor ratio
DLS ..................... dynamic light scattering
DMPC ................... dimyristoyl phosphatidylcholine
DPPC ................... dipalmitoyl phosphatidylcholine
DSC .................... differential scanning calorimetry
ED ....................... electron density
EM ...................... electro magnetic
FAME ................... fatty acid methyl ester
GC ...................... gas chromatography

List of Abbreviations

| | |
|---|---|
| GUV | giant unilamellar vesicle |
| HC | hydrocarbon-group |
| HP$\alpha$CD | hydroxypropyl-$\alpha$-cyclodextrin |
| HP$\beta$CD | hydroxypropyl-$\beta$-cyclodextrin |
| LUV | large unilamellar vesicles |
| M | methyl-group |
| M$\beta$CD | methyl-$\beta$-cyclodextrin |
| MLV | multilamellar vesicle |
| NMR | nuclear magnetic resonance |
| NSL | neutron scattering length |
| PC | phosphatidylcholine |
| PDI | polydispersity index |
| POPC | palmitoyl oleoyl phosphatidylcholine |
| POPE | palmitoyl oleoyl phosphatidylethanolamine |
| Pr$^{3+}$ | paramagnetic lanthanide ion |
| RH | resiudal headgroup |
| SANS | small-angle neutron scattering |
| SAS | small-angle scattering |
| SAXS | small-angle X-ray scattering |
| SDP | scattering density profile |
| SFG | sum-frequency generation |
| SLD | scattering length density |
| SM | sphingomyelin |
| SNS | spallation neutron source |
| SSB | solid supported bilyers |
| UPLC-MS | ultra performance liquid chromatography–mass spectrometry |
| VPD | volume probability distribution |
| WAXS | wide-angle X-ray scattering |

# 1. Introduction

## 1.1. Cell Membrane - Asymmetry in Natural Membranes

Biological membranes separate the interior of a cell from the outside environment. They actively control cellular communication and are responsible for transport through or within the membrane. Superresolution microscopy has revealed fascinating images which show that the interior of eukaryotic cells is packed with membrane surfaces, suggesting that most biochemical processes take place at membranes or in their close vicinity [1–3]. Consequently, biological membranes are moved to the fore for drug research and novel therapies which aim to interfere with their physiological malfunction, or to protect them from toxins or attacks by pathogens [4]. The cell membrane consists of a lipid bilayer with more than a 1000 different lipid species and proteins. It is believed that cellular function is due to tight coupling between these components [5–8]. Biological membranes are conceived to have an asymmetric distribution of lipids between the inner and outer side of the bilayer [8, 9]. For example in the mammalian plasma membrane high melting lipids such as sphingomyelin (SM) and phosphatidylcholine (PC) are mainly located on the outer leaflet while the negatively charged phosphatidylserine (PS) and phosphatidylethanolamine (PE) which has a negative curvature are found on the inner leaflet, see Fig. 1.1 [8, 9]. Cholesterol is located on both leaflets. Recent studies suggest that cholesterol is distributed asymmetrically between the leaflets, however, it is still debated in which monolayer it is more enriched [10–12]. Bacterial membranes show also lipid asymmetry along the bilayer normal, with phosphatidylglycerol (PG) located mainly in the outer leaflet, while phosphatidylinositol (PI) and PE are sequestered on the inner leaf. An asymmetric membrane is a system

which is not in equilibrium. Cells expend valuable energy to create and maintain asymmetry [13]. Actually, one of the first indicators of cell death is that the negatively charged PS-lipids flip to the outer side in the plasma membrane, where they normally do not reside [14, 15]. Surprisingly little is known about structural and functional consequences of an asymmetric lipid distribution.
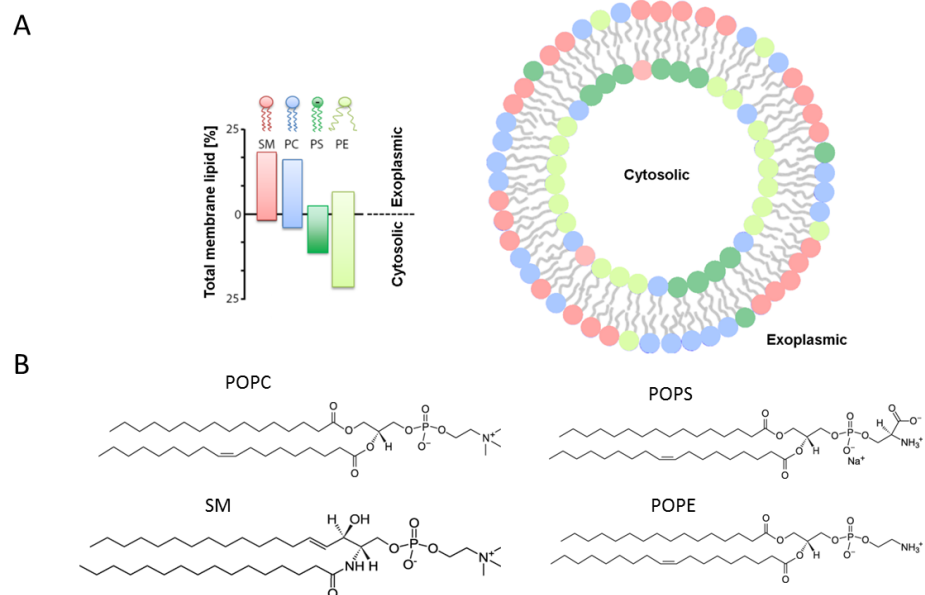


Figure 1.1.: (A) Proposed lipid distribution in a human red blood cell [9, 11], (B) including the chemical representation of the PC, PS, PE headgroups and SM. Chemical structures were taken from Avanti: avantilipids.com

## 1.2. Lipid Bilayer Model

Obtaining quantitative insight into biological processes is one of the major goals of biophysical research. Therefore, it is often useful to reduce the level of complexity. Hence, a simplified model system needs to be carefully

designed for a given biological problem [16]. For example biological membranes are complex structures of lipids, proteins and carbohydrates which build a highly dynamic, flexible and well structured material as previously mentioned. Despite the complex structure of biological membranes, it can be modeled as a lipid only membrane [17]. Such studies are often criticized, as they neglect that biological membranes consist of an average protein mass of $\sim 60\%$. This leads to doubts on the physiological relevance of such studies. However, a closer look on biological membranes shows that most of the protein mass is located either on the inner or outer side of the membrane. In numbers, only $10 - 15\%$ of matter bound by lipid headgroups is protein [18]. As a result, the properties of a lipid matrix are of significant importance to biological membranes. However, findings from model systems cannot be taken directly to describe living cells. Nonetheless, and in contrast to living cells, important fundamental properties can be studied under experimentally and chemically well defined conditions by using a variety of experimental techniques to explore their structural and dynamic behavior at different length and time scales [16]. In this work the transbilayer and intraleaflet structure of asymmetric lipid vesicles was studied.

## 1.3. Preparation of Asymmetric Vesicles

Lately, several techniques were developed to prepare free floating asymmetric lipid vesicles (aLUVs) [19–26]. The most promising approach seems to be the protocol, developed by the laboratory of Erwin London (Stony Brook, NY, USA). For that procedure a cyclodextrin (CD) mediated lipid exchange is applied to replace the outer leaflet of unilamellar vesicles with the lipids of interest. CD consists of ring shaped oligosaccharides which have a hydrophilic outer surface and a hydrophobic cavity, see Fig. 1.2. This cavity is large enough to extract a hydrophobic lipid chain from the bilayer and partially shield it from the surrounding water, which makes CD an effective catalyst to exchange lipids between vesicles through solutions [27]. Methyl-$\beta$-CD (M$\beta$CD) is mostly used as it carries out lipid exchange more efficiently than e.g. hydroxypropyl-$\alpha$-CD (HP$\alpha$CD) and hydroxypropyl-$\beta$-CD (HP$\beta$CD) [25], see Fig. 1.2 for structural details. By applying this CD mediated exchange technique it is possible to construct free

floating asymmetric lipid vesicles with a variety of lipid headgroups and acyl chain compositions. They are prepared by two pools of differently composed lipid vesicles which are mixed in the presence of CD: donor vesicles (mostly multilamellar vesicles (MLVs)) provide lipids for the outer leaflet, while extruded (or sonicated) acceptor vesicles build the inner leaflet. The preparation requires consecutive incubation processes and a final separation process of donor and acceptor vesicles, which is achieved by density or size differences between these two vesicle pools. London and co-workers used acceptor vesicles which have 25% (w/v) of sucrose entrapped in the core of acceptor vesicles. The obtained aLUVs filled with sucrose can be separated from the donor MLVs by ultracentrifugation ($190,000xg$) through a sucrose solution of intermediate density [23]. Cholesterol can also be incorporated into the asymmetric vesicles, which will not be removed during the exchange process when CD with a small enough cavity is used [25, 26, 28, 29]. For example HP$\alpha$CD [25] or M$\alpha$CD [29] does not bind to cholesterol, but it has the ability to exchange lipids, indicating that it is useful to prepare aLUVs with a predefined amount of cholesterol. The advantage of M$\alpha$CD compared to HP$\alpha$CD is that it interacts very efficiently with lipids similar to M$\beta$CD [29]. This CD mediated exchange process was also adapted to construct asymmetric supported bilayers [30].

These protocols have lead to new possibilities for a wide variety of biophysical studies. However, one drawback of the original CD mediated protocol (by the London group) is the presence of sucrose in the core of the final aLUVs. The entrapped sucrose leads to an osmotic imbalance which thins the bilayer reflecting a 30°C temperature change as shown in Fig. 1.3 [31]. Hence, it was necessary to remove the sucrose from the final asymmetric vesicles, to avoid osmotic imbalance (and the resulting thinning of the membrane). This was achieved by trapping sucrose in donor instead of the acceptor vesicle core, enhancing the difference in sedimentation by the larger size and higher density of the donor MLVs. Thus, low speed centrifugation ($20,000xg$) is sufficient to separate the aLUVs from the donor vesicles [31]. Further, this protocol allows to obtain the individual leaflet compositions by using two assays: the exchange efficiency can be determined e.g. by gas chromatography (GC), ultra performance liquid chromatography (UPLC) or differential scanning calorimetry (DSC) and the lipid distribution of choline headgroups between the inner and outer leaflet can be obtained by conducting ^{1}H-NMR experiments after adding a paramagnetic shift reagent

$Pr^{3+}$ [31, 32], see sec. 2.1 for details.

Another approach to engineer free floating asymmetric vesicles was developed by Weitz and co-workers [19]. This method is similar to the Langmuir-Schaefer/Langmuir-Blodgett technique for asymmetric supported membranes [33, 34]. As schematically illustrated in Figure 1.4B these asymmetric vesicles are engineered by two independently prepared monolayers. The sample preparation is composed of three parts: (1) an inverted emulsion where water droplets in oil are stabilized by lipids for the inner leaflet, (2) an intermediate phase of oil heavier than the inverted emulsion phase, whose lipids form a monolayer at the oil water interface, and (3) the bottom aqueous phase, containing the final asymmetric vesicles [19]. This protocol seems to be less violent compared to the CD mediated exchange, however, the possible presence of oil in the final sample is one major drawback of this approach [11].

## 1.3.1. Stability of Asymmetric Vesicles

For investigation of asymmetric lipid vesicles, it has to be considered that the systems are not at equilibrium and that lipid asymmetry will level-out with time by passive lipid flip-flop.

Cells maintain the asymmetric distribution of lipids through the interplay of active and passive lipid translocation events [13]. Active mechanisms are hypothesized to rely on the so-called floppases which move newly synthesized lipids from the inner to the outer leaflet, while the flippases restores the asymmetry of passively translocated lipids [36, 37].

As lipid translocation rates have historically always been a challenge to measure, there is only little information available. Especially, a lot of flip-flop data was obtained by using bulky lipid fluorescence dyes which might alter the physical properties of the lipid membrane significantly. For example this was shown by Liu and Conboy [38] who have studied passive flip-flop rates of isotopically asymmetric dipalmitoyl phosphatidylcholine (DPPC) in solid supported bilayers (SSBs) with sum-frequency generation (SFG) vibrational spectroscopy. The addition of a common spin label TEMPO (tetramethylpiperidinyl) to DPPC lead to a significant increase of the measured lipid
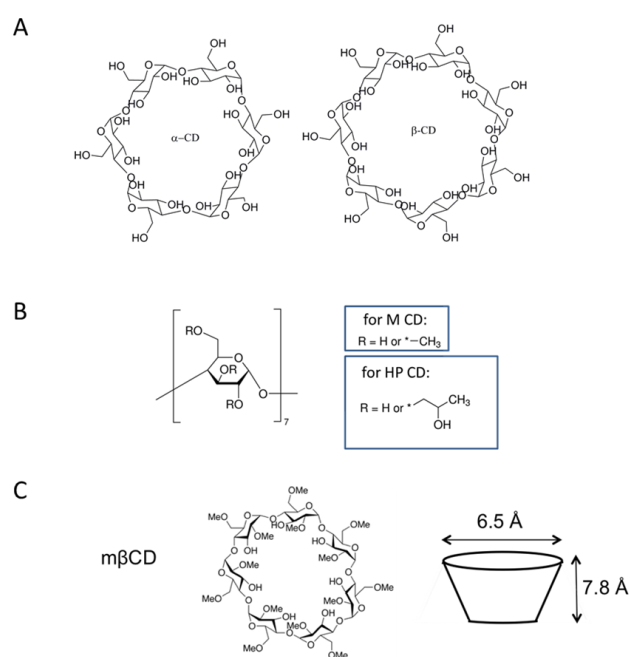
Figure 1.2.: (A) Structure of cyclodextrin. Cavity size increases from $\alpha$ to $\beta$-CD. $\alpha$-CD is a 6- while $\beta$ CD is a 7-membered sugar ring molecule (B) structure of methyl (M) and hydroxypropyl (HP) CD, (C) structure of m$\beta$CD which was used in this study. Figure modified from [35].
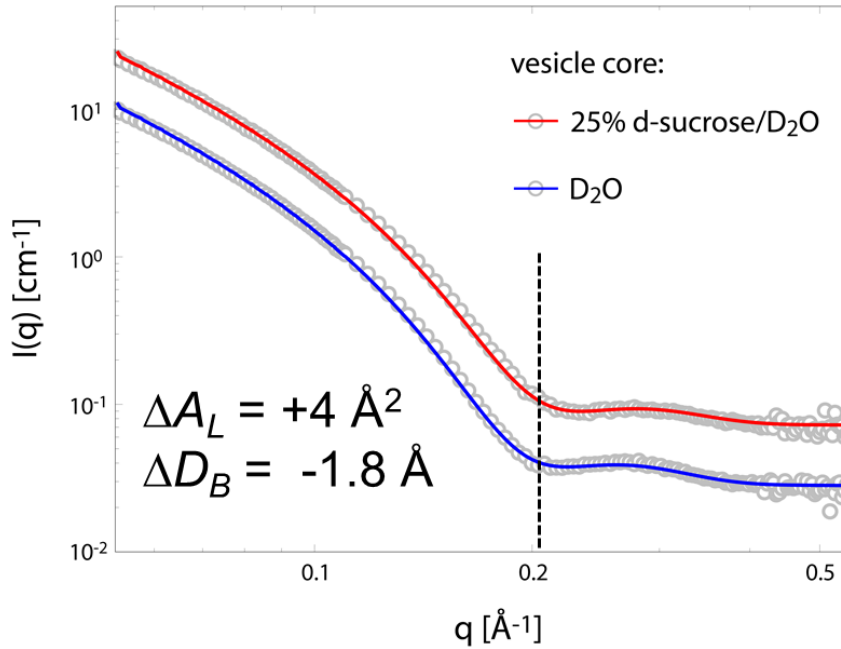
Figure 1.3.: Structural influence of heavy sucrose core acceptor vesicles: Small angle neutron scattering curves of 100 nm POPS LUVs in $D_2O$ (blue fit) and in 25%d-sucrose core in an external $D_2O$ solvent (red fit). This osmotic imbalance generates membrane tension which is shown by a decreased bilayer thickness ($D_B$) (-1.8 Å) and an increase in area per lipid (+4 Å²) compared to stress free POPS. (The position of the minimum representing the bilayer thickness of the red fit shifts to higher q-values.) This increase in area per lipid and decrease in bilayer thickness reflects a 30°C change in temperature. Figure adapted from [31].

half-life by an order of magnitude in comparison to the label free DPPC data (from 9.2 to 422 min) [11, 38]. Just recently, we have revealed that the half-life of stress-free, free floating isotopic asymmetric lipid vesicles is significantly higher compared to studies conducted on SSBs by SFG spectroscopy [39]. This discrepancy between lipid translocation rates in vesicles and SSBs can be explained by defect-mediated acceleration of lipid flip-flop in supported bilayers, where long-lived, submicron-sized defects, resulting from incomplete surface coverage, are the sites of rapid transbilayer movement [40], which is also suggested from MC simulations [39]. Half-times ($t_{1/2}$) were obtained by $^1$H-NMR by using a paramagnetic shift reagent [31, 39], which were in the order of days for vesicles incubated in fluid phase (T$\geq$ 50°C) and

# 1. Introduction
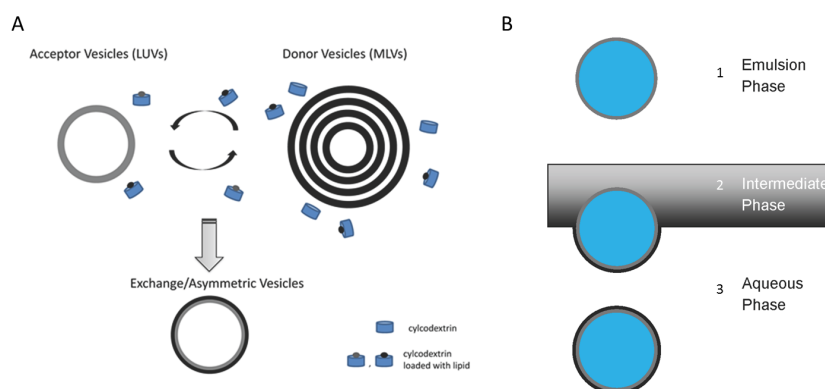


Figure 1.4.: Preparation of asymmetric vesicles. (A) Schematic illustriation of the cyclodextrin mediated exchange of the outer leaflet, and (B) illustrates the generation of asymmetric vesicles by two independently prepared monolayers. Figure adapted from [11].

too slow for being measured in gel phase (T≤ 37°C). However, significantly accelerated when the sample was incubated within the main phase transition (40°C). The increased lipid translocation rate at the phase transition can be explained by the numerousness of defect-like boundaries between lipid patches in gel and fluid phase [39]. Apart from the discrepancies of half-life values obtained by different studies, there are common trends: In general phospholipids with longer acyl chains (increased bilayer thickness) show slower flip-flip rates. This can be explained by an increase of energetic cost to transfer the polar headgroup through a thicker hydrophobic bilayer core [38, 41]. Lipid translocation rates might accelerate due to perturbation of the acyl chains [42]. For example, this may be facilitated by detergents, which are expected to accelerate transbilayer lipid movement by inducing defects into the hydrophobic structure [43].

It is important to determine which factors influence the life time of asymmetric model membranes. It was revealed by Son and London that shorter and polyunsaturated acyl chain lipids in the inner leaflet which are opposed by the highly structured SM show fast lipid translocation rates [44]. Further, fast flip-flop rates ($t_{1/2} \sim 5\,\text{h}$) were reported in single-component dimyristoyl phosphatidylcholine (DMPC) vesicles by SANS [42]. In contrast to this study, Lu et al. have reported on enhanced bending rigidity in dioleoyl phosphatidylcholine (DOPC)/DMPC inverted emulsion giant

unilamellar vesicles (GUVs), suggesting a high degree of asymmetry and as these asymmetry effects were measurable it suggests slow DMPC flip-flop when opposing a leaf consisting of DOPC [16, 45]. Furthermore, Son and London have also demonstrated that flip-flop rates are strongly affected by the polar headgroups: aLUVs with SM on the outer leaflet and the inner monolayer consisting of PS, PE and PC headgroups form stable aLUVs (slow translocation rates), while inner leaflet lipids with PG, PI, and CL polar headgroup show fast flip-flop rates [28]. In conclusion, these results suggest that lipid translocation rates are not only an intrinsic property of the single lipids, but rather depended on the model system as well as the chemical composition and environment they are located in [16].

# 1.4. Transbilayer Coupling Mechanism of Asymmetric Lipid Vesicles

So far surprisingly little is known about the structural and functional consequences of asymmetric lipid vesicles due to the lack of model systems to prepare them. However, recent developments have laid the foundation for such systematic studies. Membrane asymmetry is hypothesized to lead to transbilayer coupling which has an influence on diverse physiological processes requiring communication between for example receptors located on the outer leaflet and components of signal transduction pathways secreted in the cytoplasm [46]. Interestingly, lipid compositions of the outer leaflet prefers the formation of raft-like domains [47, 48], while lipids located on the inner leaf do not phase separate [49]. So far, theoretical treatments have contemplated coupling from intrinsic lipid curvature [50], headgroup electrostatics, cholesterol flip-flop, dynamic chain interdigitation [51, 52], or from thermal membrane fluctuations [53], revealing that transbilayer coupling does not need (however not exclude) contributions from proteins. Further, fluorescent dye partitioning experiments of asymmetric planar lipid bilayers were used to study, whether domain formation in the outer leaflet induces domains in the inner leaflet [51, 54–56]. This was true for inner leaflet mixtures consisting of at least one high melting lipid and a low melting lipid and cholesterol [54]. The influence of an asymmet-

ric lipid distribution on the structural properties of the single leaflet was determined experimentally, and by simulation: For example fluorescence anisotropy measurements have revealed that an outer leaflet consisting of SM, melts independently from an inner leaflet made of a variety of unsaturated lipids [22, 23, 26, 28]. In addition, the highly ordered SM on the outer leaflet increased the degree of inner leaflet order suggesting a significant degree of transbilayer coupling which disappears completely above the lipids phase transition [23, 24]. These studies agree with earlier reports using planar bilayers where transbilayer coupling was shown for some systems as the formation of domains on one leaflet can induce the occurrence of ordered domains on the other leaflet [51, 54–56]. Further, lateral diffusion coupling between the inner and outer leaflet was found for membranes composed of mixed (short/long, saturated/unsaterated) acyl chains. This suggests a hydrocarbon chain interdigitation-mediated mechanism [57], which was supported by theoretical considerations [52]. A study by Shlomovitz and Schick [58] suggested that the motive of trans-bilayer coupling is related to properties from the inner leaflet, which is in contradiction with almost all other findings. In particular, the difference in intrinsic curvature ($J_0$) between the main lipids of the inner leaf PS and PE ($J_0^{PE} \sim -5 * J_0^{PS}$ [58, 59]) is the driving force of leaflet coupling due to the formation of micro emulsions in the inner monolayer, which are propagating to the outer leaflet.

In this work *transmembrane* and *intraleaflet* coupling mechanisms are addressed, see Fig. 1.5. Briefly, transmembrane coupling suggests that the single leafs interact strongly with each other, leading e.g. to a cooperative melting of the bilayer, or to leaflet-averaged structural parameters, such as the area per lipid ($A_L$) that may take up a value that is intermediate between those of individual, uncoupled leaflets. In contrast, intraleaflet coupling reveals a strong coupling within the single monolayer, due to an adjustment of the individual lipid properties, resulting e.g. in separate melting of the leaflets and in individual structural properties of each leaf.

In order to determine how the two leaflets of aLUVs are coupled small and wide angle scattering techniques are ideal, as these methods allow the comparison between structural parameters (e.g. $A_L$ of outer and inner monolayer) of aLUVs and of symmetric LUVs. Additionally, differential scanning calorimetry (DSC) gave insight, whether the leaflets melt together
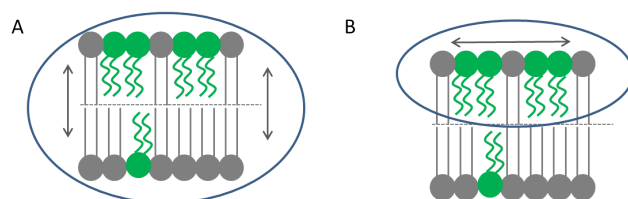
Figure 1.5.: Schematic illustration of transbilayer (A) and intraleaflet (B) coupling mechanisms.

or separately. Together, these measurements helped to draw a conclusion if transbilayer or intraleaflet coupling dominates in the single aLUV systems. Further, dynamic light scattering (DLS), which measures the size distribution profile of the vesicles was used to detect possible contaminants, such as donor MLVs, and to obtain the influence of the aLUVs preparation on the vesicles size distribution. Furthermore, images acquired by cryo transmission electron microscopy (cryo-TEM) revealed the shape of the generated aLUVs. Figure 1.6 gives an overview of the conducted experiments: Two lipid systems were studied: (1) aLUVs with hydrocarbon chain asymmetry by choosing DPPC as donor and POPC as acceptor lipid and (2) aLUVs with headgroup asymmetry (POPE/POPC). For the latter system POPC was used as donor and POPE as acceptor and vice versa, to study the influence of lipid position on the leaflet properties.
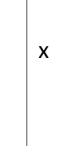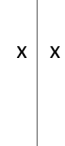
| | outer | inner | exchange efficiency | | | | lipid distribution | | stability | | structure | | |
|---|---|---|---|---|---|---|---|---|---|---|---|---|---|
| | | | DSC | GC | UPLC | NMR | DLS | NMR | DSC | SAXS | SANS | WAXS | TEM |
| asymmetry in chains | DPPC | POPC | | x | x | x | x | | | x | x | x | |
| asymmetry in polar headgroup | POPC | POPE | x | | x | x | x | x | x | x | x | x | x |
| | POPE | POPC | x | | x | x | x | x | x | x | x | x | x |

Figure 1.6.: Overview of samples and conducted experiments.

# 2. Methods

This chapter focuses on a general description of the applied methods and used models for data analyses, which were not fully given in publications. The original publications are attached in the appendix containing additional information on the experimental settings, used materials and data modeling.

## 2.1. Construction of Asymmetric Vesicles

Asymmetric large unilamellar vesicles (aLUVs) were constructed by using a CD mediated exchange process between donor and acceptor lipid vesicles [22, 23, 57]. The acceptor vesicles provide the lipids for the inner-leaflet and the donor multilamellar vesicles (MLVs) the lipids for the outer-leaf. For the preparation a donor to acceptor lipid mole ratio of 2:1 or 3:1 was used, where the lipid stock concentration was determined to be within 1% by inorganic phosphate assay [60]. This is done by measuring the amount of phosphate ($PO_4$) groups from a well defined volume of a sample and therefore the concentration can be assessed. In this procedure the organic groups of the lipids are cleaved off to measure the remaining $PO_4$ groups which are compared to a phosphate dependent calibration curve. This is done with a spectrometer (Jasco V-630 spectrophotometer) by reading the absorbance at $\lambda = 820$ nm. Donor vesicles were hydrated in 20 % (w/w) sucrose solution made from 18 MΩ-cm water (MQ water) and acceptor vesicles were prepared by first hydrating the lipid film in a 20-25 mM NaCl solution. Large unilamellar vesicles (LUVs) of the acceptor lipids were prepared by using a hand-held mini-extruder (Avanti Polar Lipids, AL) with a 100 nm pore-diameter polycarbonate filter. Therefore, the acceptor MLVs were passed through the filter 31-times at least 10°C above the phase

transition. To obtain unilamellar acceptor vesicles, lipids were doped with $5 - 10 \, \text{mol}\%$ PG. Low amounts of charged PG lipids (up to $4 \, \text{mol}\%$) were previously shown not to influence the structural parameters [61]. For PE lipids it was necessary to increase the PG concentration to $10 \, \text{mol}\%$ to ensure unilamellar acceptor vesicles.

Further, our protocol requires separation of donor and acceptor vesicles which can be accomplished most easily by taking advantage of density differences between the two populations. Figure 2.1a shows schematically the preparation of aLUVs. First, the extravesicular sucrose was removed from the donor MLVs by diluting the sample by a factor of 20 with water and by centrifugation for $30 \, \text{min}$ at $20,000 \text{x} g$. The supernatant was discarded and the pellet consisting of the donor lipids was resuspended with a M$\beta$CD solution. The donor MLV/CD mixture was incubated for $2 \, \text{h}$ at room temperature with gentle stirring. In this step the CD got loaded with donor lipids. Next, acceptor LUVs were added to the MLV/CD mixture at approximately 10°C above the acceptor lipid's phase transition for 30 - 60 min. The resultant aLUVs were separated from the donor MLVs by an 8 fold dilution with water and subsequent centrifugation at $20,000 x g$ for $30 \, \text{min}$. Then the supernatant containing the aLUVs and CD was carefully transferred to another container and the pellet was discarded. Solubilized contaminants as CD and sucrose were removed by centrifugal filtration with $100 \, \text{kDa}$ molecular weight cut-off filters, which were pre-washed with $H_2O$ at least 7 times to remove traces of glycerol. The first concentration step was followed by three cycles of successive dilution to $11 \, \text{mL}$ and concentration to $< 0.5 \, \text{mL}$ to allow for the exchange of $H_2O$ and $D_2O$ for ^{1}H-NMR and SANS experiments, besides removing CD and sucrose. [31]

As the outer leaflet of the aLUVs is not exchanged completely and small amounts of donor lipids are located on the inner leaflet, two assays need to be conducted to obtain the composition of the single leafs (see Fig. 2.1b): (1) the exchange efficiency (mole fractions of donor and acceptor lipids in the final aLUVs) needs to be determined e.g. by gas chromatography (GC), by ultra performance liquid chromatography - mass spectroscopy (UPLC-MC) or by differential scanning calorimetry (DSC) (see sec. 2.2) and (2) the lipid asymmetry is quantified by ^{1}H-NMR experiments (see sec. 2.3.1).

Further, symmetric LUVs were prepared from aLUVs, by drying aLUVs to a film under reduced atmospheric pressure using a rotary evaporator. The dried lipid film was redissolved in chloroform, to ensure complete

scrambling of the lipids, and from that point on prepared as acceptor vesicles. These LUVs are called 'scrambled' vesicles throughout the text.
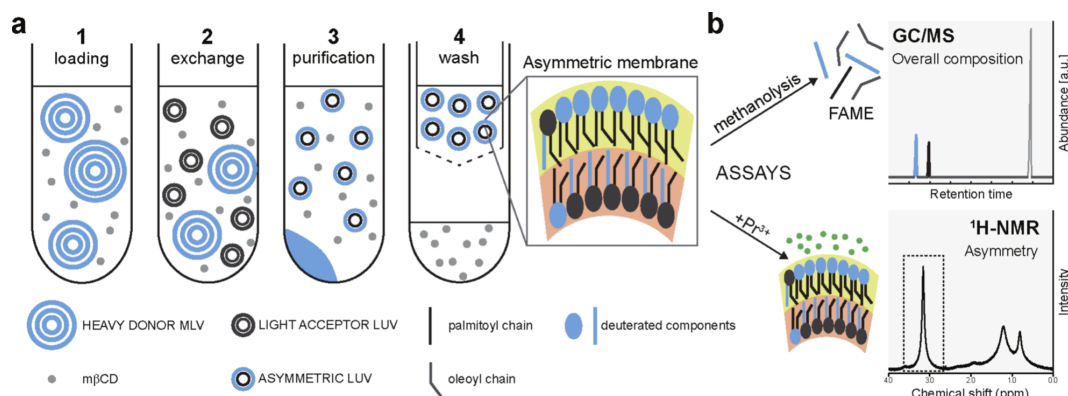


Figure 2.1.: (a) Schematic illustration of the preparation of asymmetric vesicles. (1) incubation of heavy donor MLVs (entrapped sucrose) and methyl-$\beta$ cyclodextrin (M$\beta$CD). M$\beta$CD is loaded with lipids from the donor MLVs, (2) acceptor LUVs are added to the incubation process. M$\beta$CD catalyzes lipid exchange between donor MLVs and acceptor LUVs. (3) Sucrose filled (heavy) donor MLVs are removed by centrifugation, (4) supernatant is taken and the M$\beta$CD is removed by centrifugal concentration, aLUVs are recovered from the retentate. (b) Assays to accurately determine the sample composition: GC/MS or UPLC is used to determine the overall composition of the aLUVs (see sec. 2.2.1) and $^1$H-NMR is applied to quantify lipid asymmetry in a lanthanide shift experiment (see sec. 2.3.1). Figure taken from [31].

## 2.2. Assays for Lipid Exchange

Gas chromatography (GC), ultra performance liquid chromatography - mass spectrometry (UPLC-MS) or differential scanning calorimetry (DSC) was used to determine the exchange efficiency of aLUVs by assessing the mole fraction of donor and acceptor lipids.

### 2.2.1. Chromatography Techniques (GC, UPLC-MS)

Chromatography is the general term for a number of techniques which are used to separate different substances out of a sample. Chromatographs

consist of a column capillary, where the inside is coated with a thin layered material known as stationary phase. Molecules which travel through the column are separated as they are retained by the stationary phase according to their chemical properties. Thus, different molecules elute at different times. Chromatographic techniques can then be coupled to different detector types for identification and quantification of the sample. The two main chromatography techniques which were used in this work are GC and UPLC, see Fig. 2.2 and for more details e.g. [62–64].

In GC the column is coupled to a mass-selective detector (MSD), which records the signal intensity of the analytes against the retention time, where the peak areas are proportional to the mole fractions of each component in the sample. The UPLC on the other hand is connected to a mass spectrometer (MS) giving a further dimension of information, the mass to charge ratio of the molecules, enabling the discrimination of lipid molecular species. The MS captures, ionizes, accelerates, deflects, and detects the ionized molecules separately. The gas chromatograph analysis only compounds which can be vaporized, while UPLC is applicable to liquids. Hence, for GC measurements lipids had to be converted to fatty acid methyl esters (FAMEs). Briefly, this means that the lipid headgroups are cleaved off and only the chains are analyzed (see [31] for details). Therefore, for GC it was necessary to take acceptor and donor lipids which have a chemical or isotopical difference in the chains, while UPLC requires only a chemical or isotopical difference in lipids.

For both methods the mole fraction $\chi_i$ of a single component can be determined directly from the chain (lipid) peak areas $P$:

$$\chi_i = \frac{P_i}{\sum_j P_j},$$

(2.1)

where $P_i$ states the $i^{th}$ chain (lipid) peak area and the denominator represents the sum over all mixture components $j$. This expression is valid when the chain (lipid) peak area fractions vary linearly with mixture composition. Both systems showed a deviation from linearity. Thus, it was necessary to measure a standard curve for data correction (see [31, 65] for details). Parameter uncertainties are estimated to be less than 5%.
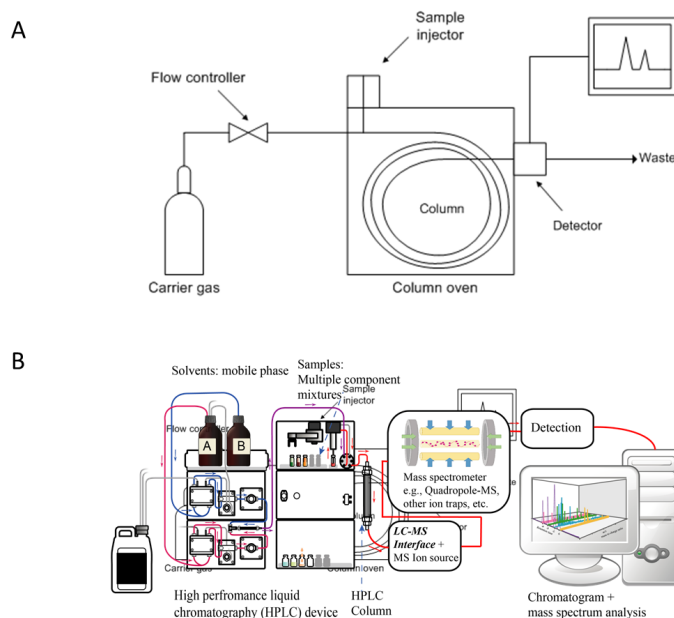
Figure 2.2.: (A) Schematic illustration of a gas chromatograph apparatus [68], and (B) of liquid chromatography tandem mass spectrometry [69].

GC measurements were conducted on an Agilent 5890A gas chromatograph (Santa Clara, CA) with a 5975C mass-selective detector operating in electron-impact mode. An HP-5MS capillary column (30 m × 0.25 mm, 0.25 µm film thickness) was used with a helium carrier at 1 mL/min and an inlet temperature of 270°C. UPLC-MS analysis was performed by an AQUITY-UPLC system (Waters, Manchester, UK) with a BEH-C18-column (2.1x150 mm, 1.7 $\mu$m) (Waters) as previously described [66]. A SYNAPT$^{TM}$G1 qTOF HD mass spectrometer (Waters) equipped with an ESI source was taken for analysis. Data acquisition was done by the MassLynx 4.1 software (Waters) and for lipid analysis the 'Lipid Data Analyser' software [67] was used. UPLC-MS experiments were conducted by Dr. Gerald N. Rechberger (Institute of Molecular Biosciences, University of Graz).

## 2.2.2. Differential Scanning Calorimetry

Apart from the determination of the exchange efficiency of aLUVs, DSC was also applied to obtain the phase transition temperatures of the single leaflets. This was performed to investigate, whether the leafs melt independently or the whole bilayer simultaneously in aLUVs. DSC is an experimental technique for studying the phase transitions and conformational changes in biological systems, such as proteins, nucleic acids, and lipids [70–72]. Thermodynamic information, such as phase transition temperature ($T_M$), transition enthalpy and cooperativity can be obtained from DSC scans. DSC uses a sample cell containing the lipid hydrated in buffer at a concentration of $\sim$1 mg/mL and a reference cell filled with the used buffer. Both cells were heated/cooled (30°C/hour) through the transition temperature (e.g. lipid phase transition) of interest. Throughout the experiment the two cells are kept at the same temperature. By heating/cooling both cells, the difference in power consumption is measured. This leads to a DSC thermogram (curve) which reveals the amount of differential power consumed to keep the two cell temperatures equal.

Calorimetric experiments were performed on a MicroCal VP-DSC high sensitivity differential scanning calorimeter (MicroCal, Inc., Northhampton, MA, USA). The phase transition temperature $T_M$ is taken from the temperature of maximum heat capacity.

The exchange efficiency was determined for POPE/POPC aLUVs via DSC. Therefore, DSC measurements were conducted on POPE/POPC mixtures (LUVs and MLVs) at various POPE concentrations with 10 mol% POPG (POPG is not considered in all labels) from $2 - 40$°C (see Fig. 2.3). To note, doping with POPG lowers the phase transition temperature ($T_M$) by 1°C [73]. A linear regression was computed through the $T_M$, which was taken as the temperature of maximum heat capacity $c_P$ of the DSC-cooling scans of LUVs and MLVs (blue and red dashed line in the inset of Fig. 2.3). To note, DSC cooling (instead of heating) scans were used as the system was equilibrated, which means that the whole sample was in fluid phase at the beginning of the scan (40°C). Especially for high POPC ($T_M \sim -3.6$°C [74]) concentrations the heating-scan phase transition is already ongoing at the initial temperature of the measurement (2°C). In addition, cooling scans
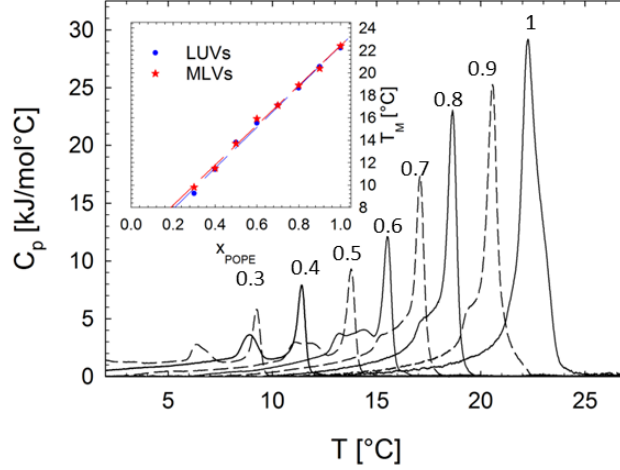
Figure 2.3.: DSC cooling thermograms of POPE/POPC mixtures at various POPE concentrations (adjacent data give the molar fractions of POPE ($x_{POPE}$)). Inset, transition temperatures $T_M$ in dependence of $x_{POPE}$ of LUVs (blue dots) and MLVs (red starts) calibration curves. Figure taken from [75].

show sharper transition peaks, due to higher cooperativity (K. Lohner, personal communication, June 22, 2017), which facilitated the determination of $T_M$. As the determined $T_M$s increase linearly with POPE concentration, it allowed us to determine the molar fraction of POPE ($x_{POPE}$) by conducting DSC scans of the scrambled samples

$$x_{POPE} = \frac{T_M - a_0}{a_1},\qquad(2.2)$$

where $T_M$ is the phase transition temperature of the scrambled sample, $a_0 = 4.2°C$, $a_1 = 18.2°C$ [75]. It has to be noted that the linear relationship between $T_M$ and $x_{POPE}$ breaks down at low POPE content. Therefore, Eq. 2.2 is not valid for $x_{POPE} < 0.3$. (POPC is supposed to melt at $\sim -3.6°C$ [74] and at even slightly lower temperatures by investigation of a cooling scan. By taking the linear regression (eq. 2.2), POPC melting transition would be at $+4.2°C$.)

## 2.3. Assay for Lipid Asymmetry

### 2.3.1. Nuclear Magnetic Resonance

Nuclear Magnetic Resonance (NMR) spectroscopy uses the physical phenomenon where nuclei in a magnetic field absorb and re-emit electromagnetic (EM) radiation. The frequency of radiation necessary to absorb the energy depends on the following properties: First, it is characteristic of the type of nucleus (e.g. $^1$H, $^{13}$C). Second, it depends on the chemical environment of the nucleus. Third, the frequency also depends on the spatial location in the magnetic field, which provides the basis for magnetic resonance imaging (MRI). However, for most spectroscopic experiments a homogeneous magnetic field through the sample is necessary. The ability of the nuclei to absorb EM radiation is due to Zeeman splitting leading to a separation of the nuclear energy levels ($\Delta E$) for spin I = 1/2 nuclei. The magnitude of the Zeeman splitting in an NMR experiment is typically in the order of the radio frequency and increases with field strength. As the Zeeman splitting depends on the magnetic field strength, NMR spectra are expressed in chemical shift which is the resonance frequency of a nucleus relative to a standard in a magnetic field. The chemical shift $\sigma$ is usually given in parts per million (ppm) by frequency:

$$\sigma = \frac{\nu_{sample} - \nu_{ref}}{\nu_{ref}},\qquad(2.3)$$

where $\nu_{sample}$ and $\nu_{ref}$ expresses the absolute resonance frequency of the sample and the standard resonance compound, respectively [76].
In our case, $^1$H-NMR is especially useful to determine the distribution of PC-headgroups between the inner and outer leaflet by using a paramagnetic shift reagent: The choline methyl group consists of nine equivalent protons leading to the strongest resonance by investigating PC-LUVs, see Fig. 2.4. Adding a paramagnetic lanthanide ion ($Pr^{3+}$) to the sample, which interacts with choline protons located on the outer leaflets only, leads to a downfield resonance shift [32]. As a result, outer and inner leaflet of the choline resonances can be separately investigated, and the integrated NMR peak area of each resonance is proportional to the number of molecules having

protiated headgroups in the corresponding leaf [32]. The choline resonance was modeled by using a Lorentzian peak for the unshifted (inner leaflet) and shifted choline (outer leaflet), see Fig. 2.4. For clarification, the deuterated choline (of head deuterated PC lipids) does not contribute to the $^1$H-NMR signal allowing the investigation of isotopically asymmetric samples, see Fig. 2.4.

Proton NMR spectra were collected on an Avance III 300 or 400 MHz spectrometer (Bruker, Billerica, MA) taking the Bruker TopSpin acquisition software, and analyzed with TopSpin 3.2.

The integrated area $R$ of both resonances is proportional to the number of molecules having protiated headgroups in the corresponding leaflet. The peak fraction of the outer leaf is defined as:

$$f^o = \frac{R^o}{R^i + R^o},$$

(2.4)

where the superscripts $o$ and $i$ represent the outer and inner leaf.

Further, it has to be considered that the surface area of the outer leaflet is slightly bigger. Therefore, the mole fraction of lipids on the outer leaflet ($X^o$) is increased compared to the inner leaflet. Additionally, $X^o$ depends on the average $A_L$ of the outer and inner leaflet ($A_L^o$ and $A_L^i$: )

$$X^o = \frac{1/A_L^o}{1/A_L^o + 1/A_L^i} * sf$$

(2.5)

where $sf$ stands for surface fraction considering the slightly bigger surface of the outer to the inner leaflet ($sf$ = 1.06 for a vesicle diameter of 130 nm, bilayer thickness of 4 nm [11]). As only one mixture component possesses a protiated choline we define the peak fraction of component $n$ on the outer leaf by

$$f_n^o = \frac{X^o \chi_n^o}{\chi_n},$$

(2.6)
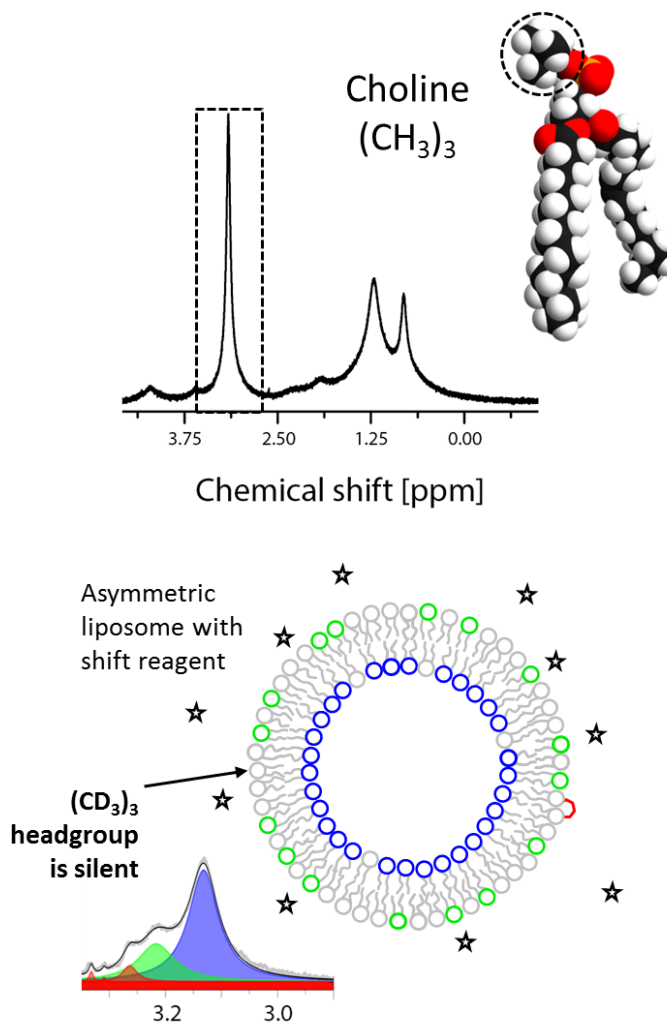
Figure 2.4.: Proton NMR of aLUVs prepared from POPC acceptor and choline deuterated POPC donor (which stays silent). Upper panel, $^1$H-NMR shows a sharp choline resonance from POPC acceptor (dashed field). Lower panel, in the presence of Pr$^{3+}$ not exchanged acceptor POPC lipids shift (green shading) relative to the unshifted population (blue shading) which reveals substantial outer leaflet donor enrichment in the aLUV sample. Minor contaminants glycerol and M$\beta$CD are shown with red shading. Figure adapted from [31].

where $\chi_n^o$ is the outer leaflet mole fraction and $\chi_n$ is the total bilayer mole fraction of component $n$, where $f_n^0$ is given by eq. 2.4 [31].

For a bilayer consisting of lipid A and B, all compositional parameters $\chi_{A,B}^{o,i}$ can be expressed as [31]:

$$
\begin{aligned}
\chi_A^o &= \frac{f_A^o \chi_A}{X^o} \\
\chi_A^i &= \frac{(1-f_A^o)\chi_A}{(1-X^o)}. \\
\chi_B^{i(o)} &= 1 - \chi_A^{i(o)}
\end{aligned}
\tag{2.7}
$$

The same approach can be used to study the life-time of asymmetric samples [39]. Therefore, aliquots of the aLUVs are taken for NMR measurements right after the preparation to obtain a value for time zero and at a series of time points of interest. It has to be noted, that $Pr^{3+}$ was added just before conducting NMR measurements. By this approach the passive lipid flip-flop rate can be studied, which is given by

$$
\Delta C(t) = \frac{2 f_{PC}^{out}(t) - 1}{2 f_{PC,0}^{out} - 1},
\tag{2.8}
$$

where $f_{PC,0}^{out}$ and $f_{PC}^{out}$ is the fraction of POPC on the outer leaf at time zero and at time $t$, respectively. To clarify, $\Delta C(t)$ of one indicates no lipid flip-flop, while zero represents a the lipid composition of a symmetric sample.

## 2.4. Vesicle Size - Quality and Distribution

### 2.4.1. Dynamic Light Scattering

A Zetasizer Nano ZSP (Malvern Instruments, Herrenberg, Germany) equipped with 10 mW laser with $\lambda = 632.8$ nm was used for determination of the size distribution profile of acceptor LUVs and aLUVs. Samples were diluted with filtered MQ-water to a concentration of $\sim 0.05$ mg/mL. Dynamic light scattering (DLS) measurements were conducted to obtain the influence of

the aLUVs preparation on the size distribution and for detecting contamination, such as donor MLVs in the aLUVs. Thus, the size distribution profile of extruded acceptor vesicles and of the final aLUVs was measured. DLS is a technique to measure the size distribution profile of small particles in solutions. Monochromatic light is shot through a polarizer into a specimen, where it is getting scattered elastically at the sample as long as the particle size is small in comparison to the wavelength ($\lambda$) of the light. The scattering intensity fluctuates over time, because of the movement of the particles in solution as they undergo Brownian motion. The scattered light shows either constructive or destructive interference with the surrounding particles, which changes over time due to these intensity fluctuations. Hence, information on the time scale of the particles movement is contained. The dynamic information of particle movement is derived by an autocorrelation function from which the diffusion coefficient $D$ can be determined. As the viscosity of the solvent is known, it is possible to assess the size distribution profile ($r$) by applying the Stokes-Einstein equation:

$$r = \frac{k_B T}{6 \pi \eta D},$$
(2.9)

where $k_B$ is the Boltzmann constant, $T$ the absolute temperature and $\eta$ the viscosity of the media [77]. For our DLS measurements the scattering at an angle of 173° was detected, which is known as backscatter detection. This reduces multiple scattering, and the influence of large contaminant particles (e.g. dust) as they scatter mainly in forward direction [78].
In DLS the mean value for the size (Z-average) and the polydispersity index (PDI), which is a dimensionless measure of the broadness of the size distribution are obtained. The PDI is defined as the squared ratio of the peak width and particle size ($PDI = (width/size)^2$). One indication of an successful sample extrusion is a $PDI < 0.1$ revealing a 'monodisperse' narrow distribution [78].

### 2.4.2. Cryo-Transmission Electron Microscopy (cryo-TEM)

Cryo transmission electron microscopy (cryo-TEM) is a complementary technique to SAS. In general, cryo-TEM is ideal to investigate a small part of

the sample, while with scattering techniques the whole illuminated sample is obtained which means that average parameters are determined. In this work cryo-TEM images were acquired to gain information about the vesicle shape in gel and fluid phase, while scattering techniques were used to determine structural parameters.

As electrons would scatter at air particles, the chamber needs to be evacuated for cryo-TEM measurements. Consequently, the liquid specimen has to be frozen for investigation. The formation of cubic ice in the sample has to be prevented, which can be achieved by very fast freezing. To note, cubic ice is water in a crystal lattice which easily absorbs the electron beam, screening the sample. For sample preparation, the following steps are performed: First a droplet of the sample is added on the grid and residual water is removed by filter paper. Afterwards it is frozen in liquid ethane as the freezing process is quick enough for water to only solidify as vitreous ice (amorphous ice). Liquid nitrogen would be at cold enough temperatures ($\sim -195°C$), however, its heat capacity is very low. Thus, as soon as the grid is dropped into the liquid nitrogen, a part of it boils off, which slows down the freezing process leading to the formation of cubic crystals. Ethane, compared to liquid nitrogen, has a much higher heat capacity and a slightly higher melting point (-188°C), which makes it capable to freeze water fast enough to reach an amorphous state. After the sample is frozen it can be stored in liquid nitrogen until it is used for measurement, see Fig. 2.5 (see e.g. [79] for further information). Images were acquired using a FEI T12, 120 kV, $LaB_6$-cathode transmission electron microscope (Hillsboro, Oregon). Our samples were prepared in a very controlled atmosphere in 99% relative humidity using a Leica EM GP plunge freezer (Wetzlar, Germany) and investigated on the TEM grids at 22°C. Cryo-TEM images were acquired at the FELMI-ZFE (Graz, Austria) by Dr. Ilse Letofsky-Papst.

## 2.5. Small/Wide Angle Scattering Techniques

Small-angle scattering (SAS) is a powerful technique to obtain information about the shape and structure of e.g. colloidal particles, proteins and liposomes. The accessible length scale of SAS experiments depends on the experimental settings, but in general it is in the range of $\sim$1 - 1000 Å.
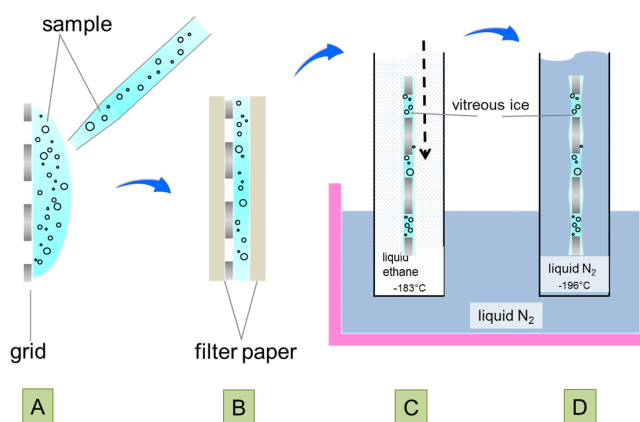
Figure 2.5.: Schematic illustration of the cryo-TEM sample preparation. A) Droplet of sample is added on the grid, B) liquid residues are removed with filter paper, C) sample is quickly frozen in liquid ethane and D) stored in liquid nitrogen till measurement. Figure adapted from [80].

SAS-techniques investigate small deflections ($\sim 0.1 - 10°$) of collimated radiation after interaction with much larger structures in comparison to the radiation wavelength (for X-rays $\lambda \sim 1\,\text{Å}$ and neutrons $\lambda \sim 5\,\text{Å}$). Hence, SAS methods are ideal to study the structure of lipid bilayers ($\sim 40\,\text{Å}$) as well as the organization of the chains in gel phase which can be determined with wide angle X-ray scattering (WAXS). Neutrons and X–rays can scatter elastically (collisions lead to a change of direction with no loss in energy) and inelastically (loss of energy during the interaction process with the sample). In SAS, only elastic scattering of X–rays and neutrons is used. These techniques and how to model scattering data are described in more detail below (see sec. 2.5.1, 2.5.2, 2.6).

## 2.5.1. Small Angle Scattering (SAXS/SANS)

X–rays are a form of electromagnetic radiation which can be produced at a synchrotron or with a home source X–ray generator, while neutrons are produced in an atomic reactor or in a spallation neutron source (SNS). In case of X–rays energies $E$ and wavelength $\lambda$ can be expressed by De Broglie's

equation:

$$E_{X-ray} = \frac{hc}{\lambda},$$ (2.10)

where $h$ is the Planck constant and $c$ the speed of light. In contrast, neutrons neutrons have a finite mass ($m = 1.674 * 10^{-27}$ kg) and therefore it is necessary to consider its kinetic energy given by

$$E_n = \frac{mv^2}{2} = \frac{h^2}{2m\lambda^2}.$$ (2.11)

Hence, for a wavelength of e.g. $\lambda = 1.5$ Å the X-ray energy is more than $200,000$ times higher compared to the energy of neutrons ($E_{X-ray} \sim 8.2$ keV, $E_n \sim 36$ meV) [81]. SAXS samples were measured with photon energies of $20$ keV ($\lambda = 0.6$ Å) at the P12 BioSAXS beamline, located at the Petra III (EMBL/DESY) in Hamburg (Germany) and with $12.5$ keV ($\lambda = 0.99$ Å) at the ESRF-BM29 in Grenoble (France). While SANS experiments were conducted at the BL-6 Extended Q-range Small Angle Neutron Scattering (EQ-SANS) instrument located at the SNS in the Oak Ridge National Laboratory (TN, USA) with a wavelength band of $\lambda = 4.0 - 7.5$ Å and $10.0 - 13.5$ Å, and at KWS-1 at the FRMII reactor (Garching, Germany) [82, 83] by $\lambda = 5$ Å. As mentioned above SAS techniques use only elastic scattering, which is characterized by zero energy transfer. Hence, the norm of the incident wavevector ($k$) is equal to the norm of the scattered wavevector ($k'$). SAS patterns are typically represented by the scattering vector $q$ which is defined as:

$$q = |\vec{k} - \vec{k'}| = \frac{4\pi sin(\theta)}{\lambda}.$$ (2.12)

SAXS measures the inhomogeneities in electron density of the sample as X–rays interact with outer shell electrons of the single atoms. Figure 2.6A illustrates the scattering cross sections of X–rays (upper-panel) and neutrons (lower panel). It can be seen that the X–ray scattering cross section increases with the size of the atoms, while for neutrons there is no obvious correlation between the atomic size and neutron scattering length density. In contrast, neutrons are scattered by atomic nuclei which can be used for contrast variation analysis, as hydrogen and its isotope deuterium scatter with

similar efficiencies, however 180° out of phase. This means that deuterium's coherent neutron scattering length (NSL) is positive while hydrogen's is negative. Hence, contrast variation in neutron experiments can be realized by taking different ratios of $D_2O$ to $H_2O$ for the solvent, or by specific deuteration of the material [84, 85]. For this work the hydrogen atoms of the headgroup or acyl chains were exchanged with deuterium atoms to obtain a large intramolecular contrast [86–89], see Fig. 2.7. It has to be noted, that the deuteration of lipids does not change the chemical nature of the material, which is a significant advantage compared to the use of bulky lipid probes which are taken for many spectroscopic techniques [16].

To obtain a good signal the net electron/neutron density $\Delta\rho(\vec{r})$ has to be high, which is defined as the difference of the average scattering length density (SLD) (electron or neutron scattering length (NSL) density (ED/NSLD)) from the sample $\rho(\vec{r})$ and the solvent $\rho_s$:

$$\Delta\rho(\vec{r}) = \rho(\vec{r}) - \rho_s, \tag{2.13}$$

where $\rho$ of a molecule is defined as:

$$\rho = \frac{\sum_i b_i}{V_m}, \tag{2.14}$$

where $b_i$ is the amount of electrons/NSL of the $i^{th}$ atom in the molecule and $V_m$ is the volume of the molecule.

In biological samples the net electron density is generally low because they contain a lot of light molecules, such as hydrocarbons which are mainly located in the lipid chain. By investigating lipid bilayers with X–rays, a good contrast (big net electron density) is obtained for the phosphate group located in the lipid's headgroup, while for SANS measurements a good signal comes from the glycerol backbone, see Fig. 2.6B. The highest structural confidence can be gained by using different contrasts obtained by neutrons and X–rays [16].

## 2.5.2. Wide Angle X-ray Scattering (WAXS)

Besides the structural parameters of the lipid bilayer which are determined in the small angle region (q $\sim 0.05 - 0.8 \, \text{Å}^{-1}$), the wide angle reflections
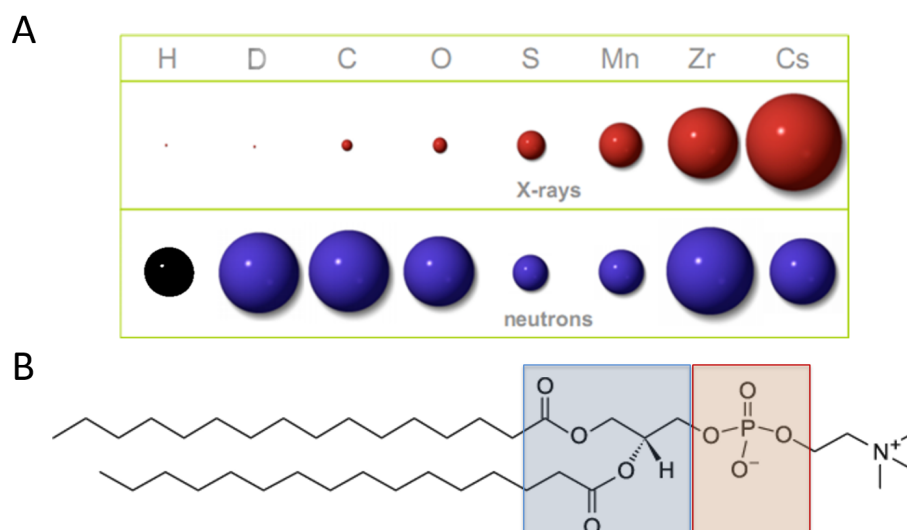
Figure 2.6.: (A) Schematic illustration of X–ray and neutron scattering cross sections: The X–ray cross section (electron scattering length density) increases with the size of atoms (upper panel), while there is no correlation between atomic size and neutron scattering cross section (lower panel). Further, the neutron scattering cross section for D is positive (blue sphere), while H has a negative one (black sphere) [90]. (B) Chemical representation of a DPPC-lipid: In SAXS measurements a good contrast is obtained from the phosphate group (red) and in SANS experiments from the glycerol backbone (blue). Chemical structure taken from Avanti: avantilipids.com.

($q \sim 1.3 - 1.6 \, \text{Å}^{-1}$) correspond to the packing of the chains in gel phase. WAXS measurements were performed in house at the SAXSpace System (Anton Paar, Austria). Cu K$\alpha$ (1.54 Å) radiation is supplied by a Genix 3D microfocus tube (Xenocs, France) with a power consumption of 30 W (anode current: I = 0.6 mA, tube voltage: V = 50 kV). It is equipped with a Eiger R 1M detector system (Dectris, Swiss) with a pixel size of $75x75 \, \mu\text{m}^2$. The q-range in the wide angle configuration reaches from 0.4 to $1.82 \, \text{Å}^{-1}$.

Chains in gel-phase pack into a 2-dimensional lattice. In contrast the lipid headgroups do not form a crystalline lattice in the gel phase, which means they contribute to diffuse scattering, however, do not diffract [91]. The 2-dimensional chain packing is for the L$_\beta$ phase (e.g. for POPE) hexagonal, or for the L$_{\beta'}$ phase (e.g for DPPC) distorted hexagonal, see Fig. 2.8. In the
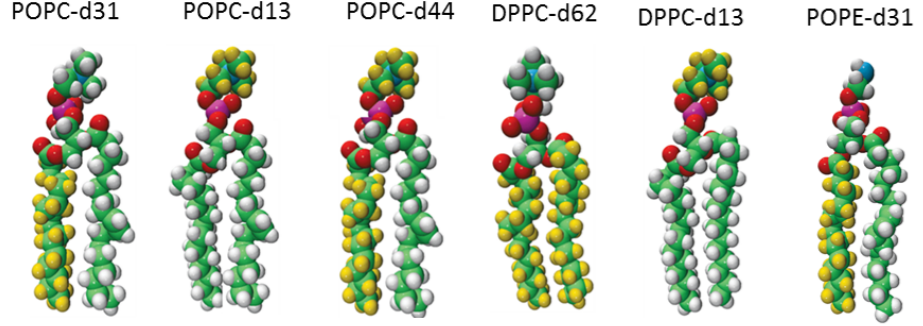
Figure 2.7.: Chemical structures of deuterated phospholipids. Lipids are displayed in space fill representation: white indicates hydrogen and yellow deuterium. Chemical structure taken from Avanti: avantilipids.com

hexagonal chain packing all neighbors are equivalent ($s_{\bar{1}1} = s_{11} = s_{20}$, where the subscripts correspond to the Miller indices), leading to a rise of the first order diffraction peak which can be fitted with a single Gaussian. For the disordered hexagonal lattice two of the six neighbors are closer compared to the other four. Consequently, the WAXS diffraction peak splits into two ($s_{\bar{1}1} = s_{11} < s_{20}$)), see Fig. 2.8. The area per hydrocarbon ($A_C$) of chains packed in a hexagonal lattice ($L_\beta$) can be determined by [92]:

$$A_C = \frac{8\pi^2}{\sqrt{3}q_{11}^2},$$

(2.15)

and for the $L_{\beta'}$ it is obtained by [93]

$$A_C = \frac{4\pi^2}{\sqrt{q_{11}^2 q_{20}^2 - q_{20}^4/4}},$$

(2.16)

where the $q_{hk}$ correspond to the hydrocarbon WAXS reflection with the Miller indices h and k. The lateral area per lipid ($A_L$) for lipids in the $L_\beta$ phase is simply

$$A_L = 2A_C,$$

(2.17)

while for the $L_{\beta'}$ phase it is
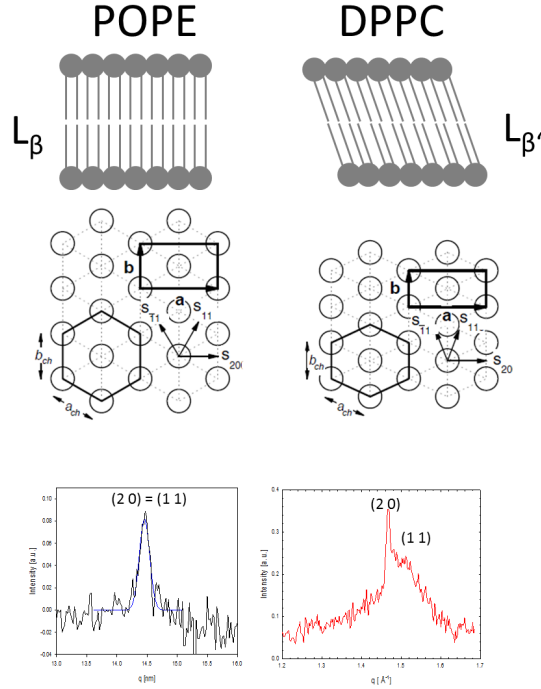
Figure 2.8.: In the $L_\beta$ phase the chains arrange in a hexagonal lattice leading to a sharp wide angle reflection which can be fitted with a Gaussian (left), while for the $L_{\beta'}$ phase the chains arrange in a distorted hexagonal lattice, leading to a split of (2 0) and (1 1) peak (right). Figure modified from [95].

$$A_L = \frac{2A_C}{cos(\theta_t)}, \tag{2.18}$$

where $\theta_t$ is the average tilt of the hydrocarbon chains. Besides $A_L$ also the correlation length of scattering domains $\xi_D$ can be estimated by using the Scherrer equation from the width of the diffraction peak. The Scherrer equation is given by [94]

$$\xi_D \simeq \frac{\lambda}{\beta cos(\theta)}, \tag{2.19}$$

where $\beta$ is the full width half maximum, after subtracting the instrumental broadening and $\theta$ is the Bragg angle.
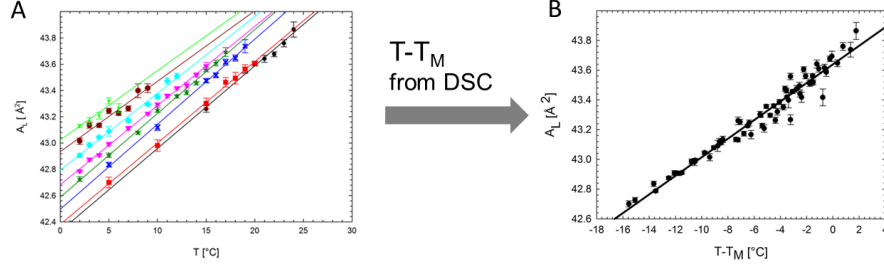
Figure 2.9.: WAXS calibration curves of POPE/POPC mixtures for $x_{POPE} = 1$ (black line) to 0.3 (green line) on absolute (A) and reduced temperature scale (B), including the calculated linear regression. Figure adapted from [75].

WAXS measurements were conducted to study the coupling mechanism of POPC/POPE aLUVs in gel-phase. Therefore, it was necessary to determine $A_L$ of symmeteric POPC/POPE (+10 mol% PG) LUVs (Fig. 2.9A). To note, the same sample compositions were taken as for DSC measurements ($x_{POPE} = 0.3 - 1.0$), see sec. 2.2.2. The obtained $A_L$ were collapsed by using the reduced temperatures $(T - T_M)$, where $T_M$ was taken from the DSC calibration curve, eq. 2.2 (Fig. 2.9B). The $A_L$ of the symmetric POPC/POPE samples is given by the calculated linear regression on the reduced temperature scale (Fig. 2.9B)

$$A_L = k(T - T_M) + A_{POPE}^{T_M}, \tag{2.20}$$

where the slope $k = 0.0625 \pm 0.0002$ Å$^2$/°C and $A_{POPE}^{T_M} = 43.6 \pm 0.002$ Å$^2$. By considering eqs. 2.20 and 2.2 it is possible to determine the $A_L$ of any symmetric POPE/POPC composition. These values were used to compare with obtained $A_L$ of aLUVs to draw conclusions on the coupling mechanism, see sec 3.4.5 for details.

## 2.6. Modeling of SAXS and SANS Data

SAXS and SANS data can be analyzed analogously. In contrast to imaging techniques, real-space information cannot be taken directly from the

measured data. Due to the loss of phase information, scattering data has to be reconstructed to obtain real space information. For lipid membranes this can be either done by a model-free approach [96] or by using special models [97]. Here, we focus on the latter route as it enables insight into structural details of lipid membranes.

Low- and high-resolution models were adapted to describe the internal transbilayer structure of aLUVs. These models were previously applied to symmetric lipid bilayers and are applicable to jointly analyze SAXS and SANS data to obtain the highest structural confidence as mentioned above. The underlying SLD profile is either described in form of slabs or by the so called scattering density profile (SDP). Structural details, such as the individual $A_L$ and the hydrocarbon thickness ($D_C$) of the single leafs were obtained by both approaches. Both models are described below, for further information see [65].

The intensity of a SAXS and SANS curve $I(q)$ can be approximated for a sufficiently diluted system and for $q > 0.03$ by

$$I(q) \approx |F_{FB}(q)|^2, \tag{2.21}$$

where $F_{FB}$ is the flat bilayer form factor which contains information about the distribution of matter across the bilayer (for further information see [98, 99]). Additionally, Brzustowicz and Brunger [100] have shown that for free floating vesicles with transmembrane asymmetry, a flat bilayer model leads to a good description of the scattered intensity.

The flat bilayer form factor ($F_{FB}$) is expressed as the Fourier transform of the SLDs:

$$\begin{aligned} |F_{FB}| &= \int_{-D_i}^{D_o} \Delta\rho(z)\exp(iqz)dz \\ &= \sqrt{F_{cos}^2 + F_{sin}^2}, \end{aligned} \tag{2.22}$$

where $\Delta\rho(z)$ is the net scattering length density, and $F_{cos} = \int_{-D_i}^{D_o} \Delta\rho\cos(qz)dz$ and $F_{sin} = \int_{-D_i}^{D_o} \Delta\rho\sin(qz)dz$ are the real and imaginary parts of $F_{FB}$. The integration proceeds over the full bilayer thickness, where $D_i$ is the innermost

distance and $D_o$ its outermost distance. To note, for symmetric bilayers the imaginary part of the Fourier transform ($F_{sin}$) is zero as a centrosymmetric system is getting investigated.

## 2.6.1. Slab Model

The advantage of the slab model is that it requires less free parameters to analyze the scattering data compared to the SDP model (see 2.6.2). To fit SANS data of aLUVs, a 4–slab model is sufficient where the slabs correspond to the headgroup (including the number of bound water molecules ($n_W$)) and hydrocarbon region on the inner and outer leaflet. However, for the SAXS data analyses an additional slab for the terminal methyl groups on both leafs needs to be included due to the significant differences in electron densities between the $CH_2$ and methyl ($CH_3$) groups resulting in a 6–slab model [65]. The bilayer's SLD profile for the 4-slab model is expressed as

$$\rho(z) = \begin{cases} \rho_{core} & z < -(D_C^i + D_H^i) \\ \rho_H^i & -(D_C^i + D_H^i) \leq z < -D_C^i \\ \rho_C^i & -D_C^i \leq z < 0 \\ \rho_C^o & 0 \leq z < D_C^o \\ \rho_H^o & D_C^o \leq z < D_C^o + D_H^o \\ \rho_S & z \geq D_C^o + D_H^o \end{cases} , \qquad (2.23)$$

where the $\rho$'s are SLDs (see Sec 2.5.1) and the $D$'s denote thicknesses of the single slabs. The superscripts $i$ and $o$ state outer and inner leaflets, respectively (see also Fig. 2.10) [31, 65]. As the SLD of the membrane core matches that of the solvent ($\rho_{core} = \rho_S$), the limits of the integral in Eq. (2.22) are well-defined, and insertion of Eq. 2.23 into Eq. 2.22 yields an analytical solution for the $|F_{FB}|$ (see [31, 65] for details).

It is possible to reduce the number of adjustable parameters by enforcing matter conservation by assuming volume incompressibility and space filling, which essentially couples the thicknesses of the individual layers to the projected $A_L$ and lipid molecular volume $V_L$, as schematically illustrated in
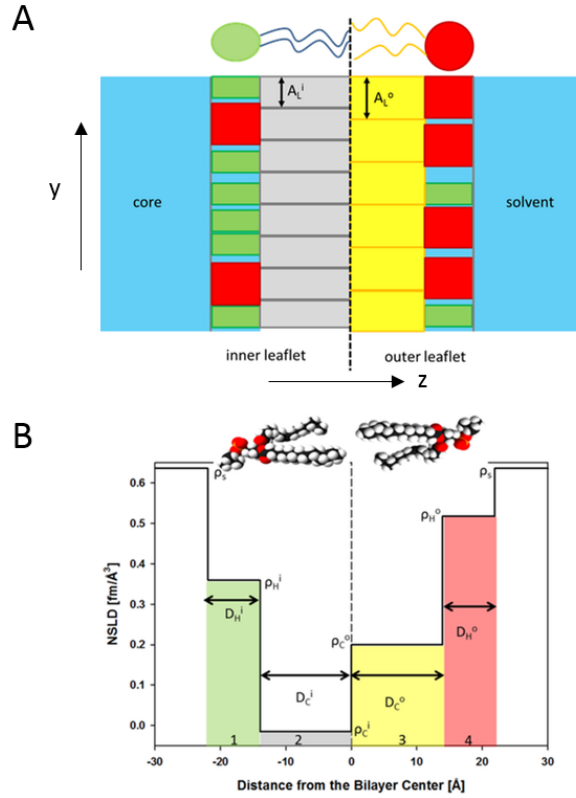
Figure 2.10.: Schematic illustration of the slab model: (A) space-filling representation of an asymmetric bilayer. Individual bilayer components (lipid-headgroups, chains and water molecules) are represented by boxes with fixed areas (representing fixed lipid volumes). The thicknesses in z direction can be different for the inner and outer leaflet, but only with a corresponding change in the projected area (y-dimension). The number of lipids can be different for the inner and outer leaflet. (B) the neutron scattering length density (NSLD) profile across the bilayer is obtained by averaging over the composition of each slab. Figure adapted form [65].

Fig. 2.10A [101–103]. The hydrocarbon chain length of each leaflet is defined as

$$D_C^{o,i} = \frac{V_C^{o,i}}{A_L^{o,i}} \tag{2.24}$$

and the total bilayer (Luzzati) thickness [104] as

$$D_B = \sum_{o,i} \frac{V_L^{o,i}}{A_L^{o,i}}.$$
(2.25)

Volumetric data for the single slabs and for the single molecular fragments of the asymmetric SDP-model (aSDP) (see Sec. 2.6.2) were taken from Kučerka et al. [105–107]. Furthermore, temperature-dependent values of $V_M$ can be found e.g. in [105, 108, 109].

SAXS data were treated very similarly to SANS, however, an additional slab on each leaflet had to be added for the terminal methyl groups as explained above. Further, due to different electron SLDs compared to NSLDs the single slabs were parsed differently (see [65] for details).

## 2.6.2. Asymmetric Scattering Density Profile Model (aSDP)

The slab model assumes sharp boundaries between the single slabs, however, this does not appear to be a realistic view, as individual lipid molecules fluctuate. The SDP-model considers these fluctuations by parsing the lipid structure into quasi-molecular fragments with a certain distribution profile [103, 110]. These quasi-molecular fragments were parsed based on MD-simulations [103].

The SDP model was adapted to describe asymmetric bilayers (aSDP-model), because of the higher spatial resolution, however, more free parameters are needed compared to the slab model. The bilayer structure is described by the SDP model in terms of one-dimensional volume probability distribution (VPD) of quasi-molecular lipid fragments. The net SLD of the SDP-model is expressed by

$$\Delta\rho(z) = \sum(\rho_n - \rho_s)P_n(z),$$
(2.26)

where $\rho_n$ and $\rho_s$ is the SLD of the $n^{th}$ molecular lipid fragment and of the solvent, while $P_n(z)$ indicates the VPD of the molecular fragments [111, 112]. Inspired by [61], each leaflet was parsed as follows: methyl (M), hydrocarbon (HC), carbonyl + glycerol (CG), and into the residula headgroup (RH) . The RH-group consists for PC lipids of choline methyl + phosphate + $CH_2CH_2N$

and for PE-lipids of CH2CH2NH3 + phosphate. The VPDs for the RH, CG and M groups are modeled as Gaussians.

$$P_n(z) = \frac{c_n}{\sqrt{2\pi}} exp\left(-\frac{(z-z_n)^2}{2\sigma_n^2}\right), \tag{2.27}$$

$$n = RH, CG, M, \tag{2.28}$$

where $c_n = V_n/(A_L\sigma_n)$ and $\sigma_n$ and $z_n$ are the width and position of the Gaussian, respectively (Fig. 2.11). The HC groups are normally described by smooth plateau-like functions using error functions [111]. However, we must also consider different contrasts in the outer and inner HC region. Therefore two separate smooth bridging functions are required, which leads to a significant increase in computational efforts. Hence, inspired by [113] two half period of a squared sine/cosine functions were applied

$$P_{HC}(z) = \begin{cases} sin\left(\frac{(z-z_{MN_i}+\sigma_{MN})}{2\sigma_{MN}}\frac{\pi}{2}\right)^2 & \text{for } z_{MN_i} - \sigma_{MN} <= z < z_{MN_i} + \sigma_{MN} \\ 1 & \text{for } z_{MN_i} + \sigma_{MN} <= z < z_{MN_o} - \sigma_{MN} \\ cos\left(\frac{(z-z_{MN_o}+\sigma_{MN})}{2\sigma_{MN}}\frac{\pi}{2}\right)^2 & \text{for } z_{MN_o} - \sigma_{MN} <= z < z_{MN_o} + \sigma_{MN} \end{cases} \tag{2.29}$$

where $z_{MN_{i,o}}$ is the 0.5-probability value for the hydrocarbon region, defining also the thickness of the inner and outer hydrocarbon layer $D_C^{i,o}$. The bridge function reaches a volume probability value of one between the squared sine/cosine functions to ensure spatial conservation, hence the probability function of the methylene regime is $P_{MN} = P_{HC} - P_M$.

In case the outer and inner bilayer leaflets contain contrasting hydrocarbon chains, two distinct methyl groups must be modeled. This was accomplished by displacing each leaflet's methyl group slightly from the bilayer midplane. However, we ensured that the combined envelope function is a single Gaussian, as observed for symmetric bilayers when both amplitudes are equal (Fig. 2.11) [65].

Following the spatial conservation, the water (solvent) probability function $P_s$ can be calculated as

$$P_s(z) = 1 - \sum_n P_n(z), \tag{2.30}$$
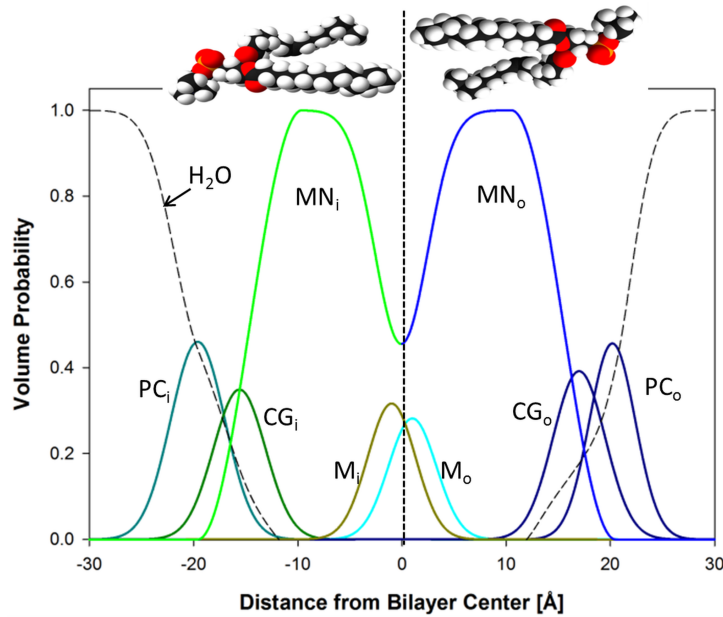
Figure 2.11.: Schematic illustration of the volume probability distribution for an asymmetric bilayer. Figure taken from [65].

with $n = RH^{o,i}, CG^{o,i}, MN^{o,i}, M^{o,i}$ [61, 110].

Structural parameters were calculated by the same approach as for the slab model (see Eq. 2.24 and 2.25) by fitting the scattering curve with the $|F_{FB}|$ (see Eq. 2.21 and 2.22).

## 2.6.3. Joint Refinement of Small Angle X–ray and Neutron Scattering Data

To fully exploit the advantages of contrast variation, all SAXS and differently contrasted SANS datasets were fitted together. For the slab model, this was accomplished by demanding the same values for $A_L^{i,o}$ and the number of bound water molecules $n_W^{i,o}$ for all SAXS and differently contrasted SANS datasets, while for the aSDP model, the VPDs of quasi-molecular fragments are the common backbone. For the joint analysis the summed square of the residuals was determined and minimized for all SANS and SAXS

data sets for a certain aLUV system by using optimization routines. For the slab and aSDP model different optimization routines were applied. Because of the small amount of free parameters of the slab model, it was sufficient to use the trust region reflective algorithm, which is related to the Levenberg-Marquardt algorithm, however, the step size is restricted in order to prevent it from overstepping [114]. This algorithm is not applicable to the aSDP-model, due to the risk that it will get stuck in a local minimum, because of the large number of adjustable parameters. To overcome this problem, a random search or stochastic algorithm, like the differential evolution (DE) algorithm [115–117] is ideal to apply. Therefore, we applied the DE algorithm, which uses a global search for the best solution. This is accomplished by starting with an initial population of solutions, which are subsequently combined and "mutated" to form new solutions that are accepted or rejected based on their agreement with experimental data [65].

# 3. Results and Discussion

This section gives an overview of all obtained results. Further details to e.g. structural/experimental parameters, and equations are explained in the original publications, which are attached at the end of this thesis.

The major goal of this work was to determine how the structural properties of the two leafs are coupled. Scattering techniques (SAXS, SANS, WAXS) are the ideal tools in this regard, as they allow to determine structural properties of the single leaflets, such as the $A_L$, thickness of the bilayer ($D_B$) and thickness of the hydrocarbon region ($D_C$).

## 3.1. Testing Models on Symmetric POPC LUVs

The adapted slab and SDP model (see sec. 2.6) were tested by standalone SAXS or SANS data and by joint analyses of SAXS and different contrasted SANS data. Therefore, we prepared four symmetric POPC LUVs samples with different internal contrasts (POPC, POPC-d13, POPC-d31, and POPC-d44). For the analysis of these datasets, the parameters of the inner and outer leafs were constrained to be identical. All samples were doped with 5 mol% POPG to ensure the formation of unilamellar vesicles and were measured in the $L_\alpha$ (fluid) phase at 20°C ($T_M$ of POPC: $\sim -3.5$°C [74]). Figure 3.1 reveals that both models are capable to fit the data, however, the fit quality determined by $\chi^2_{red}$ is improved by the aSDP model compared to the slab model. The determined structural parameters of both models agree within experimental uncertainties to prior published literature values [105, 118], see Tab. 3.1. This confirms that both models are suitable to fit symmetric POPC LUVs with different internal contrast. Additionally, it shows that lipid deuteration does not reveal changes in structural parameters.

## 3. Results and Discussion

Table 3.1.: Structural parameters of symmetric POPC vesicles determined by the joint analysis of SAXS and SANS data compared to literature values which were determined by the SDP model [105] ($SDP_L$) and by an atomistic model [118] ($ADP_L$). Parameter uncertainties are estimated to be $< 2\%$. Table adapted from [65].

| Model | $A_L$ [Å$^2$] | $D_C$ [Å] | $D_B$ [Å] | $\chi^2_{red}$ |
|---|---|---|---|---|
| Slab$_{Joint}$ | 67.5 | 13.6 | 36.9 | 54.2 |
| SDP$_{Joint}$ | 66.3 | 13.8 | 37.6 | 34.6 |
| SDP$_L$ | 62.7 | 14.6 | 39.8 | - |
| ADP$_L$ | 67.0 | 13.7 | 37.2 | - |
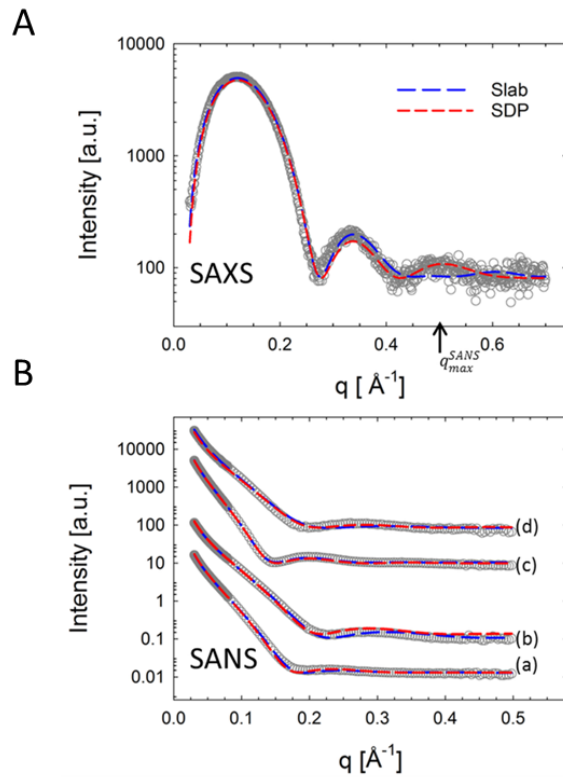


Figure 3.1.: Joint analysis of SAXS (A) and SANS (B) data from symmetric POPC LUVs with different internal contrasts, (a) POPC; (b) POPC-d13; (c) POPC-31; and (d) POPC-d44, measured at 20°C. The maximum SANS resolution is indicated by the $q^{SANS}_{max}$-arrow in the SAXS panel (A). Best fits are represented by blue dashed lines using the asymmetric slab and red-dashed line for the aSDP-model. Figure adapted from [65].

## 3.2. Testing the Models on Isotopic aLUVs

Next, we tested whether the preparation of aLUVs has an influence on structural parameters. Therefore, isotopic aLUVs composed of POPC-d44$^{don}$/POPC$^{acc}$ and *vice versa* were prepared for SANS experiments, while for SAXS measurements only one contrast (POPC$^{don}$/POPC-d13$^{acc}$) was measured, as the X–ray cross-section does not differ between hydrogen and deuterium (see Fig. 2.6). Figure 3.2 shows the best fits of the joint analysis of the slab (blue dashed line) and aSDP model (red dashed line). Again, we found that both models are capable to fit the data. The determined structural parameters agree within experimentental uncertainty with the values of symmetric POPC (see attached paper), indicating that the preparation of aLUVs does not influence the structural parameters. Further, the aSDP model has shown that the $A_L$ of the inner leaf ($A_L^i$) is slightly smaller compared to the $A_L$ of the outer leaflets ($A_L^o$), which is consistent with an earlier analysis on 20 nm diameter egg-phosphatidylcholine vesicles [119]. This was argued by the very small vesicle diameter, resulting in a curvature induced packing difference between the outer and inner layer. However, a recent spectroscopic study on LUVs has also proposed $A_L^i < A_L^o$ [120]. In order to understand the dependence of lipid packing differences on vesicle size and curvature, additional studies would be necessary, which is beyond the scope of this work. Importantly, the presented control experiments demonstrated that the preparation of aLUVs does not influence the lipid structure.

## 3.3. aLUVs with Hydrocarbon Chain Asymmetry : DPPC/POPC

As we prooved by isotopic POPC aLUVs, that the samples preparation does not influence structural parameters, we were able to study coupling mechanism of chemical aLUVs. We first prepared aLUVs with chain asymmetry. Therefore, DPPC lipids were exchanged into POPC LUVs (DPPC$^{don}$/POPC$^{acc}$). The final aLUVs consisted of 34 mole% DPPC on the outer leaflet and the inner leaf was composed of 98 mole% POPC. Firstly, aLUVs were measured at 20°C, which means that DPPC by itself would

# 3. Results and Discussion
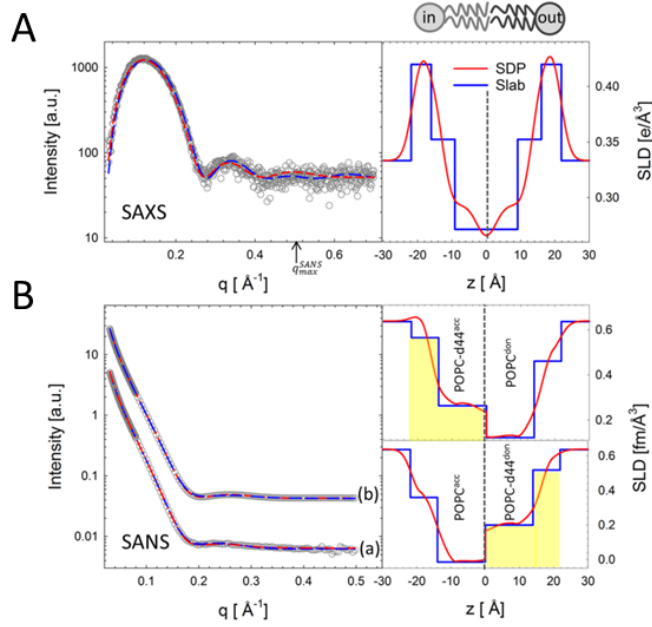


Figure 3.2.: Structural parameters for POPC aLUVs measured at 20 °C. (A) SAXS data from POPC-d13$^{acc}$/POPC$^{don}$ aLUVs, including corresponding fits (dashed lines) and electron density profiles (right). The maximum SANS resolution in reciprocal space is indicated by the $q_{max}^{SANS}$-arrow. (B) SANS data from (a) POPC-d44$^{don}$/POPC$^{acc}$ and (b) POPC$^{don}$/POPC-d44$^{acc}$ aLUVs, and corresponding fits (dashed lines) and neutron scattering length density profiles (right). Blue and red colors denote analysis using the slab and SDP models, respectively. Figure adapted from [65].

be in gel-phase ($T_M$ = 42°C) and POPC in fluid-phase ($T_M$ = −3.5°C [74]), see Fig. 3.3A. The WAXS pattern of DPPC/POPC aLUVs at 20°C (Fig. 3.3A, right) reveals a loss of the chain reflection peaks, indicating that DPPC loses its chain order when coupling to a fluid POPC bilayer. In addition to WAXS experiments, SAXS and SANS measurements were conducted and data were jointly analyzed by the slab model, see Fig. 3.3B. In order to model the scattering data it was necessary to apply two form factors, which implies the presence of coexisting domains in the outer leaflet, found also in symmetric DPPC/POPC mixtures [121]. That is, one form factor accounted for a gel-like DPPC enriched phase on the outer leaflet and fluid POPC-rich inner leaflets, while the other form factor described an all fluid symmetric

POPC enriched bilayer, see Fig. 3.3A. Interestingly, the DPPC-rich phase was less densely packed ($57\,\text{Å}^2$) compared to a typical DPPC gel-phase ($48\,\text{Å}^2$) packing, suggesting a partial fluidization due to transbilayer coupling. This result agrees with the disappearance of the sharp WAXS reflects due to an at least partial fluidization of the DPPC-rich phase. Furthermore, $\text{DPPC}^{don}/\text{POPC}^{acc}$ SAXS and different contrasts of SANS were measured at 50°C in order to assess whether there is transbilayer coupling when both lipids are in the fluid-phase, see Fig. 3.3C. A joint data analysis was conducted with both models, which showed that the structural parameter of DPPC and POPC agree with determined values for DPPC and POPC of the scrambled samples. This reveals that there is no transbilayer coupling when both lipids are in fluid phase. Additionally, by calculating the molecular average of the outer and inner leaflet, revealing that $A_L^i > A_L^o$ (Fig. 3.3). This result is expected as POPC has a larger $A_L$ compared to DPPC [105].

# 3.4. aLUVs with Headgroup Asymmetry: Lipid Sidedness of POPE/POPC

Next, we focused on aLUVs with headgroup asymmetry and on the 'lipid-sidedness' of transmembrane coupling in aLUVs. Therefore, we prepared aLUVs composed of POPC and POPE with either $\text{POPE}^{don}/\text{POPC}^{acc}$, or $\text{POPC}^{don}/\text{POPE}^{acc}$. For both systems a donor to acceptor ratio (D/A) of 3:1 and 2:1 was prepared. In general, the amount of donor lipids of D/A 3:1 was higher compared to 2:1 systems, however, more donor lipids were placed on the inner leaf for a D/A 3:1 system. Hence, we defined the degree of asymmetry ($\sum_{as}$), which is expressed as $\sum_{as} = \chi_{don}^{out} - \chi_{don}^{in}$, where $\chi_{don}^{in,out}$ represents the donor mole fraction on the inner and outer leaf, respectively. Interestingly, $\sum_{as}$ was very similar for both systems, see Tab. 3.2.

In order to determine the coupling mechanism of these two systems, a series of experiments were conducted including SAXS, SANS, WAXS, DSC and cryo-TEM [75].
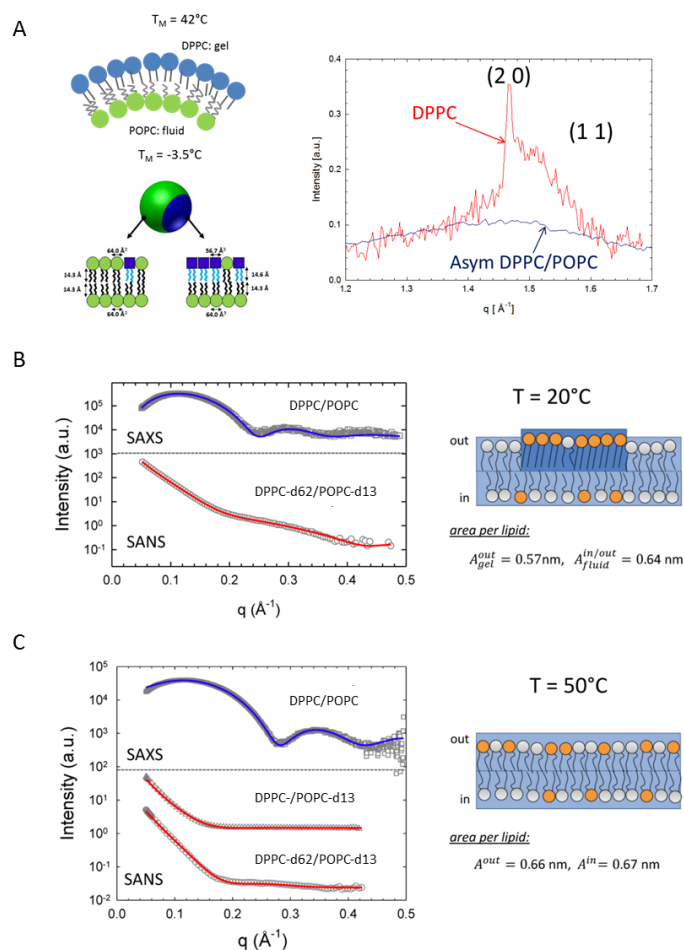
Figure 3.3.: (A) Modeling of DPPC/POPC aLUVs required the use of two asymmetric form factors (left). WAXS pattern of DPPC LUVs (red line) including DPPC/POPC aLUVs measured at 20°C (right). Determination of the lipid structure of DPPC/POPC aLUVs below (B) and above (C) the melting temperature of DPPC via a joint analysis of SAXS and SANS data using headgroup and hydrocarbon deuterated lipid variants. Figure adapted from [16].

Table 3.2.: Mole fraction of donor lipids (see secs. 2.2.2 and 2.3.1) on the inner $\chi^i_{don}$ and outer leaf $\chi^o_{don}$ of POPC$^{don}$/POPE$^{acc}$ and POPE$^{don}$/POPC$^{acc}$ aLUVs, including the degree of asymmetry [75].

| Component | $\chi^i_{don}$ | $\chi^o_{don}$ | $\Sigma_{as}$ |
|---|---|---|---|
| POPC$^{don}$/POPE$^{acc\ a}$ | 0.06 | 0.54 | 0.48 |
| POPC$^{don}$/POPE$^{acc\ b}$ | 0.11 | 0.64 | 0.53 |
| POPE$^{don}$/POPC$^{acc\ a}$ | 0.00 | 0.60 | 0.60 |
| POPE$^{don}$/POPC$^{acc\ b}$ | 0.19 | 0.76 | 0.57 |

$^a$D/A = 2:1.
$^b$D/A = 3:1.

## 3.4.1. Stability of aLUVs

Due to the different melting transitions of POPE and POPC the life-time of the samples asymmetry was determined. Especially lipids within the main phase transition exhibit an enhanced lipid flip-flop rate [39]. For that reason, consecutive DSC scans were investigated, as this technique is very sensitive to the vesicles composition. Only minor differences were detected between the single scans, which indicates that the asymmetry is maintained within the experimental time frame. In addition, $^1$H-NMR flip-flop studies were conducted for both samples in the course of five days. This study revealed that the changes of the degree of asymmetry are minor, proving evidence that the samples are stable before and during experiments (see attached manuscript).

## 3.4.2. Vesicles Size and Morphology

Temperature dependent DLS measurements were conducted from $5 - 35°C$, and showed a linear increase of vesicle size with temperature, see Fig. 3.4A. In contrast, DLS measurements of POPE LUVs (black line) revealed a significant increase of surface area at the phase transition temperature ($T_M \sim 22°C$). In order to gain deeper insight we determined the area expansion coefficient ($\alpha^T_A$) by assuming ideal spherical vesicles: $\alpha^T_A = 1/A \cdot \partial A/\partial T$, where $A$ is the vesicle's surface area (see dashed lines in Fig. 3.4A). For the gel phase $\alpha^T_A$ is

approximately two times smaller compared to the fluid phase. Interestingly, $\alpha_A^T$ of the aLUVs agrees with the fluid phase, suggesting an overall fluid behavior of aLUVs.

Additionally, DLS measurements showed that the vesicle diameter of aLUVs increases by $\sim 10\%$ compared to the initial acceptor LUVs, which could be e.g. due to vesicles morphology. Hence, cryo-TEM measurements were conducted. Figure 3.4 displays acquired images of both asymmetric samples, which show spheres in gel-phase (4°C) and in fluid phase (35°C). The occurance of spherical vesicles below the $T_M$ is unusual. Typically, symmetric LUVs in the gel-phase reveal faceted vesicles as displayed in Fig. 3.5A, which was also shown previously on GUVs, see e.g. [122]. To determine the influence from the osmotic imbalance of NaCl in the aLUVs core, we fabricated POPE LUVs, which contained 25 mM NaCl solution in the vesicles' core (see sec. 2.1 for details) and water on the outside. Cryo-TEM images have suggested that the small osmotic imbalance (resulting to a small pressure difference of $\Delta P \simeq 0.01$ bar [123]) is sufficient to achieve spherical vesicles. This could be explained through defects in gel-phase having increased flexibility. To note, $\Delta P$ is too small to induce any detectable structural leaflet change as shown by our experiments on isotopically asymmetric POPC vesicles (see sec. 3.2 ).

## 3.4.3. Structural Details Obtained by WAXS

The lateral $A_L$ of gel phase lipids of both systems was determined via WAXS by the position of the wide angle reflection, see eq. 2.15, 2.17. Figure 3.6A shows that the wide angle reflex of aLUVs (red) is much broader compared to the scrambled sample (blue), revealing a smaller correlation length of scattering domains $\xi_D$ (eq. 2.19), which suggests a smaller gel phase domain size for aLUVs compared to symmetric LUVs (see inset). Further, the WAXS reflect of POPE$^{don}$/POPC$^{acc}$ reveals a coexistence between an $L_\alpha$- and an $L_\beta$-phase, while POPC$^{don}$/POPE$^{acc}$ showed an $L_\beta$ contribution only, see Fig. 3.6B.
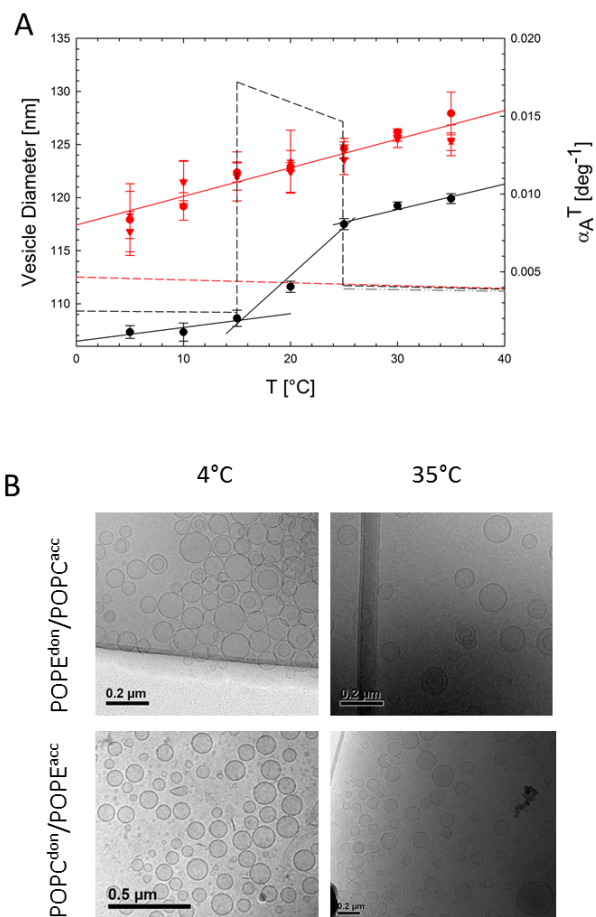
Figure 3.4.: (A) Vesicle diameter (symbols) as a function of temperature and corresponding $\alpha_{A_L}^T$ (dashed lines) for POPE$^{don}$/POPC$^{acc}$ aLUVs (red) and POPE LUVs (black) obtained from DLS. Dashed-dotted gray line displays determined $\alpha_A^T$ from scattering experiments [106]. (B) shows cryo-TEM images of POPE$^{don}$/POPC$^{acc}$ (upper panel) and POPC$^{don}$/POPE$^{acc}$ (lower panel) acquired at 4°C (left) and 35°C(right). Figure taken from [75].
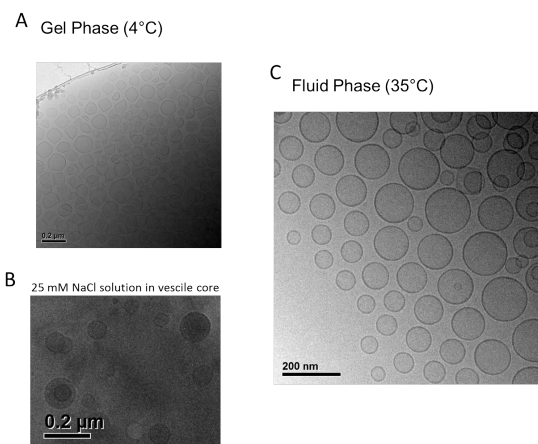
Figure 3.5.: Cryo-TEM images of POPE in gel phase (4°C) (A), containing 25 mM NaCl solution in the core (B) and in fluid phase (35°C). Figure taken from [75]

## 3.4.4. Melting Behavior and Gel-Leaflet Structure of aLUVs

Next, we wanted to gain insight into whether the leaflets melt separately or together in aLUVs and how the structural parameters of aLUVs compare with symmetric LUVs to draw conclusions on coupling mechanisms. Therefore, DSC and WAXS measurements were conducted on POPC$^{don}$/POPE$^{acc}$ and POPE$^{don}$/POPC$^{acc}$ aLUVs, see Fig. 3.8. Interestingly, only a broad single melting transition was detected when POPE was the major component of the inner leaf (POPC$^{don}$/POPE$^{acc}$), Fig. 3.8A. To note, DSC cooling scans of scrambled LUVs (gray dashed lines) (Fig. 3.8) were taken to determine the exchange efficiency, see sec. 2.2.2 for details. Further, WAXS data revealed that these aLUVs pack tighter compared to the theoretical packing density of the outer leaflet and looser than symmetric bilayers of the inner membrane composition, see Fig. 3.8A. Resultant, the average $A_L$ reveals to be a compromise between the properties of the single monolayers. Together, these results reveal transbilayer coupling, see sec. 1.4. Further, the $\xi_D$ is lower in aLUVs indicating less expressed lateral positional correlations between the hydrocarbons in contrast to their symmetric systems (smaller gel-domains (see above)), which leads most likely to an increase of defect-zones between the gel-domains and the surrounding fluid lipid environment. In contrast to that, aLUVs with POPE placed mainly on the
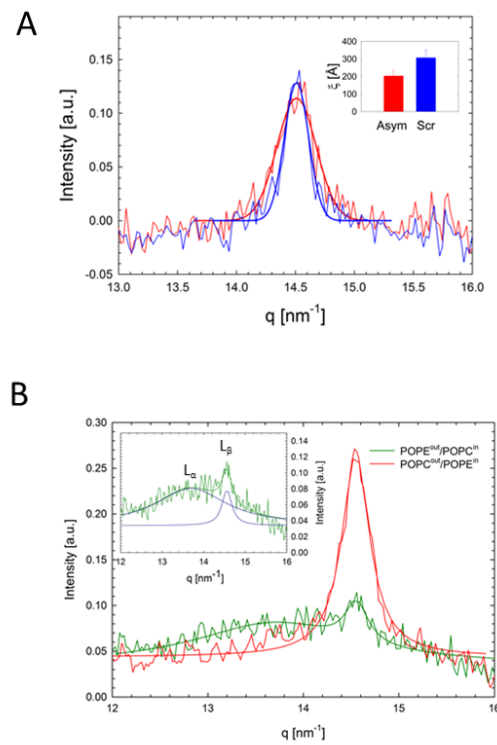
Figure 3.6.: Comparision of WAXS data of aLUVs (red) and scrambled LUVs (blue), including the fitted Gaussians. The inset shows that the average $\xi_D$ of aLUVs (red) is smaller compared to scrambled LUVs (blue). (B) WAXS data of $POPC^{don}/POPE^{acc}$ (red) revealing an $L_\beta$ phase only, while $POPE^{don}/POPC^{acc}$ (green) displays a coexistence between an $L_\beta$ and $L_\alpha$ phase. Figure adapted from [75].

outer leaflet (POPE$^{don}$/POPC$^{acc}$) shows two separate consecutive melting transitions, see Fig. 3.8B. In addition, WAXS measurements display comparable gel packing as determined for a symmetric system with the identical outer leaflets composition. It has to be noted, that the inner leaf is expected to be in fluid-phase as it consists of POPC, which does not contribute to the sharp $L_\beta$ WAXS reflect. This is affirmed by the detected overlap of a sharp $L_\beta$ and a broad $L_\alpha$ peak, see Fig. 3.6. These findings show strong intraleaflet coupling when POPE is located on the outer monolayer, see sec. 1.4.

Additionally, it has to be considered that there is an extended range of temperatures in POPE$^{don}$/POPC$^{acc}$ aLUVs, where a fluid inner monolayer coexists with an outer gel leaflet (Fig. 3.8B, right). One would expect that the different lateral expansions of gel and fluid phases lead to a significant strain within the vesicle which may result in aLUV invagination, budding or even rupture. A gel-fluid area expansion of 16% is estimated to occur across the melting transition of the outer leaf, while the fluid inner membrane would increase by only 5% in the same temperature interval (estimated from measured WAXS data and literature [105, 106]). However, cryo-TEM images yielded no evidence for morphological changes of vesicles within the phase transition regime (see Fig. 3.7), which is consistent with the high stability of aLUVs (see sec. 3.4.1). This suggests, that the melting of the gel domains occurs more or less continuously at the boundaries of the defects. Indeed, consistent with this notion $C_P$, unlike POPE$^{don}$/POPC$^{acc}$, never reached the baseline in our corresponding DSC experiments (Fig. 3.8). In addition, WAXS data showed a coexistence between the fluid phase and the gel phase (Fig. 3.6B). While this probably originates mainly from the fluid inner leaf, as discussed above, we cannot exclude contributions from a partially fluid outer leaflet. For this system $\xi_D$ is lowered as well, indicating smaller gel domains and therefore more defect zones. Since melting occurs at the boundary between gel and fluid regions and because of the high lateral expansivities in the melting regime (Fig. 3.4A), these defect zones are expected to account for the lateral space which will be needed when lipids undergo the gel to fluid phase transition. This would also explain the overall fluid melting behavior of the aLUVs and their stability across the melting transition (Fig. 3.4A).
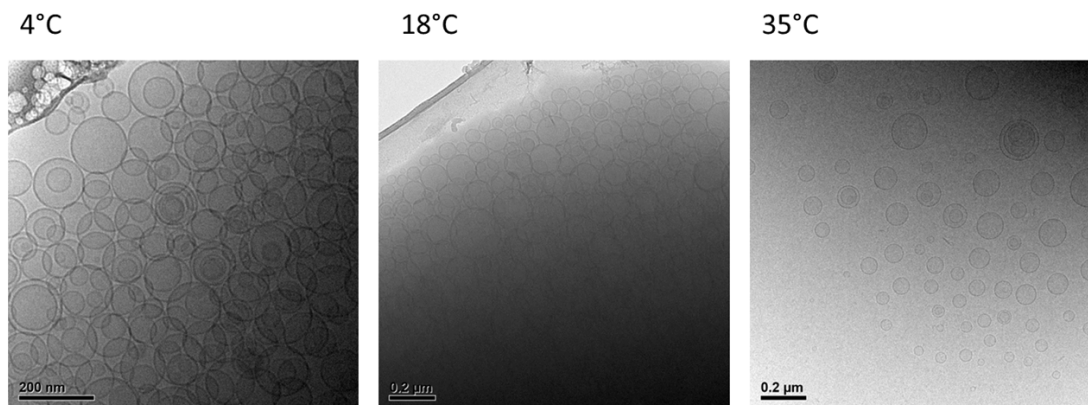
Figure 3.7.: Cryo-TEM images of POPE$^{don}$/POPC$^{acc}$ aLUVs in gel-phase (4°C), within the phase transition (18°C) and in fluid phase (35°C). Figure taken from [75].
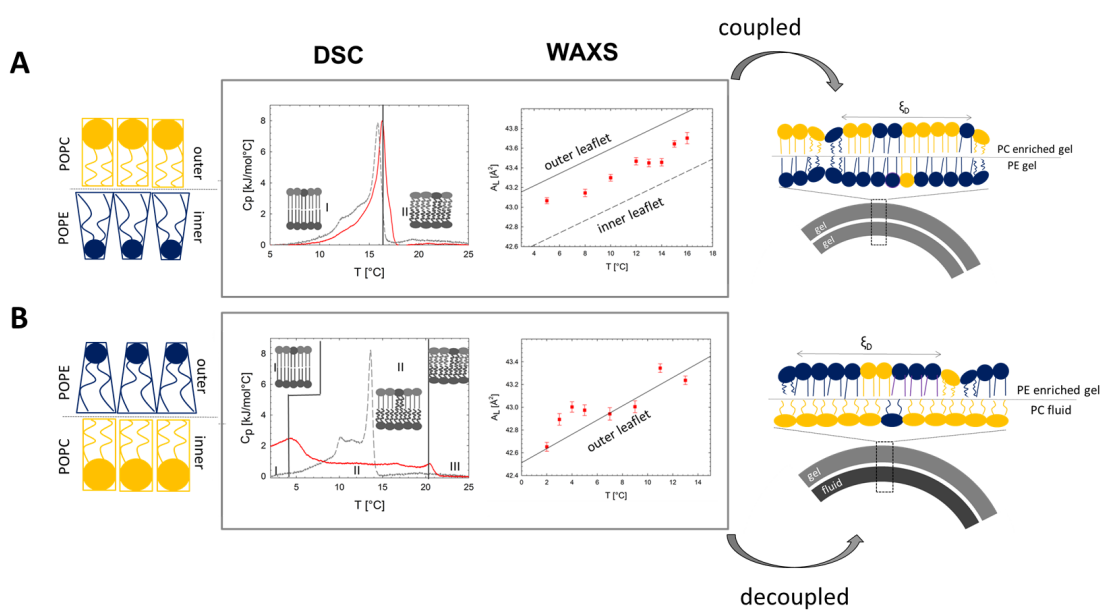


Figure 3.8.: DSC and WAXS data of POPC$^{don}$/POPE$^{acc}$ (A) and POPE$^{don}$/POPC$^{acc}$ (B) samples including the schematic illustration of lipid distribution and coupling mechanism of both samples. Figure adapted from [75].

### 3.4.5. Leaflet Structure in Fluid Phase

Furthermore, both systems were investigated at 35°C, where both lipids are in fluid-phase, by a joint analysis of differently contrasted SANS and SAXS data by the aSDP model, see sec. 2.6. The determined structural parameter agree well for both systems with values calculated from the molecular average of reported values in literature for pure POPC, POPE and POPG [105, 106, 124], see Tab. 3.3. Therefore, no coupling was detected, which agrees with DPPC/POPC aLUVs in fluid-phase (see sec. 3.3). However, it has to be noted that the uncertainty of the applied SANS/SAXS analysis is significantly higher compared to that performed with WAXS data in the gel phase ($<3\%$ to $<0.1\%$). Hence, subtle changes in structural parameters might be hidden within the uncertainty.

Table 3.3.: Leaflet specific lipid areas ($A_L^{in/out}$) of fluid aLUVs determined by the joint analysis of SANS and SAXS data, including calculated values in parenthesis [105, 106, 124]. Experimental uncertainties are within 3% [75].

|  | $A_L^{in}$ [Å$^2$] | $A_L^{out}$ [Å$^2$] |
|---|---|---|
| POPC$^{don}$/POPE$^{acc}$ | 59.7 (59.3) | 64.7 (63.0) |
| POPE$^{don}$/POPC$^{acc}$ | 64.7 (64.9) | 59.9 (60.7) |

### 3.4.6. Curvature Induced Coupling Mechansim

At this point, the question arises why the gel-phase coupling of the two systems differs significantly: As schematically illustrated in Fig. 3.8(left), POPE has a negative intrinsic curvature $J_0$ [125], which would energetically favor to locate on the inner leaflet of lipid vesicles. However, $J_0$ of POPE decreases nearly twice as fast with temperature compared to POPC [125]. In general, the intrinsic curvature strain stored within the aLUVs should increase also with temperature which would lead to a transmembrane coupling in the fluid-phase. Hence, we would expect to have a strong transbilayer coupling in the fluid-phase. However, both systems (POPC$^{don}$/POPE$^{acc}$ and POPE$^{don}$/POPC$^{acc}$) do not show (within experimental uncertainty) transmembrane coupling in the fluid-phase.

Consequently, we considered specific features of the hydrocarbon chain structure. POPE consists of one monounsaturated chain, which means that its oleoyl chain will stay kinked even within the gel-phase and requires laterally more space than all-trans palmitic chains [126–128]. Thus, POPE can be expected to reveal even in the gel-phase a significant negative $J_0$. In addition, lipids in the gel-phase experience decreased motional entropy, which means that intrinsic curvature strain can be less easily compensated by hydrocarbon chain dynamics. This might explain the abolishment of transmembrane coupling in the fluid-phase. Further, in contrast to PC, PE has a primary amine which makes it capable to form hydrogen bonds [129, 130], however, compositional differences of POPE concentration in the inner leaf of POPC$^{don}$/POPE$^{acc}$ and of the outer leaflet of POPE$^{don}$/POPC$^{acc}$ are small, which suggests that this contribution is most likely insignificant.

# 4. Conclusion

We have adapted the CD-mediated protocol to prepare stress-free, free floating aLUVs and have developed assays to accurately determine the composition of the single leaflets in order to have an improved model system to better represent the asymmetry found in most biological membranes. The advantage arising from the adapted protocol is the applicability for a wide variety of biophysical experiments. We were especially interested in studying the transmembrane coupling. Thus, a low resolution slab model and a high resolution SDP model were designed for the joint analysis of SAXS and differently contrasted SANS data of aLUVs. For the application of the aSDP model a large amount of free parameters is needed. Hence, some parameters have to be constrained to avoid nonphysical results. Due to the high amount of adjustable parameters a differential evolution algorithm was applied to avoid getting trapped in a local minimum. In contrast, the slab model has less free parameters, which means that the use of the trust region reflective algorithm was sufficient. However, the computational effort of the aSDP model are justified as the determined fit quality by the $\chi^2_{red}$ is improved. Both models were tested on symmetric POPC LUVs and isotopic asymmetric POPC aLUVs. Furthermore, the analysis of the isotopic POPC aLUVs has revealed that the sample preparation does not have an influence on the structural parameters such as area per lipid ($A_L$) and bilayer thickness ($D_B$). Interestingly, POPC aLUVs suggest also $A_L^i < A_L^o$, which is consistent with prior studies [120] and with the presence of residual curvature strain in $\sim$120 nm aLUVs. Next, the transmembrane coupling was studied on chemical asymmetric DPPC$^{don}$/POPC$^{acc}$ and on POPC$^{don(acc)}$/POPE$^{acc(don)}$ samples. In fluid phase no transmembrane coupling mechanism was determined by jointly analyzing SAXS and differently contrasted SANS data for all samples. This also agrees with earlier aLUVs studies where SM is enriched on the outer leaf [22, 24], while in gel phase coupling was detected.

## 4. Conclusion

For DPPC$^{don}$/POPC$^{acc}$ systems we have found a notable reduction of gel phase packing density on the outer leaf, while the inner fluid phase was not affected. For POPC$^{don}$/POPE$^{acc}$ strong transmembrane coupling was determined by WAXS and DSC, which however switched to intraleaflet coupling by reversing donor and acceptor lipids (POPE$^{don}$/POPC$^{acc}$). These findings suggest the energetically preferable location of POPE on the inner monolayer, due to its negative curvature. Additionally, by comparing DPPC$^{don}$/POPC$^{acc}$ to POPE$^{don}$/POPC$^{acc}$ it was seen that in the latter system the inner fluid POPC leaflet did not influence the packing density of the outer gel domains.

# 5. Outlook

This thesis contains results which were obtained over the last three years. However, this period of time was just sufficient to develop the tools which will help to pave the way for controlled studies of more complex asymmetric bilayer structures to determine how lipid asymmetry influences the transbilayer coupling mechanism. Finally, studies on more complex aLUVs and also the addition of proteins will help to better understand physiological processes. This includes for example raft-formation and transmembrane signaling, and might support the design of novel drugs which will interfere especially with the function of the membrane [4]. Here, I will give some suggestions and ideas for prospective research in this field.

In this work, we demonstrated the development of a "scattering friendly" protocol to prepare aLUVs and assess precisely the degree of asymmetry, which can be used for a wide variety of biophysical experiments. This procedure is ideal to study transbilayer and intraleaflet coupling mechanisms as shown for DPPC/POPC and POPE/POPC systems. A next step would be to include different amounts of cholesterol to investigate in which leaflet it is located predominately and to obtain information about coupling mechanisms, see sec. 2.1. Therefore, the preparation needs to be redesigned to use a M$\alpha$CD [29] instead of M$\beta$CD as it is not capable to remove cholesterol from the acceptor vesicles. The dominant position of cholesterol in a bilayer as well as the transbilayer coupling mechanisms could be studied with SANS by preparing samples with a variety of internal contrasts (e.g. deuterated cholesterol or lipids) and external contrasts (variation of $H_2O/D_2O$ in the solvent), see sec. 2.5.1. It is still a matter of debate whether cholesterol is located predominately in the outer or inner leaf [11]. On the one hand cholesterol has a negative intrinsic curvature and therefore would prefer to be placed on the inner leaf. On the other hand cholesterol preferentially interacts with saturated- or sphingolipis, as the interaction of cholesterol with lipids is given to a large extend by interaction between the planar

steroid ring of cholesterol with the lipids' acyl chains [131]. Hence, fully saturated lipids or sphingolipids can interact over the full length of the steroid ring [131]. Thus, I would expect that the predominant position of cholesterol depends significantly on the lipid composition of the investigated model systems. In order to obtain information about the coupling mechanism, it is necessary to determine some parameters with control experiments, as there will be a large amount of free parameters. For example, the distribution of PC/SM-lipids can be accurately determined via proton NMR (sec. 2.3.1). Additional GC or UPLC-MS measurements to ^{1}H-NMR studies determine the composition of the single leaflets (sec. 2.2.1). This information can be used on the one hand for SANS data analyses and on the other hand to find the $H_2O/D_2O$ ratio to contrast match the single leaflets. To note, it is only possible to design a contrast matched sample, when the exact composition of the single leafs is known. First, it would be interesting to design aLUVs with an outer leaflet consisting of a lipid mixture, which shows a liquid-ordered / liquid-disordered phase separation in symmetric systems (e.g. DSPC/DOPC/chol) [48] and the inner leaf should be composed of lipids which do not phase separate in symmetric bilayers (e.g. POPE/chol). These samples would mix homogeneously in each leaflet at high temperatures and would probably phase separate at lower temperatures due to the properties of DSPC/DOPC/chol mixtures [132] as shown for supported bilayers [54]. At first the sample has to be heated for SANS measurements to obtain homogeneously mixed leaflets to contrast match the inner and outer leaflets separately by calculated $H_2O/D_2O$ ratios, which will lead to structural parameters of the single leafs and additionally would be a control experiment whether the correct $H_2O/D_2O$ ratio was taken. It should be possible to fit the scattering curve with a single form factor. When the samples are cooled, the SANS curve provides information about the formation of domains. In order to fit these datasets separate form factors describing the single domains would be necessary. In a next step, the internal contrast of the two leaflets can be adjusted to match with the $H_2O/D_2O$ aqueous environment by using fully or partly deuterated lipids and cholesterol. No signal should be obtained at high temperatures when both leafs mix homogeneously, as shown for symmetric systems [133]. Cooling of the sample will lead to phase separation, which would be detected in the SANS signal. In addition to SANS experiments, steady-state fluorescence anisotropy measurments [22, 23] could be conducted, to gain information

whether the single leafs are in a more ordered or disordered state. All these datasets will path the way to draw conclusions about the coupling mechanisms. Furthermore, the lifetime of these asymmetric samples has to be determined by proton NMR (secs. 1.3.1, 2.3.1), which allows to study lipid flip-flop rates for PC/SM-lipids. So far lipid translocation rates were investigated by our protocol for DPPC [39], POPC (to be published) and POPE/POPC aLUVs [75]. Lipid flip-flop rates of samples with incorporated cholesterol were determined, see e.g. [42, 134]. However, whether cholesterol accelerates or reduces the translocation rates is still a matter of dispute. A study on SSBs has shown that cholesterol shortens the life-time of asymmetric bilayers [134]. In contrast, e.g. SANS studies on vesicles have revealed that lipid translocation rates were significantly hampered in the presence of cholesterol, suggesting that lipids can barely translocate in rigid membranes [42]. As explained above (sec. 1.3.1), SSBs show accelerated flip-flop rates, due to incomplete surface coverage leading to submicron-sized defects, in comparison to "our" stress-free isotopic aLUVs [39]. Therefore, I would expect to obtain more accurate flip-flop values by using our approach to prepare and quantify the leaflet composition of aLUVs.

Regarding the curvature induced packing density (see sec. 3.2) of the inner and outer leaflet, the aSDP model is capable to determine the packing density of the single leafs, which would be interesting to study in dependence of vesicle sizes of isotopic aLUVs, via SANS and SAXS. As curvature decreases with increasing vesicle size, I would expect that the differences in packing density of lipids in the outer and inner leaflet are smaller for bigger vesicles. For this approach a very monodisperse sample, which is achievable e.g. by size exclusion chromatography [135] of the acceptor vesicles, would be helpful. The vesicle size can be easily varied by taking polycarbonate filters with different pore sizes for acceptor extrusion.

A similar approach can be used for POPE/POPC aLUVs, which have revealed strong transbilayer coupling when POPE was predominantly placed mainly on the inner leaf, while intraleaflet coupling dominated for POPE located on the outer leaf. This behavior was explained with a curvature induced coupling mechanism. Therefore, by increasing the vesicle size it would be expected that both samples (POPE placed on the inner or outer leaf) behave similar. This can be investigated by conducting DSC and WAXS experiments (sec. 3.4.4).

Additionally, we have seen that the uncertainty of the structural parameters

determined by SAXS/SANS is significantly higher compared to WAXS ($<$3% to $<$0.1%). For receiving more accurate information about coupling in the fluid phase, it would be instructive to develop a procedure to determine structural parameters from the broad fluid WAXS signal. In a first step, this problem could be addressed by conducting temperature dependent WAXS measurements on well studied lipid systems, where the structural parameters are well known, in order to determine a calibration curve.

So far, we have developed assays to determine the degree of asymmetry for PC/SM lipids. For example, it has been shown that zeta potential measurements are ideal to determine the exchange efficiency of charged lipids [136]. London and co-workers have used high performance thin layer chromatography (HPTLC), combined with steady-state fluorescence anisotropy measurements to estimate the composition of the single leaflets [22]. However, a further development of assays which are sensitive to different lipid headgroups (e.g. PE,PI) would be highly desired in order to accurately determine the leaflet composition.

# Bibliography

[1] Betzig, E., G. H. Patterson, R. Sougrat, O. W. Lindwasser, S. Olenych, J. S. Bonifacino, M. W. Davidson, J. Lippincott-Schwartz, and H. F. Hess, 2006. Imaging intracellular fluorescent proteins at nanometer resolution. *Science* 313:1642–1645.

[2] Huang, B., W. Wang, M. Bates, and X. Zhuang, 2008. Three-dimensional super-resolution imaging by stochastic optical reconstruction microscopy. *Science* 319:810–813.

[3] Shim, S.-H., C. Xia, G. Zhong, H. P. Babcock, J. C. Vaughan, B. Huang, X. Wang, C. Xu, G.-Q. Bi, and X. Zhuang, 2012. Super-resolution fluorescence imaging of organelles in live cells with photoswitchable membrane probes. *Proceedings of the National Academy of Sciences* 109:13978–13983.

[4] Pabst, G., N. Kučerka, M.-P. Nieh, and J. Katsaras, editors, 2014. Liposomes, Lipid Bilayers and Model Membranes: From Basic Research to Application. CRC Press, Boca Raton, FL.

[5] Sprong, H., P. van der Sluijs, and G. van Meer, 2001. How proteins move lipids and lipids move proteins. *Nature reviews. Molecular cell biology* 2:504.

[6] Zimmerberg, J., and M. M. Kozlov, 2006. How proteins produce cellular membrane curvature. *Nature reviews. Molecular cell biology* 7:9.

[7] Escribá, P. V., J. M. González-Ros, F. M. Goñi, P. K. Kinnunen, L. Vigh, L. Sánchez-Magraner, A. M. Fernández, X. Busquets, I. Horváth, and G. Barceló-Coblijn, 2008. Membranes: a meeting point for lipids, proteins and therapies. *Journal of cellular and molecular medicine* 12:829–875.

[8] Van Meer, G., D. R. Voelker, and G. W. Feigenson, 2008. Membrane lipids: where they are and how they behave. *Nature reviews. Molecular cell biology* 9:112.

[9] Verkleij, A., P. Ververgaert, L. Van Deenen, and P. Elbers, 1972. Phase transitions of phospholipid bilayers and membranes of Acholeplasma laidlawii B visualized by freeze fracturing electron microscopy. *Biochimica et Biophysica Acta (BBA)-Biomembranes* 288:326–332.

[10] Wood, W. G., U. Igbavboa, W. E. Muller, and G. P. Eckert, 2011. Cholesterol asymmetry in synaptic plasma membranes. *Journal of neurochemistry* 116:684–689.

[11] Marquardt, D., B. Geier, and G. Pabst, 2015. Asymmetric lipid membranes: towards more realistic model systems. *Membranes* 5:180–196.

[12] Liu, S.-L., R. Sheng, J. H. Jung, L. Wang, E. Stec, M. J. O'Connor, S. Song, R. K. Bikkavilli, R. A. Winn, D. Lee, et al., 2017. Orthogonal lipid sensors identify transbilayer asymmetry of plasma membrane cholesterol. *Nature chemical biology* 13:268–274.

[13] Daleke, D. L., 2003. Regulation of transbilayer plasma membrane phospholipid asymmetry. *Journal of lipid research* 44:233–242.

[14] Schlegel, R., and P. Williamson, 2001. Phosphatidylserine, a death knell. *Cell death and differentiation* 8:551.

[15] Riedl, S., B. Rinner, M. Asslaber, H. Schaider, S. Walzer, A. Novak, K. Lohner, and D. Zweytick, 2011. In search of a novel target—phosphatidylserine exposed by non-apoptotic tumor cells and metastases of malignancies with poor treatment efficacy. *Biochimica et Biophysica Acta (BBA)-Biomembranes* 1808:2638–2645.

[16] Heberle, F. A., and G. Pabst, 2017. Complex biomembrane mimetics on the sub-nanometer scale. *Biophysical Reviews* 1–21.

[17] Simons, K., 2004. Lipid rafts: structure and function. *Journal of Molecular and Cellular Cardiology* 36:759.

[18] Heberle, F. A., and G. W. Feigenson, 2011. Phase separation in lipid membranes. *Cold Spring Harb Perspect Biol* 3:a004630.

[19] Pautot, S., B. J. Frisken, and D. Weitz, 2003. Engineering asymmetric vesicles. *Proceedings of the National Academy of Sciences* 100:10718–10721.

[20] Noireaux, V., and A. Libchaber, 2004. A vesicle bioreactor as a step toward an artificial cell assembly. *Proceedings of the national academy of sciences of the United States of America* 101:17669–17674.

[21] Lin, W. C., C. D. Blanchette, T. V. Ratto, and M. L. Longo, 2006. Lipid asymmetry in DLPC/DSPC-supported lipid bilayers: a combined AFM and fluorescence microscopy study. *Biophysical journal* 90:228–237.

[22] Cheng, H. T., Megha, and E. London, 2009. Preparation and properties of asymmetric vesicles that mimic cell membranes: effect upon lipid raft formation and transmembrane helix orientation. *Journal of Biological Chemistry* 284:6079–6092.

[23] Cheng, H. T., and E. London, 2011. Preparation and properties of asymmetric large unilamellar vesicles: interleaflet coupling in asymmetric vesicles is dependent on temperature but not curvature. *Biophysical journal* 100:2671–2678.

[24] Chiantia, S., P. Schwille, A. S. Klymchenko, and E. London, 2011. Asymmetric GUVs prepared by MbetaCD-mediated lipid exchange: an FCS study. *Biophysical Journal* 100:L1–L3.

[25] Huang, Z., and E. London, 2013. Effect of cyclodextrin and membrane lipid structure upon cyclodextrin–lipid interaction. *Langmuir* 29:14631–14638.

[26] Son, M., and E. London, 2013. The dependence of lipid asymmetry upon phosphatidylcholine acyl chain structure. *Journal of lipid research* 54:223–231.

[27] Leventis, R., and J. R. Silvius, 2001. Use of cyclodextrins to monitor transbilayer movement and differential lipid affinities of cholesterol. *Biophysical journal* 81:2257–2267.

[28] Son, M., and E. London, 2013. The dependence of lipid asymmetry upon polar headgroup structure. *Journal of lipid research* 54:3385–3393.

[29] Li, G., J. Kim, Z. Huang, J. R. S. Clair, D. A. Brown, and E. London, 2016. Efficient replacement of plasma membrane outer leaflet phospholipids and sphingolipids in cells with exogenous lipids. *Proceedings of the National Academy of Sciences* 201610705.

[30] Visco, I., S. Chiantia, and P. Schwille, 2014. Asymmetric supported lipid bilayer formation via methyl-$\beta$-cyclodextrin mediated lipid exchange: influence of asymmetry on lipid dynamics and phase behavior. *Langmuir* 30:7475–7484.

[31] Heberle, F. A., D. Marquardt, M. Doktorova, B. Geier, R. F. Standaert, P. Heftberger, B. Kollmitzer, J. D. Nickels, R. A. Dick, G. W. Feigenson, J. Katsaras, E. London, and G. Pabst, 2016. Subnanometer Structure of an Asymmetric Model Membrane: Interleaflet Coupling Influences Domain Properties. *Langmuir : the ACS journal of surfaces and colloids* 32:5195–5200.

[32] Andrews, S. B., J. Faller, J. M. Gilliam, and R. J. Barrnett, 1973. Lanthanide ion-induced isotropic shifts and broadening for nuclear magnetic resonance structural analysis of model membranes. *Proceedings of the National Academy of Sciences* 70:1814–1818.

[33] Crane, J. M., V. Kiessling, and L. K. Tamm, 2005. Measuring lipid asymmetry in planar supported bilayers by fluorescence interference contrast microscopy. *Langmuir* 21:1377–1388.

[34] Clifton, L. A., M. W. Skoda, E. L. Daulton, A. V. Hughes, A. P. Le Brun, J. H. Lakey, and S. A. Holt, 2013. Asymmetric phospholipid: lipopolysaccharide bilayers; a Gram-negative bacterial outer membrane mimic. *Journal of The Royal Society Interface* 10:20130810.

[35] Olsson, C., and G. Westman, 2013. Direct dissolution of cellulose: background, means and applications. InTech.

[36] Devaux, P. F., 1992. Protein involvement in transmembrane lipid asymmetry. *Annual review of biophysics and biomolecular structure* 21:417–439.

[37] Serra, M. V., D. Kamp, and C. W. Haest, 1996. Pathways for flip-flop of mono-and di-anionic phospholipids in the erythrocyte membrane. *Biochimica et Biophysica Acta (BBA)-Biomembranes* 1282:263–273.

[38] Liu, J., and J. C. Conboy, 2005. 1, 2-diacyl-phosphatidylcholine flip-flop measured directly by sum-frequency vibrational spectroscopy. *Biophysical journal* 89:2522–2532.

[39] Marquardt, D., F. A. Heberle, T. Miti, B. Eicher, E. London, J. Katsaras, and G. Pabst, 2017. 1H NMR Shows Slow Phospholipid Flip-Flop in Gel and Fluid Bilayers. *Langmuir* 33:3731–3741.

[40] Wu, H.-L., Y. Tong, Q. Peng, N. Li, and S. Ye, 2016. Phase transition behaviors of the supported DPPC bilayer investigated by sum frequency generation (SFG) vibrational spectroscopy and atomic force microscopy (AFM). *Physical Chemistry Chemical Physics* 18:1411–1421.

[41] John, K., S. Schreiber, J. Kubelt, A. Herrmann, and P. Müller, 2002. Transbilayer movement of phospholipids at the main phase transition of lipid membranes: implications for rapid flip-flop in biological membranes. *Biophysical journal* 83:3315–3323.

[42] Nakano, M., M. Fukuda, T. Kudo, N. Matsuzaki, T. Azuma, K. Sekine, H. Endo, and T. Handa, 2009. Flip-flop of phospholipids in vesicles: kinetic analysis with time-resolved small-angle neutron scattering. *The Journal of Physical Chemistry B* 113:6745–6748.

[43] Contreras, F., L. Sánchez-Magraner, A. Alonso, F. M. Goñi, et al., 2010. Transbilayer (flip-flop) lipid motion and lipid scrambling in membranes. *FEBS letters* 584:1779–1786.

[44] Son, M., and E. London, 2013. The dependence of lipid asymmetry upon phosphatidylcholine acyl chain structure. *Journal of lipid research* 54:223–231.

[45] Lu, L., W. J. Doak, J. W. Schertzer, and P. R. Chiarot, 2016. Membrane mechanical properties of synthetic asymmetric phospholipid vesicles. *Soft Matter* 12:7521–7528.

[46] Simons, K., and D. Toomre, 2000. Lipid rafts and signal transduction. *Nature reviews. Molecular cell biology* 1:31.

[47] Feigenson, G. W., 2009. Phase diagrams and lipid domains in multi-component lipid bilayer mixtures. *Biochimica et Biophysica Acta (BBA)-Biomembranes* 1788:47–52.

[48] Marsh, D., 2009. Cholesterol-induced fluid membrane domains: a compendium of lipid-raft ternary phase diagrams. *Biochimica et Biophysica Acta (BBA)-Biomembranes* 1788:2114–2123.

[49] Wang, T.-Y., and J. R. Silvius, 2001. Cholesterol does not induce segregation of liquid-ordered domains in bilayers modeling the inner leaflet of the plasma membrane. *Biophysical journal* 81:2762–2773.

[50] Leibler, S., and D. Andelman, 1987. Ordered and curved meso-structures in membranes and amphiphilic films. *Journal de physique* 48:2013–2018.

[51] Collins, M. D., 2008. Interleaflet coupling mechanisms in bilayers of lipids and cholesterol. *Biophysical journal* 94:L32–L34.

[52] May, S., 2009. Trans-monolayer coupling of fluid domains in lipid bilayers. *Soft Matter* 5:3148–3156.

[53] Galimzyanov, T. R., P. I. Kuzmin, P. Pohl, and S. A. Akimov, 2017. Undulations Drive Domain Registration from the Two Membrane Leaflets. *Biophysical journal* 112:339–345.

[54] Kiessling, V., C. Wan, and L. K. Tamm, 2009. Domain coupling in asymmetric lipid bilayers. *Biochimica et Biophysica Acta (BBA)-Biomembranes* 1788:64–71.

[55] Wan, C., V. Kiessling, and L. K. Tamm, 2008. Coupling of cholesterol-rich lipid phases in asymmetric bilayers. *Biochemistry* 47:2190–2198.

[56] Kiessling, V., J. M. Crane, and L. K. Tamm, 2006. Transbilayer effects of raft-like lipid domains in asymmetric planar bilayers measured by single molecule tracking. *Biophysical journal* 91:3313–3326.

[57] Chiantia, S., and E. London, 2012. Acyl chain length and saturation modulate interleaflet coupling in asymmetric bilayers: effects on dynamics and structural order. *Biophysical journal* 103:2311–2319.

[58] Shlomovitz, R., and M. Schick, 2013. Model of a raft in both leaves of an asymmetric lipid bilayer. *Biophysical journal* 105:1406–1413.

[59] Fuller, N., C. R. Benatti, and R. P. Rand, 2003. Curvature and bending constants for phosphatidylserine-containing membranes. *Biophysical journal* 85:1667–1674.

[60] Kingsley, P., and G. Feigenson, 1979. The synthesis of a perdeuterated phospholipid: 1, 2-dimyristoyl-sn-glycero-3-phosphocholine-d72. *Chemistry and Physics of Lipids* 24:135–147.

[61] Kučerka, N., J. Pencer, J. N. Sachs, J. F. Nagle, and J. Katsaras, 2007. Curvature effect on the structure of phospholipid bilayers. *Langmuir* 23:1292–1299.

[62] Swartz, M. E., 2005. UPLC™: an introduction and review. *Journal of Liquid Chromatography & Related Technologies* 28:1253–1263.

[63] Meyer, V. R., 2013. Practical high-performance liquid chromatography. John Wiley & Sons, West Sussex, United Kingdom.

[64] Guillarme, D., and J.-L. Veuthey. Guidelines for the use of UHPLC Instruments. *web site: http://unige. ch/sciences/pharm/fanal/lcap/Guidelines* 20.

[65] Eicher, B., F. A. Heberle, D. Marquardt, G. N. Rechberger, J. Katsaras, and G. Pabst, 2017. Joint small-angle X-ray and neutron scattering data analysis of asymmetric lipid vesicles. *Journal of Applied Crystallography* 50:419–429.

[66] Knittelfelder, O. L., B. P. Weberhofer, T. O. Eichmann, S. D. Kohlwein, and G. N. Rechberger, 2014. A versatile ultra-high performance LC-MS method for lipid profiling. *Journal of Chromatography B* 951:119–128.

[67] Hartler, J., M. Trötzmüller, C. Chitraju, F. Spener, H. C. Köfeler, and G. G. Thallinger, 2011. Lipid Data Analyzer: unattended identification and quantitation of lipids in LC-MS data. *Bioinformatics* 27:572–577.

[68] Offnfopt. Diagram of a gas chromatograph apparatus. `https://commons.wikimedia.org/wiki/File:Gas_chromatograph-vector.svg`. Accessed: 2017-06-20.

[69] Norena-Caro, D. Diagram of liquid chromatography tandem Mass spectrometry. `https://en.wikipedia.org/wiki/File:Liquid_chromatography_tandem_Mass_spectrometry_diagram.png`. Accessed: 2017-06-20.

[70] Heimburg, T., 2007. Statistical Models for Lipid Melting. *Thermal Biophysics of Membranes* 123–140.

[71] Hinz, H.-J., and F. P. Schwarz, 2001. Measurement and analysis of results obtained on biological substances with differential scanning calorimetry (IUPAC Technical Report). *Pure and Applied Chemistry* 73:745–759.

[72] Lohner, K., 2016. DSC Studies on the modulation of membrane lipid polymorphism and domain organization by antimicrobial peptides. *Biocalorimetry: Foundations and Contemporary Approaches; Bastos, M., Ed.; CRC Press: Boca Raton, FL, USA* 169–190.

[73] Navas, B. P., K. Lohner, G. Deutsch, E. Sevcsik, K. Riske, R. Dimova, P. Garidel, and G. Pabst, 2005. Composition dependence of vesicle morphology and mixing properties in a bacterial model membrane system. *Biochimica et Biophysica Acta (BBA)-Biomembranes* 1716:40–48.

[74] Pabst, G., A. Hodzic, J. Štrancar, S. Danner, M. Rappolt, and P. Laggner, 2007. Rigidification of neutral lipid bilayers in the presence of salts. *Biophysical journal* 93:2688–2696.

[75] Eicher, B., D. Marquardt, F. A. Heberle, I. Letofsky-Papst, G. N. Rechberger, M.-S. Appavou, J. Katsaras, and G. Pabst, 2017. Instrinsic Curvature-Mediated Transbilayer Coupling in Asymmetric Lipid Vesicles. *submitted* .

[76] James, T. L., 1998. Fundamentals of NMR. *Online Textbook: Department of Pharmaceutical Chemistry, University of California, San Francisco* 1–31.

[77] Stetefeld, J., S. A. McKenna, and T. R. Patel, 2016. Dynamic light scattering: a practical guide and applications in biomedical sciences. *Biophysical reviews* 8:409–427.

[78] Worldwide, M. I., 2011. Dynamic light scattering, Common terms defined. *Inform white paper. Malwern Instruments Limited* 1–6.

[79] Milne, J. L., M. J. Borgnia, A. Bartesaghi, E. E. Tran, L. A. Earl, D. M. Schauder, J. Lengyel, J. Pierson, A. Patwardhan, and S. Subramaniam, 2013. Cryo-electron microscopy–a primer for the non-microscopist. *The FEBS journal* 280:28–45.

[80] Courtesy of Ilse Letofsky-Papst , Institute for Electron Microscopy and Nanoanalysis, Graz University of Technology, Austria, 2017.

[81] Small Angle Scattering Methods. `https://sundoc.bibliothek.uni-halle.de/diss-online/03/03H107/t3.pdf`.

[82] Frielinghaus, H., A. Feoktystov, I. Berts, and G. Mangiapia, 2015. KWS-1: Small-angle scattering diffractometer. *Journal of large-scale research facilities JLSRF* 1:28.

[83] Feoktystov, A. V., H. Frielinghaus, Z. Di, S. Jaksch, V. Pipich, M.-S. Appavou, E. Babcock, R. Hanslik, R. Engels, G. Kemmerling, et al., 2015. KWS-1 high-resolution small-angle neutron scattering instrument at JCNS: current state. *Journal of applied crystallography* 48:61–70.

[84] Jacrot, B., 1976. The study of biological structures by neutron scattering from solution. *Reports on progress in physics* 39:911.

[85] Fitter, J., T. Gutberlet, and J. Katsaras, 2006. Neutron scattering in biology: techniques and applications. Springer Science & Business Media, Heidelberg, Germany.

[86] Zaccai, G., J. Blasie, and B. Schoenborn, 1975. Neutron diffraction studies on the location of water in lecithin bilayer model membranes. *Proceedings of the National Academy of Sciences* 72:376–380.

[87] Büldt, G., H. Gally, A. Seelig, J. Seelig, and G. Zaccai, 1978. Neutron diffraction studies on selectively deuterated phospholipid bilayers. *Nature* 271:182–184.

[88] Zaccai, G., G. Büldt, A. Seelig, and J. Seelig, 1979. Neutron diffraction studies on phosphatidylcholine model membranes: II. Chain conformation and segmental disorder. *Journal of molecular biology* 134:693–706.

[89] Léonard, A., C. Escrive, M. Laguerre, E. Pebay-Peyroula, W. Néri, T. Pott, J. Katsaras, and E. J. Dufourc, 2001. Location of cholesterol in DMPC membranes. A comparative study by neutron diffraction and molecular mechanics simulation. *Langmuir* 17:2019–2030.

[90] J. M. Carpenter "Introduction to Theory of Neutron Scattering" Presentation at Argonne National Laboratory, 2006.

[91] Raghunathan, V., and J. Katsaras, 1995. Structure of the lc phase in a hydrated lipid multilamellar system. *Physical review letters* 74:4456.

[92] McIntosh, T. J., and S. A. Simon, 1986. Area per molecule and distribution of water in fully hydrated dilauroylphosphatidylethanolamine bilayers. *Biochemistry* 25:4948–4952.

[93] Tristram-Nagle, S., R. Zhang, R. M. Suter, C. R. Worthington, W. J. Sun, and J. F. Nagle, 1993. Measurement of chain tilt angle in fully hydrated bilayers of gel phase lecithins. *Biophysical journal* 64:1097–1109.

[94] Scherrer, P., 1912. Bestimmung der inneren Struktur und der Größe von Kolloidteilchen mittels Röntgenstrahlen. *In* Kolloidchemie Ein Lehrbuch, Springer, 387–409.

[95] Marsh, D., 2013. Handbook of Lipid Bilayers, Second Edition. CRC Press, Boca Raton, FL, 2nd ed edition.

[96] Glatter, O., 1977. A new method for the evaluation of small-angle scattering data. *Journal of Applied Crystallography* 10:415–421.

[97] Heberle, F. A., J. Pan, R. F. Standaert, P. Drazba, N. Kučerka, and J. Katsaras, 2012. Model-based approaches for the determination of lipid bilayer structure from small-angle neutron and X-ray scattering data. *European Biophysics Journal* 41:875–890.

[98] Kiselev, M., P. Lesieur, A. Kisselev, D. Lombardo, and V. Aksenov, 2002. Model of separated form factors for unilamellar vesicles. *Applied Physics A: Materials Science & Processing* 74:s1654–s1656.

[99] Pencer, J., Anghel, Vinicius N. P., N. Kučerka, and J. Katsaras, 2006. Scattering from laterally heterogeneous vesicles. I. Model-independent analysis. *Journal of Applied Crystallography* 39:791–796.

[100] Brzustowicz, M. R., and A. T. Brunger, 2005. X-ray scattering from unilamellar lipid vesicles. *Journal of Applied Crystallography* 38:126–131.

[101] Kučerka, N., J. F. Nagle, S. E. Feller, and P. Balgavý, 2004. Models to analyze small-angle neutron scattering from unilamellar lipid vesicles. *Physical Review E* 69:51903.

[102] Kučerka, N., J. Pencer, M. P. Nieh, and J. Katsaras, 2007. Influence of cholesterol on the bilayer properties of monounsaturated phosphatidylcholine unilamellar vesicles. *The European Physical Journal E: Soft Matter and Biological Physics* 23:247–254.

[103] Kučerka, N., J. F. Nagle, J. N. Sachs, S. E. Feller, J. Pencer, A. Jackson, and J. Katsaras, 2008. Lipid bilayer structure determined by the simultaneous analysis of neutron and X-ray scattering data. *Biophysical journal* 95:2356–2367.

[104] Nagle, J. F., and S. Tristram-Nagle, 2000. Structure and interactions of lipid bilayer: role of fluctuations. *In* J. Katsaras, and T. Gutberlet, editors, Lipid bilayers. Structure and interactions, Springer, Berlin, Biological Physcis Series, 1–23.

[105] Kučerka, N., M.-P. Nieh, and J. Katsaras, 2011. Fluid phase lipid areas and bilayer thicknesses of commonly used phosphatidylcholines as a function of temperature. *Biochimica et Biophysica Acta (BBA)-Biomembranes* 1808:2761–2771.

[106] Kučerka, N., B. van Oosten, J. Pan, F. A. Heberle, T. A. Harroun, and J. Katsaras, 2015. Molecular structures of fluid phosphatidylethanolamine bilayers obtained from simulation-to-experiment comparisons and experimental scattering density profiles. *The Journal of Physical Chemistry B* 119:1947–1956. 25436970.

[107] Pan, J., D. Marquardt, F. A. Heberle, N. Kučerka, and J. Katsaras, 2014. Revisiting the bilayer structures of fluid phase phosphatidyl-glycerol lipids: Accounting for exchangeable hydrogens. *Biochimica et Biophysica Acta (BBA) - Biomembranes* 1838:2966–2969.

[108] Small, D. M., 1986. Physical chemistry of lipids. Plenum Press, New York, NY.

[109] Koenig, B. W., and K. Gawrisch, 2005. Specific volumes of unsaturated phosphatidylcholines in the liquid crystalline lamellar phase. *Biochimica et Biophysica Acta (BBA) - Biomembranes* 1715:65–70.

[110] Klauda, J. B., N. Kučerka, B. R. Brooks, R. W. Pastor, and J. F. Nagle, 2006. Simulation-based methods for interpreting x-ray data from lipid bilayers. *Biophysical journal* 90:2796–2807.

[111] Pabst, G., KuM.C., and J. Katsaras, 2010. Applications of neutron and X-ray scattering to the study of biologically relevant model membranes. *Chem. Phys. Lipids* 163:460–479.

[112] Marquardt, D., F. A. Heberle, J. D. Nickels, G. Pabst, and J. Katsaras, 2015. On scattered waves and lipid domains: detecting membrane rafts with X-rays and neutrons. *Soft matter* 11:9055–9072.

[113] Wiener, M. C., R. M. Suter, and J. F. Nagle, 1989. Structure of the fully hydrated gel phase of dipalmitoylphosphatidylcholine. *Biophysical journal* 55:315–325.

[114] Yuan, Y.-x., 2000. A review of trust region algorithms for optimization. *In* ICIAM. volume 99, 271–282.

[115] Price, K., R. M. Storn, and J. A. Lampinen, 2006. Differential evolution: a practical approach to global optimization. Springer Science & Business Media, Heidelberg, Germany.

[116] Storn, R., and K. Price, 1997. Differential evolution–a simple and efficient heuristic for global optimization over continuous spaces. *Journal of global optimization* 11:341–359.

[117] Price, K., and R. Storn, 1997. Differential evolution: numerical optimization made easy. *Dr. Dobb's Journal* 220:18–24.

[118] Fogarty, J. C., M. Arjunwadkar, S. A. Pandit, and J. Pan, 2015. Atomically detailed lipid bilayer models for the interpretation of small angle neutron and X-ray scattering data. *Biochimica et Biophysica Acta (BBA) - Biomembranes* 1848:662–672.

[119] Huang, C., and J. Mason, 1978. Geometric packing constraints in egg phosphatidylcholine vesicles. *Proceedings of the National Academy of Sciences* 75:308–310.

[120] Smolentsev, N., C. Luetgebaucks, H. I. Okur, de Beer, Alex G. F., and S. Roke, 2016. Intermolecular Headgroup Interaction and Hydration as Driving Forces for Lipid Transmembrane Asymmetry. *Journal of the American Chemical Society* 138:4053–4060.

[121] Svetlovics, J. A., S. A. Wheaten, and P. F. Almeida, 2012. Phase separation and fluctuations in mixtures of a saturated and an unsaturated phospholipid. *Biophysical journal* 102:2526–2535.

[122] Pataraia, S., Y. Liu, R. Lipowsky, and R. Dimova, 2014. Effect of cytochrome c on the phase behavior of charged multicomponent lipid membranes. *Biochimica et biophysica acta* 1838:2036–2045.

[123] Tables of Physical & Chemical Constants (16th edition 1995): 2.2.5 Surface tensions. `www.kayelaby.npl.co.uk`.

[124] Pan, J., X. Cheng, L. Monticelli, F. A. Heberle, N. Kučerka, D. P. Tieleman, and J. Katsaras, 2014. The molecular structure of a phosphatidylserine bilayer determined by scattering and molecular dynamics simulations. *Soft Matter* 10:3716–3725. 24807693.

[125] Kollmitzer, B., P. Heftberger, M. Rappolt, and G. Pabst, 2013. Monolayer spontaneous curvature of raft-forming membrane lipids. *Soft Matter* 9:10877–10884. 24672578.

[126] Pozo, N. B., K. Lohner, G. Deutsch, E. Sevcsik, K. A. Riske, R. Dimova, P. Garidel, and G. Pabst, 2005. Composition dependence of vesicle

morphology and mixing properties in a bacterial model membrane system. *Biochimica et Biophysica Acta (BBA)-Biomembranes* 1716:40–48.

[127] McIntosh, T. J., 1980. Differences in hydrocarbon chain tilt between hydrated phosphatidylethanolamine and phospatidylcholine bilayer. A molecular paccking model. *Biophysical journal* 29:237–245.

[128] Lohner, K., editor, 2001. Development of novel antimicrobial agents: emerging strategies. Horizon Scientific Press, Wymondham.

[129] Boggs, J. M., 1980. Intermolecular hydrogen bonding between lipids: influence on organization and function of lipids in membranes. *Canadian journal of biochemistry* 58:755–770.

[130] McIntosh, T. J., 1996. Hydration properties of lamellar and non-lamellar phases of phosphatidylcholine and phosphatidylethanolamine. *Chemistry and physics of lipids* 81:117–131.

[131] Harder, T., and K. Simons, 1997. Caveolae, DIGs, and the dynamics of sphingolipid—cholesterol microdomains. *Current opinion in cell biology* 9:534–542.

[132] Zhao, J., J. Wu, F. A. Heberle, T. T. Mills, P. Klawitter, G. Huang, G. Costanza, and G. W. Feigenson, 2007. Phase studies of model biomembranes: complex behavior of DSPC/DOPC/cholesterol. *Biochimica et Biophysica Acta (BBA)-Biomembranes* 1768:2764–2776.

[133] Heberle, F. A., R. S. Petruzielo, J. Pan, P. Drazba, N. Kučerka, R. F. Standaert, G. W. Feigenson, and J. Katsaras, 2013. Bilayer thickness mismatch controls domain size in model membranes. *Journal of the American Chemical Society* 135:6853–6859.

[134] Liu, J., K. L. Brown, and J. C. Conboy, 2013. The effect of cholesterol on the intrinsic rate of lipid flip–flop as measured by sum-frequency vibrational spectroscopy. *Faraday discussions* 161:45–61.

[135] Holzer, M., J. Momm, and R. Schubert, 2010. Lipid transfer mediated by a recombinant pro-sterol carrier protein 2 for the accurate preparation of asymmetrical membrane vesicles requires a narrow vesicle size distribution: a free-flow electrophoresis study. *Langmuir* 26:4142–4151.

[136] Markones, M., C. Zorzin, L. Kalie, S. Fiedler, and H. Heerklotz, 2017. Tuning Membrane Asymmetry: Controlled Uptake of Negatively Charged Lipids into the Outer Leaflet of Liposomes. *Biophysical Journal* 112:43a.

# Appendix A.

# List of Publications

## A.1. Attached Publications

F.A. Heberle[†], D. Marquardt[†], M. Doktorova[†], B. Geier[†], R. Standaert, P. Heftberger, B. Kollmitzer, J.D. Nickels, R.A. Dick, G. Feigenson, J. Katsaras, E. London and G. Pabst, 2016. "Subnanometer Structure of an Asymmetric Molde Membrane: Interleaflet Coupling Influences Domain Properties." *Langmuir.* 32, 5195–5200.
[†]contributed equally

**Author contributions:**
GP, FAH, EL and JK conceived the project; MD, DM and FAH designed the modified asymmetric LUV protocol; DM, MD, BG, FAH and RFS designed experiments; DM, MD, BG and FAH performed experiments; RFS gave technical support; DM, BG and FAH analyzed data; DM, MD, BG, FAH, GP and EL wrote the paper; PH, BK, JDN and RAD contributed to the project's development; GP, EL, JK and GWF gave conceptual advice.

B. Eicher, F.A. Heberle, D. Marquardt, G.N. Rechberger, J. Katsaras, and G. Pabst, 2017. "Joint small-angle X-ray and neutron scattering data analysis of asymmetric lipid vesicles." *J. Appl. Crystallogr.* 50, 419-429. 47:173–180.

**Author contributions:**
BE, FAH, DM, GP designed research; BE, FAH, DM performed research; BE, FAH developed the models; BE analyzed data; BE, FAH, JK, GP wrote the paper; GNR conducted UPLC-MS measurements.

B. Eicher, Drew Marquardt, F.A. Heberle, I. Letofsky-Papst, G. N. Rechberger, M.S. Appavou, J. Katsaras, and G. Pabst, 2017. "Instrinsic Curvature-Mediated Transbilayer Coupling in Asymmetric Lipid Vesicles." submitted.

**Author contributions:**
<u>BE</u>, FAH, DM, GP designed research; <u>BE</u>, FAH, DM performed research; <u>BE</u>, analyzed data; <u>BE</u>, GP wrote the paper; ILP performed TEM measurements; GNR conducted UPLC-MS measurements; MSA performed SANS measurements; JK gave conceptual advice.

## A.1.1. Further Publications

D. Marquardt, B. Geier, and G. Pabst, 2015. "Asymmetric Lipid Membranes: Towards More Realistic Model Systems." *Membranes* 5.2, 180-196.

D. Marquardt, F.A. Heberle, T. Miti, B. Eicher, E. London, J. Katsaras, and G. Pabst, 2017. "$^1$H NMR Shows Slow Phospholipid Flip-Flop in Gel and Fluid Bilayers." *Langmuir*, 33-3731-3741.

# Appendix B.

# Scientific publications

# LANGMUIR

# Subnanometer Structure of an Asymmetric Model Membrane: Interleaflet Coupling Influences Domain Properties

Frederick A. Heberle,[*,†,‡,+] Drew Marquardt,[*,||,⊥,+] Milka Doktorova,[#,∇,+] Barbara Geier,[||,⊥,+]
Robert F. Standaert,[§,○] Peter Heftberger,[||,⊥] Benjamin Kollmitzer,[||,⊥,◇] Jonathan D. Nickels,[†,‡]
Robert A. Dick,[∇] Gerald W. Feigenson,[∇] John Katsaras,[†,‡,◆] Erwin London,[¶] and Georg Pabst[*,||,⊥]

[†]Biology and Soft Matter Division, [‡]Joint Institute for Neutron Sciences, and [§]Biosciences Division, Oak Ridge National Laboratory, Oak Ridge, Tennessee 37831, United States

[||]Institute of Molecular Biosciences, Biophysics Division, NAWI Graz, University of Graz, Graz 8010, Austria

[⊥]BioTechMed-Graz, Graz 8010, Austria

[#]Tri-Institutional PhD Program in Computational Biology and Medicine, Weill Cornell Medical College, New York, New York 10065, United States

[∇]Department of Molecular Biology and Genetics, Cornell University, Ithaca, New York 14853, United States

[○]Department of Biochemistry and Cellular & Molecular Biology, and [◆]Department of Physics and Astronomy, University of Tennessee, Knoxville, Tennessee 37996, United States

[¶]Department of Biochemistry and Cell Biology, Stony Brook University, Stony Brook, New York 11794, United States

**S** *Supporting Information*

**ABSTRACT:** Cell membranes possess a complex three-dimensional architecture, including nonrandom lipid lateral organization within the plane of a bilayer leaflet, and compositional asymmetry between the two leaflets. As a result, delineating the membrane structure−function relationship has been a highly challenging task. Even in simplified model systems, the interactions between bilayer leaflets are poorly understood, due in part to the difficulty of preparing asymmetric model membranes that are free from the effects of residual organic solvent or osmotic stress. To address these problems, we have modified a technique for preparing asymmetric large unilamellar vesicles (aLUVs) via cyclodextrin-mediated lipid exchange in order to produce tensionless, solvent-free aLUVs suitable for a range of biophysical studies. Leaflet composition and structure were characterized using isotopic labeling strategies, which allowed us to avoid the use of bulky labels. NMR and gas chromatography provided precise quantification of the extent of lipid exchange and bilayer asymmetry, while small-angle neutron scattering (SANS) was used to resolve bilayer structural features with subnanometer resolution. Isotopically asymmetric POPC vesicles were found to have the same bilayer thickness and area per lipid as symmetric POPC vesicles, demonstrating that the modified exchange protocol preserves native bilayer structure. Partial exchange of DPPC into the outer leaflet of POPC vesicles produced chemically asymmetric vesicles with a gel/fluid phase-separated outer leaflet and a uniform, POPC-rich inner leaflet. SANS was able to separately resolve the thicknesses and areas per lipid of coexisting domains, revealing reduced lipid packing density of the outer leaflet DPPC-rich phase compared to typical gel phases. Our finding that a disordered inner leaflet can partially fluidize ordered outer leaflet domains indicates some degree of interleaflet coupling, and invites speculation on a role for bilayer asymmetry in modulating membrane lateral organization.
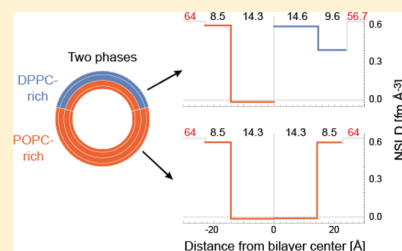
## INTRODUCTION

Cells have evolved to produce a great diversity of lipids, providing cellular membranes with remarkable functionality. Within the plasma membrane (PM) alone, hundreds of distinct lipid species serve both as a barrier to the external environment, as well as a solvent for the membrane's protein machinery. It is increasingly clear that the three-dimensional spatial organization of these lipid molecules can have profound effects on protein function.[1−3]

Synthetic liposomes (vesicles) have proven to be highly successful model systems for elucidating membrane properties that are otherwise difficult to study in vivo. In part, their utility stems from the fact that model membranes, compared to their natural counterparts, are chemically simpler and well-defined, and thereby enable stringent experimental control and detailed theoretical calculations at the molecular level. Nevertheless, the use of model systems requires a careful balancing act, where experimental tractability is weighed against biological relevance. The inherent tension between these conflicting goals is exemplified by transbilayer compositional asymmetry. While
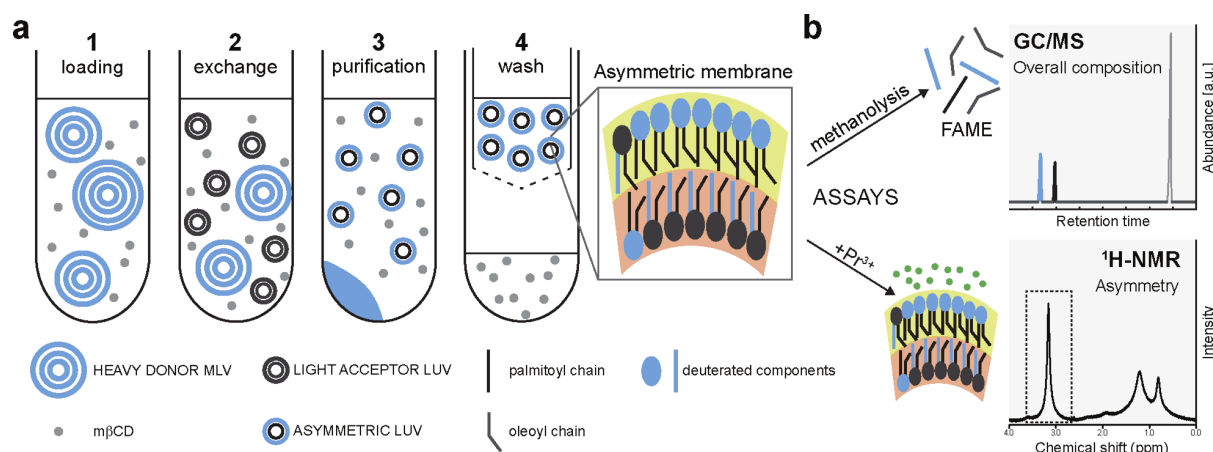
**Figure 1.** (a) Illustration of aLUV preparation: (1) methyl-$\beta$-cyclodextrin (m$\beta$CD) is loaded with lipid from donor MLVs entrapped with sucrose; (2) m$\beta$CD catalyzes lipid exchange between donor MLVs and acceptor LUVs; (3) large, heavy donor MLVs are removed by centrifugation; (4) m$\beta$CD is removed with a centrifugal concentrator, and the aLUV sample is recovered from the retentate. (b) GC is used to quantify the overall composition of the aLUVs following derivatization of acyl chains to fatty acid methyl esters (FAMEs), and $^1$H NMR is used to quantify lipid asymmetry in a lanthanide shift experiment. For a detailed description of the preparation and assays, see the Supporting Information.

the existence of asymmetry in natural cell membranes has been known since the early 1970s,[4] the vast majority of model membrane studies still employ symmetric vesicles, despite concerns about their ability to capture crucial aspects of lipid–lipid and lipid–protein interactions present in vivo.[2,5] Progress toward more realistic models of cell membranes has been hindered by the lack of a robust method for preparing asymmetric vesicles, including tools for precisely quantifying their composition and degree of asymmetry. Consequently, experimental data from asymmetric bilayers are scarce, and the effects of asymmetry on membrane structure and physical properties remain poorly understood.

Recent years have seen renewed effort toward the production of asymmetric membranes in a wide range of sample geometries, including supported[6−8] and unsupported[9] planar bilayers, and freely floating vesicles of various sizes.[10−15] Of special utility are large unilamellar vesicles (LUVs) with diameters on the order of 100 nm. Because they are amenable to study by diverse nanoanalytical techniques, LUVs have become workhorse model systems for protein–membrane interaction studies, and structural characterization using small-angle scattering, fluorescence and NMR. While protocols for asymmetric LUV (aLUV) preparation have been developed, they suffer from drawbacks that can compromise the membrane environment or hinder structural characterization. For example, inverted emulsion techniques[10,11,15] can provide excellent control of leaflet composition and achieve nearly complete asymmetry, but can trap organic solvents in the bilayer. aLUVs produced by catalyzed lipid exchange[13] are solvent-free, but have relied on a dense sucrose vesicle core for LUV purification. Entrapped sucrose presents an additional and potentially undesirable source of structural perturbation arising from sucrose-lipid interactions[16] and/or membrane tension from the resulting osmotic gradient.[17]

Here, we present a novel experimental strategy for determining asymmetric bilayer composition and structure based on differential isotopic labeling of aLUVs. A key aspect of our approach is the use of sucrose-free LUVs to minimize structural perturbations from membrane tension, which required modification of existing protocols for aLUV preparation. We have therefore organized the paper as follows.

First, we describe a modification of catalyzed lipid exchange that eliminates osmotic gradients, enabling the production of large amounts of solvent- and stress-free aLUVs with a well-defined size distribution. We use isotopic labeling to avoid fluorescent or spin-labeled lipids that can potentially perturb bilayer structure. Differentially deuterated donor and acceptor lipids enable the use of NMR and gas chromatography to precisely quantify the compositions of both leaflets following lipid exchange, while small-angle neutron scattering (SANS) is used to determine the bilayer structure with subnanometer resolution.

Next, in order to identify any structural perturbations caused by experimental conditions, we characterized aLUVs with different isotopic variants of 1-palmitoyl-2-oleoyl-sn-glycero-3-phosphatidylcholine (POPC) in the inner and outer leaflets. Within measurement uncertainty, these aLUVs were identical to symmetric POPC LUVs with respect to bilayer thickness and area per lipid.

Finally, we undertook a detailed structural characterization of aLUVs having a mixture of POPC and 1,2-dipalmitoyl-sn-glycero-3-phosphatidylcholine (DPPC) in the outer leaflet, and POPC in the inner leaflet. SANS analysis revealed both outer leaflet phase separation and interleaflet coupling, with the latter manifested as reduced lipid packing density in the outer leaflet ordered phase. We discuss the implications of this finding for lateral organization in cellular membranes.

## ■ EXPERIMENTAL SECTION

**Preparation of Asymmetric LUVs.** Solvent-free exchange protocols achieve an asymmetric lipid distribution through cyclodextrin (CD)-mediated lipid exchange between donor and acceptor vesicles.[12−14] The acceptor vesicles thus provide lipids for the aLUV inner leaflet, while the donor vesicles provide different lipids for the outer leaflet through catalyzed exchange. This process requires coincubation and eventual separation of donors and acceptors, most easily accomplished by taking advantage of density or size differences between the two vesicle populations.[12,13] Established protocols make use of density differences by trapping a concentrated sucrose solution in the acceptor LUV core, allowing aLUVs to be purified from larger, lower-density donor multilamellar vesicles (MLVs) and residual CD by ultracentrifugation.[13] Our modified protocol reversed this scheme, instead trapping sucrose between the donor lamellae (Figure 1 and
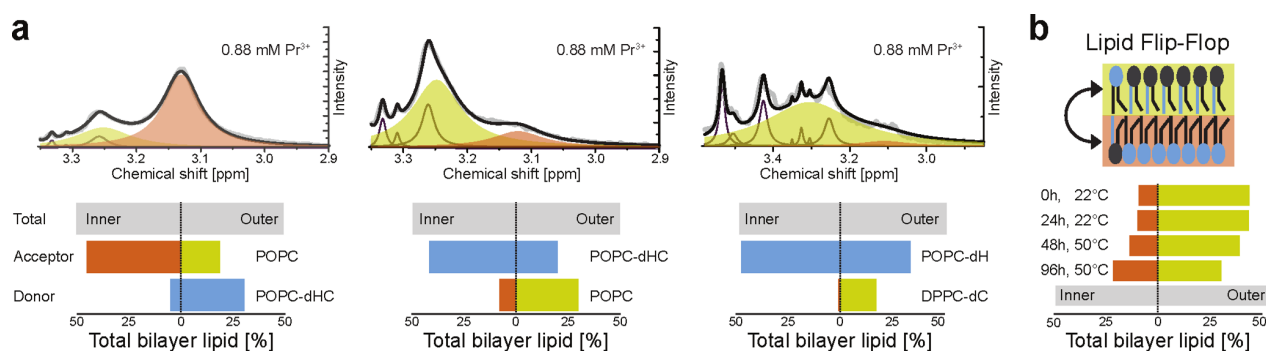
**Figure 2.** Characterization of aLUV composition. (a) Upper: $^1$H NMR spectra reveal the outer leaflet (yellow) and inner leaflet (red) population of protiated headgroup lipid, after external addition of the shift reagent Pr$^{3+}$. The black curve is the sum of fitted peaks including trace glycerol and residual mβCD (purple). Lower: the composition of three aLUV samples determined by joint GC, $^1$H NMR, and SANS analysis (see also Tables S2−S4 and Figures S4−S6). (b) The stability of POPC aLUVs is demonstrated by the inner/outer distribution of POPC donor exchanged into POPC-*dH* acceptor vesicles, shown immediately following aLUV preparation (0 h, 22 °C) and after 24 h of incubation at room temperature (24 h, 22 °C). A gradual loss of asymmetry is observed over 4 days of incubation at 50 °C.

Supporting Information Figure S2). This important change both eliminated sucrose from the aLUV core, and enhanced the difference in sedimentation velocities between donor and acceptor vesicles, due to the larger size and density of the sucrose-loaded donor MLVs. As a result, low-speed centrifugation (20 000*g*) was sufficient to achieve >95% purification of aLUVs by mass. Subsequent dilution/concentration cycles with centrifugal ultrafiltration devices (100 kDa molecular weight cutoff, 5000*g*) allowed for the efficient removal of residual sucrose and CD, as well as the ability to exchange H$_2$O with D$_2$O for small-angle neutron scattering (SANS) and $^1$H NMR experiments. Importantly, the modified protocol yielded large amounts of aLUVs suitable for sample-intensive techniques. Details of the protocol and assessment of sample purity are found in the Supporting Information.

**Characterization of aLUV Composition and Structure.** Asymmetric LUVs prepared by the new protocol were characterized for donor exchange efficiency, degree of asymmetry and nanostructure using assays designed to avoid large labels that can potentially affect membrane properties. In particular, we exploited the chemical similarity of hydrogen and deuterium, and the ability of gas chromatography (GC), NMR spectroscopy, and SANS to distinguish between protiated lipids and their deuterated counterparts.

The composition of the asymmetric vesicles' two leaflets was determined by combining two assays, each of which relies on isotopically labeled lipids. First, donor exchange efficiency was evaluated for aLUVs having differentially chain-labeled donor and acceptor. Exchange efficiency is directly given by the ratio of labeled to unlabeled lipids, and was readily quantified because the *sn*-1 fatty acid methyl ester (FAME) derivatives (i.e., methyl palmitate and methyl palmitate-*d$_{31}$*) were fully resolved by capillary gas chromatography (Figure S3). Second, the degree of asymmetry—i.e., the distribution of lipids between the two leaflets—was evaluated for aLUVs having differentially head-labeled donor and acceptor (i.e., choline vs choline-*d$_{13}$*). The choline distribution was determined using solution $^1$H NMR, which detects choline but not choline-*d$_{13}$*, by quantifying the shift of the outer leaflet choline methyl resonances in the presence of externally added paramagnetic lanthanide ion Pr$^{3+}$ (Figures S4−S6).[18] Pr$^{3+}$ does not permeate into the LUV core on the time scale of days, and the interaction is therefore specific for outer leaflet headgroups.[19] Because bilayer defects at the boundaries between gel and fluid domains may facilitate passive ion transport,[20] we also verified that phase-separated vesicles were impermeable to Pr$^{3+}$ during the time required to measure the NMR spectrum (Supporting Information Figure S8).

We used SANS to characterize bilayer structure on the subnanometer length scale. The unique scattering signatures of deuterium and hydrogen generate strong interleaflet contrast for isotopically asymmetric bilayers. Differential donor/acceptor labeling

schemes allowed us to independently determine both inner and outer leaflet structural properties, including thickness, headgroup water content, and lateral area per lipid, which is related to lipid packing density (Figures 3 and S9).

SANS data were analyzed using a four-slab bilayer model for the neutron scattering length density (NSLD) profile. The model was constrained with the compositional information obtained from GC and NMR experiments, and lipid headgroup and acyl chain volumes obtained from literature.[21,22] The addition of independent composition and volume constraints allowed us to reduce the number of fitting parameters. Full details of the model and data analysis are found in the Supporting Information.

## ■ RESULTS

**Isotopically Asymmetric POPC aLUVs.** Because aLUV preparation involves subjecting lipid vesicles to cyclodextrin and centrifugal filtration, it is important to assess structural changes caused by experimental conditions. To this end, we prepared aLUVs composed of POPC and its chain (-*dC*), headgroup (-*dH*), and fully labeled (-*dHC*) isotopic variants (Figure S1), and compared them to symmetric POPC LUVs prepared by conventional techniques.

We first examined a combination of labeled donor and acceptor lipids (POPC and POPC-*dHC*) that is amenable to both GC and $^1$H NMR analysis. This allowed us to characterize the asymmetric vesicles' inner and outer leaflet composition (details are found in the Supporting Information). Isotopically asymmetric POPC aLUVs prepared from an initial 2:1 donor/acceptor molar ratio exhibited ∼75% exchange efficiency and a high degree of asymmetry (Figure 2a and Tables S2−S3). Scrambled LUVs prepared with lipid extracted from aLUVs were found to have a symmetric transbilayer choline distribution (Supporting Information Figure S7).

To assess the stability of lipid asymmetry, we exchanged POPC donor into POPC-*dH* acceptor vesicles, and monitored POPC asymmetry with $^1$H NMR. No appreciable flip-flop was observed over 24 h (Figure 2b), consistent with previous reports for POPC ($t_{1/2} > 1000$ h at 37 °C).[23] After heating the sample to 50 °C, a gradual loss of asymmetry was observed over the course of 4 days.

Comparing different POPC aLUVs (Figure 2), small differences in exchange efficiency were observed. Because the amount of exchange depends on several factors including the ratio of donor to acceptor lipid, and the temperature and

duration of the exchange step, some sample-to-sample variation in exchange efficiency is not surprising, and further underscores the importance of precise assays for aLUV composition like those described here.

Structural parameters for isotopically asymmetric POPC aLUVs determined by SANS (Figure 3, Table S6) were (within
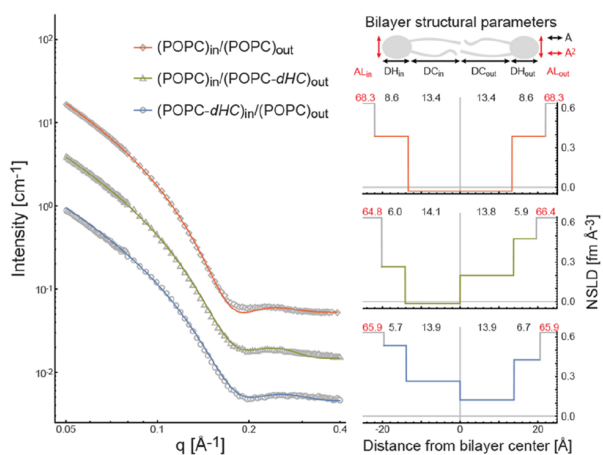


**Figure 3.** Structure of isotopically asymmetric POPC aLUVs at 20 °C determined by SANS. Left: SANS data (open symbols) and fits to the data (solid colored lines) for POPC aLUVs with different isotopic labeling of the inner and outer leaflets (Tables S2−S3). Upper right: schematic cartoon of the bilayer unit cell used to model SANS data; structural parameters obtained from the analysis include headgroup and hydrocarbon thicknesses (DH and DC, respectively) and area per lipid (AL) for inner and outer leaflets. Lower right: best-fit neutron scattering length density (NSLD) profiles color coded to SANS curves. Recovered structural parameters from left to right: inner leaflet AL, DH, and DC; outer leaflet DC, DH, and AL. Structural parameters are listed in Table S6.

error) identical to those of symmetric POPC LUVs (Table S5, Figure S8), and compared well with literature values,[21,24] indicating that sample preparation conditions did not alter the bilayer structure. In contrast, comparison of the membrane thickness of symmetric LUVs with and without a 25 wt% sucrose core indicated significant bilayer thinning in the presence of a sucrose core, consistent with osmotically generated membrane tension (Figure S11). This finding underscores the importance of stress-free vesicles for characterizing bilayer structure. Centrifugal filtration did not affect vesicle integrity or significantly alter the vesicle size distribution as judged by dynamic light scattering (Supporting Information Table S8).

Donor contamination in the form of MLVs and small unilamellar vesicles (SUVs) was not detected by SANS and NMR, respectively (Figures S12−S15), in asymmetric preparations. However, a small quantity of SUVs was found in donor-only control samples, an indication that minor contamination (<5% by mass) from donor-derived or mixed donor/acceptor SUVs may intrude in some cases. In particular, a small SUV population in POPC outer/POPC-*dHC* inner samples is inferred from the slightly larger amount of POPC found by NMR in the vesicles' inner leaflet (Figure 2a). A greater propensity for contamination is expected for lower density donor lipids, due to their reduced separation efficiency from acceptor vesicles. If complete removal of SUVs is necessary, sucrose density gradients can be employed.[13]

## Chemically Asymmetric DPPC/POPC aLUVs.

We next examined chemically asymmetric aLUVs composed of POPC and DPPC. Exchanging the high-melting donor lipid DPPC ($T_M$ 41 °C) into low-melting POPC acceptor vesicles ($T_M$ −2 °C) should increase the outer leaflet order relative to the inner leaflet. For ease of discussion, we will refer to such vesicles as "OO/DI", an abbreviation for "ordered outer/disordered inner".

Our sample preparation conditions employed a 3:1 ratio of DPPC donors to POPC acceptors, with exchange performed at room temperature. Asymmetric vesicles analyzed by GC, $^1$H NMR, and SANS were found to contain 34 mol % DPPC in the outer leaflet and 2 mol % DPPC in the inner leaflet (Figure 2a, Table S4). At room temperature, symmetric bilayers with this outer leaflet composition (i.e., DPPC:POPC = 34:66 mol %) are immiscible and contain coexisting gel and fluid phases, enriched in DPPC and POPC respectively.[25] However, different interleaflet interactions present in asymmetric bilayers may alter the compositions or properties of the coexisting phases, or abolish phase separation entirely.[9]

We found that SANS data could not be adequately modeled with a single asymmetric form factor, implying the presence of coexisting phases (Figure 4). Indeed, the data were well fitted
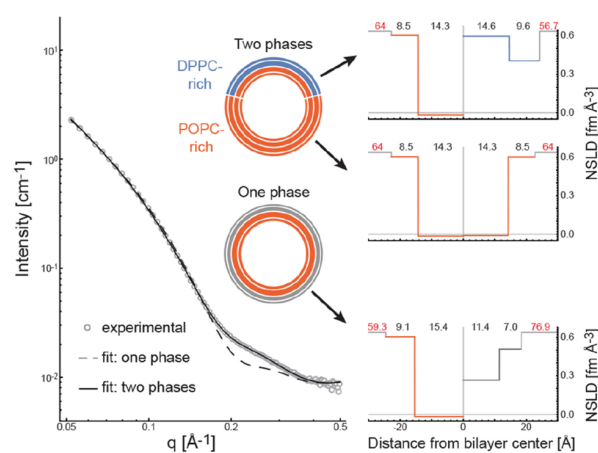


**Figure 4.** Structure of chemically asymmetric DPPC/POPC aLUVs at 20 °C determined by SANS. Left: SANS data (open circles) for aLUVs composed of DPPC-*dC* and POPC-*dH*, containing 34 mol % DPPC-*dC* in the outer leaflet and 98 mol % POPC-*dH* in the inner leaflet (Table S4). Experimental data were modeled assuming either a single outer leaflet phase (dashed line) or two outer leaflet phases (solid line) as indicated by schematic vesicles. Right: best-fit NSLD profiles for one phase (lower) and two phase (upper) models, with recovered structural parameters as in Figure 3. Structural parameters are listed in Table S7.

by a weighted sum of two bilayer form factors, corresponding to coexisting POPC- and DPPC-enriched phases in the outer leaflet and a uniform POPC phase in the inner leaflet (Figure 4 and Table S7). The possibility of two distinct vesicle populations with different compositions (which could arise from budding of phase domains) was ruled out by DLS measurements, which indicated a single LUV size distribution centered at ~130 nm both before and after lipid exchange (Supporting Information Table S8).

Importantly, best fit values of the area per lipid ($A_L$) indicate a marked reduction in lipid packing density of the DPPC-rich ordered phase (56.7 Å$^2$/molecule, Table S7), compared to

typical gel phase packing (47.2 $\text{Å}^2$ for DPPC at 20 °C).[26] The presence of 18 mol % POPC in the DPPC-rich phase is unlikely to account for this difference: assuming that the areas of individual species are additive, and using a value of 62.7 $\text{Å}^2$ for POPC at 20 °C[21] yields an $A_L$ of 50.2 $\text{Å}^2$ for the DPPC/POPC mixture. In fact, our best fit $A_L$ for the outer leaflet DPPC-rich phase lies between this value, and that of fluid phase DPPC (63.1 $\text{Å}^2$ at 50 °C).[21]

## ■ DISCUSSION

**Interleaflet Coupling in Asymmetric, Phase-Separated Bilayers.** Our observations for DPPC/POPC aLUVs suggest some degree of interleaflet coupling, whereby a leaflet senses and responds to the physical state of the apposing leaflet. Strong coupling of lipid dynamics has been observed in asymmetric giant unilamellar vesicles (GUVs) having a similar composition to our OO/DI LUVs: when the outer leaflet of POPC acceptor vesicles was partially replaced with brain or milk sphingomyelin (SM), lipid diffusion was reduced in both leaflets.[14] Interestingly, for these asymmetric OO/DI GUVs, inner leaflet structural order was almost completely decoupled from outer leaflet order. This finding is consistent with our structural modeling of asymmetric OO/DI LUVs, in which we observe no change in inner leaflet POPC packing density after partial outer leaflet exchange with the more ordered DPPC. However, we did find substantially altered properties of the outer leaflet ordered domains, which appear to be partially fluidized by coupling to a POPC inner leaflet. In contrast, for OO/DI LUVs in which the outer leaflet was almost completely replaced with SM, little or no decrease in outer leaflet order or transition temperature (relative to pure SM vesicles) was observed.[13] The lower levels of exchange in our DPPC/POPC aLUVs result in an outer leaflet DPPC-rich phase occupying a total area fraction of 0.37; however, we do not know the size and number of DPPC-rich domains, and therefore cannot exclude the possibility that boundary effects and interfacial phenomena are contributing to the observed order. It is likely that both composition (e.g., DPPC vs SM, as well as the extent of outer leaflet exchange) and temperature are important parameters for determining coupling strength in asymmetric bilayers. Establishing the rules that govern interleaflet coupling will be facilitated by the experimental strategy outlined here, which enables direct measurement of inner and outer leaflet structural properties in probe-free bilayers.

Our finding that interleaflet coupling can alter the packing of ordered domains may have implications for cell membrane organization. For example, a unifying theme of raft functionality is the selectivity of raft phases for specific proteins.[1,27] However, ordered phases in symmetric model membranes exclude most transmembrane proteins, including those thought to partition favorably into membrane rafts.[28,29] The discrepancies between protein partitioning in vitro and in vivo may be related to the relative packing density of the coexisting environments: significantly greater differences in hydrocarbon chain order are observed for coexisting liquid-disordered (Ld) and liquid-ordered (Lo) phases in model membranes, compared to coexisting phases in PM-derived vesicles.[30] Our early results suggest a previously unconsidered mechanism that can influence the relative packing density of coexisting phases, namely, bilayer asymmetry.

**Limitations of SANS Modeling.** SANS data are relatively featureless, and the possibility of a nonunique fit (especially for models having multiple free parameters) must always be considered. We chose to use a four-slab NSLD model, arguably the simplest reasonable model for asymmetric bilayer structure, in order to minimize the number of fit parameters. We also constrained as many parameters as possible, by incorporating lipid volumetric data obtained from the literature (Table S1 and eqs 15−16 in the Supporting Information), in addition to leaflet composition information from GC and NMR measurements.

Given the simplicity of the model and the number of constraints that were used, it is not surprising that fits to the SANS data are imperfect, for example near the first scattering minimum at q ∼ 0.2 $\text{Å}^{-1}$ of POPCo/POPCi aLUVs (Figure 3, red curve). The form factor of a perfectly symmetric, flat bilayer should decay to zero at the first minimum, but experimental data obtained from spherical vesicles often show nonzero intensity, even in nominally symmetric bilayers.[31] Consequently, flat bilayer form factors, like those used here, often result in poor fits at minima between scattering lobes for samples having low interleaflet contrast. Still, the fact that reasonably good fits are achieved despite the imposition of many external constraints, gives us confidence that the reported bilayer structure is essentially correct at the resolution of the slab model (i.e., ∼1 nm). The probability of a unique fit can be increased through the joint refinement of data from differently contrasted samples that share a common structure, for example DPPC/POPC aLUVs having different isotopic variants, but similar levels of exchange.

## ■ OUTLOOK

We combined SANS measurements with sensitive analytical tools for quantifying asymmetric bilayer composition, resulting in the first detailed structural characterization of an asymmetric model membrane. In aLUVs having a mixture of ordered and disordered lipids in the outer leaflet and a disordered lipid in the inner leaflet, we found distinct differences in structural properties as compared to symmetric LUVs, notably reduced gel phase packing density. Future studies of synthetic asymmetric bilayers mimicking raft phases (i.e., by incorporating cholesterol) will likely result in Ld and Lo phases with more biologically faithful properties and partitioning behaviors. More broadly, the procedures outlined here will pave the way for controlled studies of asymmetric bilayer structure and interleaflet coupling, and of the interplay between transmembrane proteins and biologically relevant membranes.

## ■ ASSOCIATED CONTENT

**ⓈSupporting Information**

The Supporting Information is available free of charge on the ACS Publications website at DOI: 10.1021/acs.langmuir.5b04562.

> Detailed experimental procedures, and theory; eight data tables [Tables S1−S8]; three figures relating to sample preparation [Figures SS1-S3]; five figures relating to NMR measurement [Figures S4−S8]; three figures relating to SANS measurements [Figures S9−S11]; four figures relating to contamination assessment [Figures S12−S15]; materials and methods (PDF)

## ■ AUTHOR INFORMATION

**Corresponding Authors**
*E-mail: heberlefa@ornl.gov.
*E-mail: drew.marquardt@uni-graz.at.

*E-mail: georg.pabst@uni-graz.at.

**Present Address**

◇Infineon Technologies Austria AG, Development Center Graz, Babenbergerstr. 10, A-8010 Graz, Austria

**Author Contributions**

⁺F.A.H., D.M., M.D., and B.G. contributed equally.

**Notes**

The authors declare no competing financial interest.

## ■ REFERENCES

(1) Lingwood, D.; Simons, K. Lipid Rafts as a Membrane-Organizing Principle. *Science* 2010, 327, 46−50.

(2) Simons, K.; Gerl, M. J. Revitalizing membrane rafts: new tools and insights. *Nat. Rev. Mol. Cell Biol.* 2010, 11, 688−699.

(3) Frewein, M.; Kollmitzer, B.; Heftberger, P.; Pabst, G. Lateral Pressure-Mediated Protein Partitioning into Liquid-Ordered/Liquid-Disordered Domains. *Soft Matter* 2016, 12, 3189.

(4) Bretscher, M. S. Membrane Structure: Some General Principles. *Science* 1973, 181, 622−629.

(5) van Meer, G.; Voelker, D. R.; Feigenson, G. W. Membrane lipids: where they are and how they behave. *Nat. Rev. Mol. Cell Biol.* 2008, 9, 112−124.

(6) Crane, J. M.; Kiessling, V.; Tamm, L. K. Measuring Lipid Asymmetry in Planar Supported Bilayers by Fluorescence Interference Contrast Microscopy. *Langmuir* 2005, 21, 1377−1388.

(7) Kiessling, V.; Crane, J. M.; Tamm, L. K. Transbilayer Effects of Raft-Like Lipid Domains in Asymmetric Planar Bilayers Measured by Single Molecule Tracking. *Biophys. J.* 2006, 91, 3313−3326.

(8) Wan, C.; Kiessling, V.; Tamm, L. K. Coupling of cholesterol-rich lipid phases in asymmetric bilayers. *Biochemistry* 2008, 47, 2190−2198.

(9) Collins, M. D.; Keller, S. L. Tuning lipid mixtures to induce or suppress domain formation across leaflets of unsupported asymmetric bilayers. *Proc. Natl. Acad. Sci. U. S. A.* 2008, 105, 124−128.

(10) Pautot, S.; Frisken, B. J.; Weitz, D. A. Engineering asymmetric vesicles. *Proc. Natl. Acad. Sci. U. S. A.* 2003, 100, 10718−10721.

(11) Hamada, T.; Miura, Y.; Komatsu, Y.; Kishimoto, Y.; Vestergaard, M.; Takagi, M. Construction of Asymmetric Cell-Sized Lipid Vesicles from Lipid-Coated Water-in-Oil Microdroplets. *J. Phys. Chem. B* 2008, 112, 14678−14671.

(12) Cheng, H. T.; Megha; London, E. Preparation and Properties of Asymmetric Vesicles That Mimic Cell Membranes: Effect Upon Lipid Raft Formation and Transmembrane Helix Orientation. *J. Biol. Chem.* 2009, 284, 6079−6092.

(13) Cheng, H. T.; London, E. Preparation and properties of asymmetric large unilamellar vesicles: interleaflet coupling in

asymmetric vesicles is dependent on temperature but not curvature. *Biophys. J.* 2011, 100, 2671−2678.

(14) Chiantia, S.; London, E. Acyl chain length and saturation modulate interleaflet coupling in asymmetric bilayers: effects on dynamics and structural order. *Biophys. J.* 2012, 103, 2311−2319.

(15) Elani, Y.; Purushothaman, S.; Booth, P. J.; Seddon, J. M.; Brooks, N. J.; Law, R. V.; Ces, O. Measurements of the effect of membrane asymmetry on the mechanical properties of lipid bilayers. *Chem. Commun.* 2015, 51, 6976−6979.

(16) Andersen, H. D.; Wang, C.; Arleth, L.; Peters, G. H.; Westh, P. Reconciliation of opposing views on membrane-sugar interactions. *Proc. Natl. Acad. Sci. U. S. A.* 2011, 108, 1874−1878.

(17) Ayuyan, A. G.; Cohen, F. S. Raft composition at physiological temperature and pH in the absence of detergents. *Biophys. J.* 2008, 94, 2654−2666.

(18) Andrews, S. B.; Faller, J. W.; Gilliam, J. M.; Barrnett, R. J. Lanthanide Ion-Induced Isotropic Shifts and Broadening for Nuclear Magnetic Resonance Structural Analysis of Model Membranes. *Proc. Natl. Acad. Sci. U. S. A.* 1973, 70, 1814−1818.

(19) Hunt, G. R. A. Kinetics of ionophore-mediated transport of Pr3+ ions through phoshpolipid membranes using 1H NMR spectroscopy. *FEBS Lett.* 1975, 58, 194−196.

(20) Papahadjopoulos, D.; Jacobson, K.; Nir, S.; Isac, T. Phase transitions in phospholipid vesicles. Fluorescence polarization and permeability measurements concerning the effect of temperature and cholesterol. *Biochim. Biophys. Acta, Biomembr.* 1973, 311, 330−348.

(21) Kučerka, N.; Nieh, M.-P.; Katsaras, J. Fluid phase lipid areas and bilayer thicknesses of commonly used phosphatidylcholines as a function of temperature. *Biochim. Biophys. Acta, Biomembr.* 2011, 1808, 2761−2771.

(22) Tristram-Nagle, S.; Liu, Y.; Legleiter, J.; Nagle, J. F. Structure of Gel Phase DMPC Determined by X-Ray Diffraction. *Biophys. J.* 2002, 83, 3324−3335.

(23) Nakano, M.; Fukuda, M.; Kudo, T.; Matsuzaki, N.; Azuma, T.; Sekine, K.; Endo, H.; Handa, T. Flip-Flop of Phospholipids in Vesicles: Kinetic Analysis with Time-Resolved Small-Angle Neutron Scattering. *J. Phys. Chem. B* 2009, 113, 6745−6748.

(24) Fogarty, J. C.; Arjunwadkar, M.; Pandit, S. A.; Pan, J. Atomically detailed lipid bilayer models for the interpretation of small angle neutron and X-ray scattering data. *Biochim. Biophys. Acta, Biomembr.* 2015, 1848, 662−672.

(25) Svetlovics, J. A.; Wheaten, S. A.; Almeida, P. F. Phase separation and fluctuations in mixtures of a saturated and an unsaturated phospholipid. *Biophys. J.* 2012, 102, 2526−2535.

(26) Sun, W. J.; Tristram-Nagle, S.; Suter, R. M.; Nagle, J. F. Structure of gel phase saturated lecithin bilayers: temperature and chain length dependence. *Biophys. J.* 1996, 71, 885−891.

(27) Lorent, J. H.; Levental, I. Structural determinants of protein partitioning into ordered membrane domains and lipid rafts. *Chem. Phys. Lipids* 2015, 192, 23.

(28) Bacia, K.; Schuette, C. G.; Kahya, N.; Jahn, R.; Schwille, P. SNAREs prefer liquid-disordered over "raft" (liquid-ordered) domains when reconstituted into giant unilamellar vesicles. *J. Biol. Chem.* 2004, 279, 37951−37955.

(29) Kahya, N.; Brown, D. A.; Schwille, P. Raft partitioning and dynamic behavior of human placental alkaline phosphatase in giant unilamellar vesicles. *Biochemistry* 2005, 44, 7479−7489.

(30) Kaiser, H. J.; Lingwood, D.; Levental, I.; Sampaio, J. L.; Kalvodova, L.; Rajendran, L.; Simons, K. Order of lipid phases in model and plasma membranes. *Proc. Natl. Acad. Sci. U. S. A.* 2009, 106, 16645−16650.

(31) Qian, S.; Heller, W. T. Peptide-Induced Asymmetric Distribution of Charged Lipids in a Vesicle Bilayer Revealed by Small-Angle Neutron Scattering. *J. Phys. Chem. B* 2011, 115, 9831−9837.

# SUB-NANOMETER STRUCTURE OF AN ASYMMETRIC MODEL MEMBRANE: INTERLEAFLET COUPLING INFLUENCES DOMAIN PROPERTIES

Frederick A. Heberle, Drew Marquardt, Milka Doktorova, Barbara Geier, Robert F. Standaert, Peter Heftberger, Benjamin Kollmitzer, Jonathan D. Nickels, Robert A. Dick, Gerald W. Feigenson, John Katsaras, Erwin London and Georg Pabst

**Table S1** Bilayer components and neutron scattering length density calculations. Molecular volumes of deuterated components are assumed to be identical to their protiated counterpart.

| Component | Formula | V [Å³] | b [fm][a] | SLD [fm Å⁻³][b] |
|---|---|---|---|---|
| 16:0-18:1 chains | $C_{32}H_{64}$ | 915.0[c] | -26.6 | -0.029 |
| 16:0(d31)-18:1 chains | $C_{32}H_{33}D_{31}$ | 915.0[c] | 296.1 | 0.322 |
| di-16:0(d31) chains | $C_{30}D_{62}$ | 810.4[c] | 613.0 | 0.756 |
| PC head in $D_2O$ | $C_{10}H_{18}NO_8P$ | 331[d] | 60.1 | 0.181 |
| PC(d13) head in $D_2O$ | $C_{10}H_5D_{13}NO_8P$ | 331[d] | 195.4 | 0.590 |
| Heavy water | $D_2O$ | 30.0 | 19.2 | 0.636 |

[a]coherent neutron scattering length; [b]scattering length density, b/V; [c]ref 1; [d]ref 2

**Table S2** Leaflet compositions for an asymmetric LUV sample prepared from POPC acceptor and POPC-*dHC* donor, determined from GC, $^1$H-NMR, and SANS modeling. Data columns from left to right indicate: bilayer mole fraction; component fraction in the outer versus inner leaflet; mole fraction of all lipids found in the outer leaflet; inner leaflet mole fraction; and outer leaflet mole fraction.

| Component | $\chi$ | $f^{out}$ | $X^{out}$ | $\chi^{in}$ | $\chi^{out}$ |
|---|---|---|---|---|---|
| POPC (acceptor) | 0.64[a] | 0.29[b] | 0.494[c] | 0.90[d] (0.45[e]) | 0.38[d] (0.19[e]) |
| POPC-*dHC* (donor) | 0.36[a] | | | 0.10[d] (0.05[e]) | 0.62[d] (0.31[e]) |
| Total | 1.00 | | | 1.00[d] (0.50[e]) | 1.00[d] (0.50[e]) |

[a]from GC; [b]from $^1$H-NMR; [c]from SANS structural modeling; [d]leaflet mole fraction; [e]total bilayer mole fraction

**Table S3** Leaflet compositions for an asymmetric LUV sample prepared from POPC-*dHC* acceptor and POPC donor, determined from GC, $^1$H-NMR, and SANS modeling. Data columns as described in Table S2 legend.

| Component | $\chi$ | $f^{out}$ | $X^{out}$ | $\chi^{in}$ | $\chi^{out}$ |
|---|---|---|---|---|---|
| POPC-*dHC* (acceptor) | 0.62[a] | | 0.50[c] | 0.84[d] (0.42[e]) | 0.40[d] (0.20[e]) |
| POPC (donor) | 0.38[a] | 0.79[b] | | 0.16[d] (0.08[e]) | 0.60[d] (0.30[e]) |
| Total | 1.00 | | | 1.00[d] (0.50[e]) | 1.00[d] (0.50[e]) |

[a]from GC; [b]from $^1$H-NMR; [c]from SANS structural modeling; [d]leaflet mole fraction; [e]total bilayer mole fraction

**Table S4** Leaflet compositions for an asymmetric LUV sample prepared from POPC-*dH* acceptor and DPPC-*dC* donor, determined from GC, $^1$H-NMR, and SANS modeling. Data columns as described in Table S2 legend.

| Component | $\chi$ | $f^{out}$ | $X^{out}$ | $\chi^{in}$ | $\chi^{out}$ |
|---|---|---|---|---|---|
| POPC-*dH* (acceptor) | 0.82[a] | | 0.512[c] | 0.98[d] (0.48[e]) | 0.66[d] (0.34[e]) |
| DPPC-*dC* (donor) | 0.18[a] | 0.95[b] | | 0.02[d] (0.01[e]) | 0.34[d] (0.18[e]) |
| Total | 1.00 | | | 1.00[d] (0.49[e]) | 1.00[d] (0.52[e]) |

[a]from GC; [b]from $^1$H-NMR; [c]from SANS structural modeling; [d]leaflet mole fraction; [e]total bilayer mole fraction

**Table S5** Refinement of symmetric POPC vesicles. Best fit parameters for differently contrasted symmetric POPC bilayers. Data were both individually and jointly modeled with a symmetric four slab scattering length density profile as described in Supporting Information Section S8. Model parameters from top to bottom indicate: area per lipid ($A_L$); number of headgroup waters ($n_W$); headgroup thickness ($D_H$); and hydrocarbon thickness ($D_C$).

| Param | Individual refinement | | | | Joint refinement |
|---|---|---|---|---|---|
| | POPC | POPC-*dH* | POPC-*dC* | POPC-*dHC* | |
| | *inner/outer* | *inner/outer* | *inner/outer* | *inner/outer* | *inner/outer* |
| $A_L$ [Å$^2$]$^a$ | 68.6 | 68.1 | 66.7 | 63.5 | 67.5 |
| $n_W$$^a$ | 8.2 | 2.0 | 8.0 | 2.0 | 7.2 |
| $D_H$ [Å]$^b$ | 8.4 | 5.7 | 8.0 | 6.1 | 8.0 |
| $D_C$ [Å]$^b$ | 13.4 | 13.4 | 13.7 | 14.4 | 13.5 |

$^a$variable parameter; $^b$derived from other model parameters, parameter uncertainties are estimated to be < 2%

**Table S6** Refinement of asymmetric POPC vesicles. Best fit parameters for two differently contrasted asymmetric POPC bilayers. Data were both individually and jointly modeled with an asymmetric four slab scattering length density profile as described in Supporting Information Section S8. Model parameters as in the Table S5 legend.

| Param | Individual refinement | | | | Joint refinement | |
|---|---|---|---|---|---|---|
| | POPC acc./POPC-*dHC* don. | | POPC-*dHC* acc./POPC don. | | | |
| | *inner* | *outer* | *inner* | *outer* | *inner* | *outer* |
| $A_L$ [Å$^2$]$^a$ | 64.8 | 66.4 | 65.9 | 65.9 | 64.8 | 66.4 |
| $n_W$$^a$ | 2 | 2 | 3.6 | 1.6 | 2 | 2 |
| $D_H$ [Å]$^b$ | 6.0 | 5.9 | 5.7 | 6.7 | 6.0 | 5.9 |
| $D_C$ [Å]$^b$ | 14.1 | 13.8 | 13.9 | 13.9 | 14.1 | 13.8 |

$^a$variable parameter; $^b$derived from other model parameters, parameter uncertainties are estimated to be < 2%

**Table S7** Refinement of chemically asymmetric aLUVs. Bilayer structural best-fit parameters for an aLUV sample prepared from POPC-*dH* acceptor and DPPC-*dC* donor, determined from fitting SANS data to an asymmetric two phase model. Model parameters from top to bottom indicate: mole fraction of DPPC within each leaflet ($\chi_{DPPC}$); area per lipid ($A_L$); number of headgroup waters ($n_W$); headgroup thickness ($D_H$); hydrocarbon thickness ($D_C$); and phase area fraction ($\alpha_k$).

| Parameter | Phase 1 | | Phase 2 | |
|---|---|---|---|---|
| | *inner* | *outer* | *inner* | *outer* |
| $\chi_{DPPC}$ | 0.019[a] | 0.024[c] | 0.019[b] | 0.82[c] |
| $A_L$ [Å$^2$] | 64.0[d] | 64.0[d] | 64.0[d] | 56.7[c] |
| $n_W$[a] | 7 | 7 | 7 | 7 |
| $D_H$ [Å][e] | 8.5 | 8.5 | 8.5 | 9.6 |
| $D_C$ [Å][e] | 14.3 | 14.3 | 14.3 | 14.6 |
| $\alpha_k$[b] | 0.63 | | 0.37 | |

[a]fixed parameter; [b]constrained from matter balance; [c]variable parameter; [d]jointly variable parameters; [e]derived from other model parameters, parameter uncertainties are estimated to be < 2%

**Table S8** LUV size and polydispersity determined by dynamic light scattering before and after centrifugal filtration. Uncertainty is estimated to be ± 5 nm. All measurements were performed at room temperature.

| Sample | Before centrifugal filtration | | After centrifugal filtration[b] | |
|---|---|---|---|---|
| | Diameter [nm] | Rel. polydisp. | Diameter [nm] | Rel. polydisp. |
| POPC LUV | 130.2 | 0.27 | 128.4 | 0.25 |
| POPC LUV[a] | 123.3 | 0.23 | 128.9 | 0.36 |
| POPC-*dH* LUV[a] | 125.1 | 0.23 | 131.1 | 0.28 |
| POPC-*dC* LUV[a] | 116.2 | 0.22 | 118.9 | 0.28 |
| DPPC-*dC* LUV[a] | 116.6 | 0.12 | 116.3 | 0.24 |
| (POPC-*dH*)in/(DPPC-*dC*)out aLUV[a,c] | 131.2 | 0.24 | 129.6 | 0.30 |

[a]vesicles prepared in 20 mM NaCl; [b]2-4 concentration/dilution cycles were performed as described in Supporting Information section S1. [c]Measurement before centrifugal filtration is of symmetric extruded acceptor LUVs, measurement after centrifugal filtration is of asymmetric LUVs.

| POPC | POPC-dC | POPC-dH | POPC-dHC | DPPC-dC |
|---|---|---|---|---|
| 16:0,18:1 | 16:0,18:1 | 16:0,18:1 | 16:0,18:1 | 16:0,16:0 |

mβCD

6.5 Å

7.8 Å
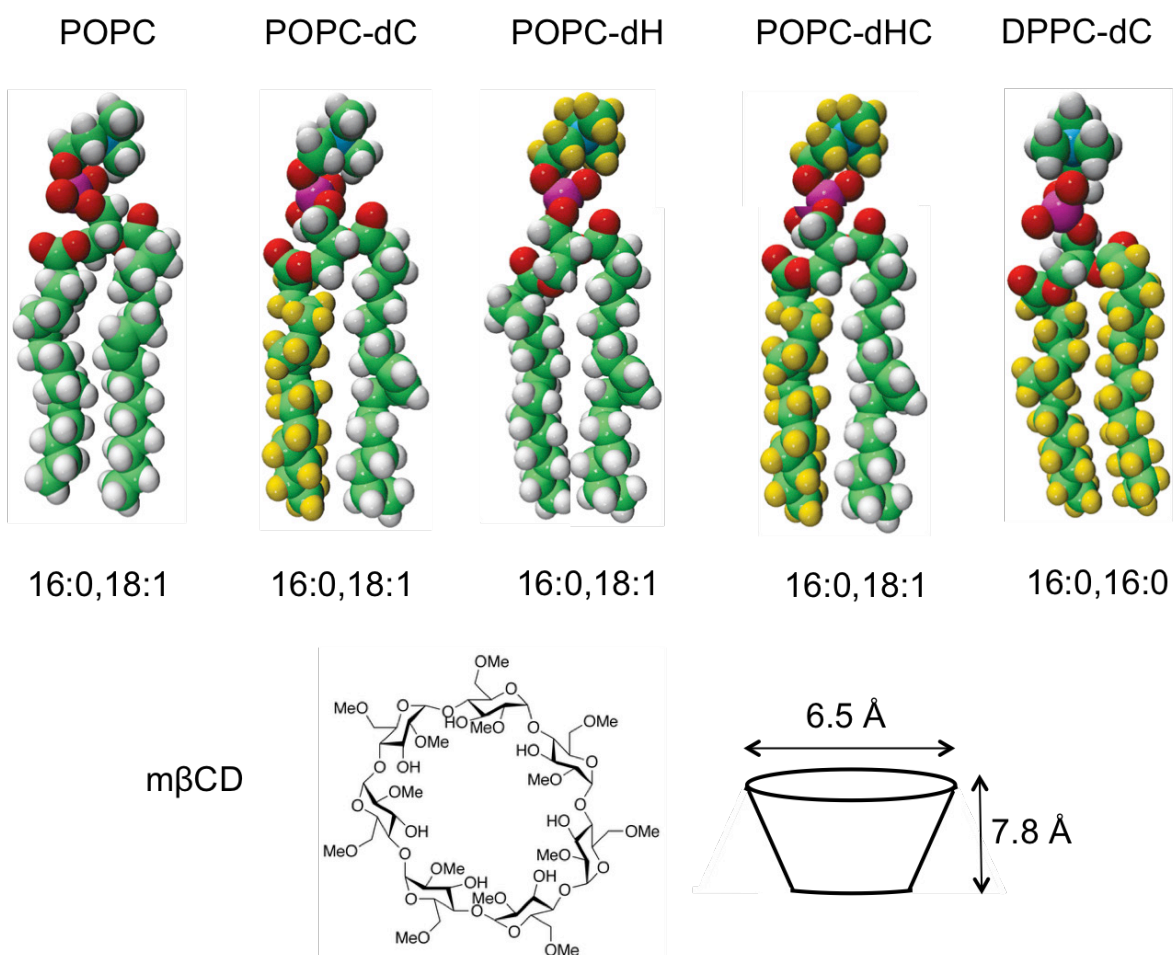
**Figure S1** | Chemical structures of phospholipids and methyl-beta-cyclodextrin (mβCD) used in this study. Lipids are displayed in space fill representation with white indicating hydrogen and yellow indicating deuterium. The label underneath each lipid shows the number of carbons and the number of double bonds in the *sn*-1 and *sn*-2 chains, respectively.
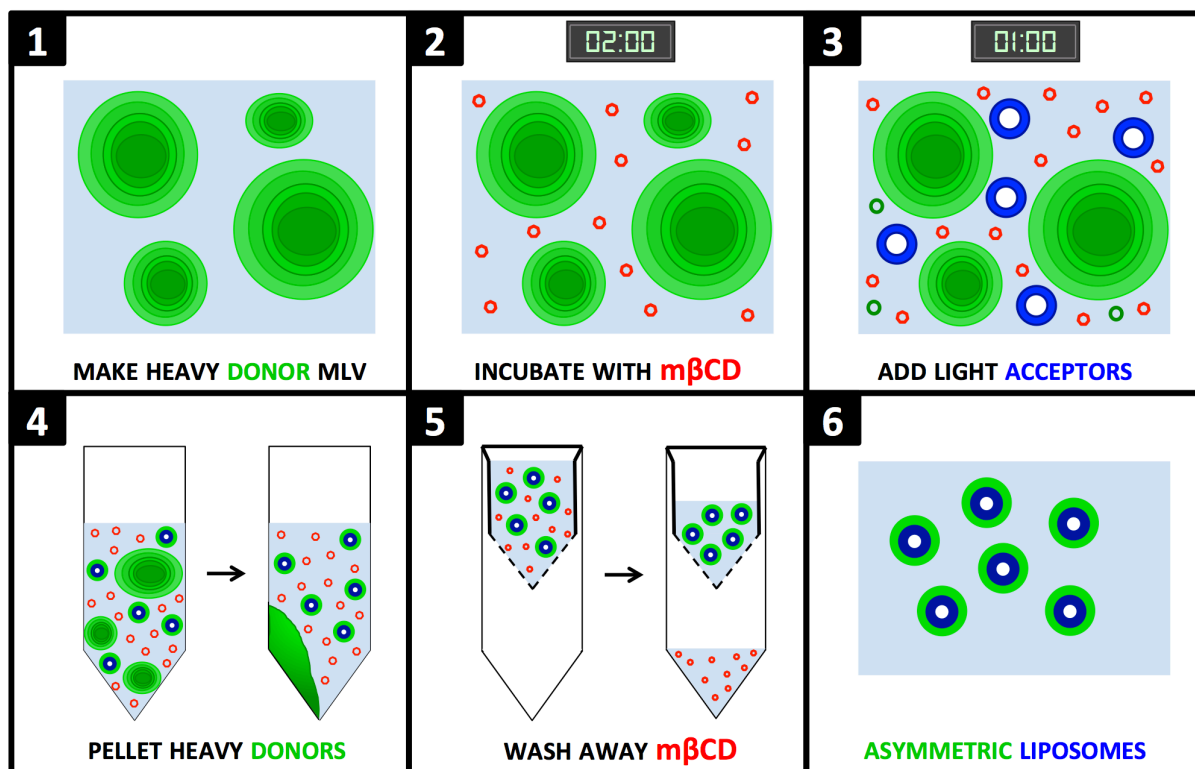
**Figure S2 | Protocol for the preparation of sucrose-free asymmetric liposomes.** *Step 1*, donor multilamellar vesicles (MLVs) are prepared in 20% (w/w) sucrose, then diluted 20-fold with water and centrifuged (supernatant is discarded). *Step 2*, aqueous methyl-beta cyclodextrin (mβCD, 35 mM) is added to the MLV pellet in an 8:1 mβCD:donor ratio and incubated for 2 h at room temperature while stirring. *Step 3*, a suspension of acceptor large unilamellar vesicles (LUVs) is added to the donor/mβCD sample to achieve a desired donor:acceptor molar ratio and an mβCD concentration of ~ 29 mM, then incubated for 1 h at room temperature while stirring. Acceptor LUVs can be prepared in low osmolarity buffer (*e.g.*, 10–30 mM NaCl) to balance residual solutes remaining after the asymmetric sample preparation. Depending on the mβCD concentration, a small fraction of the heavy donor vesicles may be dissolved and reformed as light small unilamellar vesicles (SUVs). *Step 4*, the mixture is diluted 8-fold with $H_2O$, then centrifuged for 30 min at 20K × g (pellet is discarded). *Step 5*, supernatant from Step 4 is first concentrated to 0.5−1 mL with a 100K MWCO centrifugal filter. The remaining mβCD is then removed by repeated dilution (with $H_2O$ or $D_2O$, depending on experimental needs) and concentration steps, with the filtrate discarded between steps, to achieve a desired dilution factor. *Step 6*, asymmetric sucrose-free LUVs in water are recovered from the retentate following the final wash.
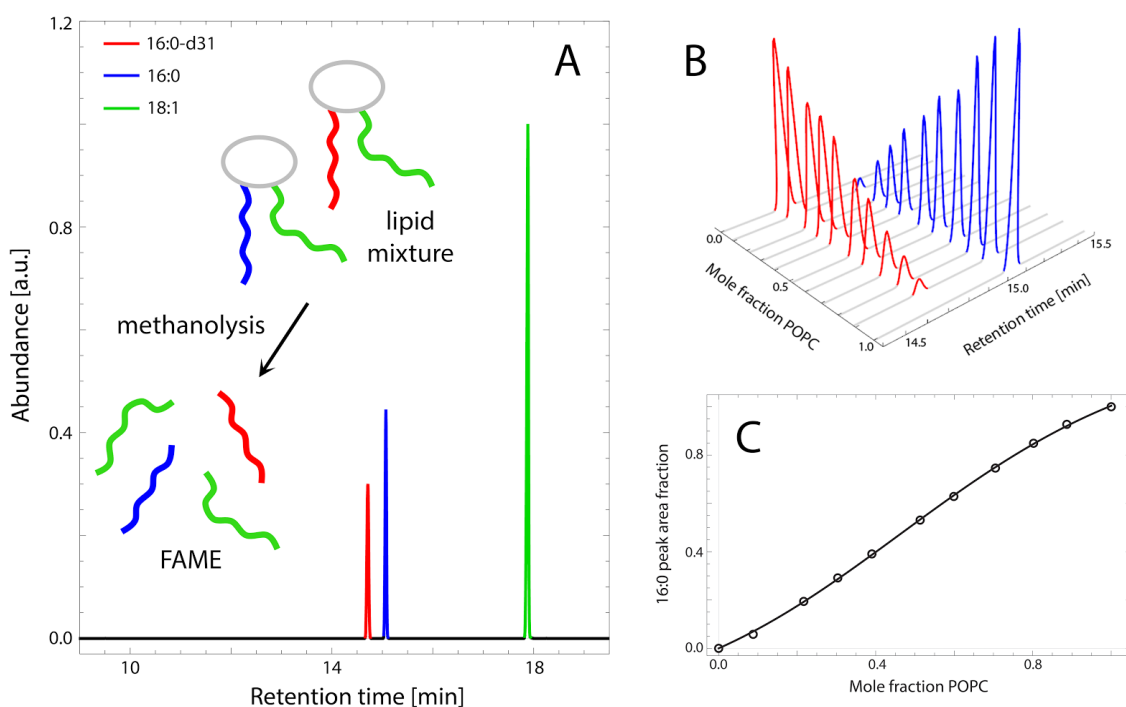
**Figure S3 | GC determines the total composition of lipid mixtures**. *A*, A lipid sample is subjected to an acid- or base-catalyzed transesterification, converting individual chains to volatile FAMEs suitable for GC analysis (inset cartoon). A binary equimolar mixture of POPC and POPC-*dC* yields a 2:1:1 ratio of methyl oleate, methyl palmitate, and methyl palmitate-d31, which is reflected in the relative peak areas from the total ion chromatogram. *B*, Changing the mixture composition alters the relative areas of the methyl palmitate and methyl palmitate-d31 peaks. The composition of an unknown sample can therefore be obtained from its peak area fraction. *C*, Detection inefficiencies result in a nonlinear dependence of peak area fraction *vs.* mixture composition. Precise quantitation of an unknown sample requires comparison to a standard curve obtained from mixtures of known composition.
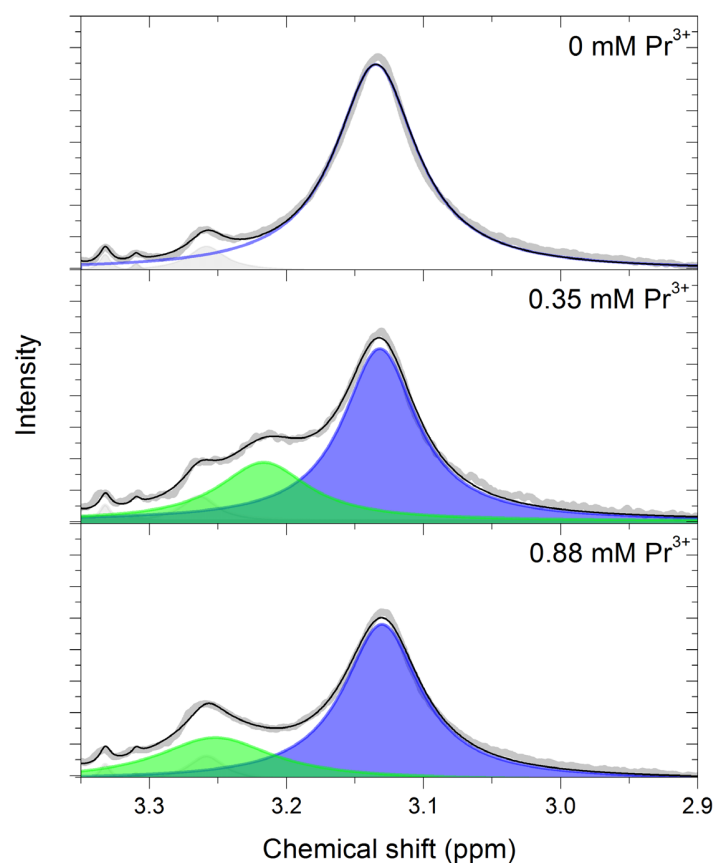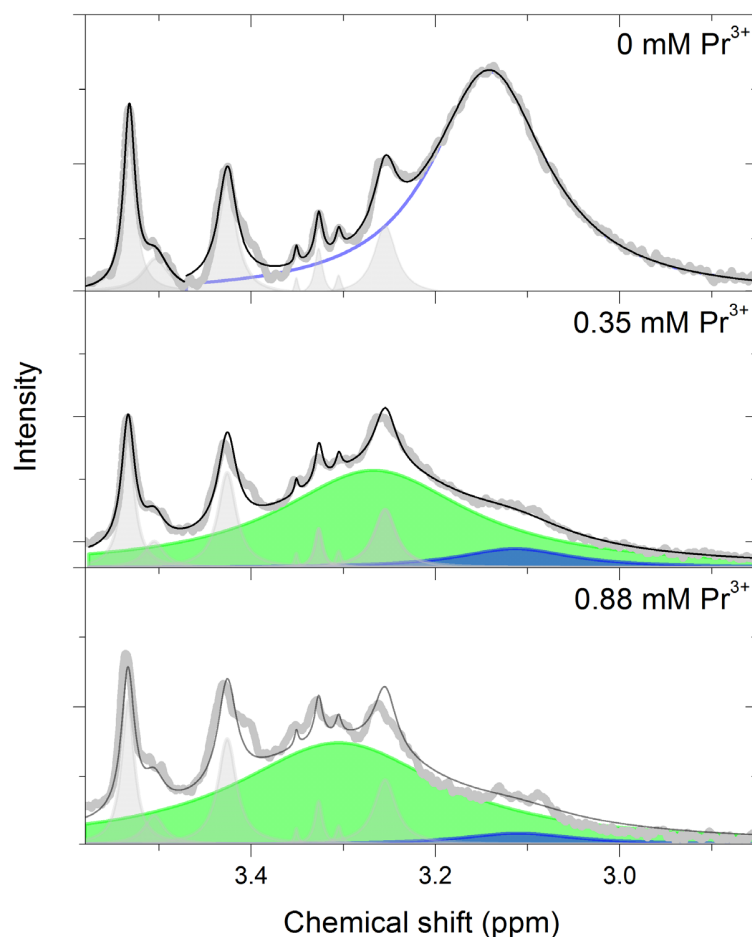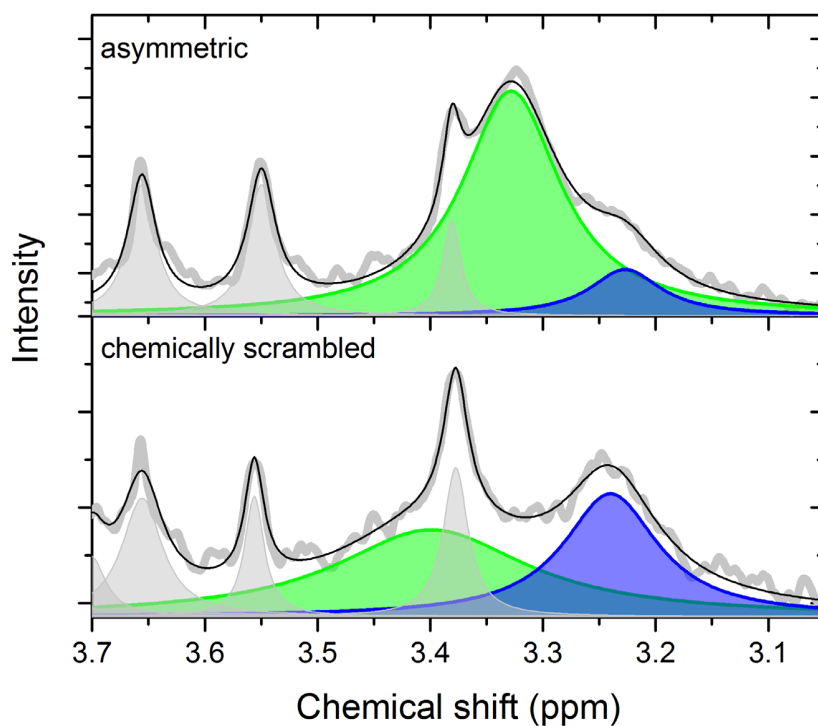
**Figure S4 | $^1$H-NMR of an aLUV sample prepared from POPC acceptor and POPC-*dHC* donor.** *Upper panel*, proton NMR shows a single choline resonance from the POPC acceptor in the absence of shift reagent (blue line), in addition to the minor contaminants glycerol and mβCD (gray shading). The sum of all fitted components is shown as a solid black line. *Lower panels*, addition of $Pr^{3+}$ selectively shifts outer leaflet choline resonances (green shading), revealing acceptor enrichment in the inner leaflet, where it is inaccessible to the shift reagent (blue shading).
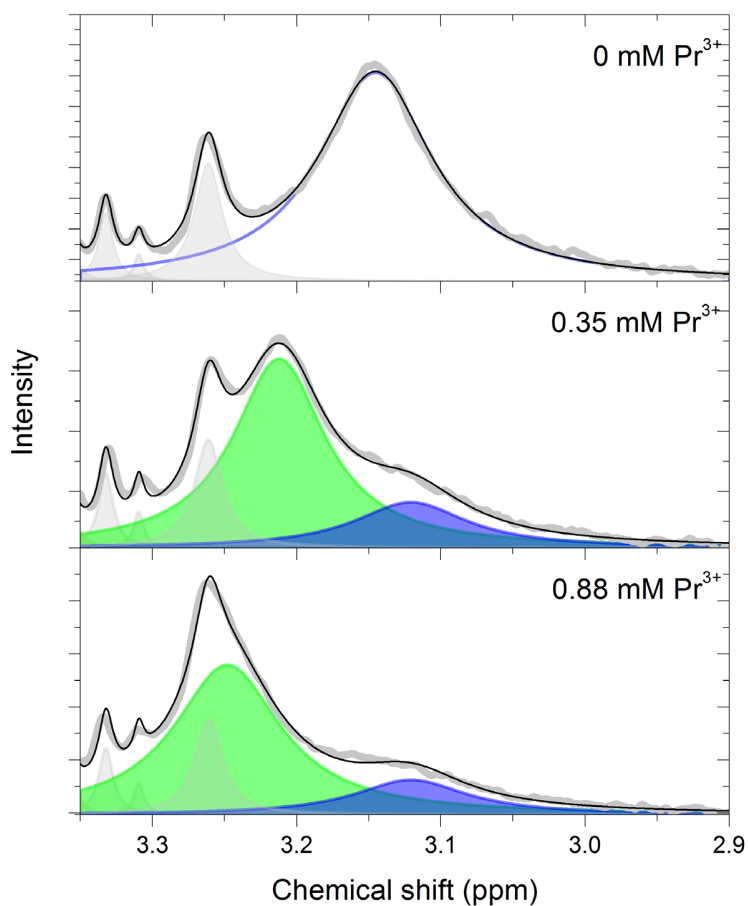
**Figure S5 | <sup>1</sup>H-NMR of an aLUV sample prepared from POPC-*dHC* acceptor and POPC donor.** *Upper panel*, proton NMR shows a single choline resonance from POPC donor in the absence of shift reagent (blue line), in addition to the minor contaminants glycerol and mβCD (gray shading). The sum of all fitted components is shown as a solid black line. *Lower panels*, addition of $Pr^{3+}$ selectively shifts outer leaflet choline resonances (green shading), revealing donor enrichment in the outer leaflet. Approximately 20 mol % of donor lipid is found in the inner leaflet, where it is inaccessible to the shift reagent (blue shading).

**Figure S6 | ¹H-NMR of an asymmetric LUV sample prepared from POPC-*dH* acceptor and DPPC-*dC* donor**. *Upper panel*, proton NMR shows a single choline resonance from DPPC-*dC* donor in the absence of shift reagent (blue line), in addition to the minor contaminants glycerol and mβCD (gray shading). The sum of all fitted components is shown as a solid black line. *Lower panels*, addition of $Pr^{3+}$ selectively shifts outer leaflet choline resonances (green shading), revealing donor enrichment in the outer leaflet. A small fraction (~ 6 mol %) of donor lipid is found in the inner leaflet, where it is inaccessible to the shift reagent (blue shading).

11

**Figure S7 | ^{1}H-NMR of an aLUV sample prepared from POPC-*dH* acceptor and POPC donor, before and after chemical scrambling**. *Upper panel*, proton NMR shows the choline resonance from POPC donor in the presence of $Pr^{3+}$. The large shifted population (green shading) relative to the unshifted population (blue shading) reveals substantial outer leaflet donor enrichment in the aLUV sample. *Lower panel,* the same sample after chemical scrambling (i.e., removal of water, dissolution in chloroform, and reformation of extruded LUVs) shows shifted and unshifted resonances with nearly equal areas, demonstrating the loss of asymmetry. Minor contaminants glycerol and mβCD are shown with gray shading.
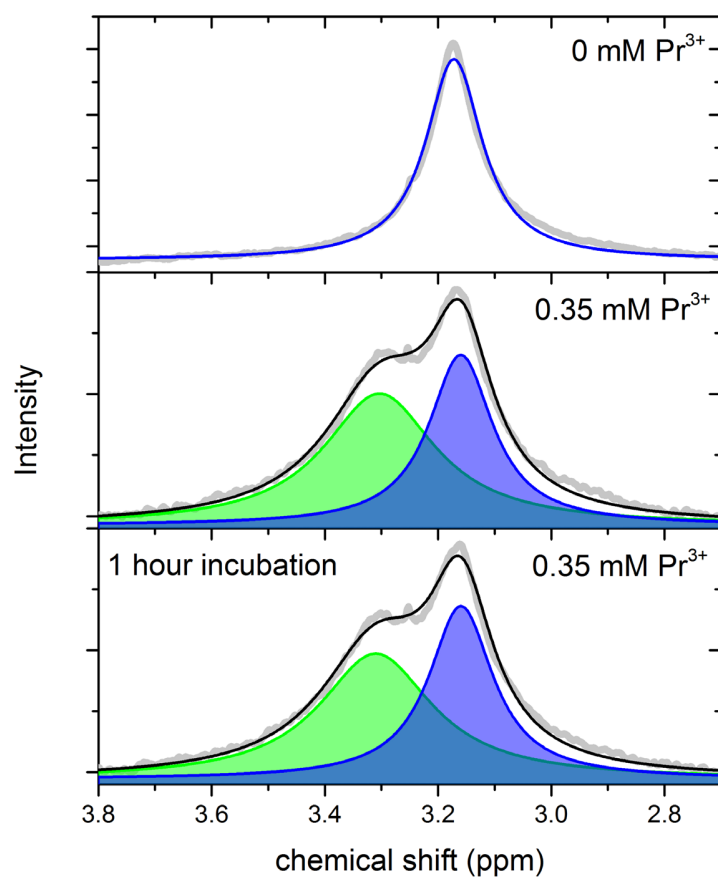
**Figure S8 | $^1$H-NMR of a symmetric, phase-separated LUV**. A single choline resonance is observed in phase-separated POPC/DPPC (1/1 molar ratio) LUVs in the absence of Pr$^{3+}$ (*upper panel*). Distinct resonances of nearly equal area corresponding to inner leaflet (blue shading) and outer leaflet (green shading) choline are observed immediately following external Pr$^{3+}$ addition (*middle panel*), and after 1 hour of incubation at room temperature (*lower panel*), demonstrating that Pr$^{3+}$ does not penetrate into the vesicle lumen during the ~ 15 minute measurement time.
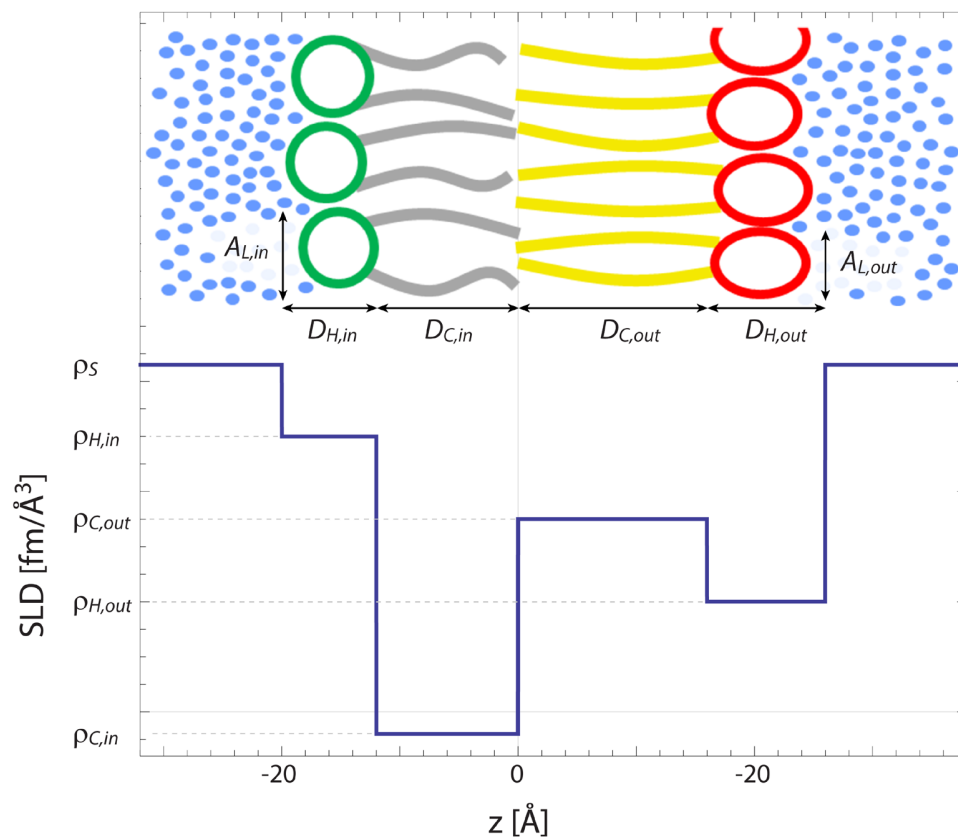
**Figure S9 | Four shell scattering length density profile for an asymmetric bilayer.** *Upper*, a schematic representation of an asymmetric bilayer. *Lower*, the corresponding scattering length density profile is represented by a simplified four slab model with parameters for slab thicknesses and scattering length densities. Parameter symbols are as defined in the Supporting Information text.
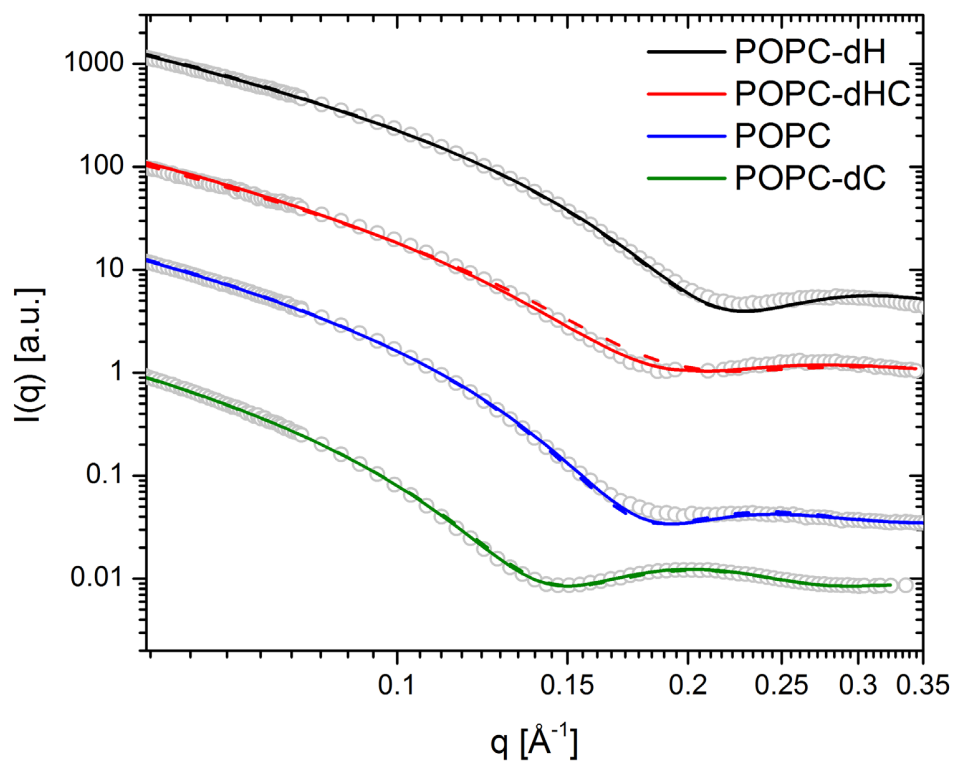
**Figure S10 | SANS data and fits for symmetric POPC vesicles**. Experimental SANS data (circles) for different contrast symmetric POPC bilayers. Data were modeled individually (solid lines) and jointly (dashed lines) with a symmetric four shell scattering length density profile as described in the Supporting Information text. Predicted scattered intensity is shown as solid lines, with best fit parameters given in Table S5. Data are vertically offset by powers of 10 for clarity.
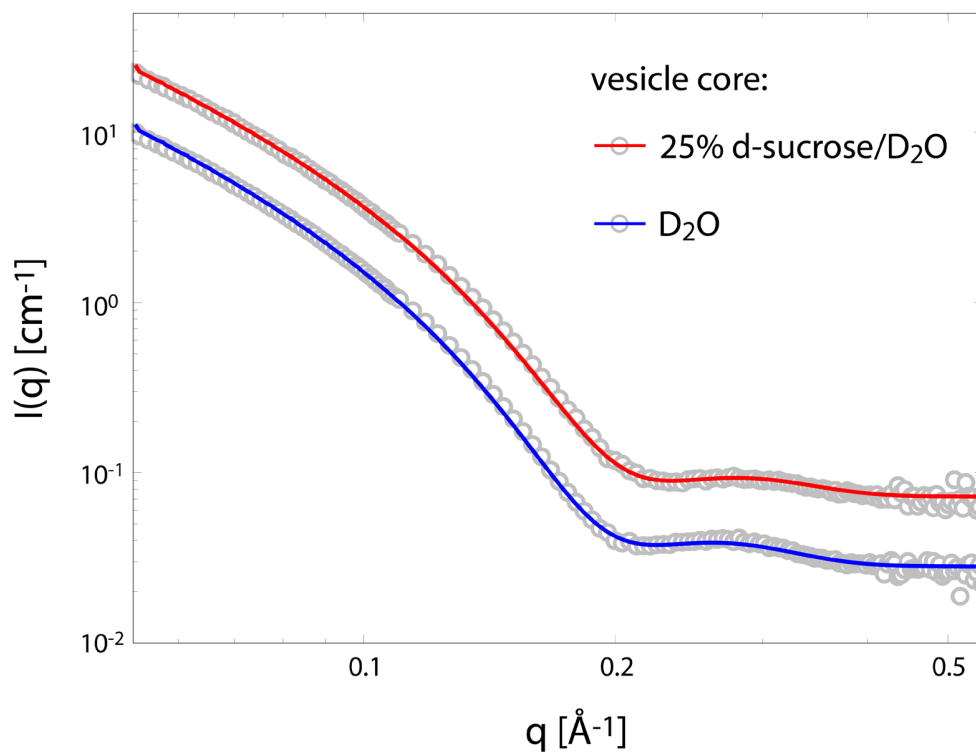
**Figure S11 | Osmotic imbalance generates membrane tension and thins POPS vesicles**.
Experimental SANS data for symmetric 100 nm diameter POPS LUVs, with different
core/solvent conditions. Osmotically stressed POPS vesicles containing a 25% d-sucrose core
(red) in an external $D_2O$ solvent show a decreased bilayer thickness ($-1.8$ Å) and an increased
area per lipid ($+4$ Å$^2$) compared to stress-free POPS vesicles prepared in $D_2O$ (blue), consistent
with vesicle swelling and lateral bilayer expansion. Data are vertically offset for clarity.
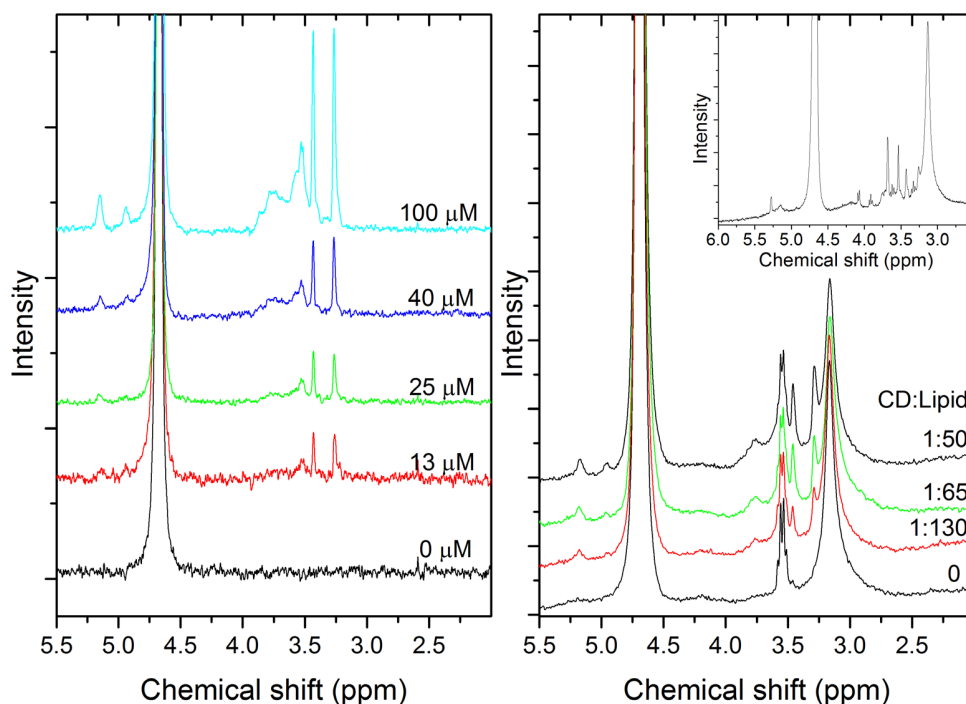
**Figure S12 | $^1$H-NMR detection mβCD**. Titration of mβCD into $D_2O$ (left) reveals the solute's detection limit with proton NMR. The characteristic CD peaks occur at 3.29 ppm and 3.46 ppm. Comparison of corresponding resonances in an asymmetric LUV sample provides a lower limit for residual mβCD concentration of 1:130 CD:lipid molar ratio. Titration of mβCD into an LUV/$D_2O$ dispersion (right) reveals the solute's quantity relative to the lipid (CD:lipid). The choline peak (3.17 ppm) was used to determine CD:lipid ratios. Spectra are vertically offset for clarity. *Inset*, proton NMR spectra of an asymmetric LUV sample reveals a low quantity of CD relative to lipid (~7:100 molar ratio). An octet at 3.6 ppm is attributed to trace glycerol contamination originating in the centrifugal filters, despite extensive pre-washing as described in the Supporting Information Section S2.
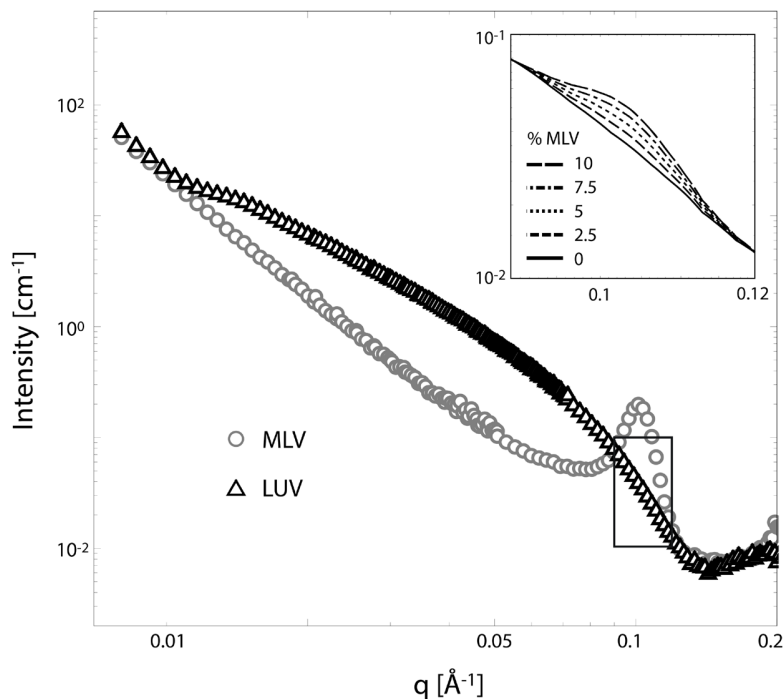
**Figure S13 | SANS is sensitive to the presence of multilamellar vesicles (MLVs).** Shown are SANS data for a 10 mM POPC-*dC* vesicle suspension in $D_2O$, before (MLVs, gray circles) and after (LUVs, black triangles) extrusion to produce 50 nm diameter LUVs. For MLVs, density correlations between the stacked bilayers give rise to Bragg scattering peaks at a length scale corresponding to integer multiples of the lamellar repeat distance (*e.g.*, the first Bragg order at *q* ~ 0.1 Å⁻¹, corresponding to a lamellar repeat distance of ~ 63 Å). Following extrusion to produce unilamellar vesicles, Bragg peaks are no longer observed, and vesicles exhibit the typical form factor for a dilute spherical shell particle. The inset shows a weighted sum of the black and gray curves as indicated in the inset legend, demonstrating the sensitivity of SANS to MLV contamination.
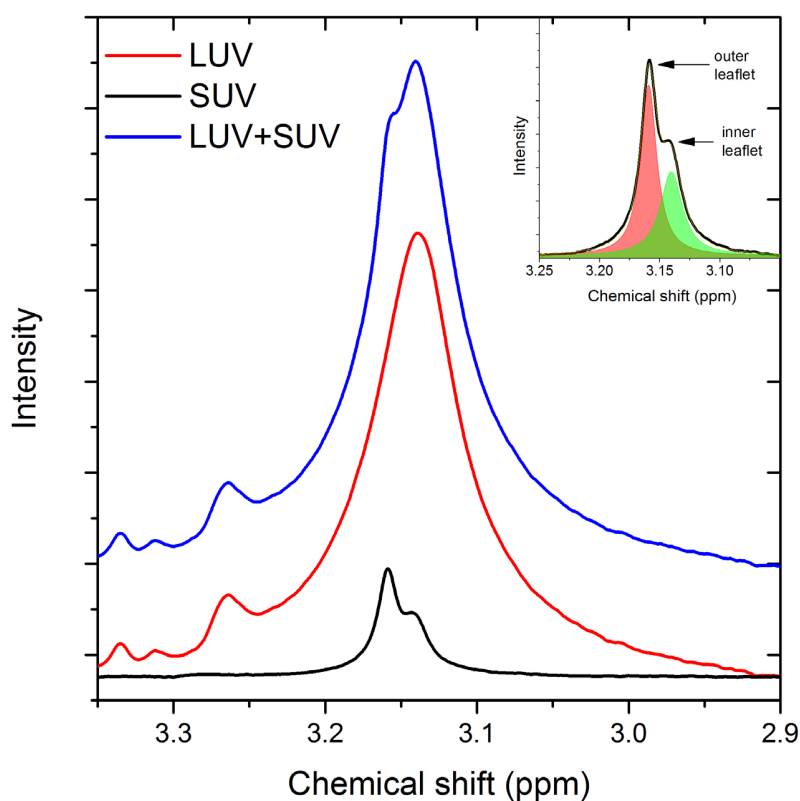
**Figure S14 | ^{1}H-NMR is sensitive to the presence of small unilamellar vesicles (SUVs).** Shown are choline resonances from 14.6 mM POPC LUVs (red) and 5.3 mM POPC SUVs (black), as well as the sum of the LUV and SUV spectra (blue curve, offset for clarity). The shoulder at 3.16 ppm demonstrates that ~ 27 mol % SUV can be easily identified in the presence of LUVs. *Inset*, small unilamellar vesicles (SUVs) give rise to a split choline resonance even in the absence of extravesicular shift reagent. This is due to both lipid number density and packing differences between the inner (green area) and outer (red area) leaflet. SUVs were obtained from an acceptor-free prep with omitted washing steps.
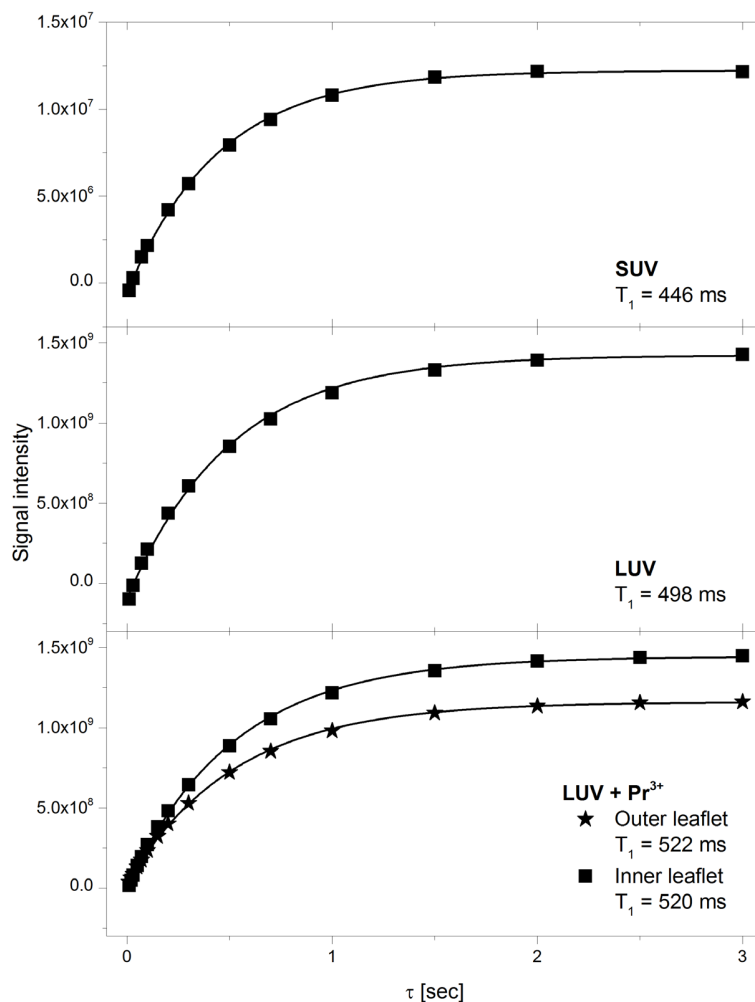
**Figure S15 | ¹H-NMR T1 relaxation measurements reveal SUVs and LUVs relax at the same rate, and Pr³⁺ does not change the T1 of the outer leaflet.** *Upper*, SUVs generated from incubation of donor MLVs with mβCD. *Middle*, relaxation of symmetric LUVs. *Bottom*, relaxation of inner (square) and outer (star) leaflets of symmetric LUVs in the presence of extravesicular shift reagent Pr³⁺. Since the T1 relaxation times are identical, peak areas do not need to be scaled for the given spectrometer parameters.

**S1. Methods**

**Materials.** 1-palmitoyl-2-oleoyl-*sn*-glycero-3-phosphocholine (16:0/18:1 PC, POPC), 1-palmitoyl-d31-2-oleoyl-*sn*-glycero-3-phosphocholine [16:0(d31)/18:1 PC, POPC-*dC*], 1-palmitoyl-2-oleoyl-*sn*-glycero-3-phosphocholine-1,1,2,2-d4-N,N,N-trimethyl-d9 [16:0/18:1 PC(d13), POPC-*dH*], 1-palmitoyl-d31-2-oleoyl-*sn*-glycero-3-phosphocholine-1,1,2,2-d4-N,N,N-trimethyl-d9 [16:0(d31)/18:1 PC(d13), POPC-*dHC*], 1,2-dipalmitoyl-d62-*sn*-glycero-3-phosphocholine [di-16:0(d31) PC, DPPC-*dC*], 1-palmitoyl-2-oleoyl-*sn*-glycero-3-phospho-(1′-*rac*-glycerol) (sodium salt) [16:0/18:1 PG, POPG], and 1-palmitoyl-d31-2-oleoyl-*sn*-glycero-3-phospho-(1′-*rac*-glycerol) (sodium salt) [16:0(d31)/18:1 PG, POPG-*dC*] were purchased from Avanti Polar Lipids (Alabaster, AL) and used as received. Lipid stock solutions were prepared by dissolving dry lipid powder in HPLC-grade chloroform, and phospholipid stock concentration was determined to within 1% by inorganic phosphate assay.[3] Methyl-beta-cyclodextrin (mβCD) was purchased from Acros Organics (Thermo Fisher Scientific, Waltham, MA) and prepared as a 35 mM stock solution in $H_2O$. Fig. S1 shows representative structures of lipids and mβCD. Praseodymium(III) nitrate hexahydrate {$Pr(NO_3)_3$ $6H_2O$} ($Pr^{3+}$) was purchased from Alfa Aesar (Ward Hill, MA) and prepared as a 100 mM stock solution in $D_2O$. Centrifugal filter devices (Amicon Ultra-15, 100,000 Da molecular weight cutoff) were purchased from EMD Millipore (Billerica, MA) and washed seven times with $H_2O$ prior to use to remove trace glycerol. Ultrapure $H_2O$ was obtained from a High-Q purification system (Wilmette, IL), and 99.9% $D_2O$ was purchased from Cambridge Isotopes (Andover, MA).

**S2. Preparation of asymmetric liposomes.** Phospholipid films were prepared by transferring the desired volumes of stock solutions to a glass scintillation vial with a syringe (Hamilton USA, Reno, NV) and then drying the organic solvent with an $N_2$ stream and gentle heating, followed by overnight drying *in vacuo* (~12 h). Acceptor films were doped with 5 mol % of the anionic lipid POPG to prevent formation of paucilamellar vesicles, which are known to form in extruded neutral liposomes of 100 nm diameter or larger.[1,4] The isotopic variant of POPG used (*i.e.*, POPG or POPG-*dC*) was always chosen to match that of the acceptor chains, and for data analysis its asymmetric distribution was assumed to be identical to that of the acceptor PC.

Donor multilamellar vesicles (MLVs) were prepared by hydrating a preheated (50 °C) lipid film with 20% (w/w) sucrose solution to a lipid concentration of 20 mg/mL, followed by vigorous vortexing to disperse the lipid. The resulting MLV suspension was incubated at 50 °C for 1 h with intermittent vortexing, and then subjected to three freeze/thaw cycles between -78 and 50 °C to facilitate equilibration of sucrose across lamellae. The MLV suspension was then diluted 20-fold with $H_2O$ and centrifuged at

21

20,000 × g for 30 min at 20 °C, after which time the supernatant was discarded, and the pellet was re-suspended with 35 mM mβCD solution to an 8:1 mβCD:lipid molar ratio. The MLV/mβCD mixture was incubated at room temperature for 2 h with gentle stirring.

Acceptor large unilamellar vesicles (LUVs) were prepared by hydrating a preheated (40 °C) lipid film with 20 mM NaCl solution to a concentration of 10−12 mg/mL, followed by vigorous vortexing to disperse the lipid. The resulting MLV suspension was incubated at 40 °C for 1 h with intermittent vortexing, and then subjected to five freeze/thaw cycles as described above. LUVs were prepared using a hand-held miniextruder (Avanti Polar Lipids, Alabaster, AL) assembled with a 100 nm pore-diameter polycarbonate filter, by passing the vesicle suspension through the filter 31 times at room temperature. LUV size was measured with dynamic light scattering (DLS) using a BI-200SM Research Goniometer and Laser Light Scattering system (Brookhaven Instruments, Holtsville, NY). Mean vesicle diameters were typically ~ 125 nm, with a relative polydispersity (distribution width divided by mean diameter) of ~ 0.25.

Asymmetric LUVs were prepared by mixing acceptor LUVs with the donor MLV/mβCD suspension, at a donor:acceptor molar lipid ratio of 2:1 (for POPC donor/POPC acceptor samples) or 3:1 (for the DPPC donor/POPC acceptor sample). The mixture was stirred at room temperature for 1 h, and then diluted 8-fold with $H_2O$ and centrifuged at 20,000 × g for 30 min to pellet remaining donor MLVs. The pellet was discarded, and the supernatant (containing asymmetric LUVs, mβCD, and residual sucrose) was concentrated to ~ 1 mL using a prewashed 100K MWCO centrifugal filter device at 5,000 × g. Soluble contaminants (*i.e.*, mβCD and sucrose) were removed by successive dilution/concentration cycles, whereby the sample was diluted with $D_2O$ to the filter device's capacity (~ 11 mL) and then centrifuged at 5,000 × g to obtain a final retentate volume of 0.5−1 mL. The time for centrifugal filtration varied depending on the phase state of the lipids and the quantity of asymmetric vesicles being washed, and ranged from 30-60 min per wash. Typically, four such cycles reduced the mβCD concentration by a factor of > 10, and exchanged > 99% of $H_2O$ with $D_2O$. The asymmetric vesicle preparation is summarized in Fig. S2. The final yield was estimated as not less than half of the initial acceptor amount.

**S3. Gas chromatography (GC).** Phospholipids were converted to fatty acid methyl esters (FAMEs) *via* acid catalyzed methanolysis. Briefly, 5−10 μL of an aqueous vesicle suspension (containing 20−100 μg total lipid) was dispensed into a 13 × 100 mm screw top glass culture tube, followed by addition of 1 mL methanolic HCl (1 M) prepared with concentrated HCl and methanol.[5] The sample was vortexed, sealed under Ar, and incubated at 85 °C for 1 h. After cooling to room temperature, 1 mL $H_2O$ was added and

the sample was vortexed. FAMEs were extracted with 1 mL hexane and vigorous vortexing, followed by low-speed centrifugation (500 × g) for 10 min. Finally, 800 μL of the upper (hexane) phase were transferred to an autosampler vial and brought to 1 mL with hexane, for injection into the GC column.

GC analysis was performed on an Agilent 5890A gas chromatograph (Santa Clara, CA) with a 5975C mass-sensitive detector operating in electron-impact mode. An HP-5MS capillary column (30 m × 0.25 mm, 0.25 μm film thickness) was used with a helium carrier at 1 mL/min and an inlet temperature of 270 °C. A 1 μL aliquot of FAME dissolved in hexane was injected in splitless mode using an Agilent 7693A automatic liquid sampler. After sample injection, the following column temperature program was initiated: 2 min at 60°C; 20 °C/min to 170 °C; 5 °C/min to 240 °C; 30 °C/min to 300 °C; 2 min at 300°C, for a total run time of 25.5 min. Total ion chromatogram peaks were assigned and integrated using GC/MSD ChemStation Enhanced Data Analysis software (Agilent Technologies, Santa Clara, CA).

**S4. Determination of total bilayer composition using GC**. Lipid mixture composition can be determined from GC, provided there are chemical or isotopic differences between chains of the constituent lipids. In principle, the mole fraction $\chi$ of each mixture component $i$ can be determined directly from a set of unique chain peak areas $\mathcal{A} = \{A_i\}$:

$$\chi_i = \frac{A_i}{\sum_j A_j}, \qquad (1)$$

where $A_i$ denotes the $i^{\text{th}}$ chain peak area and the denominator is a sum over all mixture components $j$, $A_j \in \mathcal{A}$. For this relationship to be strictly valid, chain peak area fractions must vary linearly with mixture composition. In practice, we found a slight deviation from linearity which necessitated the use of standard curves (Fig. S3). Briefly, standard two-component FAME samples covering a range of compositions and containing 20−100 μg total lipid, were prepared by dispensing lipid stock solutions into glass culture tubes. Chloroform was removed by an $N_2$ stream and gentle heating, followed by derivatization and extraction of FAMEs as described above. Peak area fractions $a_i$ were plotted *vs.* component mole fraction $\chi_i$ and fitted to a four-parameter function:

$$a_i = \frac{a\chi_i^2 + b\chi_i}{a\chi_i^2 + b\chi_i + c(1 - \chi_i)^2 + d(1 - \chi_i)}, \qquad (2)$$

using Mathematica 10.0 (Wolfram Research, Champaign, IL) to obtain a standard curve, from which the composition of unknown samples was determined.

**S5. Proton nuclear magnetic resonance spectroscopy ($^1$H-NMR).** $^1$H-NMR spectra were collected on an Avance III 400 MHz spectrometer (Bruker, Billerica, MA) using Bruker TopSpin acquisition software, and analyzed with TopSpin 3.2. Lipid suspensions in $D_2O$ were brought to a total volume of 600 μL (for a total lipid concentration of ~ 5 mM) and loaded into 5 mm NMR tubes (Wilmad LabGlass, Vineland, NJ). A standard $^1$H pulse sequence with a 30º flip angle and 1 s delay time was employed to collect 32–256 transients at 21 ºC. $^1$H-NMR data were processed with a line-broadening parameter of 1 Hz. The distribution of protiated choline between inner and outer vesicle leaflets (described further below) was determined by addition of the shift reagent $Pr^{3+}$.[6] Briefly, 2 μL of 100 mM $Pr^{3+}$/$D_2O$ solution was dispensed directly into the NMR tube, which was then capped and inverted a minimum of three times to mix the contents. Typically, several such $Pr^{3+}$ additions were made, with spectra obtained between titrations. Analysis of choline and mβCD resonances was performed using Origin 8.5 software (OriginLab, Northampton, MA) and built-in nonlinear least-squares optimization tools. Resonances for the 9 identical choline protons were modeled using a single Lorentzian in the absence of $Pr^{3+}$, or two Lorentzian peaks in the presence of $Pr^3$. In most cases, spectra obtained from 2–3 successive $Pr^{3+}$ titrations were separately modeled to determine the inner:outer leaflet ratio (and associated uncertainty) as described below. The reported outer leaflet fraction (Tables S2-S4) represents the average value obtained from these fits, with final uncertainty determined by error propagation.

**S6. Evaluation of bilayer asymmetry with $^1$H-NMR.** The paramagnetic lanthanide ion $Pr^{3+}$ interacts with choline protons, shifting their resonance downfield as shown in Figs. S4-S6. Because the ion's association and disassociation rates are fast relative to the NMR time scale, an average of shifted and unshifted resonances is obtained, and as such the extent of the observed shift depends on the molar ratio of $Pr^{3+}$ and lipid. When $Pr^{3+}$ is added externally to a vesicle suspension, the shift is selective for outer leaflet protiated choline, due to the low bilayer permeability of $Pr^{3+}$ and the short-range distance dependence (inverse $r^3$) of the lanthanide-proton interaction. As a result, inner and outer leaflet protiated choline resonances can be separately resolved,[7] and the integrated area $R$ of each resonance is proportional to the number of molecules having protiated headgroups in the corresponding leaflet. We define the outer leaflet peak fraction:

$$f^{out} = \frac{R^{out}}{R^{in} + R^{out}}, \qquad (3)$$

where the superscript denotes the inner (*in*) or outer (*out*) leaflet. If all bilayer components possess protiated headgroups, $f^{out}$ directly yields the mole fraction of all bilayer lipids found in the outer leaflet, $X^{out}$:

$$X^{out} = \frac{\sum_j N_j^{out}}{\sum_j N_j} \equiv f^{out}, \qquad (4)$$

where $N$ and $N^{out}$ denote number of molecules in the whole bilayer and in the outer leaflet, respectively, and the summations are performed over all mixture components. (Note that this equation assumes that the chemical shifts of all cholines are identical.) For a bilayer with an equal number of lipids in both leaflets, $X^{out} = 0.5$. However, $X^{out}$ can be influenced by geometric constraints (for example the differences in outer and inner leaflet volumes in highly curved vesicles[8]) or by differences in lipid packing in the inner and outer leaflets of asymmetric bilayers.

In a mixture of PC lipids, the assay is selective for a single species provided all other mixture components possess a deuterated choline. In this way, the distribution of donor and acceptor PC lipids can be separately established for differentially labeled samples. If one and only one mixture component (component *i*) possesses a protiated choline, we define the single-component outer leaflet peak fraction, $f_i^{out}$ as:

$$f_i^{out} = \frac{N_i^{out}}{N_i} = \frac{X^{out}\chi_i^{out}}{\chi_i} \qquad (5)$$

where all symbols are as defined above. Combining the two previous equations and rearranging gives an expression for the outer leaflet mole fraction of component *i*, $\chi_i^{out}$, in terms of experimentally determined quantities, $f_i^{out}$ and $f^{out}$ from NMR and $\chi_i$ from GC:

$$\chi_i^{out} = \frac{f_i^{out}\chi_i}{f^{out}} \qquad (6)$$

**S7. Small-angle neutron scattering (SANS).** Neutron scattering experiments were performed at the BL-6 extended Q-range small-angle neutron scattering (EQ-SANS) instrument of the Spallation Neutron Source (SNS) located at Oak Ridge National Laboratory (ORNL). Lipid vesicle samples were loaded into

1 or 2 mm path length quartz banjo cells (Hellma USA, Plainview, NY) and mounted in a temperature-controlled cell holder with ~ 1 °C accuracy. Data were taken at a 1.3 m sample-to-detector distance (SDD) with a 4.0–7.5 Å wavelength band, and at a 4.0 m SDD with a 10.0–13.5 Å wavelength, for a total scattering vector of $0.005 < q < 0.5$ Å$^{-1}$. Scattered neutrons were collected with a two-dimensional (1 × 1 m) $^3$He position-sensitive detector (ORDELA, Inc., Oak Ridge, TN) with 256 × 192 pixels. The 2D data were reduced using software provided by ORNL. During reduction, data were corrected for detector pixel sensitivity, dark current, and sample transmission, and background scattering from water was subtracted. The one-dimensional scattered intensity $I$ vs. $q$ [$q = 4\pi \sin(\theta) / \lambda$, where $\lambda$ is the neutron wavelength and $2\theta$ is the scattering angle relative to the incident beam] was obtained by radial averaging of the corrected 2D data. The scattering contribution from residual mβCD was accounted for by direct subtraction of a scaled $I(q)$ curve obtained for mβCD in aqueous solution.

**S8. Determination of bilayer structure from SANS.** In general, scattering from a dilute vesicle suspension contains contributions from both bilayer structure and vesicle size and shape. Provided the relevant length scales (*i.e.*, the bilayer thickness and vesicle radius) are well-separated, the scattered intensity can be expressed as a product of form factors:

$$I(q) \propto S(q)|F_{TS}(q)|^2|F_{FB}(q)|^2 \qquad (7)$$

where $S(q)$ is an interparticle structure factor accounting for intervesicle interference (equal to unity in the infinite dilution limit), $F_{TS}$ is the scattering amplitude of a thin spherical shell, and $F_{FB}$ is the scattering amplitude of an infinite flat bilayer sheet.[9] $F_{TS}$ contains information about vesicle size and polydispersity, while $F_{FB}$ contains information about the distribution of matter within the bilayer. For the dilute, 100 nm diameter vesicles used in this study, $S(q)|F_{TS}(q)|^2 \approx constant$ for $q > 0.05$ Å$^{-1}$, such that the contribution from $F_{FB}$ dominates the observed intensity at large scattering vectors. Therefore, a suitable expression for $F_{FB}(q)$ is needed to model the data at $q > 0.05$ Å$^{-1}$, in order to obtain information about bilayer asymmetry.

As a reciprocal space quantity, the flat bilayer form factor is related to the bilayer's real space matter distribution through a Fourier transform:

$$|F_{FB}(q)|^2 = \left( \int_{-D^{in}}^{D^{out}} [\rho(z) - \rho_S] \cos(qz) dz \right)^2 + \left( \int_{-D^{in}}^{D^{out}} [\rho(z) - \rho_S] \sin(qz) \, dz \right)^2 \qquad (8)$$

where $\rho(z)$ is the projected scattering length density (SLD) in the direction normal to the bilayer plane, $\rho_S$ is the scattering length density of the solvent (water), and the integral is evaluated over the full bilayer thickness.[10] We simplify the asymmetric bilayer's SLD profile by considering four slabs of independent $\rho$ and thickness $D$, in addition to the SLD of the vesicle core and external solvent. This model is represented graphically in Fig. S9 and mathematically as:

$$\rho(z) = \begin{cases} \rho_{Core} & z < -(D_C^{in} + D_H^{in}) \\ \rho_H^{in} & -(D_C^{in} + D_H^{in}) \leq z < -D_C^{in} \\ \rho_C^{in} & -D_C^{in} \leq z < 0 \\ \rho_C^{out} & 0 \leq z < D_C^{out} \\ \rho_H^{out} & D_C^{out} \leq z < D_C^{out} + D_H^{out} \\ \rho_S & z \geq D_C^{out} + D_H^{out} \end{cases}, \qquad (9)$$

where superscripts *in* and *out* refer to the inner and outer leaflets, respectively. Provided the core SLD matches that of the solvent ($\rho_{Core} = \rho_S$), the asymmetric form factor has an analytical solution:

$$|F_{FB}(q)|^2 = \frac{1}{q^2} \Big[ \{ (\rho_C^{out} - \rho_C^{in}) + (\rho_C^{in} - \rho_H^{in}) \cos(D_C^{in} q) - (\rho_C^{out} - \rho_H^{out}) \cos(D_C^{out} q)$$

$$+ (\rho_H^{in} - \rho_S) \cos((D_C^{in} + D_H^{in})q) - (\rho_H^{out} - \rho_S) \cos((D_C^{out} + D_H^{out})q) \}^2$$

$$+ \{ (\rho_C^{in} - \rho_{H,in}) \sin(D_C^{in} q) + (\rho_C^{out} - \rho_H^{out}) \sin(D_C^{out} q)$$

$$+ (\rho_H^{in} - \rho_S) \sin((D_C^{in} + D_H^{in})q) + (\rho_H^{out} - \rho_S) \sin((D_C^{out} + D_H^{out})q) \}^2 \Big]. \qquad (10)$$

We now seek expressions for the slab SLDs and thicknesses in terms of physically meaningful parameters related to the asymmetric bilayer's composition and structure.[11] Assuming uniform lipid mixing with each leaflet, the volumes (or scattering lengths) of the outer and inner headgroup slabs are given as mole fraction-weighted sums of the component headgroup volumes (or scattering lengths) plus associated water:

$$V_H^j = \sum_i \chi_i^j V_{H,i} + n_W^j V_W, \qquad (11)$$

$$b_H^j = \sum_i \chi_i^j b_{H,i} + n_W^j b_W, \qquad (12)$$

where $V_H$ is the headgroup volume in Å$^3$, $b$ is the coherent neutron scattering length in fm, $n_W$ is the average number of bound waters per headgroup, $\chi$ is the component mole fraction, the subscript $i$ indexes the bilayer's lipid components, and the superscript $j$ indexes the two leaflets. The analogous expressions for the hydrocarbon slabs are:

$$V_C^j = \sum_i \chi_i^j V_{C,i}, \qquad (13)$$

$$b_C^j = \sum_i \chi_i^j b_{C,i}. \qquad (14)$$

The slab thicknesses and scattering length densities follow directly:

$$\rho_{H(C)}^j = b_{H(C)}^j / V_{H(C)}^j, \qquad (15)$$

$$D_{H(C)}^j = V_{H(C)}^j / A_L^j, \qquad (16)$$

where $D$ is the slab thickness in Å, and $A_L$ is the average area per lipid in Å$^2$. With lipid volumes and scattering lengths constrained by independent measurements (Table S1), the model has four free structural parameters [$A_L^{in}$, $A_L^{out}$, $n_W^{in}$, $n_W^{out}$] in addition to the compositional parameters $\chi_i^{in}$, $\chi_i^{out}$. For a two-component bilayer (e.g., lipids A and B) in which the lipids are uniformly mixed, the compositional parameters are given by (cf. Eqs. 4-6):

$$\chi_A^{out} = \frac{f_A^{out} \chi_A}{X^{out}}, \qquad (17)$$

$$\chi_A^{in} = \frac{(1 - f_A^{out}) \chi_A}{(1 - X^{out})}, \qquad (18)$$

$$\chi_B^{in(out)} = 1 - \chi_A^{in(out)}, \qquad (19)$$

where $\chi_A$ and $f_A^{out}$ are obtained with GC and NMR experiments, respectively, and $X^{out}$ (cf. Eq. 4) is given by the inner and outer leaflet areas per lipid:

$$X^{out} = \frac{1/A_L^{out}}{1/A_L^{out} + 1/A_L^{in}}. \qquad (20)$$

Compositional parameters for isotopically asymmetric POPC bilayers obtained from GC, NMR, and SANS experiments are given in Tables S2-S3. Structural parameters obtained from SANS analysis of isotopically asymmetric POPC bilayers are given in Table S6, with data and best-fit curves shown in Fig. 3a. For comparison, structural parameters obtained from a joint refinement of symmetric POPC variants are found in Table S5, with data and best-fit curves shown in Fig. S10.

For $k$ coexisting bilayer phases, assuming negligible interference, the observed intensity is given by a weighted sum of asymmetric form factors for each phase:

$$I_{obs}(q) \propto |F_{obs}(q)|^2 = \sum_k \alpha_k |F_{FB,k}(q)|^2, \qquad (21)$$

where $\alpha_k$ is the phase area fraction given. For a binary mixture of two coexisting phases (*e.g.*, phases 1 and 2), four bilayer compartments must be considered, namely the outer and inner leaflets of phases 1 and 2. Using superscripts $i$ and $o$ to refer to the inner and outer leaflets, respectively, the unconstrained model has eight structural parameters ($A_L^{i1}$, $A_L^{i2}$, $A_L^{o1}$, $A_L^{o2}$, $n_W^{i1}$, $n_W^{i2}$, $n_W^{o1}$, $n_W^{o2}$) and four compositional parameters ($\chi_A^{i1}, \chi_A^{i2}, \chi_A^{o1}, \chi_A^{o2}$), in addition to the phase 1 area fraction $\alpha_1$ ($\alpha_2 = 1 - \alpha_1$). Some parameters can be constrained by matter balance combined with independent measurements. For example, with the bilayer mole fraction and leaflet distribution of component A (*i.e.*, $\chi_A$ and $f_A^o$) independently determined from GC and NMR experiments, $\alpha_1$ is given by:

$$\alpha_1 = \frac{A_L^{i1} A_L^{o1}[A_L^{i2}\chi_A^{o2} - (A_L^{i2} + A_L^{o2})\chi_A f_A^o]}{A_L^{i2} A_L^{o1} A_L^{o2}\chi_A f_A^o - A_L^{i1}\{A_L^{o1} A_L^{o2}\chi_A f_A^o + A_L^{i2}[A_L^{o2}\chi_A^{o1} - A_L^{o1}\chi_A^{o2} + (A_L^{o1} - A_L^{o2})\chi_A f_A^o]\}}, \qquad (22)$$

and the inner leaflet phase 2 mole fraction of component A is given by:

$$\chi_A^{i2} = \frac{A_L^{i2} A_L^{o1}(\chi_A^{i1} - \chi_A)\chi_A^{o2} - A_L^{i1}\chi_A[(A_L^{i2} + A_L^{o2})\chi_A^{o1} - A_L^{i2}\chi_A^{o2}](f_A^o - 1) - A_L^{o1}\chi_A[(A_L^{i2} + A_L^{o2})\chi_A^{i1} - A_L^{i2}\chi_A^{o2}]f_A^o}{A_L^{i1} A_L^{o2}\chi_A^{o1} - (A_L^{i1} + A_L^{o1})A_L^{o2}\chi_A f_A^o}, \qquad (23)$$

leaving 11 free parameters, an unacceptably large number. Therefore, additional assumptions were made when modeling DPPC/POPC aLUVs in order to reduce the number of free parameters to a reasonable level: (1) the number of headgroup waters for both leaflets was fixed to 7; and (2) given the small amount of DPPC found in the inner leaflet by NMR, we assumed that the inner leaflet was a uniform fluid phase and that the DPPC-poor phase was symmetric, allowing us to jointly vary three parameters (*i.e.*, $A_L^{i1} =$

$A_L^{i2} = A_L^{o1}$). The final model had four adjustable parameters as indicated in Table S7, which lists all structural and compositional parameters obtained from the fit (data and best-fit curves are shown in Fig. 3b). Compositional parameters obtained from GC, NMR, and SANS analysis are given in Table S4, where $X^{out}$ is given by:

$$X^{out} = \frac{\alpha_1/A_L^{o1} + (1 - \alpha_1)/A_L^{o2}}{\alpha_1(1/A_L^{o1} + 1/A_L^{i1}) + (1 - \alpha_1)(1/A_L^{o2} + 1/A_L^{i2})}. \quad (24)$$

**S9. Assessment of sample contamination**. We define a contaminant as any impurity whose presence can affect (or hinder the determination of) the asymmetric LUV bilayer structure. In this context, the most problematic contaminants are mβCD and residual donor or mixed donor/acceptor vesicles that resist sedimentation. These are typically lighter donor multilamellar vesicles (MLVs), or small unilamellar vesicles (SUVs, diameter < 30 nm) formed during the exchange process. As a lipid carrier molecule, mβCD facilitates outer leaflet exchange and may perturb the bilayer structure, while residual vesicles can bias the determination of the asymmetric leaflet compositions.

We assessed mβCD contamination by establishing the ^{1}H-NMR detection limits of specific mβCD resonances in $D_2O$ in the absence and presence of LUVs (Fig. S12), from which we estimate a lower detection limit of 1:130 CD:lipid molar ratio. Asymmetric LUVs typically contained < 1:10 CD:lipid after three wash steps (Fig. S12 inset**)**.

The presence of residual vesicles can be assessed with a variety of techniques. Vesicles containing multiple lamellae (including contaminating donor MLVs) exhibit a series of Bragg peaks in the SANS intensity at $q = 2\pi n/D$, where $D$ is the lamellar repeat distance and $n$ is an integer. As illustrated in Fig. S13, mixtures of LUVs and MLVs show characteristic excess scattering near the first Bragg order ($n = 1$, ~ 0.1 Å$^{-1}$). The absence of Bragg scattering in asymmetric samples is confirmed by a good fit between data and model (which assumes unilamellar vesicles), as well as simple visual inspection of the data.

A less obvious form of residual vesicle contamination is the presence of SUVs with diameter < 30 nm, which can be generated upon lengthy exposure of lipid vesicles to mβCD. GC measurements of donor-only control samples revealed 1−2% of the total donor mass in the recovered sample, which was subsequently identified as SUVs with ^{1}H-NMR lineshape analysis (Fig. S14). Briefly, the SUV choline resonance is characterized by the appearance of two peaks even in the absence of shift reagent,

attributable to packing differences in the inner and outer leaflets of highly curved vesicles.[7] The SUV choline resonance width is ~ 0.25 ppm—considerably narrower than the LUV width—with inner and outer resonances separated by 0.019 ppm (7.6 Hz). However, despite their considerable line width differences, the similarity of the spin-lattice relaxation time (T1) values for LUV and SUVs (Fig. S15) precludes the ability to isolate the SUV component by varying the delay time. NMR measurements of asymmetric samples did not indicate the presence of SUVs (Fig. 2a, Figs. S4-S6), although low contamination levels may fall below the detection threshold (Fig. S14). If complete removal of SUVs is necessary, sucrose density gradients can be employed prior to mβCD removal.

## References

1       Kučerka, N., Nieh, M. P. & Katsaras, J. *Biochim. Biophys. Acta* **1808**, 2761-2771 (2011).

2       Tristram-Nagle, S., Liu, Y., Legleiter, J. & Nagle, J.F. *Biophys. J.* **83**, 3324-3335 (2002).

3       Kingsley, P. B. & Feigenson, G. W. *Chem. Phys. Lipids* **24**, 135-147 (1979).

4       Fogarty, J. C., Arjunwadkar, M., Pandit, S. A. & Pan, J. *Biochim. Biophys. Acta* **1848**, 662-672 (2015).

5       Ichihara, K. & Fukubayashi, Y. *J. Lipid Res.* **51**, 635-640 (2010).

6       Andrews, S.B., Faller, J.W., Gilliam, J.M. & Barrnett, R.J. *Proc. Natl. Acad. Sci. USA* **70**, 1814-1818 (1973).

7       Perly, B., Smith, I. C., Hughes, L., Burton, G. W. & Ingold, K. U. *Biochim. Biophys. Acta* **819**, 131-135 (1985).

8       Berden, J.A., Barker, R. W. & Radda, G. K. *Biochim. Biophys. Acta* **375**, 186-208 (1975).

9       Pencer, J., Krueger, S., Adams, C.P. & Katsaras, J. *J. Appl. Crystallogr.* **39**, 293-303 (2006).

10      Kučerka, N., Pencer, J., Sachs, J.N., Nagle, J.F. & Katsaras, J. *Langmuir* **23**, 1292-1299 (2007).

11      Kučerka, N., Nagle, J.F., Feller, S.E. & Balgavý, P. *Phys. Rev. E* **69**, 051903 (2004).

# Joint small-angle X-ray and neutron scattering data analysis of asymmetric lipid vesicles

Barbara Eicher,[a,b] Frederick A. Heberle,[c,d,e] Drew Marquardt,[a,b] Gerald N. Rechberger,[f,g] John Katsaras[e,h] and Georg Pabst[a,b]*

[a]Instiute of Molecular Biosciences, Biophysics Division, University of Graz, Austria, [b]BioTechMed-Graz, Graz, 8010, Austria, [c]The Bredesen Center for Interdisciplinary Research and Graduate Education, University of Tennessee, Knoxville, TN, USA, [d]Joint Institute for Biological Sciences, Oak Ridge National Laboratory, Oak Ridge, TN, USA, [e]Biology and Soft Matter Division, Oak Ridge National Laboratory, Oak Ridge, TN, USA, [f]Instiute of Molecular Biosciences, University of Graz, Austria, [g]Omics-Center Graz, BioTechMed-Graz, Austria, and [h]Shull Wollan Center, Oak Ridge National Laboratory, Oak Ridge, TN, USA. *Correspondence e-mail: georg.pabst@uni-graz.at

Low- and high-resolution models describing the internal transbilayer structure of asymmetric lipid vesicles have been developed. These models can be used for the joint analysis of small-angle neutron and X-ray scattering data. The models describe the underlying scattering length density/electron density profiles either in terms of slabs or through the so-called scattering density profile, previously applied to symmetric lipid vesicles. Both models yield structural details of asymmetric membranes, such as the individual area per lipid, and the hydrocarbon thickness of the inner and outer bilayer leaflets. The scattering density profile model, however, comes at a cost of increased computational effort but results in greater structural resolution, showing a slightly lower packing of lipids in the outer bilayer leaflet of ∼120 nm diameter palmitoyl-oleoyl phosphatidylcholine (POPC) vesicles, compared to the inner leaflet. Analysis of asymmetric dipalmitoyl phosphatidylcholine/POPC vesicles did not reveal evidence of transbilayer coupling between the inner and outer leaflets at 323 K, i.e. above the melting transition temperature of the two lipids.

## 1. Abbreviations

$A_L$: area per lipid
aLUV: asymmetric large unilamellar vesicle
aSDP: asymmetric scattering density profile
CD: cyclodextrin
CG: glycerol group
DE: differential evolution
DPPC: dipalmitoyl phophatidylcholine
$F_{FB}$: form factor of a flat bilayer sheet
GC: gas chromatography
HC: hydrocarbon group
LUV: large unilamellar vesicle
m$\beta$CD: methyl-$\beta$-cyclodextrin
M: methyl group
MLV: multilamellar vesicles
MS: mass spectrometry
PC: phophatidylcholine
POPC: palmitoyl-oleoyl phosphatidylcholine
SDD: sample–detector distance
SDP: scattering density profile
SFF: separated form factor
SLD: scattering length density
UPLC: ultra-performance liquid chromatography
$V_L$: lipid molecular volume
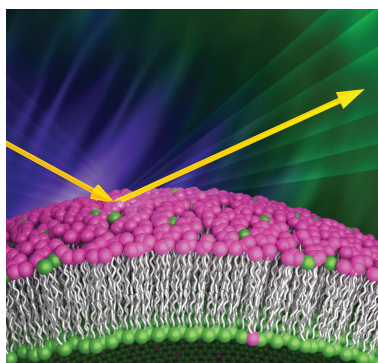
OPEN ACCESS

## 2. Introduction

Most biological membranes are asymmetric. For example, mammalian plasma membranes contain mainly phosphatidyl-choline (PC) and sphingomyelin in their outer (exoplasmic) leaflets, while phosphatidylserine and phosphatidylethanol-amine are the major lipid groups of their inner (cytosolic) leaflets (Verkleij *et al.*, 1973; Devaux, 1991). Bilayer asymmetry is thought to affect various membrane properties including electrostatic potential, surface charge, permeability and stability, in addition to structural parameters such as bilayer thickness, and even the thicknesses of the individual leaflets (Devaux, 1991). However, until recently progress in studying the biophysics of asymmetric bilayers has been hampered by the lack of protocols pertaining to their forma-tion (Marquardt, Geier & Pabst, 2015).

In a series of papers, London and co-workers introduced a method using cylclodextrin (CD)-mediated lipid exchange for producing solvent-free free-floating asymmetric vesicles of different sizes (Cheng *et al.*, 2009; Chiantia & London, 2013). (Note that the name asymmetric lipid vesicle refers to a vesicle whose bilayer leaflets are compositionally different.) We recently modified this technique to produce stress-free asym-metric large unilamellar vesicles (aLUVs) amenable to inter-rogation by different biophysical techniques (Heberle *et al.*, 2016). These include small-angle X-ray and neutron scattering (SAXS and SANS, respectively), techniques which are well known for their abilities to probe membrane structure at the sub-nanometre scale without the need for extrinsic probes (Pabst *et al.*, 2010; Marquardt, Heberle *et al.*, 2015). Over the years, several concepts have been developed to model symmetric lipid bilayers in terms of scattering length density (SLD) profiles. In general, these models consist of step func-tions or 'slabs' (*e.g.* Riske *et al.*, 2001; King *et al.*, 1985; Pencer & Hallett, 2000; Schmiedel *et al.*, 2001), Gaussians (*e.g.* Wiener & White, 1992; Pabst *et al.*, 2000; Nagle & Tristram-Nagle, 2000), or some combination of the two. A particularly influ-ential method of determining membrane structure at high resolution is the scattering density profile (SDP) model developed by Kučerka and co-workers (Klauda *et al.*, 2006; Kučerka *et al.*, 2008), which allows for the joint analysis of X-ray and neutron data. More recently, an all-atom model for the SLD was developed, which has an even higher internal resolution than the SDP (Fogarty *et al.*, 2015).

Brzustowicz & Brunger (2005) were the first to report a smooth SLD model function to analyze SAXS data from asymmetric (*i.e.* noncentrosymmetric) lipid vesicles. Later, Kučerka and co-workers described an SDP-based model for asymmetric bilayers (Kučerka, Pencer, Sachs *et al.*, 2007), which exploited SANS/SAXS contrast variation (Pabst *et al.*, 2010; Marquardt, Heberle *et al.*, 2015). However, their model did not consider isotopic labeling of only one bilayer leaflet (Heberle *et al.*, 2016), which is needed to precisely define the center of the asymmetric bilayer in order to disentangle leaflet-specific thicknesses and lipid packing densities. To this end, we have developed an asymmetric SDP model ('aSDP') that allows for this feature. In addition, we describe a slab model that also allows for the joint analysis of SAXS and

SANS data, but at a lower spatial resolution. The main advantage of the slab model is that fewer parameters are needed to fit the data.

Here, we evaulate the efficacy of both the slab and SDP models using isotopically labeled aLUVs composed of palmitoyloleoyl phosphatidylcholine (POPC) and dipalmitoyl phosphatidylcholine (DPPC), as well as their deuterated variants. Despite the significant difference in spatial resolu-tion, the two models yield comparable values for the area per lipid $A_L$ and the thicknesses of the inner and outer hydro-carbon layers $d_C$. However, the quality of the fits, as judged by their reduced $\chi^2_{red}$ values, are better when using the aSDP model. Finally, our analysis of fluid DPPC/POPC aLUVs revealed that the inner and outer membrane leaflets are structurally decoupled from each other at 323 K, above the melting transition temperature of the two lipids.

## 3. Materials and methods

### 3.1. Sample preparation

All lipids, including their isotopes (POPC-d13, POPC-d31, POPC-d44, DPPC-d13, DPPC-62) were purchased from Avanti Polar Lipids (Alabaster, AL, USA) and used without further purification (see Fig. S6 of the supporting information for details of chemical structures). D$_2$O (99.8%) was obtained from Alfa Aesar (Ward Hill, MA, USA) and from Euroiso-top (Saarbrücken, Germany). Methyl-$\beta$-cyclocextrin (m$\beta$CD) was obtained from Sigma–Aldrich (St Louis, MO, USA). All solvents were of pro analysis quality. Lipid stock solutions were prepared by dissolving weighed amounts of dry lipid powder in chloroform. The lipid stock solution concentration was determined to within 1% by inorganic phosphate assay (Kingsley & Feigenson, 1979). Appropriate volumes of the stock solutions were dried under a stream of nitrogen and placed under vacuum for at least 12 h, leading to a thin lipid film on the bottom of a glass vial.

aLUVs were prepared using cyclodextrin-mediated lipid exchange as previously described (Heberle *et al.*, 2016). Briefly, acceptor vesicles composed of the inner leaflet lipids were prepared by first hydrating the dry lipid films in a 20 m$M$ NaCl aqueous solution made from 18 M$\Omega$ cm water (lipid concentration 10 mg ml$^{-1}$). The resulting multilamellar vesi-cles (MLVs) were incubated at 313 K for 1 h with intermittent vortex mixing, followed by five freeze/thaw cycles using liquid nitrogen. LUVs were prepared using a hand-held mini-extruder (Avanti Polar Lipids, Alabaster, AL, USA) with a 100 nm pore-diameter polycarbonate filter. The MLV suspension was passed through the filter a total of 31 times at room temperature. LUV formation was facilitated by doping the lipids with 5 mol% POPG or POPG-d31 (matching the isotopic composition of the inner leaflet POPC or POPC-d31 lipids). Such low amounts of the charged lipid were previously shown to not affect the membrane structure of phosphatidyl-cholines (Kučerka, Pencer, Sachs *et al.*, 2007). Vesicle size was measured by dynamic light scattering using a Zetasizer NANO ZSP (Malvern, UK) or a BI-200SM Research Goniometer

Light Scattering system (Brookhaven Instruments, Holtsville, NY, USA). Mean vesicle diameters were typically ~120 nm (±5 nm).

Donor multilamellar vesicles (20 mg ml$^{-1}$ total lipid concentration) composed of the outer leaflet lipids were prepared by hydrating the dry lipid films in water containing 20%($w/w$) sucrose using vortex mixing in combination with three freeze/thaw cycles. Donor MLVs were then diluted 20-fold with water and centrifuged for 30 min at 20 000 $g$ in order to remove extravesicular sucrose. The resulting pellet was re-suspended in a 35 m$M$ m$\beta$CD solution at a lipid:m$\beta$CD ratio of 1:8 and incubated for 2 h at room temperature, while being gently stirred.

Lipid exchange was initiated by mixing acceptor and donor vesicle suspensions (donor/acceptor ratio $D/A = 2$ for POPC aLUVs and $D/A = 3$ for DPPC/POPC aLUVs) and allowed to proceed for 1 h at room temperature. The resultant aLUVs were diluted eightfold with water and then separated from the donor MLVs *via* centrifugation at 20 000 $g$ for 30 min. The supernatant containing the aLUVs (as well as residual CD and sucrose) was then concentrated to <0.5 ml with a centrifugal ultrafiltration device (100 kDa molecular weight cutoff, 11 ml volume, 5000 $g$). The initial concentration step was followed by three cycles of successive dilution to 11 ml and concentration to <0.5 ml, effectively removing residual CD and sucrose, and allowing for the exchange of $H_2O$ with $D_2O$ for SANS and $^1$H NMR experiments. The mean diameter of the aLUVs was ~120 nm (±5 nm), a diameter (within measurement uncertainty) identical to that of the acceptor LUVs prior to exchange. Lipid exchange efficiency and inner/outer leaflet distribution were determined by gas chromatography and mass spectrometry (GC–MS), or ultra performance liquid chromatography and mass spectrometry (UPLC–MS), combined with $^1$H NMR measurements, as detailed by Heberle *et al.* (2016) and in the supporting information. We demonstrated previously that membrane structural parameters are not altered by this preparation (Heberle *et al.*, 2016).

In some cases, symmetric LUVs were prepared from aLUVs by chemical scrambling as follows. aLUVs were dried to a film under reduced atmospheric pressure using a rotary evaporator with the water bath set to 303–323 K. The dried film was then redissolved in chloroform. From that point on, the sample preparation was identical to that of the acceptor LUVs, as described above. We refer to these LUVs as 'scrambled' vesicles throughout the text.

### 3.2. Small-angle neutron scattering

Neutron scattering experiments were performed at the BL-6 extended-Q-range small-angle neutron scattering (EQ-SANS) instrument of the Spallation Neutron Source, located at Oak Ridge National Laboratory (ORNL), and KWS-1 at the FRM II reactor (Munich–Garching, Germany) (Frieling-haus *et al.*, 2015; Feoktystov *et al.*, 2015). Samples were loaded into 1 or 2 mm path length quartz banjo cells or 1 mm path length 404 000-QX quartz cuvettes (Hellma, Jena, Germany),

and mounted in a temperature-controlled cell holder with ~1 K accuracy. Typical measurement times were 30 min. EQ-SANS data were taken at two sample-to-detector distances (SDDs), 1.3 and 4.0 m, using wavelength bands of $\lambda$ = 4.0–7.5 Å and $\lambda$ = 10.0–13.5 Å, respectively, corresponding to scattering vector magnitudes of $q$ = 0.005–0.5 Å$^{-1}$. Data were collected with a two-dimensional $^3$He position-sensitive detector and reduced to one-dimensional $I(q)$ scattering curves using *Mantid* (Arnold *et al.*, 2014). KWS-1 data were obtained with a two-dimensional scintillation detector using neutrons of $\lambda$ = 5 Å (wavelength spread FWHM: $\Delta\lambda/\lambda$ = 0.1) and two SDDs, 1.21 and 7.71 m, yielding a $q$ range of 0.005–0.42 Å$^{-1}$. Data were corrected for detector pixel sensitivity, dark current, sample transmission and background scattering from $D_2O$ using the *QTIKWS* software from JCNS (Garching, Germany).

### 3.3. Small-angle X-ray scattering

SAXS data for POPC aLUVs were collected at the P12 BioSAXS beamline, located at the storage ring PETRA III (EMBL/DESY) in Hamburg, Germany (Blanchet *et al.*, 2015). This beamline delivers a total photon flux of $5 \times 10^{12}$ s$^{-1}$ focused to a spot of 120 × 200 µm (full width at half-maximum). The combination of 20 keV ($\lambda$ = 0.6 Å) photons and SDD = 3.1 m yielded an accessible $q$ range of 0.04–0.92 Å$^{-1}$. A Pilatus 2M detector (Dectris, Switzerland) was used for data collection. SAXS data from DPPC/POPC aLUVS were obtained at the ESRF BM29 BioSAXS beamline (Pernot *et al.*, 2013) (Grenoble, France) using a Pilatus 1M detector (Dectris, Switzerland), with $\lambda$ = 0.99 Å and SDD = 2.869 m, yielding an accessible $q$ range of 0.003–0.5 Å$^{-1}$. At both beamlines, samples were transferred prior to measurement into multi-well plates and equilibrated for 10 min in a temperature-controlled block. An automated system delivered 20–35 µl of the lipid sample into a preheated glass capillary. For each sample, 20 (P12) or ten (BM29) frames were recorded with an exposure time of 0.095 s (P12) or 0.5 s (BM29). The water background was measured before and after each sample. To determine the occurrence of possible radiation damage, data collected in subsequent frames were compared by a standard F-test (Petoukhov *et al.*, 2007). Data treatment was performed using the *ATSAS* suite (Petoukhov *et al.*, 2012).

### 4. Models

It was shown previously (Kiselev *et al.*, 2002; Pencer *et al.*, 2006) that coherent scattering from symmetric LUVs can be approximated under certain conditions by

$$I(q) \simeq S(q) |F_{TS}(q)|^2 |F_{FB}(q)|^2, \qquad (1)$$

where $F_{TS}$ is the form factor of a thin spherical shell (containing information about vesicle size and polydispersity), $F_{FB}$ is the form factor of a flat bilayer sheet (containing information about the distribution of matter across the bilayer) and $S$ is the interparticle structure factor (accounting

for interactions between the particles, and equal to unity for a sufficiently diluted system). Equation (1) is often referred to as the separated form factor (SFF) approximation and is valid when the length scales of vesicle radius and bilayer thickness are well separated, such that $F_{TS}$ and $F_{FB}$ can be treated independently (Pencer *et al.*, 2006). As shown by the same authors, ~5 nm thick bilayers and vesicles larger than 50 nm have negligible contributions to $F_{TS}$ for $q > 0.03$ Å$^{-1}$, and the scattered intensity can be approximated by $F_{FB}$ only.

Brzustowicz & Brunger (2005) demonstrated that, for freely floating vesicles with transmembrane asymmetry, a flat bilayer model provides a good description of the scattered intensity. This enables us to apply the SFF method to aLUV data, with the caveat that inner and outer membrane leaflets cannot be unambiguously assigned without *a priori* knowledge of the membrane's composition. In our case, leaflet compositions were obtained independently using solution NMR in combination with GC–MS or UPLC–MS [see Heberle *et al.* (2016) and supporting information §1].

The flat bilayer form factor can be expressed as

$$|F_{FB}| = \int_{-D_i}^{D_o} \Delta\rho \exp(iqz)\, dz$$
$$= (F_{cos}^2 + F_{sin}^2)^{1/2}, \tag{2}$$

where $\Delta\rho$ is the difference between the SLDs of the membrane and the solvent, and $F_{cos} = \int_{-D_i}^{D_o} \Delta\rho \cos(qz)\, dz$ and $F_{sin} = \int_{-D_i}^{D_o} \Delta\rho \sin(qz)\, dz$ are the real and imaginary parts of $F_{FB}$. The integral extends over the full bilayer thickness, that is from its innermost distance $D_i$ to its outermost distance $D_o$.

### 4.1. Asymmetric slab models

**4.1.1. Four-slab model.** The four-slab model has been used previously for analyzing aLUV SANS data (Heberle *et al.*, 2016). For completeness, we summarize its main features below. The bilayer's SLD profile is given by

$$\rho(z) = \begin{cases} \rho_{core} & z < -(D_C^i + D_H^i), \\ \rho_H^i & -(D_C^i + D_H^i) \leq z < -D_C^i, \\ \rho_C^i & -D_C^i \leq z < 0, \\ \rho_C^o, & 0 \leq z < D_C^o, \\ \rho_H^o & D_C^o \leq z < D_C^o + D_H^o, \\ \rho_S & z \geq D_C^o + D_H^o, \end{cases} \tag{3}$$

where $\rho$ are SLDs and $D$ are the thicknesses of the individual slabs. The superscripts o and i denote outer and inner leaflets, respectively (see also Fig. 1). If the SLD of the membrane core matches that of the solvent ($\rho_{core} = \rho_S$), the limits of the integral in equation (2) are well defined, yielding

$$F_{cos} = \frac{1}{q}\left\{ \sum_{o,i}(\rho_C^{o,i} - \rho_H^{o,i})\sin(D_C^{o,i}q) \right.$$
$$\left. + \sum_{o,i}(\rho_H^{o,i} - \rho_S)\sin[(D_C^{o,i} + D_H^{o,i})q] \right\}, \tag{4}$$

where $\sum_{o,i}$ denotes the sum over either all outer or all inner leaflet parameters ($\rho_C^i, D_C^i, \rho_C^o, D_C^o, \rho_H^i, \ldots$), respectively, and

$$F_{sin} = \frac{1}{q}\left\{ (\rho_C^o - \rho_C^i) + \sum_{o,i}(-1)^n(\rho_C^{o,i} - \rho_H^{o,i})\cos(D_C^{o,i}q) \right.$$
$$\left. + \sum_{o,i}(-1)^n(\rho_H^{o,i} - \rho_S)\cos[(D_C^{o,i} + D_H^{o,i})q] \right\}, \tag{5}$$

where $n \in \mathbb{N}$ and

$$n = \begin{cases} even & \text{for inner leaflet i,} \\ odd & \text{for outer leaflet o.} \end{cases}$$

Following the approach used by Kučerka and co-workers (Kučerka *et al.*, 2004, 2008; Kučerka, Pencer, Nieh & Katsaras, 2007), it is possible to reduce the number of adjustable parameters by enforcing matter conservation (*i.e.* by assuming volume incompressibility and space filling), which essentially couples the thicknesses of the individual layers to the projected area per lipid $A_L$ and lipid molecular volume $V_L$ (Fig. 1 upper panel). However, we must first consider that aLUVs will differ in the type and number of lipids in the outer and inner leaflets. This is accounted for by introducing
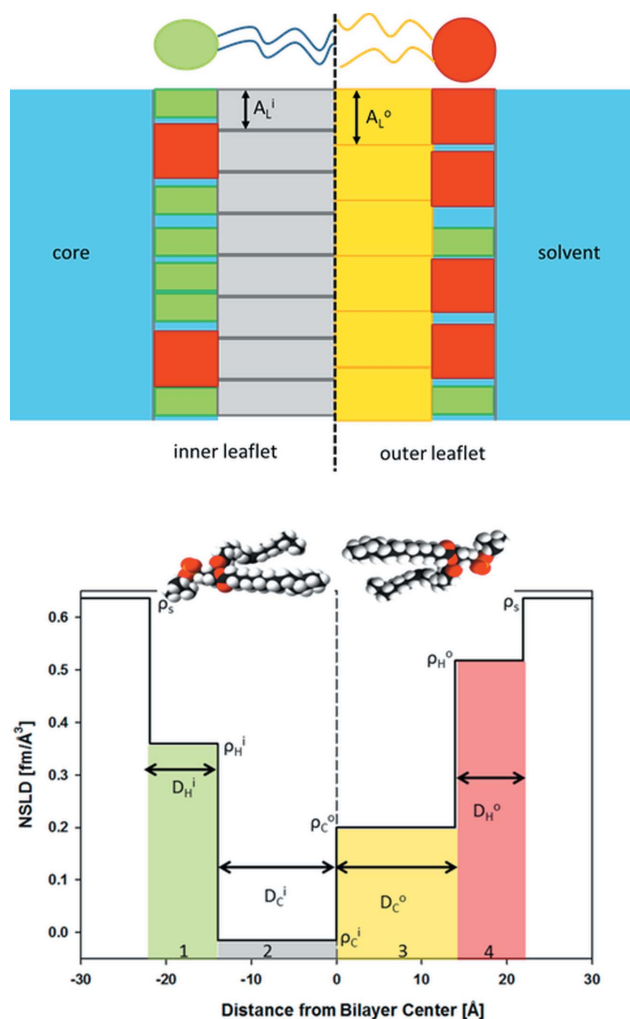


**Figure 1**
Schematic illustration of the four-slab model. Upper, space-filling representation of an asymmetric bilayer. Lower, the neutron scattering length density (NSLD) profile across the bilayer is obtained by averaging the composition of each slab.

different leaflet molar ratios $\chi^{o,i}$ for the inner and outer leaflet lipids. Small differences between the surface areas of the inner and outer leaflets lead to an additional scaling of $\chi^{o,i}$, as detailed in the supporting information (§2). The number of headgroup-bound water molecules, $n_W$, will also in general be different for each leaflet. The average molecular volumes of the lipid headgroup and hydrocarbon layers are then calculated as mole-fraction-weighted sums:

$$V_H^{o,i} = \chi_{don}^{o,i} V_H^{don} + \chi_{acc}^{o,i} V_H^{acc} + n_W^{o,i} V_W,$$
$$V_C^{o,i} = \chi_{don}^{o,i} V_C^{don} + \chi_{acc}^{o,i} V_C^{acc}. \qquad (6)$$

Similarly, the corresponding average coherent neutron scattering lengths are given by

$$b_H^{o,i} = \chi_{don}^{o,i} b_H^{don} + \chi_{acc}^{o,i} b_H^{acc} + n_W^{o,i} b_W,$$
$$b_C^{o,i} = \chi_{don}^{o,i} b_C^{don} + \chi_{acc}^{o,i} b_C^{acc}. \qquad (7)$$

Super/subscripts 'don' and 'acc' differentiate, respectively, between donor and acceptor lipids, $V_W$ is the molecular volume of water, $n_W$ is the number of bound water molecules, and $\chi_{don}^{o,i} = 1 - \chi_{acc}^{o,i}$. Lipid volumes can be determined by either independent experiments (Greenwood *et al.*, 2006; Hodzic *et al.*, 2008; Murugova & Balgavý, 2014) or atomistic simulation (Petrache *et al.*, 1997). For the present work we used volumes determined experimentally by densitometry and reported by Kučerka *et al.* (2011). Hence, the $\rho$s and $D$s in equation (4) can be replaced by $\rho_{H(C)}^{o,i} = b_{H(C)}^{o,i}/V_{H(C)}^{o,i}$ and $D_{H(C)}^{o,i} = V_{H(C)}^{o,i}/A_L^{o,i}$, reducing the number of adjustable parameters to four ($A_L^{o,i}$, $n_W^{o,i}$). In this work, $\chi_{don,acc}^{o,i}$ was independently determined by GC–MS and NMR analysis of the aLUV composition for each sample (supporting information). Alternatively, $\chi_{don(acc)}^{o,i}$ can be a free parameter if it is unknown, or constrained in order to account for any uncertainty in its determination by analytical methods.

A complication we encountered was that the different contrast aLUV preparations showed a small but non-negligible variation of outer leaflet exchange (see *e.g.* Table S6). In order to account for this, we approximated the $A_L$ in each leaflet by a composition-weighted sum of the areas of its constituent lipids:

$$A_L^{o,i} = \chi_{don}^{o,i} A_L^{don} + \chi_{acc}^{o,i} A_L^{acc}, \qquad (8)$$

where the lipid areas of donor and acceptor lipids $A_L^{don(acc)}$ are now adjustable parameters. Finally, we defined the hydrocarbon chain length of each leaflet as $d_C^{o,i} = V_C^{o,i}/A_L^{o,i}$ and the total bilayer (Luzzati) thickness as $d_B = \sum_{o,i} V_L^{o,i}/A_L^{o,i}$ (Nagle & Tristram-Nagle, 2000).

**4.1.2. Six-slab model.** For SAXS analysis, an additional slab for the terminal methyl group of each leaflet must be added owing to the significant differences in electron densities between $CH_2$ and $CH_3$ groups, resulting in a six-slab model for the electron density profile:

$$\rho(z) = \begin{cases} \rho_{core} & z < -(D_M^i + D_C^i + D_H^i), \\ \rho_H^i & -(D_M^i + D_C^i + D_H^i) \leq z < -(D_M^i + D_C^i), \\ \rho_C^i & -(D_M^i + D_C^i) \leq z < -D_M^i, \\ \rho_M^i & -D_M^i \leq z < 0, \\ \rho_M^o & 0 \leq z < D_M^o, \\ \rho_C^o & D_M^o \leq z < D_M^o + D_C^o, \\ \rho_H^o & D_M^o + D_C^o \leq z < D_M^o + D_C^o + D_H^o, \\ \rho_S & z \geq D_M^o + D_C^o + D_H^o, \end{cases} \qquad (9)$$

where subscripts 'M' denote the central methyl slabs (Fig. 2).

From equation (9) we calculate the real and imaginary parts of the form factor:

$$F_{cos} = \frac{1}{q} \left\{ \sum_{o,i}(\rho_C^{o,i} - \rho_H^{o,i}) \sin[(D_C^{o,i} + D_M^{o,i})q] \right.$$
$$+ \sum_{o,i}(\rho_M^{o,i} - \rho_C^{o,i}) \sin(D_M^{o,i} q)$$
$$\left. + \sum_{o,i}(\rho_H^{o,i} - \rho_S) \sin[(D_M^{o,i} + D_H^{o,i} + D_C^{o,i})q] \right\} \qquad (10)$$

and

$$F_{sin} = \frac{1}{q} \left\{ (\rho_M^o - \rho_M^i) + \sum_{o,i}(-1)^n (\rho_C^{o,i} - \rho_H^{o,i}) \cos[(D_C^{o,i} + D_M^{o,i})q] \right.$$
$$+ \sum_{o,i}(-1)^n (\rho_M^{o,i} - \rho_C^{o,i}) \cos(D_M^{o,i} q)$$
$$\left. + \sum_{o,i}(-1)^n (\rho_H^{o,i} - \rho_S) \cos[(D_M^{o,i} + D_C^{o,i} + D_H^{o,i})q] \right\}, \qquad (11)$$

where $n \in \mathbb{N}$,

$$n = \begin{cases} even & \text{for inner leaflet i,} \\ odd & \text{for outer leaflet o.} \end{cases}$$

Using similar arguments as in §4.1.1, the electron densities and slab thicknesses can be replaced by $\rho_j^{o,i} = b_j^{o,i}/V_j^{o,i}$ and $D_j^{o,i} = V_j^{o,i}/A_L^{o,i}$, where $b_j$ now refers to the number of electrons for each slab $j = H, C, M$. We further parsed the
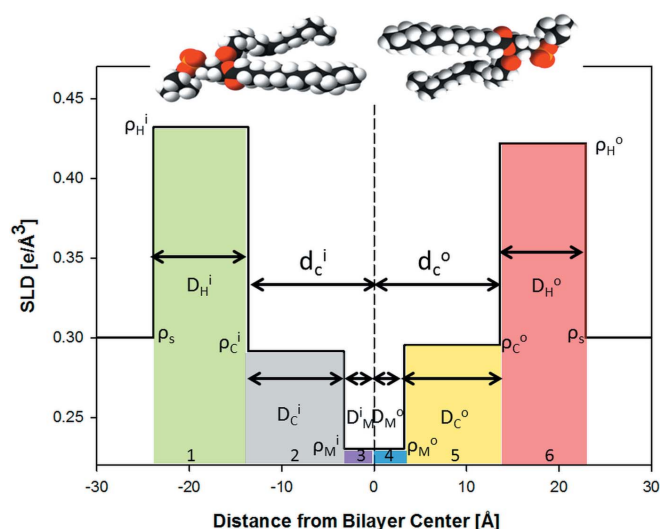


**Figure 2**
Schematic illustration of the six-slab electron density profile model.

headgroup and methyl slabs to account for their contributions to the neighboring hydrocarbon methylene region:

$$
\begin{aligned}
V_H^{don,acc} &= V_H + (1 - p_{CG})V_{CG}, \\
V_C^{don,acc} &= (1 - p_M)V_C + p_{CG}V_{CG}, \\
V_M^{don,acc} &= V_M + p_M V_C, \\
b_H^{don,acc} &= b_H + (1 - p_{CG})b_{CG}, \\
b_C^{don,acc} &= (1 - p_M)b_C + p_{CG}b_{CG}, \\
b_M^{don,acc} &= b_M + p_M b_C,
\end{aligned}
\tag{12}
$$

where $V_{CG}$ and $V_M$ are the respective volumes of the carbonyl-glycerol (CG) and methyl groups, and $p_{CG} \in [0, 1]$ distributes the lipid's CG contributions between the headgroup and hydrocarbon regions ($p_M$ does the same for methyl slabs). Volumes and electron densities are then calculated according to equations (6) and (7), where $V_M^{o,i}$ and $b_M^{o,i}$ are determined analogously to $V_C^{o,i}$ and $b_C^{o,i}$.

Volumetric data for the individual slabs were taken from the literature (Kučerka *et al.*, 2011). Temperature-dependent values of $V_M$ can be found, for example, in the work of Small (1986), Koenig & Gawrisch (2005) and Kučerka *et al.* (2011). Depending on whether $\chi_{don(acc)}^{o,i}$ is known or not, the six-slab model has either six ($A_L^{o,i}$, $n_W^{o,i}$, $p_{CG}$, $p_M$) or eight adjustable parameters. Finally, we note that the electron density contrast between acyl chains of the inner and outer leaflets is generally weak. However, this contrast can in principle be enhanced by introducing brominated or fluorinated lipids into one of the leaflets (McIntosh *et al.*, 1996; Hristova & White, 1998).

## 4.2. SDP model for asymmetric membranes

The SDP model describes the bilayer structure in terms of one-dimensional volume probability profiles (VPPs) of quasi-molecular lipid fragments. The VPPs are scaled by either the fragment's total coherent neutron scattering length (in the case of SANS) or the number of electrons (in the case of SAXS) to obtain the SLD profile (Pabst *et al.*, 2010; Marquardt, Heberle *et al.*, 2015). Inspired by Kučerka, Pencer, Sachs *et al.* (2007), we parse each leaflet of the asymmetric bilayer as follows: choline methyl + phosphate + $CH_2CH_2N$ (PC); carbonyl + glycerol (CG); hydrocarbon (HC); and methyl (M) groups. The volume probabilities for the PC, CG and M groups are modeled as Gaussians:

$$
P_n(z) = \frac{c_n}{(2\pi)^{1/2}} \exp\left[-\frac{(z - z_n)^2}{2\sigma_n^2}\right]
\tag{13}
$$

for $n$ = PC, CG, M, where $c_n = V_n/(A_L \sigma_n)$ and $\sigma_n$ and $z_n$ are the width and position of the distribution, respectively (Fig. 3). The HC groups are described by smooth plateau-like functions using error functions (Pabst *et al.*, 2010). However, our modeling must also account for the different contrasts in the inner and outer HC layers, which require two separate smooth bridging functions, leading to a significant increase in computational resources. We therefore applied [following Wiener *et al.* (1989)] a half-period squared sine/cosine function:

$$
P_{HC}(z) = \begin{cases}
\sin\left(\dfrac{z - z_{MN_i} + \sigma_{MN}}{2\sigma_{MN}}\dfrac{\pi}{2}\right)^2 \\
\quad \text{for } z_{MN_i} - \sigma_{MN} \le z < z_{MN_i} + \sigma_{MN}, \\
1 \quad \text{for } z_{MN_i} + \sigma_{MN} \le z < z_{MN_o} - \sigma_{MN}, \\
\cos\left(\dfrac{z - z_{MN_o} + \sigma_{MN}}{2\sigma_{MN}}\dfrac{\pi}{2}\right)^2 \\
\quad \text{for } z_{MN_o} - \sigma_{MN} \le z < z_{MN_o} + \sigma_{MN}.
\end{cases}
\tag{14}
$$

Here, $z_{MN_{i,o}}$ is the 0.5-probability value for the hydrocarbon region (and thus also defines the thickness of the inner and outer leaflet hydrocarbon regions $d_C^{i,o}$, in accordance with its definition as a Gibbs dividing surface) and $2\sigma_{MN}$ is the width of the squared sine/cosine functions. The probability function of the methylene regime is $P_{MN} = P_{HC} - P_M$.

We note two additional modifications to the SDP description for symmetric bilayers. Firstly, the choline and phosphate groups are combined into a single Gaussian in order to decrease the number of fitting parameters. The ensuing decrease in structural resolution is, however, within experimental error, as determined from fits of previously reported POPC form factors (Kučerka *et al.*, 2011) using either combined or separate headgroup Gaussians. Secondly, in some cases, two distinct methyl groups must be modeled, for example when the outer and inner bilayer leaflets contain contrasting hydrocarbon chains. This is achieved by displacing each leaflet's methyl group slightly from the bilayer midplane, ensuring, however, that their combined envelope function is a single Gaussian, as observed in symmetric bilayers when both amplitudes are equal (Fig. 3).

The water (solvent) probability function $P_S$ is defined as $P_S(z) = 1 - \sum_n P_n(z)$, with $n$ = $PC^{o,i}$, $CG^{o,i}$, $MN^{o,i}$, $M^{o,i}$ (Klauda *et al.*, 2006; Kučerka, Pencer, Sachs *et al.*, 2007).

For the real part of $F_{FB}$ we then calculate
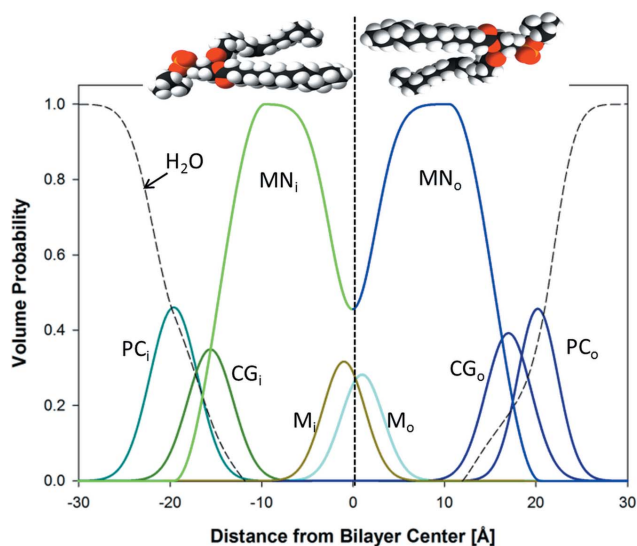


**Figure 3**
Schematic illustration of the volume probability distribution for an asymmetric bilayer.

$$F_{\cos} = \sum_m \left\{ \sum_{o,i} \Delta \rho_m^{o,i} c_m^{o,i} \sigma_m^{o,i} \cos(qz_m^{o,i}) \exp\left[ -\frac{(q\sigma_m^{o,i})^2}{2} \right] \right\}$$
$$- \sum_{o,i} \Delta \rho_{MN}^{o,i} c_M^{o,i} \sigma_M \cos(qz_M^{o,i}) \exp\left[ -\frac{(q\sigma_M^{o,i})^2}{2} \right]$$
$$+ \sum_{o,i} (-1)^n \frac{\pi^2 \Delta \rho_{MN}^{o,i} \cos(q\sigma_{MN}) \sin(qz_{MN}^{o,i})}{-\pi^2 q + 4q^3 \sigma_{MN}^2},$$

$$n \in \mathbb{N}, \quad n = \begin{cases} \text{even} & \text{for inner leaflet i,} \\ \text{odd} & \text{for outer leaflet o,} \end{cases} \quad (15)$$

where $\sum_m$ denotes the sum over the PC, CG and M groups. For the imaginary part of $F_{FB}$ we calculate

$$F_{\sin} = \sum_m \left\{ \sum_{o,i} \Delta \rho_m^{o,i} c_m^{o,i} \sigma_m^{o,i} \sin(qz_m^{o,i}) \exp\left[ -\frac{(q\sigma_m^{o,i})^2}{2} \right] \right\}$$
$$- \sum_{o,i} \Delta \rho_{MN}^{o,i} c_M^{o,i} \sigma_M \sin(qz_M^{o,i}) \exp\left[ -\frac{(q\sigma_M^{o,i})^2}{2} \right]$$
$$+ \sum_{o,i} (-1)^n q^{-1} \Delta \rho_{MN}^{o,i} \left[ 1 - \frac{\pi^2 \cos(qz_{MN}^{o,i}) \cos(q\sigma_{MN})}{\pi^2 - 4q^2 \sigma_{MN}^2} \right],$$

$$m = \text{PC, CG, M}, \quad n = \begin{cases} \text{even} & \text{for inner leaflet i,} \\ \text{odd} & \text{for outer leaflet o.} \end{cases} \quad (16)$$

Several additional constraints were imposed during the fitting procedure. On the basis of previous results showing that the distance $z_{CG} - z_{MN}$ between the carbonyl-glycerol group and the hydrocarbon/headgroup interface lies between 0.45 and 1.1 Å for different PC lipids (Kučerka *et al.*, 2011), we fixed this value to 1 Å. Additionally, the locations of the methyl groups were fixed at a distance of 1 Å from the bilayer center, *i.e.* $|z_M| = 1$ Å, and $\sigma_M$ was set to the value obtained by fitting the sum of inner and outer leaflets $P_M$ to the envelope function given for the corresponding symmetric bilayers (Kučerka *et al.*, 2011). This yielded $\sigma_M = 2.38$ Å for DPPC and $\sigma_M = 2.02$ Å for POPC bilayers. Finally, as mentioned, our aSDP model combines the choline and phosphate groups into a single Gaussian probability function. However, in order to obtain reasonable $\sigma_{PC}$ values, the form factors reported for POPC and DPPC by Kučerka *et al.* (2011) were refitted with our aSDP model.

After these constraints were applied, six adjustable parameters remained for the aSDP model: $z_n^{o,i}$ and $\sigma_n^{o,i}$, where $n =$ PC, CG, MN (if needed $\chi_{don(acc)}^{o,i}$ can also be varied). In order to account for variations in outer lipid exchange efficiency, when jointly analyzing different contrast data sets obtained from different physical samples, these parameters can be rewritten as a weighted sum of values for the individual donor and acceptor lipid species:

$$z_n^{o,i} = (\chi_{don}^{o,i} z_{n,don} + \chi_{acc}^{o,i} z_{n,acc}) \quad (17)$$

and

$$\sigma_n^{o,i} = (\chi_{don}^{o,i} \sigma_{n,don} + \chi_{acc}^{o,i} \sigma_{n,acc}). \quad (18)$$

To increase the stability of the fits, we derived the individual $z_n$ and $\sigma_n$ values of the acceptor and donor lipids by scaling their reported values in single-component bilayers (Kučerka *et*

*al.*, 2011). For example, $z_{n,don} = a_1 \tilde{z}_{n,don}$ and $z_{n,acc} = a_2 \tilde{z}_{n,acc}$, $\tilde{z}_n$ being the reported literature value, and $a_1$ and $a_2$ being the fitted scaling parameters. The observed variations in $a_1$ and $a_2$ were between 0.96 and 1.04. Structural parameters were calculated analogously to the slab model using $A_L^{o,i} = V_{MN}^{o,i}/d_C^{o,i}$, where $d_C^{o,i} = z_{MN}^{o,i}$, and $d_B = \sum_{o,i} V_L^{o,i}/A_L^{o,i}$.

### 4.3. Joint analysis of SANS and SAXS data

In order to fully exploit the benefits of contrast variation, all SANS and SAXS data were fitted simultaneously in a joint analysis taking into account the appropriate experimental resolution (see *e.g.* Feigin & Svergun, 1987). In the case of the asymmetric slab models, this was achieved by requiring common values for $A_L^{o,i}$ and $n_W^{o,i}$ for all data sets. For the aSDP model, the volume probability distributions of quasi-molecular fragments serve as a common backbone for a joint SANS/SAXS data analysis. The applied optimization function $\chi_{red}^2$ included all SANS and SAXS data sets for a given aLUV system. Specific weighting schemes took into account the importance of matching the first minimum displayed in the SANS data, as well as the SAXS intensity modulations at high $q$ vector magnitudes. This was achieved by decreasing the experimentally determined uncertainties in these regions by a factor of 0.1–0.5. Further, the SAXS data were weighted by a factor of 0.5 with respect to the SANS data. The reported $\chi_{red}^2$ values were recalculated after releasing all constraints and weights to avoid any influence from the specific weighting.

Different optimization routines were also applied. In the case of the asymmetric slab model the small number of free parameters allowed us to apply the trust region reflective algorithm, which is similar to the Levenberg–Marquardt algorithm, but with a restricted step size, thereby preventing it from overstepping (Yuan, 2000). Because of the large number of adjustable parameters in the aSDP model, there is an inherent danger that a deterministic search algorithm (such as the one used for the asymmetric slab model) will become trapped in a local minimum. In this case, random search or stochastic algorithms, such as the differential evolution (DE) algorithm (Price *et al.*, 2006; Storn & Price, 1997; Price & Storn, 1997), offer a different strategy. For example, the DE algorithm performs a global search for the best solution starting from an initial population of solutions; these are subsequently combined and/or 'mutated' to form new solutions that are accepted or rejected on the basis of their agreement with experimental data.

The uncertainties of the joint SAXS/SANS analysis were determined to be <2% for symmetric systems and <3% for asymmetric systems. These values were estimated by a variation of initial (starting) parameters, number of iterations and termination tolerances.

## 5. Results and discussion

### 5.1. Testing models on symmetric LUVs

All models were assessed for their ability to reproduce previously reported structural data for symmetric bilayers. To

**Table 1**
Structural parameters of DPPC$^{don}$/POPC$^{acc}$ aLUVs and LUVs obtained after scrambling.

Parameter uncertainties are estimated to be <2%.

| Model | $A_L$ (Å$^2$) | $d_C$ (Å) | $d_B$ (Å) | $\chi^2_{red}$ |
|---|---|---|---|---|
| Slab$_{SAXS}$† | 65.3 | 14.0 | 38.2 | 1.1 |
| Slab$_{SANS}$‡ | 67.5 | 13.6 | 36.9 | 94.5 |
| Slab$_{Joint}$§ | 67.5 | 13.6 | 36.9 | 54.2 |
| SDP$_{SAXS}$† | 63.7 | 14.4 | 39.2 | 0.6 |
| SDP$_{SANS}$‡ | 66.8 | 13.7 | 37.3 | 142.2 |
| SDP$_{Joint}$§ | 66.3 | 13.8 | 37.6 | 34.6 |
| SDP$_L$¶ | 62.7 | 14.6 | 39.8 | – |
| ADP$_L$†† | 67.0 | 13.7 | 37.2 | – |

† Analysis of SAXS data only.  ‡ Joint analysis of different contrast SANS data only. SANS data were previously published by Heberle *et al.* (2016) and are reanalyzed here. § Joint analysis of SANS and SAXS data. ¶ From Kučerka *et al.* (2011).  †† From Fogarty *et al.* (2015).

this end, we prepared four symmetric LUV samples with different internal contrasts (*i.e.* POPC, POPC-d13, POPC-d31 and POPC-d44). SANS data were taken from the work of Heberle *et al.* (2016) and reanalyzed jointly with new data from SAXS experiments. In the analyis of these datasets, we constrained $A_L$ and $d_C$ from the inner and outer leaflets to be identical. The corresponding SANS and SAXS data and their fits are shown in Fig. 4. Structural parameters determined from the joint analysis (Table 1) were also compared with results obtained by analyzing each dataset individually. The latter comparison shows that $A_L$ obtained from standalone SAXS data was smaller than that obtained from standalone SANS
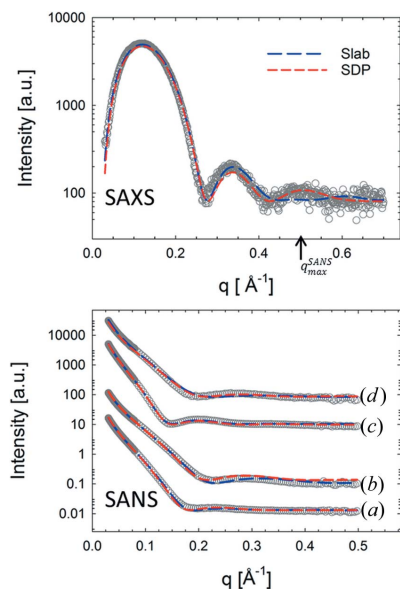


**Figure 4**
Joint analysis of SAXS (top panel) and SANS (bottom panel) data from symmetric POPC LUVs with different internal contrasts, namely (*a*) POPC, (*b*) POPC-d13, (*c*) POPC-31 and (*d*) POPC-d44 (*T* = 293 K). The maximum SANS resolution in reciprocal space is indicated by the $q_{max}^{SANS}$ arrow in the SAXS panel. Dashed lines are best fits using the asymmetric slab (blue long-dashed line) and SDP models (red short-dashed line). Data are offset vertically for clarity. The SANS data in the lower panel were previously published by Heberle *et al.* (2016) and are reanalyzed here.

data, while $d_C$ and $d_B$ were larger for the SAXS analysis than for the SANS analysis owing to the inverse relationship between lipid area and bilayer thickness. The jointly analyzed values are, however, closer to those obtained by SANS, which can be understood by the fact that the applied definitions for $A_L$, $d_C$ and $d_B$ depend on the position of the glycerol backbone, to which neutrons are most sensitive. Furthermore, the slab and SDP models yielded practically identical values for $A_L$ and $d_B$ when all data sets were included. In terms of fit quality, $\chi^2_{red}$ were generally smaller for the SDP model, which we attribute to the model's higher intrinsic resolution. Note that the high $\chi^2_{red}$ values of SANS are due to the four different contrasts that were fitted simultaneously.

It is instructive to compare our results with the literature values listed in Table 1. Within experimental uncertainty, we find good agreement with the results of Kučerka *et al.* (2011), who also applied an SDP-based analysis similar to ours but who did not use lipid isotopes, and a re-evaluation of these data in terms of an atomistic model (Fogarty *et al.*, 2015).

## 5.2. Testing the models using isotopic aLUVs

We next analyzed aLUVs composed of different POPC isotopes in the inner and outer leaflets, *i.e.* POPC$^{acc}$/POPC-d44$^{don}$ and POPC-d44$^{acc}$/POPC$^{don}$ for SANS and POPC-d13$^{acc}$/POPC$^{don}$ for SAXS. This labeling scheme allowed us to unambiguously resolve the structure of the inner and outer bilayer leaflets. For both samples, we achieved approximately 60% exchange of the outer leaflet lipids (see Table S3 for details). SANS data previously reported by Heberle *et al.* (2016) were reanalyzed together with new SAXS data using both models.

Fig. 5 shows the corresponding SAXS and SANS data, and their fits obtained from joint analysis. Results of the structural parameters are presented in Table 2. On average, the structural parameters are, within experimental uncertainty, equal to those obtained for symmetric LUVs. This is consistent with our previous finding that the aLUV preparation does not alter the membrane structure (Heberle *et al.*, 2016). Analysis using the slab model yielded larger values for $n_W$ and $A_L$ for the inner leaflet compared to the outer leaflet. This result appears to be physically unrealistic, considering that previous studies found that membrane curvature induces a greater packing density (smaller $A_L$) for inner leaflet lipids (Huang & Mason, 1978; Smolentsev *et al.*, 2016). We therefore constrained the inner leaflet $n_W$ and $A_L$ values not to exceed the outer leaflet values, which resulted in both leaflets having identical values for these parameters. An alternative interpretation is that inner leaflet lipids may protrude out of the membrane to avoid lateral compression, leading to a rougher inner surface (Brzustowicz & Brunger, 2005) and to $n_W^i > n_W^o$, which can then result in $A_L^i > A_L^o$. Comparing the $\chi^2_{red}$ values of the constrained and unconstrained fits (Table 2), as well as fit residuals (Fig. S1), we conclude that these scenarios cannot be distinguished owing to the inherent resolution limitations of the slab model.

**Table 2**

Structural parameters of POPC aLUVs.

Values in parentheses for the slab model correspond to results obtained upon removing area constraints. Parameter uncertainties are estimated to be <3%.

| Model | $A_L$ (Å$^2$) | | $d_C$ (Å) | | $d_B$ (Å) | $\chi^2_{red}$ |
|---|---|---|---|---|---|---|
| | Outer | Inner | Outer | Inner | | |
| Slab$_{Joint}$† | 65.5 (63.8) | 65.5 (67.8) | 14.0 (14.4) | 14.0 (13.5) | 38.0 (37.9) | 7.0 (6.3) |
| aSDP$_{Joint}$† | 65.7 | 63.4 | 14.0 | 14.4 | 38.6 | 6.6 |

† Joint analysis of SANS and SAXS data. The SANS data were previously published by Heberle *et al.* (2016) and are reanalyzed here.

**Table 3**

Structural parameters of DPPC$^{don}$/POPC$^{acc}$ aLUVs and LUVs obtained after scrambling.

Parameter uncertainties are estimated to be <3%.

| Model (sample) | $A_L$ (Å$^2$) | | $d_C$ (Å) | |
|---|---|---|---|---|
| | DPPC | POPC | DPPC | POPC |
| Slab (aLUV) | 61.7 | 68.7 | 14.5 | 13.7 |
| aSDP (aLUV) | 62.6 | 67.9 | 14.3 | 13.9 |
| Slab (LUV†) | 64.9 | 67.8 | 13.8 | 13.8 |
| SDP (LUV†) | 64.9 | 69.1 | 13.8 | 13.7 |

† Scrambled.

In the case of the aSDP model, unconstrained fits led to $A_L^i < A_L^o$, and consequently to $d_C^i > d_C^o$. To further understand the coupling of vesicle size/curvature to lipid packing differences of the inner and outer leaflets, additional studies would be needed that are beyond the scope of the current work. We note that $A_L^i < A_L^o$ is consistent with an earlier analysis of 20 nm diameter vesicles (Huang & Mason, 1978), which because of their smaller radius resulted in significant differences between $A_L^i$ and $A_L^o$. However, $A_L^i < A_L^o$ was also suggested for 100 nm vesicles in a recent spectroscopic study (Smolentsev *et al.*, 2016).

### 5.3. DPPC/POPC asymmetric membranes

Fig. 6 shows the aSDP analysis of DPPC$^{don}$/POPC$^{acc}$ aLUVs using two different contrasts (*i.e.* DPPC-d62$^{don}$/POPC-d13$^{acc}$ and DPPC$^{don}$/POPC-d13$^{acc}$). The analysis also included scrambled DPPC$^{don}$/POPC$^{acc}$ vesicles (see §3) in order to examine the impact of transbilayer lipid asymmetry on structure. Data analyzed in terms of the slab model are presented in Fig. S2. A previous analysis of outside gel/inside fluid DPPC/POPC aLUVs at room temperature showed a partial fluidization of the outer leaflet, observed as a significantly larger $A_L$ as compared to typical gel-phase values (Heberle *et al.*, 2016). In order to determine whether such a transbilayer coupling persists in fluid aLUVs, we carried out experiments at 323 K, *i.e.* above the melting temperature of both lipids.



**Figure 5**
Structural parameters for POPC aLUVs measured at 293 K. Top panel, SAXS data (open circles) from POPC-d13$^{acc}$/POPC$^{don}$ aLUVs, and corresponding fits (dashed lines) and electron density profiles (right). The maximum SANS resolution in reciprocal space is indicated by the $q_{max}^{SANS}$ arrow. Bottom panel, SANS data (open circles) from (*a*) POPC$^{acc}$/POPC-d44$^{don}$ and (*b*) POPC-d44$^{acc}$/POPC$^{don}$ aLUVs and corresponding fits (dashed lines), and neutron scattering length density profiles (right). Blue and red colors denote analysis using the slab and SDP models, respectively. Structural parameters are listed in Table 2. The SANS data in the lower panel were previously published by Heberle *et al.* (2016) and are reanalyzed here.



**Figure 6**
SDP analysis (red lines) of DPPC$^{don}$/POPC$^{acc}$ aLUVs (open circles) and scrambled LUVs (filled triangles). The panels on the right show the corresponding SLDs (red: aLUVs; dashed black: scrambled LUVs). The different contrast samples for SANS experiments were DPPC-d62$^{don}$/POPC-d13$^{acc}$ ($a_{asym}$/$a_{scram}$) and DPPC$^{don}$/POPC-d13$^{acc}$ ($b_{asym}$/$b_{scram}$). The maximum SANS resolution in reciprocal space is indicated by the $q_{max}^{SANS}$ arrow in the SAXS panel. Data are offset vertically for clarity.

# research papers

**Table 4**
Structural parameters averaged over different contrasts obtained from SDP analysis of DPPC/POPC aLUVs.

Parameter uncertainties are estimated to be <3%.

| System | $A_L$ (Å$^2$) | | $d_C$ (Å) | | $d_B$ (Å) |
|---|---|---|---|---|---|
| | Outer | Inner | Outer | Inner | |
| aLUVs | 65.7 | 67.2 | 14.1 | 14.0 | 38.0 |
| Scrambled | 67.8 | 67.8 | 13.9 | 13.9 | 37.2 |

Analysis of the aLUV composition yielded significant differences in samples with different contrasts ($\chi^o_{DPPC-d62}$ = 0.35–0.45 and $\chi^i_{POPC-d13}$ = 0.85–0.92, see Table S6). Data were therefore analyzed according to equations (8), (17) and (18), *i.e.* in terms of the individual structures of DPPC and POPC lipids.

The results from this analysis (Table 3) show good agreement for the different structural parameters of asymmetric and scrambled samples. The areas for DPPC ($A_L$ = 63.1 Å$^2$) and POPC ($A_L$ = 67.3 Å$^2$) were also consistent with those from a previous analysis of single-component bilayers at 323 K (Kučerka *et al.*, 2011). Because the differences between structural parameters obtained in aLUVs and those reported for corresponding single-component bilayers are within experimental uncertainties, we conclude that there is no transbilayer structural coupling in DPPC/POPC aLUVs when both leaflets are in the fluid phase. However, we cannot exclude the possibility of transbilayer coupling in fluid membranes with a higher outer leaflet exchange and/or for different lipid systems. We further note that there is an overall good agreement between the results obtained through the slab and aSDP models.

In order to examine leaflet-specific structural features of DPPC/POPC aLUVs, we calculated the molecular averages of $A_L$, $d_C$ and $d_B$ according to the aLUV compositions (Table 4). Compared to scrambled LUVs, $A_L^i$ is slightly larger than $A_L^o$, leading to $d_C^i < d_C^o$. This is in contrast to our findings for POPC aLUVs (Table 2), where the inner leaflet was somewhat more densely packed than the outer leaflet. This result was not unexpected, however, since POPC has a larger area per lipid than DPPC at 323 K (Kučerka *et al.*, 2011; Fogarty *et al.*, 2015) (see also Table 3). The inner leaflet – which is essentially pure POPC – thus has a larger average $A_L$ than the outer leaflet, which contains a substantial amount of DPPC in addition to POPC.

## 6. Conclusion

We have adapted a low-resolution slab model and a high-resolution SDP model for the joint SANS/SAXS analysis of asymmetric lipid vesicles. These new models provide analytical tools to study putative interleaflet coupling mechanisms in asymmetric bilayers, which better represent the asymmetry found in most biological membranes.

Application of the aSDP model requires a large number of adjustable parameters, some of which were constrained in order to avoid nonphysical results (see also *e.g.* Table S5).

Additionally, we applied a DE algorithm to prevent the optimization routine from becoming trapped in local minima. In the case of the slab model, which has fewer free parameters, the trust region reflective algorithm was sufficient. On the basis of the fit quality, as judged by $\chi^2_{red}$, the extra computational effort required by the aSDP model is justified. However, in cases where only SANS data are available, the slab model may provide a more reliable analysis. In order to apply this model to SAXS data, an additional slab for the methyl groups is needed.

Both models were tested on isotopically labeled variants of POPC and DPPC/POPC aLUVs. Interestingly, our analysis of POPC aLUVs suggested $A_L^i < A_L^o$, consistent with the presence of residual curvature strain in our 120 nm diameter aLUVs. Furthermore, in the case of fluid DPPC/POPC aLUVs at 323 K, we did not find transbilayer coupling of the individual leaflet structures. We believe that, together with the recently reported protocol for preparing aLUVs (Heberle *et al.*, 2016), this work sets the stage for future studies of multicomponent aLUVs (*e.g.* including cholesterol) that are needed to understand the complex structure of asymmetric membranes on the sub-nanometre level.

## 7. Related literature

For further literature related to the supporting information, see Hartler *et al.* (2011), Knittelfelder *et al.* (2014) and Perly *et al.* (1985).

## References

Arnold, O. *et al.* (2014). *Nucl. Instrum. Methods Phys. Res. Sect. A*, **764**, 156–166.

Blanchet, C. E., Spilotros, A., Schwemmer, F., Graewert, M. A., Kikhney, A., Jeffries, C. M., Franke, D., Mark, D., Zengerle, R., Cipriani, F., Fiedler, S., Roessle, M. & Svergun, D. I. (2015). *J. Appl. Cryst.* **48**, 431–443.

Brzustowicz, M. R. & Brunger, A. T. (2005). *J. Appl. Cryst.* **38**, 126–131.

Cheng, H.-T., Megha & London, E. (2009). *J. Biol. Chem.* **284**, 6079–6092.

Chiantia, S. & London, E. (2013). *Encyclopedia of Biophysics*, pp. 1250–1253. London: Springer.

Devaux, P. F. (1991). *Biochemistry*, **30**, 1163–1173.

Feigin, L. A. & Svergun, D. I. (1987). *Structure Analysis by Small-Angle X-ray and Neutron Scattering.* New York: Plenum Press.

Feoktystov, A. V., Frielinghaus, H., Di, Z., Jaksch, S., Pipich, V., Appavou, M.-S., Babcock, E., Hanslik, R., Engels, R., Kemmerling, G., Kleines, H., Ioffe, A., Richter, D. & Brückel, T. (2015). *J. Appl. Cryst.* **48**, 61–70.

Fogarty, J. C., Arjunwadkar, M., Pandit, S. A. & Pan, J. (2015). *Biochim. Biophys. Acta*, **1848**, 662–672.

Frielinghaus, H., Feoktystov, A., Berts, I. & Mangiapia, G. (2015). *J. Large-Scale Res. Facilities*, **1**, 28.

Greenwood, A. I., Tristram-Nagle, S. & Nagle, J. F. (2006). *Chem. Phys. Lipids*, **143**, 1–10.

Hartler, J., Trotzmuller, M., Chitraju, C., Spener, F., Kofeler, H. C. & Thallinger, G. G. (2011). *Bioinformatics*, **27**, 572–577.

Heberle, F. A., Marquardt, D., Doktorova, M., Geier, B., Standaert, R. F., Heftberger, P., Kollmitzer, B., Nickels, J. D., Dick, R. A., Feigenson, G. W., Katsaras, J., London, E. & Pabst, G. (2016). *Langmuir*, **32**, 5195–5200.

Hodzic, A., Rappolt, M., Amenitsch, H., Laggner, P. & Pabst, G. (2008). *Biophys. J.* **94**, 3935–3944.

Hristova, K. & White, S. H. (1998). *Biophys. J.* **74**, 2419–2433.

Huang, C.-H. & Mason, J. (1978). *Proc. Natl Acad. Sci. USA*, **75**, 308–310.

King, G. I., Jacobs, R. E. & White, S. H. (1985). *Biochemistry*, **24**, 4637–4645.

Kingsley, P. & Feigenson, G. (1979). *Chem. Phys. Lipids*, **24**, 135–147.

Kiselev, M., Lesieur, P., Kisselev, A., Lombardo, D. & Aksenov, V. (2002). *Appl. Phys. Mater. Sci. Process.* **74**, s1654–s1656.

Klauda, J. B., Kučerka, N., Brooks, B. R., Pastor, R. W. & Nagle, J. F. (2006). *Biophys. J.* **90**, 2796–2807.

Knittelfelder, O. L., Weberhofer, B. P., Eichmann, T. O., Kohlwein, S. D. & Rechberger, G. N. (2014). *J. Chromatogr. B*, **951**, 119–128.

Koenig, B. W. & Gawrisch, K. (2005). *Biochim. Biophys. Acta*, **1715**, 65–70.

Kučerka, N., Nagle, J. F., Feller, S. E. & Balgavý, P. (2004). *Phys. Rev. E*, **69**, 051903.

Kučerka, N., Nagle, J. F., Sachs, J. N., Feller, S. E., Pencer, J., Jackson, A. & Katsaras, J. (2008). *Biophys. J.* **95**, 2356–2367.

Kučerka, N., Nieh, M.-P. & Katsaras, J. (2011). *Biochim. Biophys. Acta*, **1808**, 2761–2771.

Kučerka, N., Pencer, J., Nieh, M. P. & Katsaras, J. (2007). *Eur. Phys. J. E Soft Matter Bio. Phys.* **23**, 247–254.

Kučerka, N., Pencer, J., Sachs, J. N., Nagle, J. F. & Katsaras, J. (2007). *Langmuir*, **23**, 1292–1299.

Marquardt, D., Geier, B. & Pabst, G. (2015). *Membranes*, **5**, 180–196.

Marquardt, D., Heberle, F. A., Nickels, J. D., Pabst, G. & Katsaras, J. (2015). *Soft Matter*, **11**, 9055–9072.

McIntosh, T. J., Simon, S. A., Vierling, P., Santaella, C. & Ravily, V. (1996). *Biophys. J.* **71**, 1853–1868.

Murugova, T. & Balgavý, P. (2014). *Phys. Chem. Chem. Phys.* **16**, 18211–18216.

Nagle, J. F. & Tristram-Nagle, S. (2000). *Biochim. Biophys. Acta*, **1469**, 159–195.

Pabst, G., Kučerka, N., Nieh, M.-P., Rheinstädter, M. & Katsaras, J. (2010). *Chem. Phys. Lipids*, **163**, 460–479.

Pabst, G., Rappolt, M., Amenitsch, H. & Laggner, P. (2000). *Phys. Rev. E*, **62**, 4000–4009.

Pencer, J. & Hallett, F. (2000). *Phys. Rev. E*, **61**, 3003–3008.

Pencer, J., Krueger, S., Adams, C. P. & Katsaras, J. (2006). *J. Appl. Cryst.* **39**, 293–303.

Perly, B., Smith, I. C. P., Hughes, L., Burton, G. W. & Ingold, K. U. (1985). *Biochim. Biophys. Acta Biomembranes*, **819**, 131–135.

Pernot, P. *et al.* (2013). *J. Synchrotron Rad.* **20**, 660–664.

Petoukhov, M. V., Franke, D., Shkumatov, A. V., Tria, G., Kikhney, A. G., Gajda, M., Gorba, C., Mertens, H. D. T., Konarev, P. V. & Svergun, D. I. (2012). *J. Appl. Cryst.* **45**, 342–350.

Petoukhov, M. V., Konarev, P. V., Kikhney, A. G. & Svergun, D. I. (2007). *J. Appl. Cryst.* **40**, s223–s228.

Petrache, H. I., Feller, S. E. & Nagle, J. F. (1997). *Biophys. J.* **72**, 2237–2242.

Price, K. & Storn, R. (1997). *Dr Dobb's J.* **220**, 18–24.

Price, K., Storn, R. M. & Lampinen, J. A. (2006). *Differential Evolution: a Practical Approach to Global Optimization.* Berlin, Heidelberg: Springer Science and Business Media.

Riske, K. A., Amaral, L. Q. & Lamy-Freund, M. T. (2001). *Biochim. Biophys. Acta*, **1511**, 297–308.

Schmiedel, H., Jörchel, P., Kiselev, M. & Klose, G. (2001). *J. Phys. Chem. B*, **105**, 111–117.

Small, D. M. (1986). *Physical Chemistry of Lipids.* New York: Plenum Press.

Smolentsev, N., Lütgebaucks, C., Okur, H. I., de Beer, A. G. F. & Roke, S. (2016). *J. Am. Chem. Soc.* **138**, 4053–4060.

Storn, R. & Price, K. (1997). *J. Glob. Opt.* **11**, 341–359.

Verkleij, A. J., Zwaal, R. F. A., Roelofsen, B., Comfurius, P., Kastelijn, D. & van Deenen, L. L. M. (1973). *Biochim. Biophys. Acta*, **323**, 178–193.

Wiener, M., Suter, R. & Nagle, J. (1989). *Biophys. J.* **55**, 315–325.

Wiener, M. C. & White, S. H. (1992). *Biophys. J.* **61**, 434–447.

Yuan, Y. (2000). *ICIAM 99: Proceedings of the Fourth International Congress on Industrial and Applied Mathematics, Edinburgh 5–9 July 1999*, edited by J. M. Ball & J. C. R. Hunt, pp. 271–282. Oxford: Clarenden Press.

# Supplementary Material

## Joint SAXS/SANS Data Analysis of Asymmetric Lipid Vesicles

*Barbara Eicher, Frederick A. Heberle, Drew Marquardt, Gerald N. Rechberger, John Katsaras, Georg Pabst*

## 1 Determination of the bilayer lipid composition via GC/MS and UPLC

The determination of the total bilayer composition has been described in detail previously by [2]. For completeness, we summarize its main features below. Lipid mixture composition can be determined by gas chromatography and mass spectrometry (GC/MS) and ultra performance liquid chromatography and mass spectrometry (UPLC-MS). For GC/MS it is necessary that there are chemical or isotopic differences between chains of the constituent lipids while for UPLC-MS a difference in lipid mass is sufficient. For GC/MS (UPLC-MS) the mole fraction $\chi_i$ of a single component can be determined directly from a set of chain (lipid) peak areas $P$:

$$\chi_i = \frac{P_i}{\sum_j P_j},\qquad(1)$$

where $P_i$ represents the $i^{th}$ chain (lipid) peak area and the denominator is the sum over all mixture components $j$. This relationship is strictly valid when the chain (lipid) peak area fractions vary linearly with mixture composition. A slight deviation from linearity was found which lead to the use of a standard curves (see [2] for details). UPLC-MS data was corrected by a calibration curve of 1:1:1 mole ratio of DPPC/POPC/POPG composition. In brief, samples of 0.1-100 $\mu$g with identical mole ratios of these three components were measured, peak areas integrated and an over all measurements averaged correction factor determined depending on the detectability of the single lipids. Parameter uncertainties are estimated to be less than 5%. Lipid analysis for the isotopically asymmetric samples was conducted using GC/MS (for details see [2]) and for chemically asymmetric samples was performed by UPLC-MS. UPLC-MS measurements were conducted by using an AQUITY-UPLC system (Waters, Manchester, UK) equipped with a BEH-C18-column (2.1x150 mm, 1.7 $\mu$m) (Waters) was used for sample separation as previously described [3]. A binary gradient was applied. Solvent A consisted of water/methanol (1/1, v/v), solvent B was 2-propanol. Both solvents contained phosphoric acid (8 $\mu$M), ammonium acetate (10 mM) and formic acid (0.1 vol%). A SYNAPT$^{TM}$G1 qTOF HD mass spectrometer (Waters) equipped with an ESI source was used for analysis. Data acquisition was done by the MassLynx 4.1 software (Waters), for lipid analysis the 'Lipid Data Analyser' software [1] was used.

# 2 Evaluation of bilayer asymmetry via $^1$H-NMR

The evaluation of the bilayer asymmetry was presented in detail in [2]. In short, $^1$H-NMR spectra were collected on an Avance III 300 or 400 MHz spectrometer (Bruker, Billerica, MA) using the Bruker TopSpin acquisition software, and analyzed with TopSpin 3.2. The paramagnetic lanthanide ion $Pr^{3+}$ interacts with choline protons, shifting their resonance downfield as shown in [2]. By adding $Pr^{3+}$ to a vesicle suspension, the shift is selective for outer leaflet protiated choline, leading to a separate resolution of the protiated choline resonances from the inner and outer leaflet [5]. The integrated area $R$ of each resonance is proportional to the number of molecules having protiated headgroups in the corresponding leaflet. The outer leaflet peak fraction is defined as:

$$f^{out} = \frac{R^{out}}{R^{in} + R^{out}}, \tag{2}$$

where the superscripts 'out' and 'in' indicate the outer and inner leaflet. When all lipids posses protiated headgroups, $f^{out}$ directly yields the mole fraction of all bilayer lipids found in the outer leaflet:

$$X^{out} = \frac{\sum_j N_j^{out}}{\sum_j N_j} \equiv f^{out}, \tag{3}$$

where $N$ and $N^{out}$ denote the number of molecules in the whole bilayer and in the outer leaflet and the summation is performed over all components of the mixture. For a bilayer with an equal number of lipids in the leaflets $X^{out} = 0.5$. We assumed that $X^{out} = 0.53$ following [4] by assuming a vesicle size of 100 nm and a bilayer thickness of 50 Å. For a sample consisting of PC lipids the assay is selective for a single species provided all other components have a deuterated choline to silence their signal. If only one mixture component possesses a protiated choline we define the single-component outer leaflet peak fraction $f_i^{out}$ as:

$$f_i^{out} = \frac{N_i^{out}}{N_i} = \frac{X^{out}\chi_i^{out}}{\chi_i}, \tag{4}$$

where $\chi_i^{out}$ stands for the outer leaflet mole fraction of component $i$. Combining the two previous equations gives the following expression for the outer leaflet mole fraction of component $i$:

$$\chi_i^{out} = \frac{f_i^{out}\chi_i}{f^{out}}. \tag{5}$$

For a two component bilayer (e.g. lipid A and B), all compositional parameters $\chi_i^{out,in}$ can be expressed as:

$$
\begin{aligned}
\chi_A^{out} &= \frac{f_A^{out}\chi_A}{X^{out}} \\
\chi_A^{in} &= \frac{(1-f_A^{out})\chi_A}{(1-X^{out})}. \\
\chi_B^{in(out)} &= 1 - \chi_A^{in(out)}
\end{aligned}
\tag{6}
$$

# 3 Structural Data

Table S1: Structural parameters for symmetric POPC vesicles at $20\,^\circ$C obtained from the slab-model. Values in parenthesis are determined by setting $p_{CG}$ as a fit parameter. SANS data were previously published in [2] and are reanalyzed here.

| | Slab$_{SAXS}$ * | Slab$_{SANS}$ † | Slab$_{Joint}$ ‡ |
|---|---|---|---|
| V$_{lipid}$ [Å$^3$] | 1247 | 1247 | 1247 |
| V$_{head}$ [Å$^3$] | 331 | 331 | 331 |
| A$_L$ (Å$^2$) | 65.3 (67.6§) | 67.5 | 67.5 (67.5§) |
| n$_W$ | 8.4 (8.4§) | 7.9 | 9.9 (8.4§) |
| p$_{CG}$ | 1 (0.77§) | - | 1 (0.55§) |
| p$_M$ | 0.63 (0.54§) | - | 0.68 (0.46§) |
| $\chi^2_{red}$ | 1.1 (1.1§) | 94.5 | 54.2 (50.9§) |

* Analysis of SAXS data only.
† Analysis of different contrasts of SANS data only.
‡ Joint Analysis of SANS and SAXS data.
§ $p_{CG}$ was set as a fit parameter.

Table S2: Structural parameters of symmetric POPC vesicles 20 °C determined with the SDP-model. SANS data were previously published in [2] and are reanalyzed here.

| | SAXS * | Joint Analysis$_{SANS}$ † | Joint Analysis$_{SANS\&SAXS}$ ‡ |
|---|---|---|---|
| $V_{lipid}$§ [Å$^3$] | 1247 | 1247 | 1247 |
| $V_{head}$§ [Å$^3$] | 331 | 331 | 331 |
| $V_{PC}$§ [Å$^3$] | 191.98 | 191.98 | 191.98 |
| $V_{CG}$§ [Å$^3$] | 139.02 | 139.02 | 139.02 |
| $V_{MN}$§ [Å$^3$] | 811.37 | 811.37 | 811.37 |
| $V_{M}$§ [Å$^3$] | 104.63 | 104.63 | 104.63 |
| $A_L$ [Å$^2$] | 63.7 | 66.8 | 66.3 |
| $\sigma_{PC}$ | 2.60 | 2.68 | 2.62 |
| $\sigma_{CG}$ | 2.34 | 2.52 | 2.55 |
| $\sigma_M$§ | 2.02 | 2.02 | 2.02 |
| $\sigma_{MN}$ | 5.04 | 5.13 | 5.14 |
| $|z_{PC}|$ | 19.41 | 18.34 | 18.94 |
| $|z_{CG}|$ | 15.38 | 14.71 | 14.81 |
| $|z_M|$§ | 1.00 | 1.00 | 1.00 |
| $|z_{Mn}|$ | 14.38 | 13.71 | 13.81 |
| $\chi^2_{red}$ | 0.6 | 142.2 | 34.6 |

* Analysis of SAXS data only.
† Analysis of different contrasts of SANS data only.
‡ Joint analysis of SANS and SAXS data.
§ fixed parameter

Table S3: Leaflet composition of isotopic aLUVs determined by GC/MS and $^1$H-NMR. $\chi_i$ indicates the total bilayer mole fraction, $f_i^{out}$ (protiated) the fraction of a given component found in the outer leaflet and $\chi^{out}$ ($\chi^{in}$) represents the mole fraction of all components in outer and inner leaflet. Data were previously published in [2] and are reanalyzed here.

| Component | $\chi_i$ | $f^{out}$ | $\chi^{out}$ | $\chi_i^{in}$ | $\chi_i^{out}$ |
|---|---|---|---|---|---|
| POPC$^{acc}$ | 0.64* | 0.29† | 0.53‡ | 0.96 (0.45§) | 0.35 (0.19§) |
| POPC-d44$^{don}$ | 0.36* | | | 0.04 (0.02§) | 0.65 (0.34§) |
| Total | 1.00 | | | 1.00 (0.47§) | 1.00 (0.53§) |
| | | | | | |
| POPC-d44$^{acc}$ | 0.62* | | 0.53‡ | 0.83 (0.40§ ) | 0.43 (0.23§) |
| POPC$^{don}$ | 0.38* | 0.79† | | 0.17 (0.08§) | 0.57 (0.30§) |
| Total | 1.00 | | | 1.00 (0.47§) | 1.00 (0.53§) |

* from GC/MC
† from $^1$H-NMR
‡ calculated for 100 nm vesicles assuming 50 Å bilayer thickness
§ total bilayer mole fraction

Table S4: Structural parameters for isotopic asymmetric POPC LUVs at 20 °C obtained from the slab model. SANS data were previously published in [2] and are reanalyzed here.

| | SAXS* | Joint Analysis$_{SANS}$* | Joint Analysis$_{SANS\&SAXS}$* |
|---|---|---|---|
| $V_{lipid}$ [Å$^3$] | 1247 | 1247 | 1247 |
| $V_{head}$ [Å$^3$] | 331 | 331 | 331 |
| $A_L^{out}$ [Å$^2$] | 66.7 (65.3§) | 65.4 (64.6§) | 65.5 (63.8§) |
| $A_L^{in}$ [Å$^2$] | 66.7 (68.3§) | 65.4 (66.6§) | 65.5 (67.8§) |
| $n_{W_{out}}$ | 13 (12.6§) | 4.7 (2.3§) | 6.4 (4.6§) |
| $n_{W_{in}}$ | 7.0 (7.4§) | 4.6 (6.2§) | 6.4 (8.6§) |
| $p_{CG}$ | 1.0 (1.0§) | - | 1.0 (1.0§) |
| $p_M$ | 0.67 (0.67§) | - | 0.58 (0.58§) |
| $\chi_{red}^2$ | 1.34 (1.33§) | 16.3 (13.0§) | 7.0 (6.3§) |

* Analysis of SAXS data only (it cannot not be distsinguished between inner and outer leaflet by fit SAXS data only.)
† Analysis of different contrasts of SANS data only.
‡ Joint analysis of SANS and SAXS data.
§ Unconstrained ($A_L^{in}$ is allowed to exceed $A_L^{out}$ as well as $n_{w_{out}}$ can be smaller to $n_{w_{in}}$).

Table S5: Structural parameters obtained by SDP-analysis at $20\,^{\circ}$C for iso-topic aLUVs. SANS data were previously published in [2] and are reanalyzed here.

|  | SAXS[*] | Joint Analysis$_{SANS}$[†] | Joint Analysis$_{SANS\&SAXS}$[‡] |
|---|---|---|---|
| $V_{lipid}$[§] [$\text{Å}^3$] | 1247 | 1247 | 1247 |
| $V_{head}$[§] [$\text{Å}^3$] | 331 | 331 | 331 |
| $V_{PC}$[§] [$\text{Å}^3$] | 191.98 | 191.98 | 191.98 |
| $V_{CG}$[§] [$\text{Å}^3$] | 139.02 | 139.02 | 139.02 |
| $V_{MN}$[§] [$\text{Å}^3$] | 811.37 | 811.37 | 811.37 |
| $V_{M}$[§] [$\text{Å}^3$] | 104.63 | 104.63 | 104.63 |
| $A_{out}$ [$\text{Å}^2$] | 64.5 | 66.9 | 65.7 |
| $A_{in}$ [$\text{Å}^2$] | 63.2 | 63.5 | 63.4 |
| $\sigma_{PCin}$ | 2.655 | 2.59 | 2.70 |
| $\sigma_{PCout}$ | 2.5413 | 2.68 | 2.57 |
| $\sigma_{CGin}$ | 2.53 | 2.56 | 2.52 |
| $\sigma_{CGout}$ | 2.51 | 2.56 | 2.44 |
| $\sigma_{M}$[§] | 2.02 | 2.02 | 2.02 |
| $\sigma_{MN}$ | 5.14 | 5.08 | 5.04 |
| $|z_{PCin}|$ | 18.77 | 20.09 | 19.10 |
| $|z_{PCout}|$ | 19.58 | 19.14 | 19.87 |
| $|z_{CGin}|$ | 15.49 | 15.43 | 15.44 |
| $|z_{CGout}|$ | 15.20 | 14.69 | 14.94 |
| $|z_{M}|$[§] | 1.00 | 1.00 | 1.00 |
| $|z_{MNin}|$ | 14.49 | 14.43 | 14.44 |
| $|z_{MNout}|$ | 14.20 | 13.69 | 13.94 |
| $\chi^2_{red}$ | 4.5 | 8.7 | 6.6 |

[*] Analysis of SAXS data only.
[†] Analysis of different contrasts of SANS data only.
[‡] Joint analysis of SANS and SAXS data.
[§] fixed parameter

6
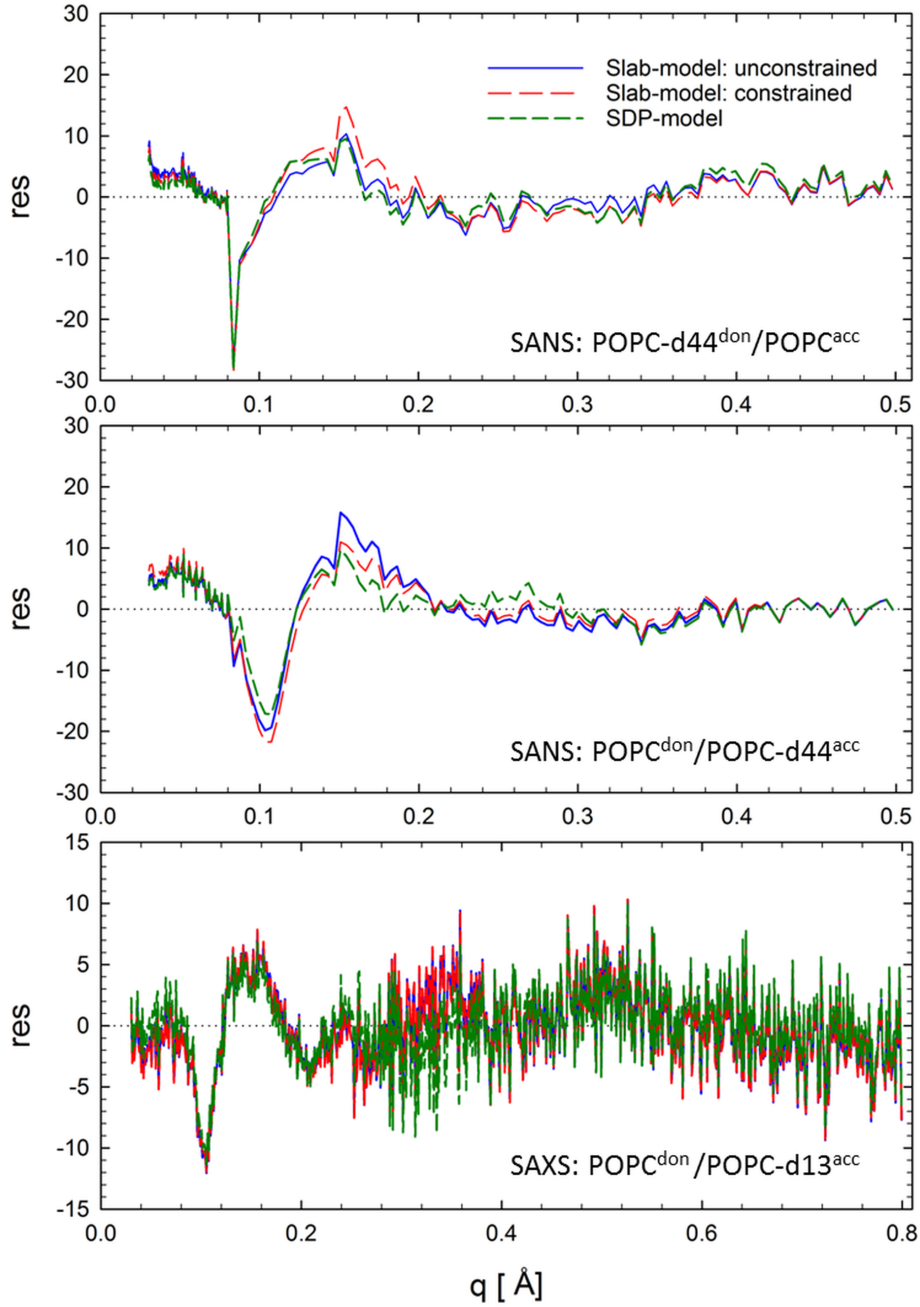
Figure S1: Residuals of isotropic aLUVs obtained by either applying the slab model without constraints (blue line), constraining the fit to $n_W^{in} < n_W^{out}$ and $A_L^{in} < A_L^{out}$ (red dashed line) or applying the SDP-model (green short-dashed line) for POPC-d44$^{don}$/POPC$^{acc}$ (top panel), POPC$^{don}$/POPC-d44$_{acc}$ (middle panel) and for SAXS experiments (lower panel). It can be seen that the difference in residuals of the constrained and unconstrained fits cannot be distinguished. SANS data were previously published in [2] and are reanalyzed here.

Table S6: Leaflet composition of chemical aLUVs determined by UPLC-MS and $^1$H-NMR. $\chi_i^{out}$ ($\chi_i^{in}$) indicates the mole fraction of all components in outer and inner leaflet.

|  | Component | $\chi_i$ | $\chi^{out}$ | $\chi_i^{in}$ | $\chi_i^{out}$ |
|---|---|---|---|---|---|
| SANS | POPC-d13 (acceptor) | 0.72* | 0.53‡ | 0.92 (0.43§) | 0.57 (0.29§) |
| | DPPC-d64 (donor) | 0.28* | | 0.08 (0.04) | 0.43 (0.24) |
| | Total | 1.00 | | 1.00 | 1.00 |
| SANS | POPC-d13 (acceptor) | 0.74* | 0.53‡ | 0.85 (0.40§) | 0.65 (0.34§) |
| | DPPC (donor) | 0.26* | | 0.15 (0.07§) | 0.35 (0.19§) |
| | Total | 1.00 | | 1.00 | 1.00 |
| SAXS | POPC-d13 (acceptor) | 0.73* | 0.53‡ | 0.91 (0.43§) | 0.57 (0.30§) |
| | DPPC (donor) | 0.27* | | 0.09 (0.04§) | 0.43 (0.23§) |
| | Total | 1.00 | | 1.00 | 1.00 |

* from UPLC
‡ calculated for 100 nm vesicles assuming 50 Å bilayer thickness
§ total bilayer mole fraction

Table S7: Structural parameters of chemical DPPC/POPC aLUVs obtained by the slab model at 50 °C.

| | SAXS* | | Joint Analysis$_{SANS}$† | | Joint Analysis$_{SANS\&SAXS}$‡ | |
|---|---|---|---|---|---|---|
| | DPPC | POPC | DPPC | POPC | DPPC | POPC |
| $V_{lipid}$§ [Å$^3$] | 1228.5 | 1275.5 | 1228.5 | 1275.5 | 1228.5 | 1275.5 |
| $V_{head}$§ [Å$^3$] | 331 | 331 | 331 | 331 | 331 | 331 |
| $A_L$ [Å$^2$] | 64.9 | 69.7 | 61.7 | 65.7 | 61.7 | 68.7 |
| $n_W$ | 6.6 | 6.6 | 7.2 | 7.2 | 4.7 | 4.3 |
| $p_{CG}$§ | 1.00 | | - | | 1.00 | |
| $p_M$ | 0.54 | | - | | 0.49 | |
| $\chi_{red}^2$ | 31.1 | | 323.5 | | 137.8 | |

* Analysis of SAXS data only.
† Analysis of different contrasts of SANS data only.
‡ Joint analysis of SANS and SAXS data.
§ fixed parameter

Table S8: Structural parameter of scrambled DPPC/POPC LUVs determined by the slab model at $50\,^{\circ}$C.

| | SAXS[*] | | Joint Analysis$_{SANS}$[†] | | Joint Analysis$_{SANS\&SAXS}$[‡] | |
|---|---|---|---|---|---|---|
| | DPPC | POPC | DPPC | POPC | DPPC | POPC |
| $V_{lipid}$[§] [Å$^3$] | 1228.5 | 1275.5 | 1228.5 | 1275.5 | 1228.5 | 1275.5 |
| $V_{head}$[§] [Å$^3$] | 331 | 331 | 331 | 331 | 331 | 331 |
| $A_L$ [Å$^2$] | 63.4 | 68.4 | 64.9 | 66.5 | 64.9 | 67.8 |
| $n_W$ | 5.3 | 4.9 | 3.2 | 3.2 | 5.0 | 5.0 |
| $p_{CG}$[§] | 1.00 | | - | | 1.00 | |
| $p_M$ | 0.51 | | - | | 0.51 | |
| $\chi^2_{red}$ | 13.0 | | 241.1 | | 45.1 | |

[*] Analysis of SAXS data only.

[†] Analysis of different contrasts of SANS data only.

[‡] Joint analysis of SANS and SAXS data.

[§] fixed parameter

9

Table S9: Structural parameters of chemical aLUVs determined by the SDP model at 50 °C.

| | SAXS[*] | | Joint Analysis$_{SANS}$[†] | | Joint Analysis$_{SANS\&SAXS}$[‡] | |
|---|---|---|---|---|---|---|
| | DPPC | POPC | DPPC | POPC | DPPC | POPC |
| $V_{lipid}$[§] [Å$^3$] | 1228.5 | 1275.5 | 1228.5 | 1275.5 | 1228.5 | 1275.5 |
| $V_{head}$[§] [Å$^3$] | 331 | 331 | 331 | 331 | 331 | 331 |
| $V_{PC}$[§] [Å$^3$] | 191.98 | 191.98 | 191.98 | 191.98 | 191.98 | 191.98 |
| $V_{CG}$[§] [Å$^3$] | 139.02 | 139.02 | 139.02 | 139.02 | 139.02 | 139.02 |
| $V_{MN}$[§] [Å$^3$] | 787.77 | 835.54 | 787.77 | 835.54 | 787.77 | 835.54 |
| $V_{M}$[§] [Å$^3$] | 109.73 | 108.54 | 109.73 | 108.54 | 109.73 | 108.54 |
| $A_L$ [Å$^2$] | 62.2 | 64.9 | 62.2 | 66.6 | 62.6 | 67.9 |
| $\sigma_{PC}$ | 2.37 | 4.37 | 2.37 | 2.65 | 2.34 | 2.61 |
| $\sigma_{CG}$ | 2.18 | 2.38 | 2.21 | 2.50 | 2.09 | 2.55 |
| $\sigma_{M}$[§] | 2.38 | 2.02 | 2.38 | 2.02 | 2.38 | 2.02 |
| $\sigma_{MN}$ | 5.68 | 5.20 | 5.54 | 5.13 | 5.43 | 5.13 |
| $|z_{PC}|$ | 19.18 | 16.64 | 19.97 | 19.41 | 19.71 | 17.12 |
| $|z_{CG}|$ | 15.42 | 15.56 | 15.42 | 15.16 | 15.33 | 14.91 |
| $|z_{M}|$[§] | 1.00 | 1.00 | 1.00 | 1.00 | 1.00 | 1.00 |
| $|z_{MN}|$ | 14.42 | 14.56 | 14.42 | 14.16 | 14.33 | 13.91 |
| $\chi^2_{red}$ | 4.2 | | 303.1 | | 141.3 | |

[*] Analysis of SAXS data only.

[†] Analysis of different contrasts of SANS data only.

[‡] Joint analysis of SANS and SAXS data.

[§] fixed parameter

10

Table S10: Structural parameters of scrambled DPPC/POPC LUVs determined by the SDP model at 50 °C.

| | SAXS[*] | | Joint Analysis$_{SANS}$[†] | | Joint Analysis$_{SANS\&SAXS}$[‡] | |
|---|---|---|---|---|---|---|
| | DPPC | POPC | DPPC | POPC | DPPC | POPC |
| V$_{lipid}$[§] [Å$^3$] | 1228.5 | 1275.5 | 1228.5 | 1275.5 | 1228.5 | 1275.5 |
| V$_{head}$[§] [Å$^3$] | 331 | 331 | 331 | 331 | 331 | 331 |
| V$_{PC}$[§] [Å$^3$] | 191.98 | 191.98 | 191.98 | 191.98 | 191.98 | 191.98 |
| V$_{CG}$[§] [Å$^3$] | 139.02 | 139.02 | 139.02 | 139.02 | 139.02 | 139.02 |
| V$_{MN}$[§] [Å$^3$] | 787.77 | 835.54 | 787.77 | 835.54 | 787.77 | 835.54 |
| V$_M$[§] [Å$^3$] | 109.73 | 108.54 | 109.73 | 108.54 | 109.73 | 108.54 |
| A$_L$ [Å$^2$] | 63.3 | 69.3 | 63.4 | 68.2 | 64.4 | 69.1 |
| $\sigma_{PC}$PC | 2.26 | 3.01 | 2.26 | 2.67 | 2.40 | 2.70 |
| $\sigma_{CG}$ | 2.25 | 2.63 | 2.21 | 2.52 | 2.22 | 2.54 |
| $\sigma_M$[§] | 2.38 | 2.02 | 2.38 | 2.02 | 2.38 | 2.02 |
| $\sigma_{MN}$ | 5.47 | 5.08 | 5.72 | 6.38 | 5.56 | 5.16 |
| $|z_{PC}|$ | 19.62 | 17.79 | 20.24 | 19.41 | 19.32 | 17.64 |
| $|z_{CG}|$ | 15.19 | 14.60 | 15.20 | 14.90 | 14.94 | 14.64 |
| $|z_M|$[§] | 1.00 | 1.00 | 1.00 | 1.00 | 1.00 | 1.00 |
| $|z_{MN}|$ | 14.19 | 13.60 | 14.20 | 13.90 | 13.94 | 13.67 |
| $\chi^2_{red}$ | | 1.09 | | 61.4 | | 18.7 |

[*] Analysis of SAXS data only.

[†] Analysis of different contrasts of SANS data only.

[‡] Joint analysis of SANS and SAXS data.

[§] fixed parameter

11

Table S11: Structural parameter of chemical aLUVs and scrambled LUVs for the outer/inner leaflet determined from values obtained in table S7,S8,S9, S10.

| Model | Components | $d_{Co}$ [Å] | $d_{Ci}$ [Å] | $d_B$ [Å] | $A_L^{out}$ [Å$^2$] | $A_L^{in}$ [Å$^2$] |
|---|---|---|---|---|---|---|
| | SANS$_1$* | 14.11 | 13.81 | 37.74 | 66.5 | 68.1 |
| AsymSlab$_{Joint}$ | SANS$_2$† | 14.03 | 13.87 | 37.79 | 66.2 | 67.6 |
| | SAXS$_1$‡ | 14.09 | 13.82 | 37.82 | 65.6 | 68.1 |
| | SANS$_1$* | 14.09 | 14.01 | 38.09 | 65.5 | 67.1 |
| AsymSDP$_{Joint}$ | SANS$_2$† | 14.05 | 13.97 | 37.96 | 66.0 | 67.1 |
| | SAXS$_1$‡ | 14.09 | 13.94 | 37.98 | 65.6 | 67.4 |
| | SANS$_1$* | 13.90 | 13.90 | 37.68 | 67.0 | 67.0 |
| ScramSlab$_{Joint}$ | SANS$_2$† | 13.90 | 13.90 | 37.68 | 67.1 | 67.1 |
| | SAXS$_1$‡ | 13.90 | 13.90 | 37.68 | 67.1 | 67.1 |
| | SANS$_1$* | 13.91 | 13.91 | 37.26 | 67.8 | 67.8 |
| ScramSDP$_{Joint}$ | SANS$_2$† | 13.91 | 13.91 | 37.22 | 67.9 | 67.9 |
| | SAXS$_1$‡ | 13.90 | 13.90 | 37.25 | 67.8 | 67.8 |

* DPPC-d64$^{don}$/POPC-d13$^{acc}$ (SANS)
† DPPC$^{don}$/POPC-d13$^{acc}$ (SANS)
‡ DPPC$^{don}$/POPC-d13$^{acc}$ (SAXS)
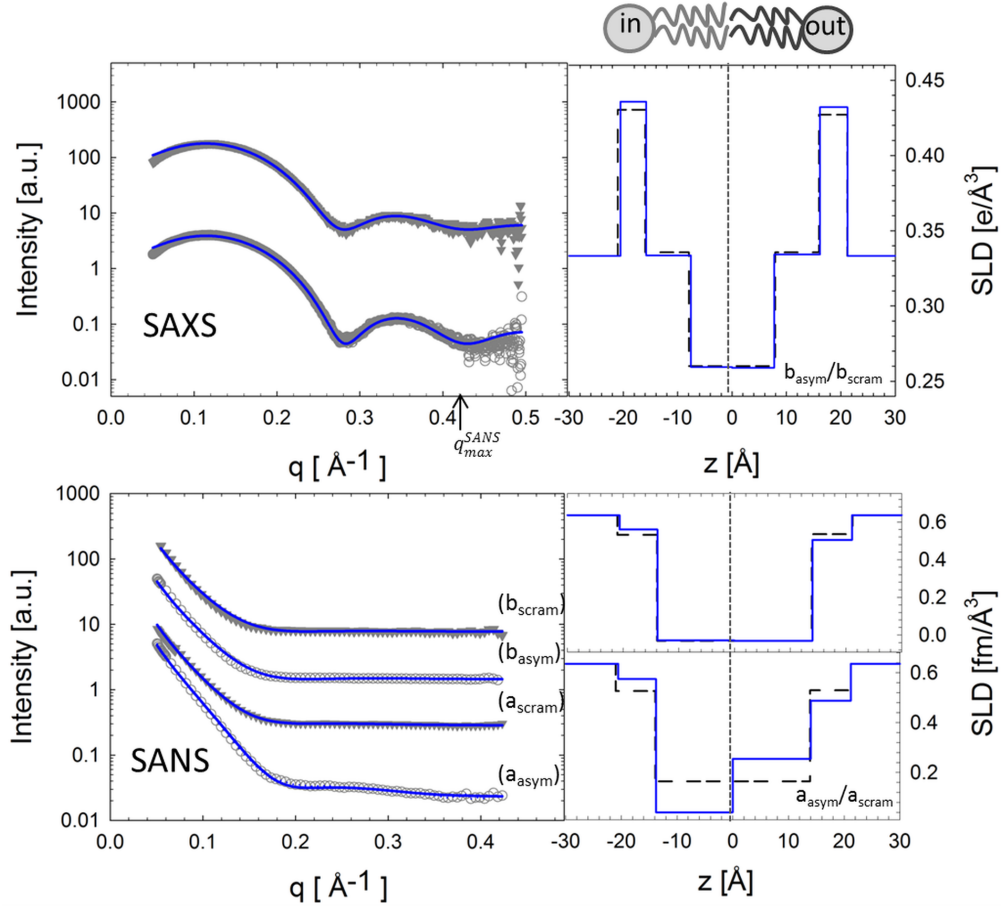
Figure S2: Slab analysis (blue lines) of DPPC$^{don}$/POPC$^{acc}$ aLUVs (open circles) and scrambled LUVs (filled triangles). Panels on the right show the corresponding SLDs (blue: aLUVs; dashed: scrambled LUVs). The different contrast samples for SANS experiments were DPPC-d62$^{don}$/POPC-d13$^{acc}$ (a$_{asym}$/a$_{scram}$) and DPPC$^{don}$/POPC-d13$^{acc}$ (b$_{asym}$/b$_{scram}$). Data were offset vertically for clarity.
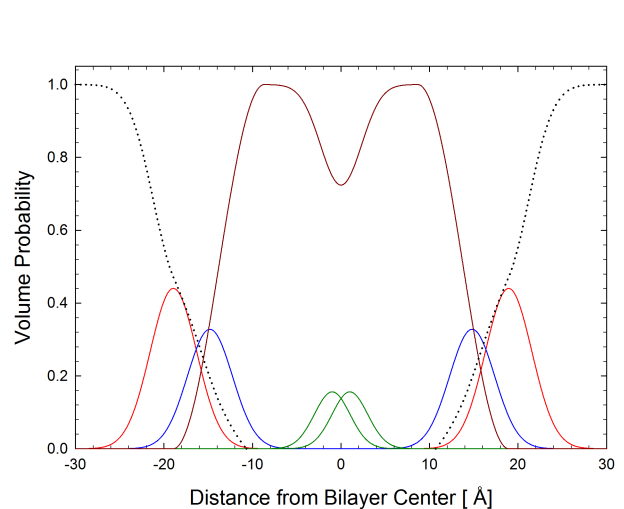
Figure S3: SDP analysis of POPC-LUVs measured at 20 °C, showing the volume probability distribution of the joint ananylsis of SANS and SAXS data.
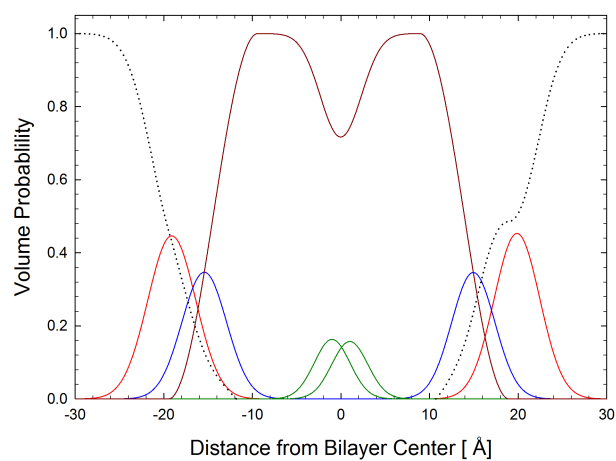


Figure S4: SDP analysis of POPC-aLUVs measured at 20 °C, showing the volume probability distribution of the joint ananylsis of SANS and SAXS data.
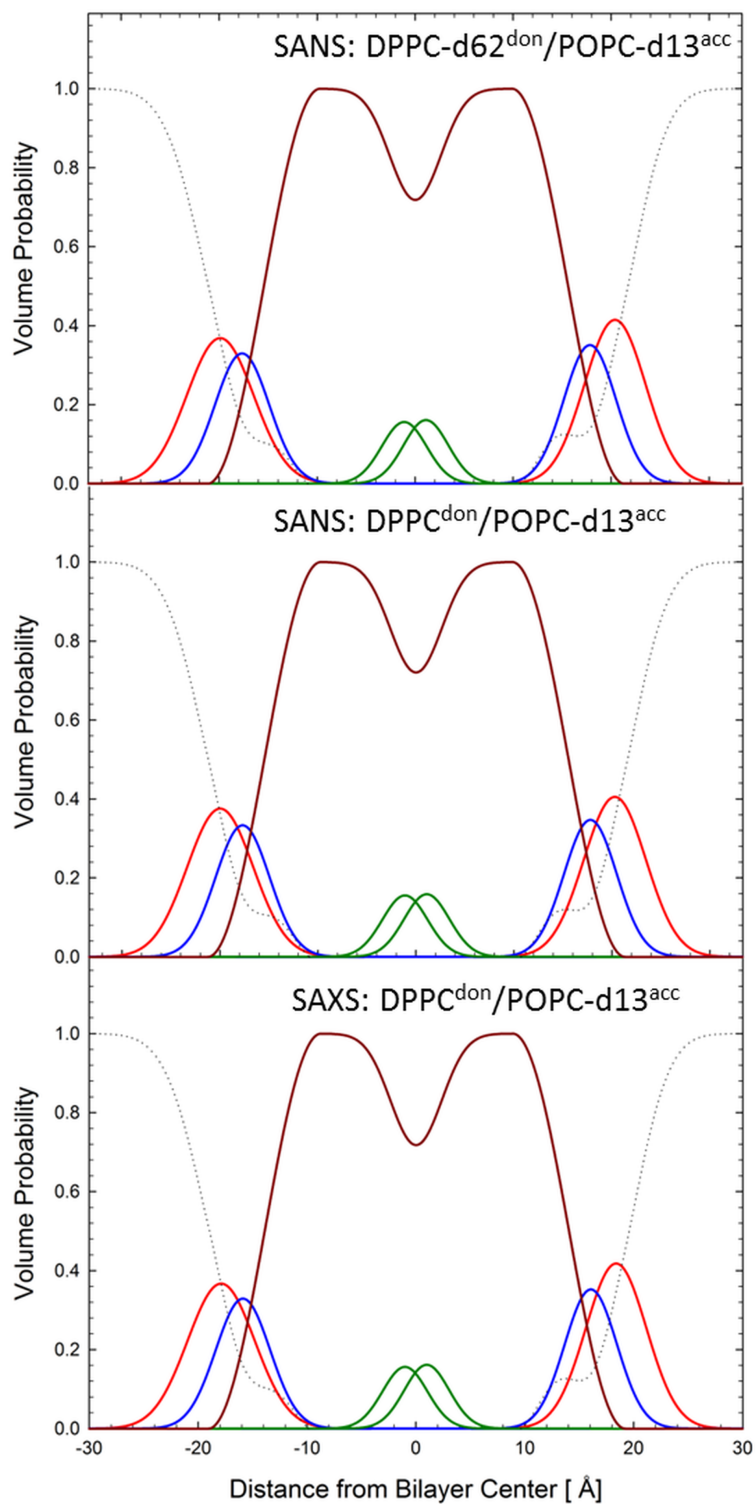
Figure S5: SDP analysis of chemical-aLUVs measured at 50 °C, showing the volume probability distribution of the joint analysis of the structure of DPPC/POPC for different conrasts (upper two panels for SANS measurements, lower panel SAXS) which show a slightly different exchange efficiency.
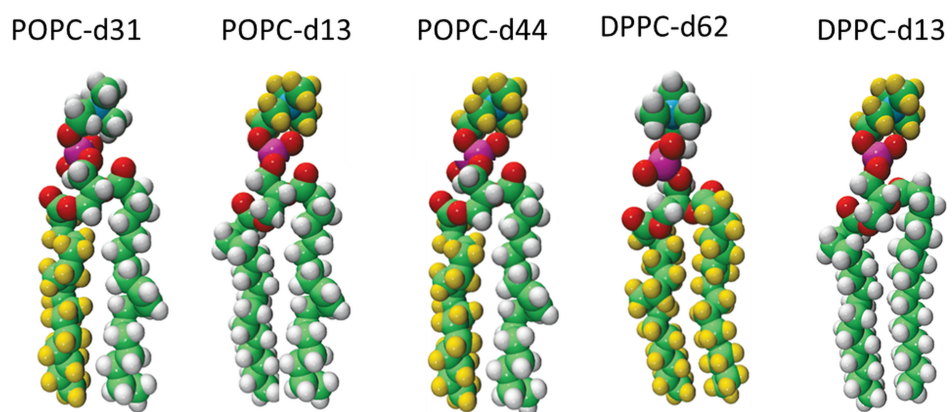
Figure S6: Chemical structures of deuterated phospholipids. Lipids are displayed in space fill representation: white indicating hydrogen and yellow deuterium.

# References

[1] Jürgen Hartler, Martin Trötzmüller, Chandramohan Chitraju, Friedrich Spener, Harald C Köfeler, and Gerhard G Thallinger. Lipid data analyzer: unattended identification and quantitation of lipids in lc-ms data. *Bioinformatics*, 27(4):572–577, 2011.

[2] Frederick A Heberle, Drew Marquardt, Milka Doktorova, Barbara Geier, Robert F Standaert, Peter Heftberger, Benjamin Kollmitzer, Jonathan D Nickels, Robert A Dick, Gerald W Feigenson, et al. Sub-nanometer structure of an asymmetric model membrane: Interleaflet coupling influences domain properties. *Langmuir*, 32(20):5195–5200, 2016.

[3] Oskar L Knittelfelder, Bernd P Weberhofer, Thomas O Eichmann, Sepp D Kohlwein, and Gerald N Rechberger. A versatile ultra-high performance lc-ms method for lipid profiling. *Journal of Chromatography B*, 951:119–128, 2014.

[4] Drew Marquardt, Barbara Geier, and Georg Pabst. Asymmetric lipid membranes: Towards more realistic model systems. *Membranes*, 5(2):180–196, 2015.

[5] B. Perly, I. C. P. Smith, L. Hughes, G. W. Burton, and K. U. Ingold. Estimation of the location of natural $\alpha$-tocopherol in lipid bilayers by 13c-nmr spectroscopy. *Biochimica et Biophysica Acta (BBA) - Biomembranes*, 819(1):131–135, 9/25 1985.

# Instrinsic Curvature-Mediated Transbilayer Coupling in Asymmetric Lipid Vesicles

Barbara Eicher[†,‡], Drew Marquardt[∓], Frederick A. Heberle[±,⋆,°],
Ilse Letofsky-Papst[§,∩], Gerald N. Rechberger[∨,×], Marie-Sousai
Appavou[∪], John Katsaras[±], and Georg Pabst[†,‡] [*]

[†]   *University of Graz, Institute of Molecular Biosciences, Biophysics Division,
NAWI Graz, Humboldstr. 50/III, A-8010 Graz, Austria.*

[‡]   *BioTechMed-Graz, Austria.*

[∓] *Department of Chemistry and Biochemistry, University of Windsor, Windsor,
ON, Canada.*

[±]*Joint Institute for Biological Sciences, Oak Ridge National Laboratory, Oak Ridge,
TN, USA.*

[⋆] *The Bredesen Center for Interdisciplinary Research and Graduate Education,
University of Tennessee, Knoxville, TN, USA.*

[°] *Biology and Soft Matter Division, Oak Ridge National Laboratory, Oak Ridge,
TN, USA.*

[§]   *Institute for Electron Microscopy and Nanoanalysis, Graz University of Technology, 8010 Graz, Austria*

[∩] *Graz Center for Electron Microscopy, 8010 Graz, Austria.*

<sup>∨</sup> *Instiute of Molecular Biosciences, University of Graz, Austria.*

<sup>×</sup> *Omics-Center, BioTechMed-Graz.*

<sup>∪</sup>*Jülich Centre for Neutron Science (JCNS) at Heinz Maier-Leibnitz Zentrum (MLZ), Forschungszentrum Jülich GmbH, Lichtenbergstr. 1, 85748 Garching, Germany.*

<sup>*</sup> Correspondence: georg.pabst@uni-graz.at

## Abstract

We measured the effect of intrinsic lipid curvature, $J_0$, on structural properties of asymmetric vesicles, with palmitoyl-oleoyl-phosphatidylethanolamine (POPE; $J_0 < 0$), or palmitoyl-oleoyl-phosphatidylcholine ($J_0 \sim 0$) enrichment in outer or inner leaflets. Electron microscopy and dynamic light scattering were applied for determining vesicle size and morphology, while X-ray and neutron scattering combined with calorimetric experiments and solution NMR yielded insight on leaflet-specific lipid packing and melting processes. Below the melting temperature we observed strong interleaflet coupling for asymmetric vesicles with an inner leaflet enriched in POPE, only, which was expressed in a synchronous melting and a mutual adjustment of lipid packing in both monolayers, respectively. No coupling was observed in vesicles with reversed lipid asymmetry. In this case the leaflets melted independently and did not affect each other's intrinsic structure. Furthermore, we found no evidence for transbilayer structural coupling the above the melting temperature regardless of the leaflet distribution of POPE. Our results are consistent with an energetically preferred location of POPE on the inner side of the lipid bilayer also found in natural membranes leading to a coupling of inner and outer leaflets. The loss of this mechanism in the fluid phase is most likely due to entropic contributions.

*Key words: leaflet-specific membrane structure; lipid asymmetry; phase separation; transbilayer coupling*

# Introduction

Lipid asymmetry is a hallmark of biological membranes (1, 2). In particular, prototypical mammalian plasma membranes are conceived to be composed of an outer leaflet enriched in high-melting lipids, such as sphingomyelin (SM) and phosphatidylcholine (PC), while phosphatidylserine (PS) and phosphatidylethanolamine (PE) lipids are thought to be predominantly located in the inner leaflet (3, 4). The preferred leaflet partitioning of the most abundant lipid of mammalian plasma membranes, cholesterol, is matter of dispute, however (5, 6).

One of the enduring questions related to plasma membrane architecture and lipid asymmetry concerns the potential functional coupling of one leaflet to the other, which may influence diverse physiological processes that require communication between e.g. receptors secreted to the extracellular side of membranes and components of signal transduction pathways located in the cytoplasm (7). It is particularly intriguing that the lipid composition of the outer leaflet favors the formation of raft-like domains (8, 9), while lipids found in inner leaflets do not phase separate (10). Theoretical treatments have considered coupling originating from intrinsic lipid curvature (11, 12), headgroup electrostatics, cholesterol flip-flop, dynamic chain interdigitation (13, 14) or thermal membrane fluctuations (15) showing that interleaflet coupling does not necessitate (but at the same time does not exclude) contributions from protein components.

First experimental insight on transbilayer domain coupling has been obtained in planar bilayers about a decade ago, showing that a phase separating lipid mixture in one leaflet may indeed induce ordering and domains in the other (16–18). Furthermore, the strength of coupling increased with chain melting temperature

of lipids in the distal leaflet (17), a finding which was also reproduced in molecular dynamics (MD) simulations (19). A different MD study, using coarse-grained lipids, found that transbilayer coupling affects rotational and lateral lipid diffusion dynamics (20).

In symmetric solid supported membranes with coexisting fluid lipid domains, a significant threshold for shear stress was reported for moving like domains out of register, indicating strong transbilayer coupling of the domains (21), although no dependence on the hydrocarbon length was observed in similar experiments (22), suggesting that dynamic (partial) chain interdigidation does not provide a significant contribution to interleaflet coupling. Other reports on solid supported asymmetric bilayers did not find domain registration (23, 24). However, this might be at least partially related to subtleties in preparing planar membranes that can lead to a rapid loss of asymmetry (25, 26). Hence, free-floating lipid vesicles, which exhibit slow lipid flip-flop (27) and can be engineered reliably with lipid asymmetry (28, 29), appear to be amenable systems for studying transbilayer coupling mechanisms.

Asymmetric lipid vesicles enriched in SM in the outer monolayer and with inner leaflets composed of monounsaturated PC, PS, disaturated PC and PS/PE mixtures showed independent melting of both leaflets (28, 30). At the same time, increased order of the inner fluid monolayer in the presence of a gel outer leaflet indicated weak coupling, however (30). For asymmetric vesicles of mixed chain lipids in one leaflet a slowing down of lateral diffusion in the other leaflet was reported due to partial chain interdigitation (31). Interestingly, this did not affect overall lipid order.

Recently, we performed small-angle neutron and X-ray scattering (SANS, SAXS) experiments on asymmetric vesicles composed of PCs, and observed significant effects on lipid packing in outer leaflet gel domains enriched in dipalmitoyl-phosphatidylcholine (DPPC) originating from fluid inner leaflet palmitoyl-oleoyl-phosphatidylcholine (POPC) (29). This effect vanished, however, when both leafs were in the fluid phase (32).

The present work focuses on the 'sidedness' of transmembrane coupling in asymmetric large unilamellar vesicles (aLUVs). In particular, we engineered aLUVs composed of POPC and palmitoyl-oleoyl-phosphatidylethanolamine (POPE) with either $POPC^{out}/POPE^{in}$, or $POPE^{out}/POPC^{in}$ asymmetry, where superscripts 'in', 'out' refer to the inner and outer leaflet, respectively. Combing a series of experiments, including SAXS, SANS, wide-angle X-ray scattering (WAXS), differential scanning calorimetry (DSC), dynamic light scattering (DLS) and cryo-transmission electron microscopy (TEM) we observed strongly coupled leaflets when POPE was enriched in the inner monolayer, only. This was expressed by a synchronous melting of both leaflets and a mutual alignment of the lipid packing densities in each leaflet. In turn, aLUVs with reversed asymmetry (i.e. POPE enriched in the outer leaflet) exhibited a largely decoupled melting of the two monolayers. This provides evidence for an intrinsic curvature-mediated mechanism that energetically favors POPE, which has a significant negative intrinsic curvature, to be located on the inner leaflet. Further, we find no evidence for transbilayer coupling in the fluid phase, independent of POPE sidedness, indicating that the loss of coupling is most likely due to entropic contributions and that neither intrinsic curvature nor partial chain interdigiation are of significance in

this case.

# Materials and Methods

## Sample Preparation

POPC, POPE and palmitoyl phosphatidylglycerol (POPG), as well as chain perdeuterated POPE-d31 and POPG-d31 were obtained from Avanti Polar Lipids (Alabaster, AL, USA) and used without further purification. $D_2O$ was purchased from Euroiso-top (Saarbrücken, Germany) and methyl-$\beta$-cyclodextrin (m$\beta$CD) from Sigma-Aldrich (Vienna, Austria), while purified water ($18\,M\Omega/cm$) was obtained from Purelab UHQ, Elga. Lipid stock solutions were prepared by dissolving weighed amounts of dry lipid powder in chloroform and assayed for lipid concentration to within 1% uncertainty using standard procedures (33). Appropriate volumes were taken from the stocks, dried under a stream of nitrogen and finally placed into vacuum for at least 12 hours to remove residual organic solvent.

Engineering of aLUVs followed the previously established protocol involving CD-mediated lipid exchange between acceptor and donor vesicles (29). Specifically, acceptor vesicles were prepared in $25\,mM$ NaCl solution to a lipid concentration of $10\,mg/mL$. All acceptor vesicles were doped with $10\,mol\%$ POPG or POPG-d31 matching the isotopic composition of the inner leaflet hydrocarbons. Doping vesicles with PG facilitates LUV formation (see below). Throughout the present work we report POPE/POPC* molar ratios, only, where the asterisk indicates the presence of POPG. During hydration, samples were incubated for one hour at least 10℃ above the lipid's melting transition ($T_M$) with intermittent

vortex mixing, followed by 5 freeze/thaw cycles of the hydrated vesicles using liquid nitrogen. Finally, LUVs were obtained by passing the lipid dispersions 31 times ($T > T_M + 10$℃) through 100 nm pore-diameter polycarbonate filters using a hand-held mini-extruder (Avanti Polar Lipids, Alabaster, AL, USA). In turn, donor vesicles (composed of the outer leaflet lipids) were prepared in the form of multilamellar vesicles (MLVs) by hydrating the dry films in 20% (w/w) aqueous sucrose solution at a lipid concentration of 20 mg/mL, followed by an 1-hour incubation at $T > T_M + 10$℃, with intermittent vortex mixing, and 3 freeze/thaw cycles. Finally, donor MLVs were diluted by a factor of 20 with water and centrifuged for 30 min at 20,000 $\times g$ to remove extravesicular sucrose.

Lipid exchange was initiated by re-suspending the pellet containing donor vesicles in 35 mM m$\beta$CD (lipid:m$\beta$CD = 1:8) followed by a 2 h incubation at room temperature while being gently stirred. Next, acceptor LUVs were added to the m$\beta$CD/donor solution and again gently stirred for 30 min ($T > T_M + 10$℃ for POPE acceptor vesicles and $T$ = room temperature for POPC acceptor vesicles). Two different donor/acceptor molar ratios (D/A = 2 and D/A = 3) were applied yielding different lipid exchange (see below). Dispersions containing the final aLUVs were diluted by a factor of seven with water and centrifuged at 20,000 $\times g$ for 30 min. The supernatant (containing aLUVs, residual CD and sucrose) was removed carefully and concentrated with a centrifugal ultrafiltration device (100 kDa cutoff) to <0.5 mL. Finally, sucrose and CD were removed by repeated washing in either $D_2O$ for ^{1}H-NMR and SANS experiments, or in $H_2O$ for all other experiments.

For control experiments on vesicles with the same, but symmetric lipid com-

position, aLUVs were dried down to a film under reduced atmospheric pressure using a rotary evaporator (Heidolph, Germany) with the water bath set to 40℃. The dried lipid film was redissolved in chloroform and from that point on prepared as acceptor vesicles including the extrusion step. The resulting LUVs are called 'scrambled' vesicles throughout the present report. Further, we prepared symmetric LUVs with known POPE/POPC* composition for DSC and WAXS calibration experiments (see below) by mixing appropriate amounts of organic lipid stock solution. The protocol for obtaining LUVs from these samples was identical to that applied for acceptor vesicles.

## Exchange efficiency and lipid distribution

### Differential scanning calorimetry (DSC)

DSC experiments were performed on a MicroCal VP-DSC high sensitivity differential scanning calorimeter (MicroCal, Inc., Northhampton, MA, USA) at a scan rate of 30℃/h and used to (i) to determine the total lipid exchange achieved and (ii) to measure the thermotropic behavior of the aLUVs. Data were corrected for sample concentration and background was subtracted by using a linear baseline using MicroCal Origin.

Symmetric LUVs prepared at various POPE/POPC* molar ratios showed thermograms typical for binary lipid mixtures with a liquidus peak at $T_M$ and a solidus peak that became more prominent upon increasing POPC concentration (Fig. 1). Note that doping POPE with 10 mol% POPG lowers the $T_M$ by about 1.0℃ (34). Throughout the present work only cooling scans were considered. Further, the lowest POPE fraction $\chi_{POPE}$ measured was 0.3. Both decisions were motivated
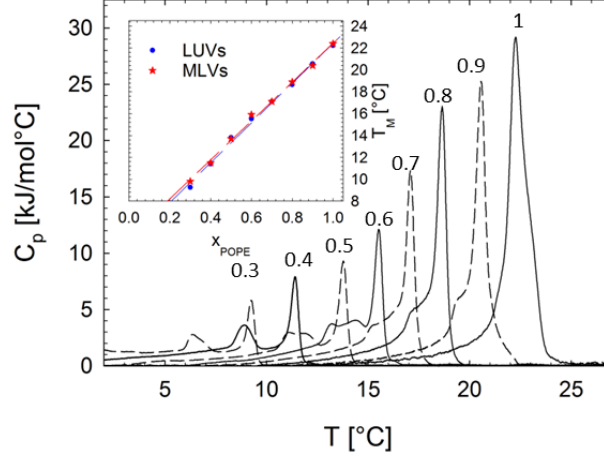
Figure 1: DSC cooling thermograms of POPE/POPC* mixtures. Numbers adjacent to heat capacity ($c_P$) maxima indicate the given $\chi_{POPE}$. The inset shows the concentration dependence of the $T_M$'s of LUVS and MLVs, which serve as control (supplementary Fig. S5).

by the low melting transition of POPC ($\sim -3.5$℃ (35)) and instrumental limitations, which did not allow us to measure below 2℃. This would lead to artifacts in heating scans due to the inability to equilibrate the system at low temperatures. Due to hysteresis effects cooling scans report a $T_M$ that is about 1.2 - 2.0℃ lower than for heating scans. The presented analysis was performed on the second cooling scan of each sample.

The obtained $T_M$'s were found to increase linearly with POPE concentration in the studied compositional range ($T_M = a_0 + a_1\chi_{POPE}$), with $a_0 = 4.2\pm0.5$℃ and $a_1 = 18.2\pm 0.2$℃ (Fig. 1, inset). This allowed us to determine lipid exchange from DSC data of scrambled LUVs.

## Ultra performance liquid chromatography - mass spectrometry (UPLC-MS)

Alternatively, lipid exchange was determined by ultra performance liquid chromatography - tandem mass spectrometry (UPLC-MS) as described previously (32). UPLC-MS measurements were conducted with an AQUITY-UPLC system (Waters, Manchester, UK) equipped with a BEH-C18-column (2.1x150 mm, 1.7 $\mu$m) (Waters) was used for sample separation (36). A SYNAPT$^{TM}$G1 qTOF HD mass spectrometer (Waters) equipped with an ESI source was used for analysis. Data acquisition was done by the MassLynx 4.1 software (Waters), for lipid analysis the 'Lipid Data Analyser' software (37) was used. For UPLC-MS the mole fraction $\chi_i$ of a single component can be determined directly using

$$\chi_i = \frac{P_i}{\sum_i P_i},\qquad(1)$$

where $P_i$ is the area of the i$^{th}$ lipid peak. This relationship is strictly valid when the lipid peak area fractions vary linearly with mixture composition. UPLC-MS data was corrected by a calibration curve of 1:1:1 mole ratio of POPE/POPC/POPG composition measured at concentrations varying between 0.1-100 $\mu$g. Parameter uncertainties are estimated to be less than 5%.

## Solution Nuclear Magnetic Resonance ($^1$H-NMR)

$^1$H-NMR was used to determine the degree of asymmetry following previous protocols (29). Briefly, $^1$H-NMR spectra were collected on an Avance III 300 or 400 MHz spectrometers (Bruker, Billerica, MA) using the Bruker TopSpin acquisition

software, and processed with TopSpin 3.2. A standard $^1$H pulse sequence with a 30° flip angle and 2 s delay time was used to collect 32 transients at 35°C or 50°C. Data were processed with a line-broadening parameter of 2 Hz.

The outer leaflet fraction of POPC $f_{PC}^{out}$ relative to the inner leaflet was determined by quantifying the shifted and not-shifted choline resonance intensities after addition of 1 $\mu$l of a 1 mM $Pr(NO_3)_3$ $6H_2O$ ($Pr^{3+}$) solution, see the Supporting Information (SI) and Fig. S1 for further details. Data were averaged over three consecutive measurements. Combined with the total fraction of POPC ($\chi_{POPC}$), determined by the above detailed exchange efficiency assays, the mole fraction of POPC in each leaflet follows from

$$\chi_{PC}^{out} = \frac{f_{PC}^{out} \chi_{POPC}}{X^{out}}, \tag{2}$$

where $X^{out}$ corresponds to the fractional number difference of outer and inner leaf lipids due to vesicle geometry, see the SI for further details. Complementary composition of outer leaflet POPE and inner leaflet POPC was derived from $f_{PC}^{in} = 1 - f_{PC}^{out}$ and $\chi_{PE}^{out/in} = 1 - \chi_{PC}^{out/in}$. Similar experiments allowed to assess aLUV stability by following the decay of shifted choline resonance intensity (27). Specifically, passive lipid transbilayer diffusion rates were derived from

$$\Delta C = \frac{2f_{PC}^{out} - 1}{2f_{PC,0}^{out} - 1}, \tag{3}$$

where $f_{PC,0}^{out}$ is fraction of POPC on the outer leaf at time zero, i.e. immediately after aLUV preparation. Note that these measurements were taken on aliquots of aLUVs incubated at a given temperature, where $Pr^{3+}$ was added immediately

before each NMR scan.

## Vesicle size and morphology

### Dynamic light scattering (DLS)

Vesicle size was measured by dynamic light scattering (DLS) using a ZetasizeNANO ZSP (Malvern, UK) equipped with a 10 mW laser with $\lambda = 632.8$ nm. Measurements were conducted in glass cuvettes at a fixed measurement angle of 173°. At each temperature samples were equilibrated for 5 minutes before starting the experiment. We report averaged values from three consecutive measurements, each consisting of 15 frames (exposure time: 10 s) as well as the polydispersity index $(PDI = (width/size)^2)$.

### Cryo-transmission electron microscopy (TEM)

All TEM images were recorded with a Gatan system mounted on a Tecnai12 electron microscope from FEI Company, equipped with a LaB6 filament operating at 120 kV. Electron micrographs were recorded on a Gatan Bioscan CCD 1k×1k camera. A Leica EM GP grid plunger, which allowed temperature control between $4 - 60$°C at a relative humidity of 99% was used to spot samples on EM support grids (holey carbon film on copper grid). After carefully blotting excess sample with filter paper TEM grids were plunged rapidly into liquid ethane to prevent the formation of ice-crystals. Samples were subsequently stored in liquid nitrogen until measurement.

## Membrane structural parameters

### Gel domains/leafs – WAXS

WAXS experiments were performed using SAXSpace (Anton Paar, Graz, Austria), equipped with a Eiger R 1M detector system (Dectris, Baden-Daettwil, Switzerland) and a 30 W-Genix 3D microfocus X-ray generator (Xenocs, Sassenage, France), supplying Cu-K$\alpha$ ($\lambda = 1.54\,\text{Å}$) radiation. WAXS was recorded by setting the sample-to-detector distance (SDD) to 180 mm.

All samples were contained in a $\mu$-cell glass capillary (Anton Paar, Graz, Austria; diameter: 1 $\mu$m) and equilibrated for 10 min at each temperature to within $\pm 0.1°$C using a Peltier stage (TC Stage 150, Anton Paar, Austria). The exposure time was set to 1 hour (6 frames, each 10 min long). Data integration was performed using SAXStreat (Anton Paar, Austria). Background scattering originating from water and capillary was subtracted after smoothing using the ATSAS suite (38).

WAXS data analysis was performed in the range $q = 1.3 - 1.6$ Å$^{-1}$. In the gel phase, the acyl chains of the studied lipid mixtures pack on a 2D-hexagonal lattice allowing us to calculate the area per lipid directly from the position ($q_{11}$) of the chain correlation peak (39)

$$A_L = \frac{16\pi^2}{\sqrt{3}q_{11}^2}.$$ (4)

In order to disentangle the POPE* and POPC* $A_L$'s, a series of WAXS experiments were performed on the same symmetric lipid mixtures studied by DSC (see above). The resulting data (Fig. S7) can be collapsed on a single curve us-
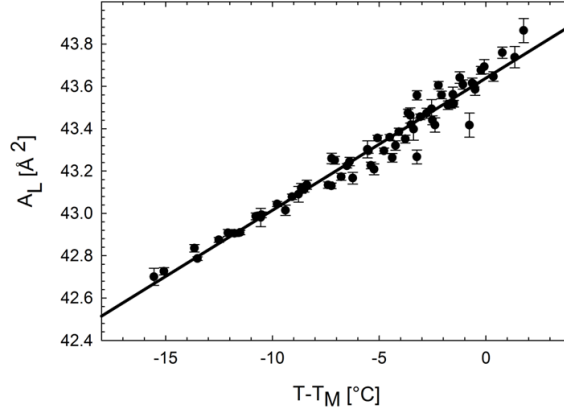
Figure 2: Gel area per lipid calibration curve determined from WAXS. Data on absolute temperatures are shown in Fig. S7.

ing reduced temperatures $(T - T_M)$, where $T_M$ was determined from DSC data (Fig. 2).

A linear regression $(A_L = k \cdot (T - T_M) + A_{POPE}^{T_M})$ yielded $k = 0.0625 \pm 0.0002$ Å$^2$/°C and $A_{POPE}^{T_M} = 43.6 \pm 0.002$ Å$^2$. The latter value corresponds to the area per lipid of POPE* at the $T_M$. Note that due to the presence of POPG this value is ~0.8 Å$^2$ higher than that of pure POPE (34, 40). Assuming linear additivity, the apparent area per POPC* molecule at a given temperature in the gel phase is then derived from

$$A_{POPC} = \frac{A_L - \chi_{POPE} A_{POPE}}{1 - \chi_{POPE}}, \tag{5}$$

where $A_{POPE}$ is the measured area per lipid of POPE*, taken from the linear regression (Fig. 2). This allowed us to calculate the average $A_L$ of any (symmetric) POPE/POPC* mixture below the $T_M$.

Further, the lateral correlation parameter of scattering domains $\xi_D$, which is

a measure for the size of gel domains, was estimated using the Scherrer equation

$$\xi_D \simeq \frac{\lambda}{\beta cos(\theta)}, \tag{6}$$

where $\beta$ is the full width at half maximum of the chain correlation peak, corrected for instrumental broadening, and $\theta$ is the Bragg angle.

## Fluid leafs – SAXS /SANS

SAXS experiments were performed at the P12 BioSAXS beamline, located at the storage ring PETRA III (EMBL/DESY) in Hamburg (41). Samples were exposed to a total photon flux of $5x10^{12}$ s$^{-1}$ at 20 keV with an X-ray beam focused to $120\times120\,\mu$m. Data was collected by a Pilatus 2M detector (Dectris, Switzerland) at SDD = 3.1 m. For measurements, samples were transferred into temperature-controlled multi-well plates and equilibrated for 10 min at a given temperature. A robot delivered 20-35 $\mu$L of the sample into a pre-heated glass capillary. For each sample 20 frames were recorded with an exposure time of 0.045 s. Background was measured before and after each sample. To detect possible radiation damage, data collected in subsequent frames were compared using a standard F-test (42). Primary data treatment was performed using ATSAS (38).

Neutron scattering experiments were performed at KWS-1 (FRM II, Munich-Garching, Germany) (43, 44) and at the BL-6 extended Q-range small angle neutron scattering (EQ-SANS) instrument of the Spallation Neutron Source at the Oak Ridge National Laboratory (ORNL). Samples were loaded into 1 mm path length 404,000-QX quartz cuvettes (Hellma, Jena, Germany) or 1 mm banjo cells, and mounted in a temperature-controlled holder ($\Delta T \sim \pm 1°$C). Typical measure-

ment times were 30 min. At KWS-1 data were obtained with a two-dimensional scintillation detector using neutrons of $\lambda = 5$ Å (wavelength spread: $\Delta\lambda/\lambda = 0.1$) at SDD = 1.21 m and SDD = 7.71 m, yielding a total $q$-range of $0.005 - 0.42$ Å$^{-1}$. Data were corrected for detector pixel sensitivity, dark current, sample transmission, and background scattering from $D_2O$ using the QTIKWS software from JCNS (Garching, Germany). EQ-SANS data were measured at two SDDs, 1.3 and 4.0 m, using wavelength bands of $\lambda = 4.0$-7.5 Å and $\lambda = 10.0$-13.5 Å, which corresponds to a $q$-range of 0.005-0.5 Å$^{-1}$. Data were collected with a 2-dimensional $^3$He position sensitive detector and reduced to one-dimensional $I(q)$ scattering curves by using *Mantid* (45).

Structural parameters of each leaflet were determined by a joint analysis of SANS and SAXS data using the asymmetric scattering density (aSDP) model (32). Briefly, the scattered intensity (SAXS or SANS) of aLUVs $I(q)$ can be approximated for sufficiently dilute systems and for $q > 0.03$ by

$$I(q) \approx |F_{FB}(q)|^2, \tag{7}$$

where $|F_{FB}|^2$ is the flat bilayer form factor, which contains information about the distribution of matter across the bilayer (46, 47). The aSDP model describes bilayer structure in terms of one-dimensional volume probability profiles (VPPs) of quasi molecular lipid fragments. Specifically, each leaflet was parsed into methyl (M), hydrocarbon (HC), carbonyl + glycerol (CG) and residual head (RH) groups. The latter group contains the choline methyl + phosphate groups in the case of PC and $CH_2CH_2NH_3$ + phosphate groups in the case of PE. In order to reduce the number of adjustable parameters, a single Gaussian was used to describe the

RH group in each leaf. The corresponding scattering length densites (SLD) and volumes were derived from molecular averages according to the leaflet composition using previously reported data (48, 49). Further, the effect of rapid hydrogen/deuterium exchange occurring in the primary amines of PE heads was taken into account for SANS data analysis (49, 50). Analogously to RH, the VPPs of the M and CG groups were also modeled by Gaussians, while smooth plateau-like functions were used to describe the HC groups (32).

The lateral area per lipid in each leaf were calculated using

$$A_L^{o,i} = \frac{V_C^{o,i}}{D_C^{o,i}}, \tag{8}$$

where $V_C$ is the acyl chain volume including M and HC groups and $D_C$ is hydrocarbon chain length given by the distance between the bilayer center and 50%-probability value of the HC group. All SAXS/SANS data were analyzed jointly, i.e. using a single optimization procedure. For further details of the aSDP model and data analysis principles see (32).

# Results

## Characterization of aLUV composition

To address the 'sidedness' of lipid distributions we engineered aLUVs with POPE acceptor and POPC donor vesicles, denoted as POPC$^{out}$/POPE$^{in}$, as well as POPC acceptor and POPE donor vesicles, denoted as POPE$^{out}$/POPC$^{in}$. For each system two batches with different D/A ratios were prepared and assessed for

their composition as detailed in the previous section.

The resulting leaflet compositions are presented in Tab. 1. Interestingly, we found donor lipid also on the inner leaf of the aLUVs. This might be partially due to residual small unilamellar vesicles as discussed before (29). The increase of donor lipid on the inner monolayer with D/A for both systems indicates that this is inherently related to the CD-mediated exchange process. To obtain a measure for the degree of asymmetry we define $\Sigma_{as} = \chi^o_{don} - \chi^i_{don}$, where $\chi^{o,i}_{don}$ are the mole fractions of donor lipid on the outer and inner leaflets, respectively. The resulting values show insignificant differences for the two different D/A's for both sample systems. This suggests that all studied systems display a similar degree of asymmetry. The agreement of lipid composition determined by UPLC-MS on independently prepared aLUVs shows a good overall sample reproducibility.

Table 1: Leaflet composition of studied aLUVs.

| Component | $\chi^i_{POPC}$ | $\chi^i_{POPE}$ | $\chi^o_{POPC}$ | $\chi^o_{POPE}$ | $\Sigma_{as}$ |
|---|---|---|---|---|---|
| POPC$^{out}$/POPE$^{in\ a}$ | $0.06^c$ | $0.94^c$ | $0.54^c$ | $0.46^c$ | $0.48^c$ |
|  | $(0.10^d)$ | $(0.90^d)$ | $(0.68^c)$ | $(0.32^c)$ | $(0.58^d)$ |
| POPC$^{out}$/POPE$^{in\ b}$ | $0.11^c$ | $0.89^c$ | $0.64^c$ | $0.36^c$ | $0.53^c$ |
| POPE$^{out}$/POPC$^{in\ a}$ | $1.00^c$ | $0.00^c$ | $0.40^c$ | $0.60^c$ | $0.60^c$ |
|  | $(1.00^d)$ | $(0.00^d)$ | $(0.33^d)$ | $(0.67^d)$ | $(0.67^d)$ |
| POPE$^{out}$/POPC$^{in\ b}$ | $0.81^c$ | $0.19^c$ | $0.24^c$ | $0.76^c$ | $0.57^c$ |

$^a$D/A = 2.
$^b$D/A = 3.
$^c$using DSC for lipid exchange.
$^d$using UPLC-MS for lipid exchange.

## Stability of asymmetric vesicles

Because of the different melting temperatures of POPE and POPC, the stability of lipid asymmetry is of concern, in particular due to increased lipid flip-flop in the phase transition regime (27) and the differential area expansivities in the gel and fluid phases (40, 48, 49).

Our ^{1}H-NMR experiments revealed a 14 % decrease of asymmetry when incubated at 35°C for nearly five days (Table 2). When equilibrated at 10°C the observed change of asymmetry was insignificant within the uncertainty of the measurement. All presented experiments (DSC, DLS, TEM, WAXS) were performed within less than a day, and all SAXS/SANS experiments were finished after three days of sample preparation. Hence, we expect no significant contribution from changes in lipid distribution to our results.

Table 2: Decay of normalized bilayer asymmetry determined from ^{1}H-NMR.

| | $POPE^{out}/POPC^{in}$ | | $POPC^{out}/POPE^{in}$ | |
|---|---|---|---|---|
| | 10°C | 35°C | 10°C | 35°C |
| time (h) | $\Delta C$ | $\Delta C$ | $\Delta C$ | $\Delta C$ |
| 0 | 1.00±0.04 | 1.00 ± 0.04 | 1.00 ± 0.09 | 1.00 ±0.08 |
| 20 | 1.07± 0.20 | 0.98 ± 0.04 | 1.00 ± 0.09 | 0.97 ± 0.07 |
| 70 | 1.00 ± 0.09 | 0.91 ± 0.05 | 0.94 ± 0.07 | 0.93 ± 0.08 |
| 118 | 0.96 ± 0.03 | 0.86 ± 0.03 | 0.98 ± 0.07 | 0.94 ± 0.05 |

Stability was further assessed by DSC, which is a highly sensitive technique to detect changes in lipid composition. Only small changes in the thermograms of three consecutive cooling scans were detected (Fig. S4), indicating that there is no significant lipid scrambling across the melting transition of the aLUVs. We further performed cryo-TEM experiments on aLUVs incubated in the phase transition

regime. No evidence for vesicle invagination or rupture was observed (Fig. S2).

## Size and morphology

Temperature-induced changes in POPC$^{out}$/POPE$^{in}$ aLUV size were measured by DLS. Data revealed a linear change of vesicle size between $5 - 35$℃ (Fig. 3 $A$). The polydispersity in turn did not exhibit any temperature dependency, but in general increased from $PDI < 0.1$ for acceptor vesicles to $PDI \sim 0.1 - 0.2$ for aLUVs. The linear increase of vesicle size with temperature is interesting, because the melting transition of symmetric bilayers is usually associated with significant changes in lipid volume and area (see, e.g. (51)). Indeed, DLS measurements on POPE* LUVs, showed vesicle size changes consistent with a melting at $T_M = 22$℃, as determined by DSC (Fig. 3 $A$).

To gain more insight we determined the surface area extension coefficient $\alpha_S^T = 1/S \cdot \partial S/\partial T$ assuming ideal spherical vesicles with an outer surface area $S$. For POPE* LUVs $\alpha_S^T$ is about two times smaller in the gel than in the fluid phase, with a significant jump in the melting regime (Fig. 3 $A$). In turn, $\alpha_S^T$ is monotonously increasing throughout the whole studied temperature range for aLUVs, with a value close to that of fluid POPE*. This indicates overall fluid-like behavior of the aLUVs, which is further substantiated by the excellent agreement with the lipid area extension coefficient $\alpha_{A_L}^T$ reported for fluid POPE from SANS/SAXS experiments (49).

Comparing POPE* and POPE/POPC* vesicle diameters on absolute scale reveals an $\sim$10% increase of vesicle size during lipid exchange. This could be due to a change in vesicle morphology, e.g. aLUVs could become non-spherical, or be-
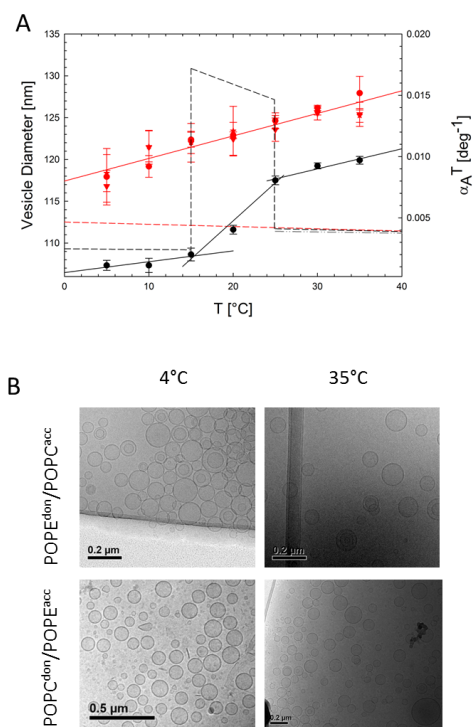
Figure 3: Vesicle size (symbols) as a function of temperature and corresponding $\alpha_S^T$, and $\alpha_{A_L}^T$ (lines) for POPE$^{out}$/POPC$^{in}$ (D/A = 2) aLUVs (red) and POPE* LUVs (black) as determined from DLS (panel A). Dashed-dotted gray line represents $\alpha_{A_L}^T$ reported from scattering experiments (49). Panel B shows corresponding cryo-TEM images of POPE$^{out}$/POPC$^{in}$ (upper panel) and POPC$^{out}$/POPE$^{in}$ (lower panel) measured at 4℃ (left column) and 35℃ (right column).

cause of residual osmotic pressure imposed by an imbalance of NaCl concentration, between the inner and outer vesicle aqueous phase. We therefore performed cryo-TEM experiments at selected temperatures. Data revealed a majority of spherical aLUVs both at low and high temperature (Fig. 3 *B*). This is in contrast to a faceted shape displayed by POPE* LUVs in the gel phase (Fig. S3 *A*), previously reported for giant unilamellar vesicles in the gel phase (52).

In order to check on the influence of osmotic imbalance of NaCl we prepared POPE* LUVs with a 25 mM NaCl core. Indeed, we observed spherical vesicles by TEM (Fig. S3 *B*). The osmotic pressure resulting from the NaCl core of aLUVs can be estimated by the Laplace equation $\Delta P = 2\gamma/R$, where $\gamma$ represents the surface tension and R the vesicle radius. Using $R = 65$ nm and $\gamma = 41$ $\mu$N/m (53) we calculate $\Delta P \simeq 0.01$ bar, which is too small to induce any detectable change of nanoscopic leaflet structure, consistent with our previous reports (29, 32). However, defect lines in the gel phase can be expected to have increased flexibility, which appears to be sufficient to render the vesicles spherical even at low osmotic pressures.

## Leaflet structure and thermotropic behavior

### Melting of asymmetric leaflets

Phase transitions occurring in POPE$^{out}$/POPC$^{in}$ and POPC$^{out}$/POPE$^{in}$ aLUVs were studied by DSC. Comparison of cooling scans of the two types of aLUVs reveal distinct behavior (Fig. 4). A single, but broad, melting transition was observed when POPE is the major component on the inner leaf. In turn, the melting of aLUVs with POPE being the major component on the outer leaf was

significantly broader with two major bordering melting transitions. Similar overall characteristics were observed for D/A = 2 aLUVs (Fig. S6).

Thus, POPE$^{out}$/POPC$^{in}$ aLUVs display an extended range of gel$^{out}$/fluid$^{in}$ coexistence, while POPC$^{out}$/POPE$^{in}$ aLUVs melt cooperatively indicating strong interleaflet coupling. Further, the high temperature melting transitions ($T_M^{PE/PC}$) of POPE$^{out}$/POPC$^{in}$ aLUVs can be compared to the $T_M$ found for symmetric LUVs with the same outer leaflet composition. For both D/A ratios $T_M^{PE/PC}$ was $\sim 2 - 5$℃ higher than the expected $T_M$. This indicates lipid domain formation (gel-fluid phase coexistence) within the outer monolayers, consistent with the occurrence of several heat capacity maxima, which was particularly pronounced for aLUVs prepared at D/A = 2 (Fig. S6 *B*).

## Lipid packing in gel phase leaflets

Lipid lateral areas were determined from WAXS. The most distinct difference in WAXS signal between aLUVs and scrambled LUVs was the width of the chain correlation peak, being much broader for aLUVs (Fig. 5 *A*). This signifies a smaller gel phase domain size for aLUVs, which can be also expressed in terms of the average chain correlation length $\xi_D$. In general $\xi_D$ ranged between $200 - 300\,\text{Å}$, and, averaged over all temperatures, $\xi_D^{aLUV} < \xi_D^{LUV}$ (Fig. 5 *A*, insert). This provides evidence that gel-phase lipids are less well-packed in aLUVs. Moreover, no additional peaks or shoulders were observed. Hence, lipid packing is dominated by POPE on a 2D-hexagonal lattice with non-tilted hydrocarbons in aLUVs, i.e. they form a L$_\beta$ phase.

In order to reveal the effect of lipid packing density in one leaflet to the other we
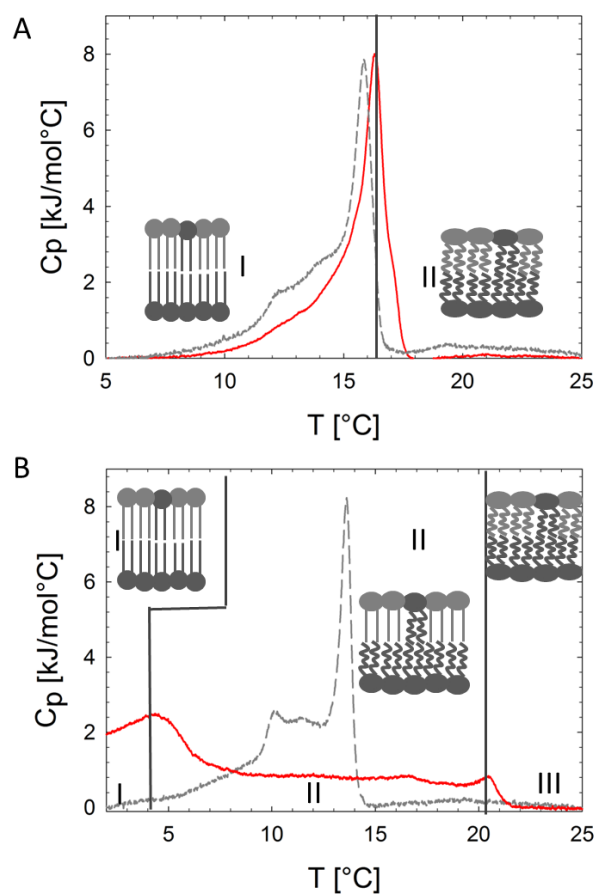
Figure 4: DSC cooling scans of POPC$^{out}$/POPE$^{in}$ (panel A) and POPE$^{out}$/POPC$^{in}$ (panel B) aLUVs (D/A = 3) (red lines). Transitions of corresponding scrambled LUVs are shown as gray dashed lines. Insets show schematics of leaflet structure. See Fig. S6 for corresponding D/A = 2 data.

compared the $A_L$'s determined directly from WAXS of aLUVs to those calculated from their given monolayer composition (see Materials and Methods). In general, a gel-phase chain correlation peak was detectable up to somewhat higher temperatures in $POPC^{out}/POPE^{in}$ than in $POPE^{out}/POPC^{in}$ (Fig. 5 $B, C$) indicating higher stability of aLUVs enriched in POPE on the inner leaflet.

For $POPC^{out}/POPE^{in}$, both leaflets form a gel phase in the data range shown in Fig. 5 $C$. Interestingly, the comparison to theoretical $A_L$'s shows that lipids pack in the aLUVs on average more tightly than in decoupled monolayers of equal outer leaflet composition, but less dense than in decoupled monolayers of equal inner leaflet composition, respectively. That is, the observed lipid packing in aLUVs is a compromise between inner and outer leaflet lipids and neither of the two leaflets appears to dominate over the other.

In the case of $POPE^{out}/POPC^{in}$ aLUVs WAXS data reflects coexistence of an inner POPC-enriched fluid leaflet and an outer leaflet dominated by POPE-enriched gel domains (Fig. 5$B$). In particular, we observed an additional broad peak centered at $q \sim 13.8$ nm$^{-1}$, typical for hydrocarbons in the $L_\alpha$ phase (see, e.g. (54)). Note that fluid patches on the outer leaflet will also contribute to this peak. If we calculate the molecular averaged $A_L$ using Eq. (5) according to the outer leaflet composition, assuming that all POPC in the outer leaflet is also in the gel phase we find good agreement with experimental data (Fig. 5 $D$).This provides additional evidence that the two leaflets are not coupled. Note that assuming all outer leaflet POPC is residing within fluid domains would lower the calculated $A_L$'s by about 0.2 Å$^2$. In reality the amount of fluid POPC most likely changes with temperature in the here presented data range. A determination of these
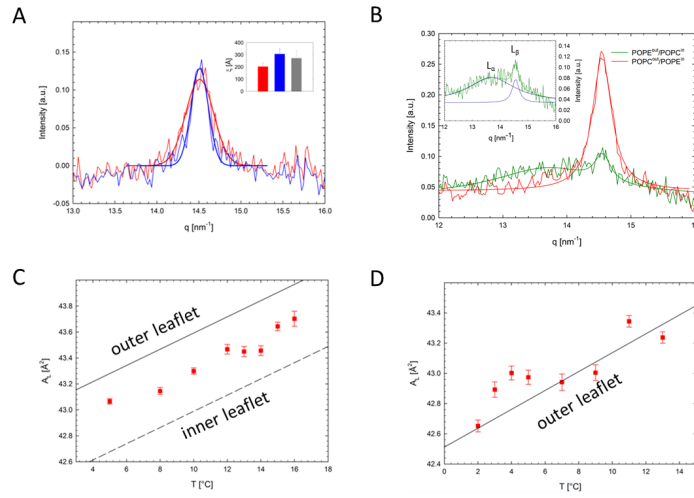
Figure 5: Wide-angle scattering and lipid packing in gel-phase aLUVs. Panel A compares WAXS data of aLUVs (red) and scrambled LUVs (blue). Solid lines correspond to Gaussian fits. The insert compares the average $\xi_D$ of aLUVs and LUVs. Panel B compares WAXS data of POPE$^{out}$/POPC$^{in}$ (blue, T = 10℃) and POPC$^{out}$/POPE$^{in}$ (red, T = 5℃). The POPE$^{out}$/POPC$^{in}$ data contain an additional broad peak originating from fluid hydrocarbons (insert). Panel C shows the areas per lipid for POPC$^{out}$/POPE$^{in}$ and panel D for POPE$^{out}$/POPC$^{in}$ aLUVs as a function of temperature (symbols). Solid lines correspond to theoretical $A_L$'s of the outer leaf and the dashed line to theoretical $A_L$'s of the inner leaf calculated from the given leaflet composition.

details is beyond the scope of the present study.

## Lipid packing in all-fluid leaflets

In the fluid phase, hydrocarbon chain-chain correlations are weak and WAXS data do not allow for an unambiguous analysis of lipid packing in each leaflet. We therefore applied a joint analysis of SANS/SAXS data as detailed in the Materials and Methods section.

Three contrasts were analyzed for $POPC^{out}/POPE^{in}$ aLUVs and their scrambled analogs (Fig. 6, and Fig. S10). Application of the aSDP model yielded reasonable agreement with experimental data. For details of obtained parameters, see Table S1. Resulting $A_L$ values are reported in Tab. 3 and show an average lower packing density of lipids in the outer leaflet as compared to the inner leaflet ($\Delta A_L \sim 4\text{Å}^2$). However, this relates to the leaflet's lipid composition as demonstrated by the $A_L$ calculated from molecular averages of reported values of pure POPE (49), POPC (48) and POPG (50) (Tab. 3). The remarkable agreement between measured and calculated $A_L$'s shows that the lipid areas in each leaflet result from averaging molecular packing properties of POPE and POPC lipids and not from adjusting to lipid packing in the opposing leaflet. Analysis of $POPE^{out}/POPC^{in}$ aLUVs yielded comparable results (Fig. S9, Tab. 3), however with the difference that the average packing of lipids in the inner leaf is less dense than in the outer monolayer. The good agreement to $A_L$ calculated from their composition again demonstrates that the structural difference between the two leaflets relates to compositional differences and not to any transbilayer coupling mechanism. Further, $\Delta A_L$ was similar for $POPC^{out}/POPE^{in}$ aLUVs. Consequently,

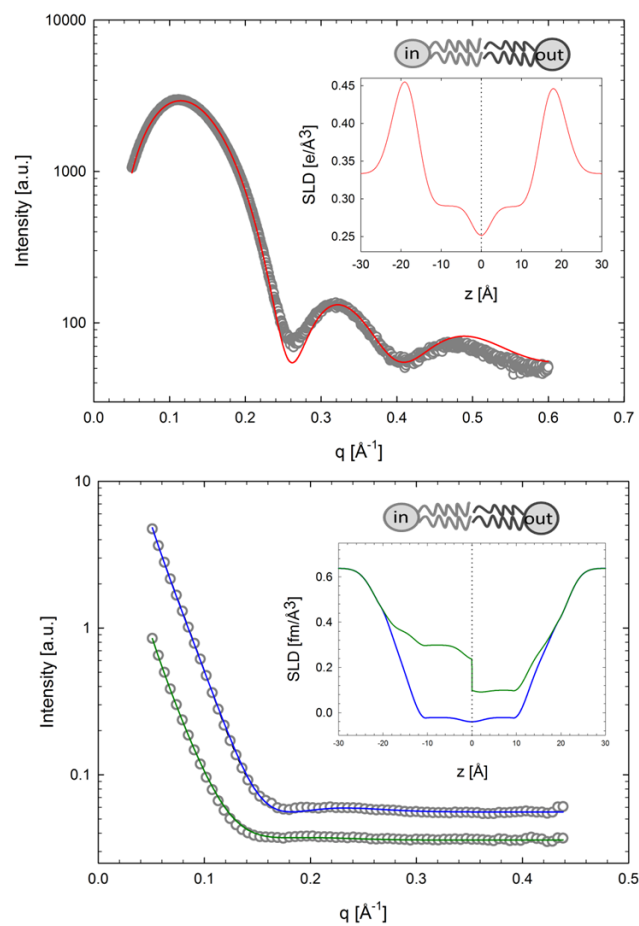Figure 6: Joint analysis of SAXS (top panel) and SANS (lower panel) data of POPC$^{out}$/POPE$^{in}$ aLUVs at 35℃. Solid lines show best fits using the aSDP model (blue line POPC$^{out}$/POPE$^{in}$; green line POPC$^{out}$/POPE-d31$^{in}$). Insets show the corresponding electron and neutron scattering length density profiles.

we conclude that fluid leaflets POPC$^{out}$/POPE$^{in}$ and POPE$^{out}$/POPC$^{in}$ aLUVs behave independently from each other. We note, however, that the experimental uncertainty of the WAXS data analysis ($< 0.1\%$) is significantly smaller than that of the joint SANS/SAXS data fits ($< 3\%$). Moreover, the observed changes on lipid packing densities in the gel phase due to transbilayer coupling amount to less the 1% (Fig. 5). Hence, subtle features of transbilayer coupling in all-fluid POPE/POPC aLUVs might be not detected.

Table 3: Leaflet specific lipid areas of fluid aLUVs (D/A = 2). Experimental uncertainties are within 3%.

| | $A_L^{in}$ [Å$^2$] | $A_L^{out}$ [Å$^2$] |
|---|---|---|
| POPC$^{don}$/POPE$^{acc}$ | 59.7 (59.3$^a$) | 64.7 (63.0$^a$) |
| POPE$^{don}$/POPC$^{acc}$ | 64.7 (64.9$^a$) | 59.9 (60.7$^a$) |

$^a$ calculated from leaflet composition using data reported in (48–50).

# Discussion

We studied POPC$^{out}$/POPE$^{in}$ and POPE$^{out}$/POPC$^{in}$ aLUVs over an extended range of temperatures using an array of experimental techniques resulting in a comprehensive picture of membrane structure on the microscopic to nanoscopic length scales. Cryo-TEM and DLS reported on the overall morphology and size of the vesicles, while DSC combined with WAXS and SAXS/SANS experiments yielded insight into layer specific structural details.

We found significant coupling in POPC$^{out}$/POPE$^{in}$ aLUVs within the gel phase. In the fluid phase of POPC$^{out}$/POPE$^{in}$, and also for POPE$^{out}$/POPC$^{in}$ aLUVs at all temperatures no transbilayer coupling was detected (Fig. 7). We

first turn to $POPC^{out}/POPE^{in}$ at low temperatures. Here, our DSC experiments showed a single transition peak around 16.5℃ (Fig. 4) indicating cooperative melting of both leaflets. Our WAXS data analysis demonstrated that this coupling leads to a partial fluidization of the inner leaflet combined with a more densely packed outer monolayer as compared to uncoupled leafs with equal lipid composition (Fig. 5). The average lipid packing in outer and inner leafs of this system therefore appears to be a compromise between the monolayer specific properties. Intriguingly, however, lateral positional correlations between the hydrocarbons were less expressed in aLUVs as compared to their symmetric counterparts (Fig. 5). This suggests an enrichment of defect zones in aLUVs (Fig. 7 *A*).

In the case of $POPE^{out}/POPC^{in}$ aLUVs (Fig. 7 *B*) leaflet-melting occurred independently (Fig. 4) and the lipid's hydrocarbon chain packing in the gel-domains of the outer leaflet corresponded to a normal $L_\beta$ phase, also in terms of $A_L$ values (Fig. 5 *B*, *D*). This is in contrast to our previous observation for $DPPC^{out}/POPC^{in}$ aLUVs at low temperatures, where a significant disordering of the gel-like domains on the outer leaf was observed, while the inner POPC layer did not differ from a pure POPC bilayer in terms of structure (29). Hence, $POPE^{out}/POPC^{in}$ is uncoupled even at low temperatures. Due to the different lateral expansivities of gel and fluid phases this leads to significant strain within the vesicle that may result in aLUV invagination, or even rupture upon increasing temperature. Area expansion is particularly pronounced across the melting transition with an increase of $\sim 16\%$, while a fluid membrane would expand in the same temperature interval by 5%, only (estimated from measured WAXS data and literature (48, 49)). However, TEM experiments yielded no evidence for significant morphological changes of vesicles in
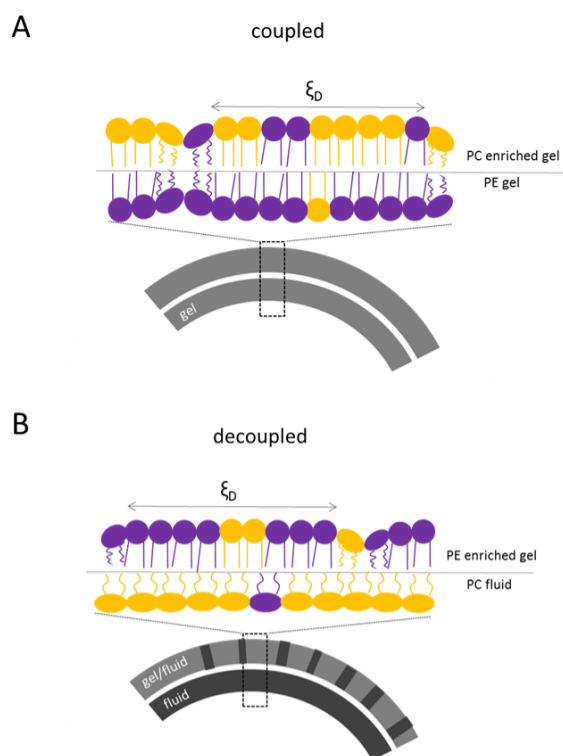
Figure 7: Schematic lipid distribution and transbilayer coupling in POPC$^{out}$/POPE$^{in}$ (panel A) and POPE$^{out}$/POPC$^{in}$ aLUVs (panel B).

the phase transition regime (Fig. S2), consistent with the high aLUV stability seen in repeated DSC scans (Fig. S4) and overall slow lipid flip-flop (Tab. 2). Instead, our DLS data showed a fluid-like expansion of the vesicle surface area over the complete temperature range, including the gel-fluid coexistence regime (Fig. 3 *A*). This can be rationalized by considering the increased number of defects in the gel phase regions of the outer monolayer as evidenced in a smaller $\xi_D$ as compared to symmetric vesicles (Fig. 5 *A*). Further, the fact that $c_P$ never reaches baseline level (Fig. 4 *B* & Fig. S6 *B*) indicates that melting of gel domains in the outer monolayer occurs continuously throughout the gel-fluid coexistence regime. We therefore speculate that gel domain melting at the boundaries of the defect zones occurs with similar high expansivities as observed in the phase transition regime of POPE* LUVs (Fig. 3 *A*). This would yield an overall fluid-like aLUV expansion, which avoids any vesicle shape changes across the melting regime.

Transbilayer coupling has been discussed with diverse mechanisms, including molecular models (partial hydrocarbon chain interdigitation, cholesterol flip-flop (13, 14)) and continuum models (intrinsic curvature, electrostatic coupling, entropic membrane undulations (11–15)). Due to the significant negative $J_0$ of POPE as compared to POPC (55) a intrinsic curvature-mediated coupling appears to the most likely explanation for the presently studied system. This would indeed favor energetically a location POPE in the inner leaflet of lipid vesicles. This can be further tested by changing the aLUV size, as the effect should be more pronounced for highly curved small vesicles, and would eventually disappear at larger vesicle sizes. However, this is beyond the scope of this work.

Intriguingly however, $J_0$ of POPE decreases almost twice as fast with temper-

ature than POPC (55). Consequently, the intrinsic curvature strain stored within the aLUVs should increase with temperature leading to an expected pronounced interleaflet coupling in the fluid phase. Yet, regardless of the predominating location of POPE all-fluid aLUVs do not exhibit any signature of coupling (Tab. 3).

The disparity can be reconciled, however, considering the hydrocarbon chain structure. POPE is a monounsaturated lipid, which means that its oleoyl chains will remained kinked even within the gel phase and require laterally more space than all-$trans$ palmitic chains. This is also expressed in its $A_L$, which is about $3-4$ Å$^2$ larger than that of dipalmitoyl phosphatidylethanolamine (34, 56, 57). Hence, even within the gel phase POPE can be expected to display a significantly negative $J_0$. Additionally, lipids in the gel phase experience decreased motional entropy. That is, intrinsic curvature strain can be less easily compensated by hydrocarbon chain dynamics. The latter effect may explain the abolishment of transbilayer coupling in the fluid phase. Alternatively, experimental limitations of determining $A_L$ in the fluid phase with comparable accuracy than in the gel phase might also account for this finding. Further technological developments that address this issue are currently conceived in our laboratories.

Finally, the observed coupling for POPC$^{out}$/POPE$^{in}$ might also at least partially be due to the intermolecular hydrogen bonding abilities of PE's (58). However, compositional differences of POPE concentration in the inner/outer leaflets of POPC$^{out}$/POPE$^{in}$ and POPE$^{out}$/POPC$^{in}$ are small (Tab. 1) making this contribution likely to be insignificant.

# Conclusion

We provide experimental evidence of an intrinsic-curvature mediated coupling in gel phase $POPC^{out}/POPE^{in}$ aLUVs emphasizing the energetically preferred location of POPE on the inner leaflet of plasma membranes (1–4). Interestingly, within current experiment resolution, this mechanism appears to be abolished in the physiologically more relevant fluid phase. This finding agrees also with our recent report on $DPPC^{out}/POPC^{in}$ aLUVs (32) and aLUVs enriched in SM on the outer leaflet (30, 59). That is, the structure of presently studied fluid membranes are dominated by layer-specific membrane properties only and not those of the opposing leaflet. Consequently, hydrocarbon chain interdigiation (13, 22) even if present does not provide a sufficiently strong mechanical interlock between the two leaflets. Noting that hydrocarbon chain asymmetry was reported to influence lipid diffusion but not order in the opposing leaf (31), we cannot exclude, presently, any effects on the lipid's lateral mobility. Experiments currently planned in our laboratories will address this issue. Future experiments will also focus on the role of cholesterol in mechanical coupling of fluid membranes. Cholesterol was deliberately excluded from the present study in order to keep the analysis tractable, but is known to diffuse rapidly between the two leaflets (60), and has also a significant negative intrinsic curvature (55) which might contribute to coupling of fluid asymmetric membranes. Tools developed in the past two years (27, 29, 32) will allow us to address these issues in detail.

# Author Contributions

# Acknowledgments

# References

1. Verkleij, A. J., P. H. Ververgaert, L. L. van Deenen, and P. F. Elbers, 1972. Phase transitions of phospholipid bilayers and membranes of Acholeplasma laidlawii B visualized by freeze fracturing electron microscopy. *Biochim Biophys Acta* 288:326–332.

2. Bretscher, M. S., 1972. Asymmetrical lipid bilayer structure for biological membranes. *Nat New Biol* 236:11–12.

3. Devaux, P. F., and R. Morris, 2004. Transmembrane asymmetry and lateral domains in biological membranes. *Traffic* 5:241–246.

4. Marquardt, D., B. Geier, and G. Pabst, 2015. Asymmetric lipid membranes: towards more realistic model systems. *Membranes* 5:180–196.

5. Mondal, M., B. Mesmin, S. Mukherjee, and F. R. Maxfield, 2009. Sterols are mainly in the cytoplasmic leaflet of the plasma membrane and the endocytic recycling compartment in CHO cells. *Mol Biol Cell* 20:581–588.

6. Liu, S.-L., R. Sheng, J. H. Jung, L. Wang, E. Stec, M. J. O'Connor, S. Song, R. K. Bikkavilli, R. A. Winn, D. Lee, K. Baek, K. Ueda, I. Levitan, K.-P. Kim, and W. Cho, 2017. Orthogonal lipid sensors identify transbilayer asymmetry of plasma membrane cholesterol. *Nat Chem Biol* 13:268–274.

7. Simons, K., and D. Toomre, 2000. Lipid rafts and signal transduction. *Nat Rev Mol Cell Biol* 1:31–39.

8. Feigenson, G. W., 2009. Phase diagrams and lipid domains in multicomponent lipid bilayer mixtures. *Biochim Biophys Acta* 1788:47–52.

9. Marsh, D., 2009. Cholesterol-induced fluid membrane domains: a compendium of lipid-raft ternary phase diagrams. *Biochim Biophys Acta* 1788:2114–2123.

10. Wang, T. Y., and J. R. Silvius, 2001. Cholesterol does not induce segregation of liquid-ordered domains in bilayers modeling the inner leaflet of the plasma membrane. *Biophys J* 81:2762–2773.

11. Leibler, S., and D. Andelman, 1987. Ordered and curved meso-structures in membranes and amphiphilic films. *J Phys (Paris)* 48:2013–2018.

12. Shlomovitz, R., and M. Schick, 2013. Model of a raft in both leaves of an asymmetric lipid bilayer. *Biophys J* 105:1406–1413.

13. Collins, M. D., 2008. Interleaflet coupling mechanisms in bilayers of lipids and cholesterol. *Biophys J* 94:L32–L34.

14. May, S., 2009. Trans-monolayer coupling of fluid domains in lipid bilayers. *Soft Matter* 5:3148–3156. `ISI:000269062900002`.

15. Galimzyanov, T. R., P. I. Kuzmin, P. Pohl, and S. A. Akimov, 2017. Undulations Drive Domain Registration from the Two Membrane Leaflets. *Biophys J* 112:339–345.

16. Kiessling, V., J. M. Crane, and L. K. Tamm, 2006. Transbilayer effects of raft-like lipid domains in asymmetric planar bilayers measured by single molecule tracking. *Biophys J* 91:3313–3326.

17. Wan, C., V. Kiessling, and L. K. Tamm, 2008. Coupling of cholesterol-rich lipid phases in asymmetric bilayers. *Biochemistry* 47:2190–2198.

18. Collins, M. D., and S. L. Keller, 2008. Tuning lipid mixtures to induce or suppress domain formation across leaflets of unsupported asymmetric bilayers. *Proc Natl Acad Sci U S A* 105:124–128.

19. Polley, A., S. Mayor, and M. Rao, 2014. Bilayer registry in a multicomponent asymmetric membrane: Dependence on lipid composition and chain length. *J Chem Phys* 141:064903.

20. Perlmutter, J. D., and J. N. Sachs, 2011. Interleaflet interaction and asymmetry in phase separated lipid bilayers: molecular dynamics simulations. *J Am Chem Soc* 133:6563–6577.

21. Blosser, M. C., A. R. Honerkamp-Smith, T. Han, M. Haataja, and S. L. Keller, 2015. Transbilayer Colocalization of Lipid Domains Explained via Measurement of Strong Coupling Parameters. *Biophys J* 109:2317–2327.

22. Horner, A., S. A. Akimov, and P. Pohl, 2013. Long and short lipid molecules experience the same interleaflet drag in lipid bilayers. *Phys Rev Letters* 110:268101.

23. Stottrup, B. L., S. L. Veatch, and S. L. Keller, 2004. Nonequilibrium behavior in supported lipid membranes containing cholesterol. *Biophys J* 86:2942–2950.

24. Crane, J. M., and L. K. Tamm, 2004. Role of Cholesterol in the Formation and Nature of Lipid Rafts in Planar and Spherical Model Membranes. *Biophys J* 86:2965–2979.

25. Crane, J. M., V. Kiessling, and L. K. Tamm, 2005. Measuring lipid asymmetry in planar supported bilayers by fluorescence interference contrast microscopy. *Langmuir* 21:1377–1388.

26. Garg, S., J. Rühe, K. Lüdtke, R. Jordan, and C. A. Naumann, 2007. Domain registration in raft-mimicking lipid mixtures studied using polymer-tethered lipid bilayers. *Biophys J* 92:1263–1270.

27. Marquardt, D., F. A. Heberle, T. Miti, B. Eicher, E. London, J. Katsaras, and G. Pabst, 2017. 1H NMR Shows Slow Phospholipid Flip-Flop in Gel and Fluid Bilayers. *Langmuir* 33:3731–3741.

28. Cheng, H. T., Megha, and E. London, 2009. Preparation and properties of asymmetric vesicles that mimic cell membranes: effect upon lipid raft formation and transmembrane helix orientation. *J Biol Chem* 284:6079–6092.

29. Heberle, F. A., D. Marquardt, M. Doktorova, B. Geier, R. F. Standaert, P. Heftberger, B. Kollmitzer, J. D. Nickels, R. A. Dick, G. W. Feigenson, J. Katsaras, E. London, and G. Pabst, 2016. Subnanometer Structure of an Asymmetric Model Membrane: Interleaflet Coupling Influences Domain Properties. *Langmuir* 32:5195–5200.

30. Cheng, H. T., and E. London, 2011. Preparation and properties of asymmet-

ric large unilamellar vesicles: interleaflet coupling in asymmetric vesicles is dependent on temperature but not curvature. *Biophys J* 100:2671–2678.

31. Chiantia, S., and E. London, 2012. Acyl chain length and saturation modulate interleaflet coupling in asymmetric bilayers: effects on dynamics and structural order. *Biophys J* 103:2311–2319.

32. Eicher, B., F. A. Heberle, D. Marquardt, G. N. Rechberger, J. Katsaras, and G. Pabst, 2017. Joint small-angle X-ray and neutron scattering data analysis of asymmetric lipid vesicles. *J Appl Crystallogr* 50:419–429.

33. Kingsley, P., and G. W. Feigenson, 1979. The synthesis of a perdeuterated phospholipid: 1,2-dimyristoyl-sn-glycero-3-phosphocholine-d72. *Chem Phys Lipids* 24:135–147.

34. Pozo, N. B., K. Lohner, G. Deutsch, E. Sevcsik, K. A. Riske, R. Dimova, P. Garidel, and G. Pabst, 2005. Composition dependence of vesicle morphology and mixing properties in a bacterial model membrane system. *Biochim Biophys Acta* 1716:40–48.

35. Pabst, G., A. Hodzic, J. Strancar, S. Danner, M. Rappolt, and P. Laggner, 2007. Rigidification of neutral lipid bilayers in the presence of salts. *Biophys J* 93:2688–2696.

36. Knittelfelder, O. L., B. P. Weberhofer, T. O. Eichmann, S. D. Kohlwein, and G. N. Rechberger, 2014. A versatile ultra-high performance LC-MS method for lipid profiling. *J Chromatogr B Analyt Technol Biomed Life Sci* 951-952:119–128.

37. Hartler, J., M. Trotzmuller, C. Chitraju, F. Spener, H. C. Kofeler, and G. G. Thallinger, 2011. Lipid Data Analyzer: unattended identification and quantitation of lipids in LC-MS data. *Bioinformatics* 27:572–577.

38. Petoukhov, M. V., D. Franke, A. V. Shkumatov, G. Tria, A. G. Kikhney, M. Gajda, C. Gorba, H. D. T. Mertens, P. V. Konarev, and D. I. Svergun, 2012. New developments in the ATSAS program package for small-angle scattering data analysis. *J Appl Crystallography* 45:342–350.

39. McIntosh, T. J., and S. A. Simon, 1986. Area per molecule and distribution of water in fully hydrated dilauroylphosphatidylethanolamine bilayers. *Biochemistry* 25:4948–4952.

40. Marsh, D., 2013. Handbook of Lipid Bilayers, Second Edition. CRC Press, Boca Raton, FL, 2nd ed edition.

41. Blanchet, C. E., A. Spilotros, F. Schwemmer, M. A. Graewert, A. Kikhney, C. M. Jeffries, D. Franke, D. Mark, R. Zengerle, F. Cipriani, S. Fiedler, M. Roessle, and D. I. Svergun, 2015. Versatile sample environments and automation for biological solution X-ray scattering experiments at the P12 beamline (PETRA III, DESY). *J Appl Crystallography* 48:431–443.

42. Petoukhov, M. V., P. V. Konarev, A. G. Kikhney, and D. I. Svergun, 2007. ATSAS 2.1 – towards automated and web-supported small-angle scattering data analysis. *J Appl Crystallogr* 40:s223–s228.

43. Frielinghaus, H., A. Feoktystov, I. Berts, and G. Mangiapia, 2015. KWS-1: Small-angle scattering diffractometer. *J Large-Scale Res Facilities* 1:A28.

44. Feoktystov, A. V., H. Frielinghaus, Z. Di, S. Jaksch, V. Pipich, M.-S. Appavou, E. Babcock, R. Hanslik, R. Engels, G. Kemmerling, H. Kleines, A. Ioffe, D. Richter, and T. Brueckel, 2015. KWS-1 high-resolution small-angle neutron scattering instrument at JCNS: current state. *J Appl Crystallography* 48:61–70.

45. Arnold, O., J. C. Bilheux, J. M. Borreguero, A. Buts, S. I. Campbell, L. Chapon, M. Doucet, N. Draper, R. Ferraz Leal, M. A. Gigg, V. E. Lynch, A. Markvardsen, D. J. Mikkelson, R. L. Mikkelson, R. Miller, K. Palmen, P. Parker, G. Passos, T. G. Perring, P. F. Peterson, S. Ren, M. A. Reuter, A. T. Savici, J. W. Taylor, R. J. Taylor, R. Tolchenov, W. Zhou, and J. Zikovsky, 2014. Mantid—data analysis and visualization package for neutron scattering and SR experiments. *Nucl Instr Meth Phys Res* 764:156–166.

46. Kiselev, M. A., P. Lesieur, A. M. Kisselev, D. Lombardo, and V. L. Aksenov, 2002. Model of separated form factors for unilamellar vesicles. *Appl. Phys. A* 74:s1654–s1656.

47. Pencer, J., Anghel, Vinicius N. P., N. Kučerka, and J. Katsaras, 2006. Scattering from laterally heterogeneous vesicles. I. Model-independent analysis. *J Appl Crystallogr* 39:791–796.

48. Kučerka, N., M. P. Nieh, and J. Katsaras, 2011. Fluid phase lipid areas and bilayer thicknesses of commonly used phosphatidylcholines as a function of temperature. *Biochim Biophys Acta* 1808:2761–2771.

49. Kučerka, N., B. van Oosten, J. Pan, F. A. Heberle, T. A. Harroun, and J. Katsaras, 2015. Molecular structures of fluid phosphatidylethanolamine bilayers

obtained from simulation-to-experiment comparisons and experimental scattering density profiles. *J Phys Chem B* 119:1947–1956.

50. Pan, J., X. Cheng, L. Monticelli, F. A. Heberle, N. Kučerka, D. P. Tieleman, and J. Katsaras, 2014. The molecular structure of a phosphatidylserine bilayer determined by scattering and molecular dynamics simulations. *Soft Matter* 10:3716–3725. 24807693.

51. Heimburg, T., 1998. Mechanical aspects of membrane thermodynamics. Estimation of the mechanical properties of lipid membranes close to the chain melting transition from calorimetry. *Biochim Biophys Acta* 1415:147–162.

52. Pataraia, S., Y. Liu, R. Lipowsky, and R. Dimova, 2014. Effect of cytochrome c on the phase behavior of charged multicomponent lipid membranes. *Biochim Biophys Acta* 1838:2036–2045.

53. Kaye & Laby Online. Tables of Physical & Chemical Constants (16th edition 1995): 2.2.5 Surface tensions. `www.kayelaby.npl.co.uk`.

54. Boulgaropoulos, B., M. Rappolt, B. Sartori, H. Amenitsch, and G. Pabst, 2012. Lipid sorting by ceramide and the consequences for membrane proteins. *Biophys J* 102:2031–2038. 22824266.

55. Kollmitzer, B., P. Heftberger, M. Rappolt, and G. Pabst, 2013. Monolayer spontaneous curvature of raft-forming membrane lipids. *Soft Matter* 9:10877–10884. 24672578.

56. McIntosh, T. J., 1980. Differences in hydrocarbon chain tilt between hy-

drated phosphatidylethanolamine and phosphatidylcholine bilayers. A molecular packing model. *Biophys J* 29:237–245.

57. Lohner, K., A. Latal, G. Degovics, and P. Garidel, 2001. Packing characteristics of a model system mimicking cytoplasmic bacterial membranes. *Chem Phys Lipids* 111:177–192.

58. Boggs, J. M., 1980. Intermolecular hydrogen bonding between lipids: influence on organization and function of lipids in membranes. *Can J Biochem* 58:755–770.

59. Chiantia, S., P. Schwille, A. S. Klymchenko, and E. London, 2011. Asymmetric GUVs prepared by MbetaCD-mediated lipid exchange: an FCS study. *Biophys J* 100:L1–L3.

60. Bennett, W. F. D., J. L. MacCallum, M. J. Hinner, S. J. Marrink, and D. P. Tieleman, 2009. Molecular view of cholesterol flip-flop and chemical potential in different membrane environments. *J Am Chem Soc* 131:12714–12720.

# Supplementary Material

## Instrinsic Curvature-Mediated Transbilayer Coupling in Asymmetric Lipid Vesicles

*Barbara Eicher, Drew Marquardt, Frederick Heberle, Ilse Letofsky-Papst, Gerald N. Rechberger, Marie-Sousai Appavou, John Katsaras, and Georg Pabst*

## 1 Evaluation of bilayer asymmetry via $^1$H-NMR

The paramagnetic lanthanide ion $Pr^{3+}$ interacts with choline protons, shifting their resonance downfield as shown in (1), see Fig. S2. By adding $Pr^{3+}$ to a vesicle suspension, the shift is selective for outer leaflet protiated choline, leading to a separate resolution of the protiated choline resonances from the inner and outer leaflet (2). The integrated area $R$ of each resonance is proportional to the number of molecules having protiated headgroups in the corresponding leaflet (Fig. S2). The outer leaf's peak fraction is defined as:

$$f^{out} = \frac{R^{out}}{R^{in} + R^{out}},$$

(1)

where the superscripts 'out' and 'in' indicate the outer and inner leaflet. When all lipids posses protiated headgroups, $f^{out}$ directly yields the mole fraction of all bilayer lipids found in the outer leaflet:

$$X^{out} = \frac{\sum_j N_j^{out}}{\sum_j N_j} \equiv f^{out},$$

(2)

where $N$ and $N^{out}$ denote the number of molecules in the whole bilayer and in the outer leaflet and the summation is performed over all components of the mixture. For a bilayer with an equal number of lipids in the leaflets $X^{out} = 0.5$. However, POPE and POPC have different $A_L$ (3, 4) which means that $X^{out}$ is defined by the area per lipid of the inner ($A_L^{in}$) and of the outer leaflet ($A_L^{out}$):

$$X^{out} = \frac{1/A_L^{out}}{1/A_L^{out} + 1/A_L^{in}} * 1.06,$$

(3)

where the factor 1.06 considers the slightly bigger surface of the outer to the inner leaflet (5) by assuming a vesicle size of 130 nm and a bilayer thickness of 40 Å. As only one mixture component possesses a protiated choline (POPC) we define the single-component outer leaflet peak fraction $f_{PC}^{out}$ as:

$$f_{PC}^{out} = \frac{N_{PC}^{out}}{N_{PC}} = \frac{X^{out}\chi_{PC}^{out}}{\chi_{PC}},$$

(4)

where $\chi_{PC}^{out}$ stands for the outer leaflet mole fraction of POPC. Combining the two previous equations gives the following expression for the outer leaflet mole fraction of POPC:

$$\chi_{PC}^{out} = \frac{f_{PC}^{out} \chi_{PC}}{f_{PC}^{out}}. \tag{5}$$

For a two component POPC/POPE bilayer, all compositional parameters $\chi_{PC/PE}^{out,in}$ can be expressed as:

$$
\begin{array}{rcl}
\chi_{PC}^{out} & = & \frac{f_{PC}^{out} \chi_{PC}}{X^{out}} \\
\chi_{PC}^{in} & = & \frac{(1-f_{PC}^{out}) \chi_{PC}}{(1-X^{out})} \\
\chi_{PE}^{in(out)} & = & 1 - \chi_{PC}^{in(out)}
\end{array}
. \tag{6}
$$

# 2 Supplementary Figures
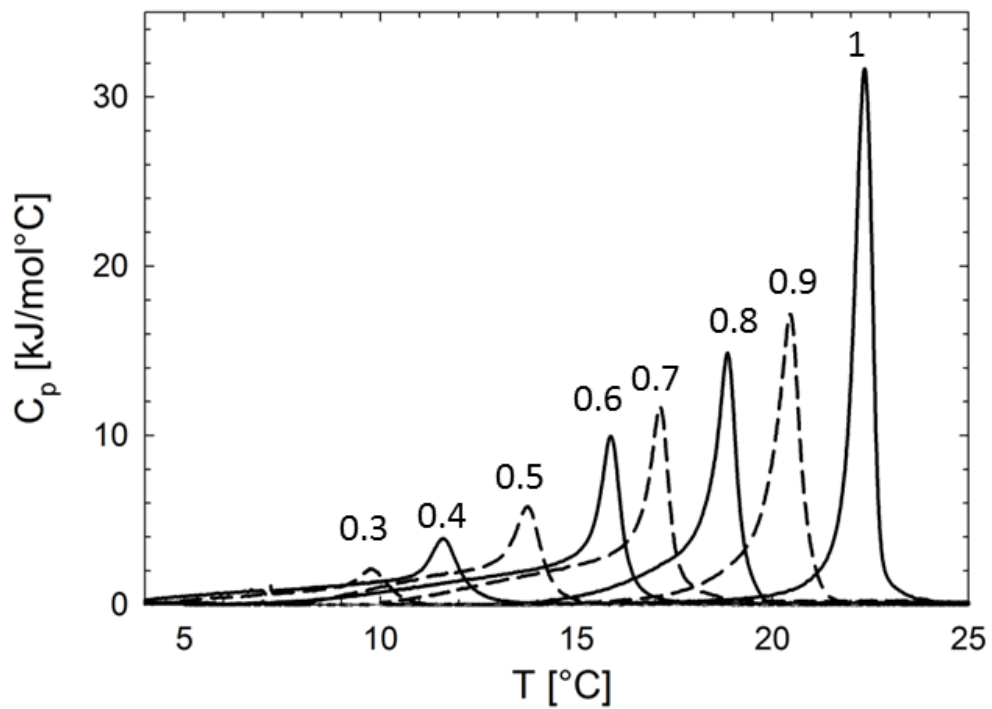


Figure S1: DSC cooling thermograms of POPE/POPC* MLV mixtures (numbers adjacent to data give the molar fractions of POPE.
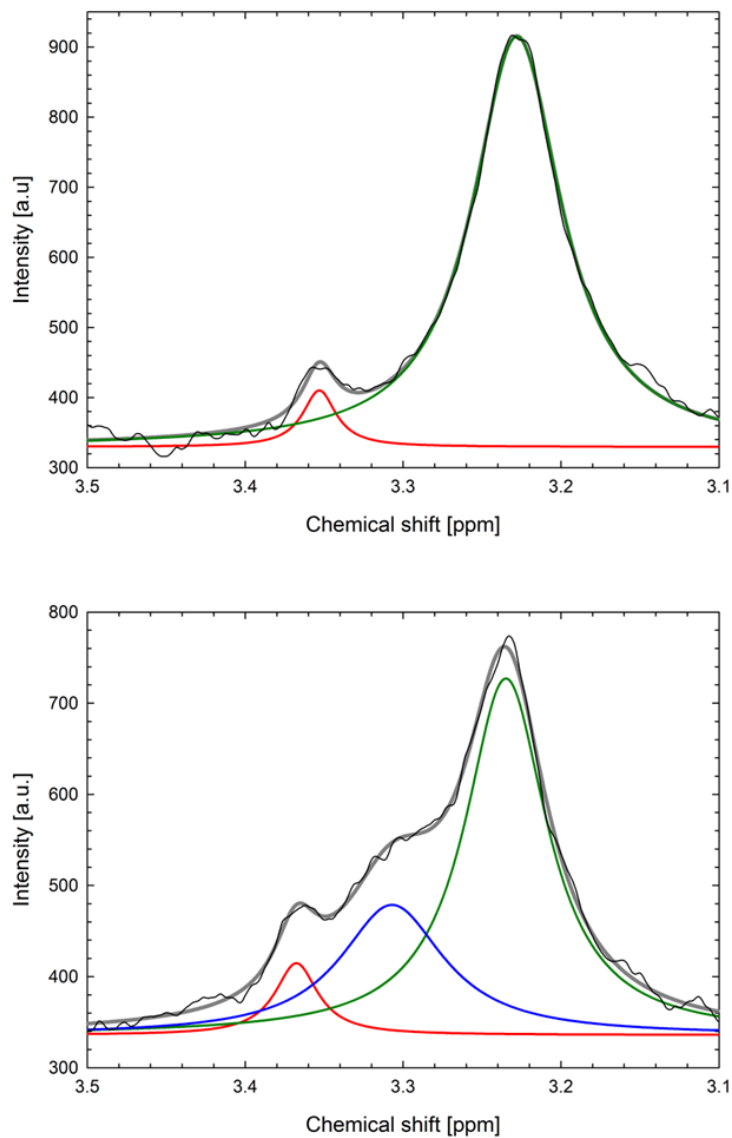
Figure S2: *Upper panel*: ^{1}H-NMR shows the choline resonance (green Lorentzian) from POPC acceptor lipids, while the red Lorentzian considers the contribution of residual m$\beta$CD. *Lower panel*: ^{1}H-NMR signal in the presence of the shift reagent $Pr^{3+}$. The shifted population (blue Lorentzian) relative to the unshifted population (green) reveals inner leaflet acceptor enrichment in the aLUVs.
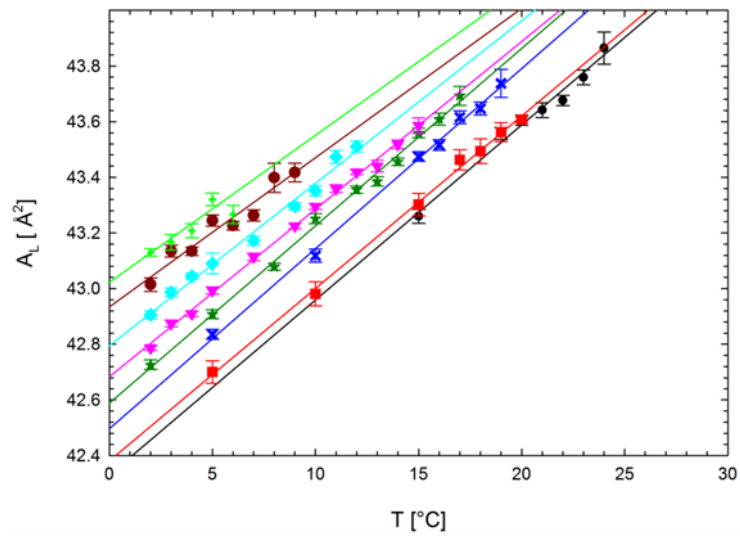
Figure S3: Temperare dependence of areas per lipid for different POPE/POPC* mixtures. The increase of POPC concentration leads to a progressive upshift of lipid areas (black line: $\chi_{POPE} = 1$, green line: $\chi_{POPE} = 0.3$)
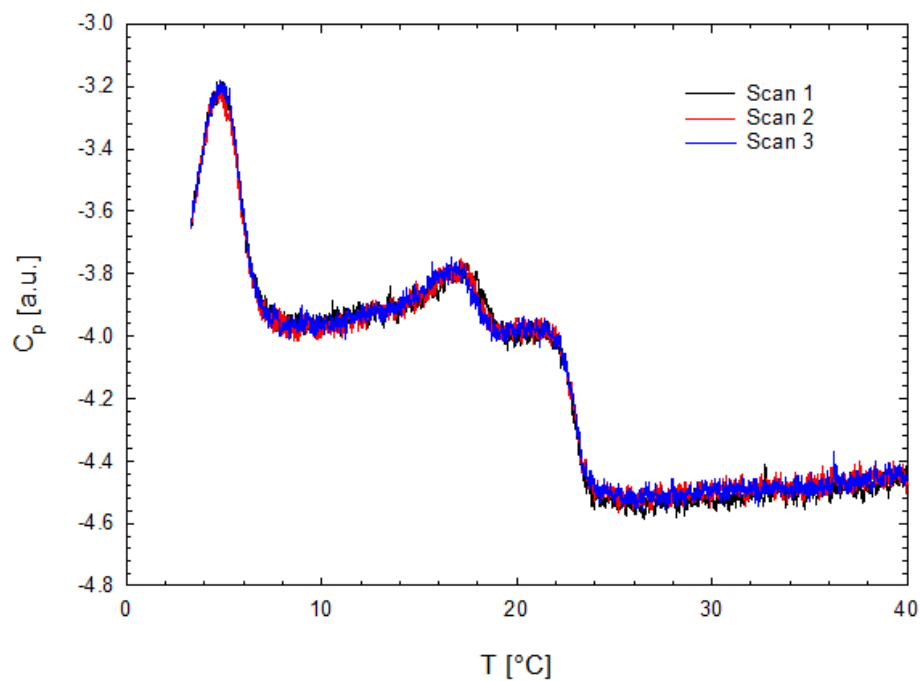
Figure S4: Three consecutive heating scans of POPE$^{out}$/POPC$^{in}$ (D/A = 3). Data were background subtracted, but not normalized.
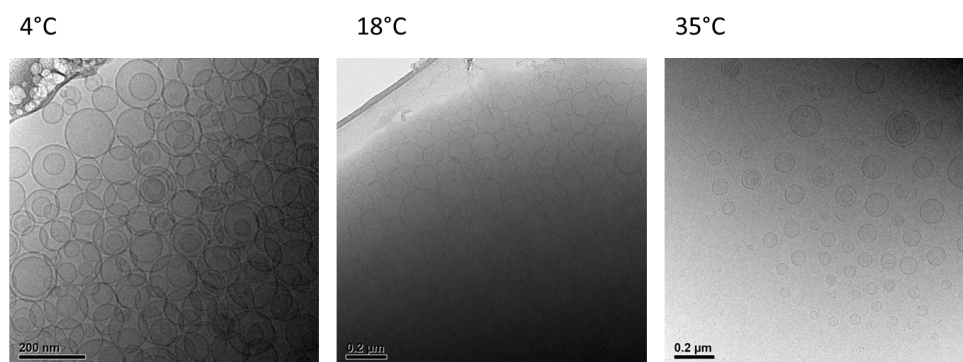


Figure S5: Cryo-TEM images of POPE$^{out}$/POPC$^{in}$ aLUVs at different temperatures. The middle panel corresponds to the phase transition regime.

A  Gel Phase (4°C)

C  Fluid Phase (35°C)

0.2 µm
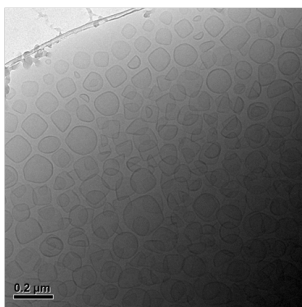
B  25 mM NaCl solution in vescile core

0.2 µm

200 nm
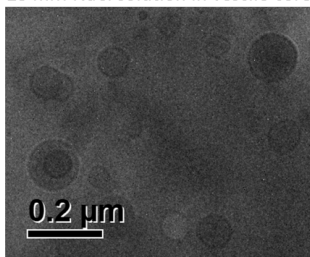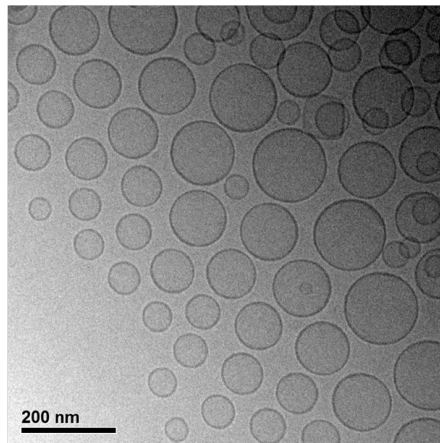
Figure S6: Cryo-TEM images of POPE* LUVs in the gel-phase without (panel A) and with a 25 mM NaCl core (panel B). Panel C shows the LUVs in fluid phase.
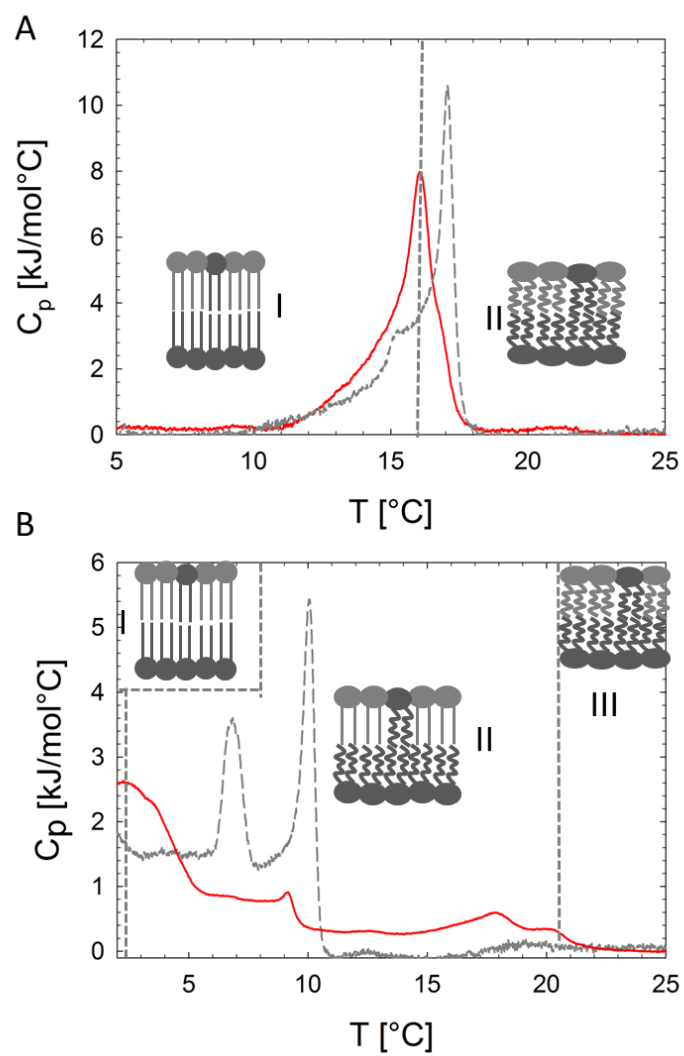
Figure S7: DSC cooling scans of POPC$^{out}$/POPE$^{in}$ (panel A) and POPE$^{out}$/POPC$^{in}$ (panel B) aLUVs (D/A = 2) (red lines). Transitions of corresponding scrambled LUVs are shown as gray dashed lines. Insets show schematics of leaflet structure.
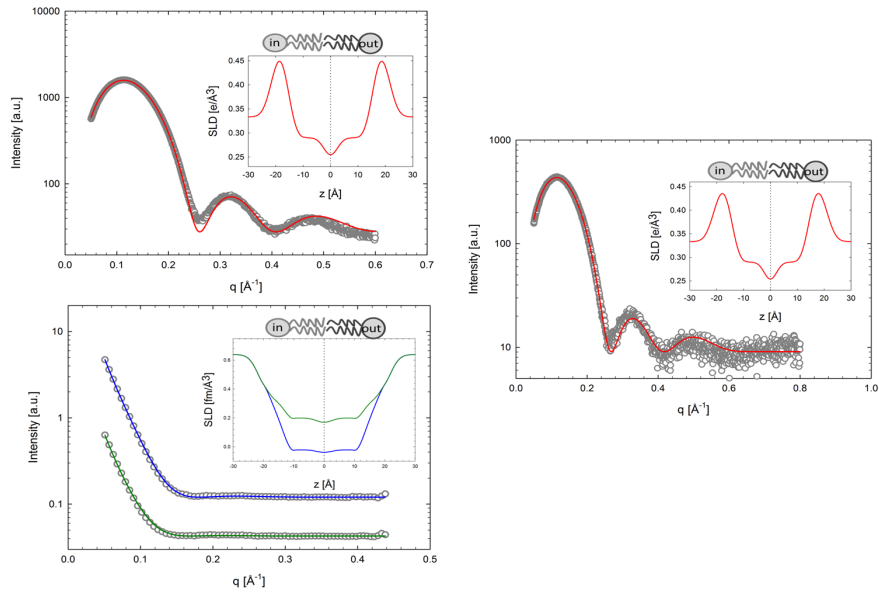
Figure S8: Analysis of scattering data of scrambled POPE/POPC LUVs ($T = 35$℃). *Left panel*: SAXS (*top*) and SANS (*lower*) data of POPC$^{don}$/POPE$^{acc}$ LUVs. *Right panel*: SAXS data of POPE$^{don}$/POPC$^{acc}$ LUVs. Solid lines correspond to best fits using the SDP model. SANS data has been obtained at two contrasts (blue line: POPC$^{don}$/POPE$^{acc}$, green line: POPC$^{don}$/POPE-d31$^{acc}$). Inserts show the corresponding scattering length density profiles.
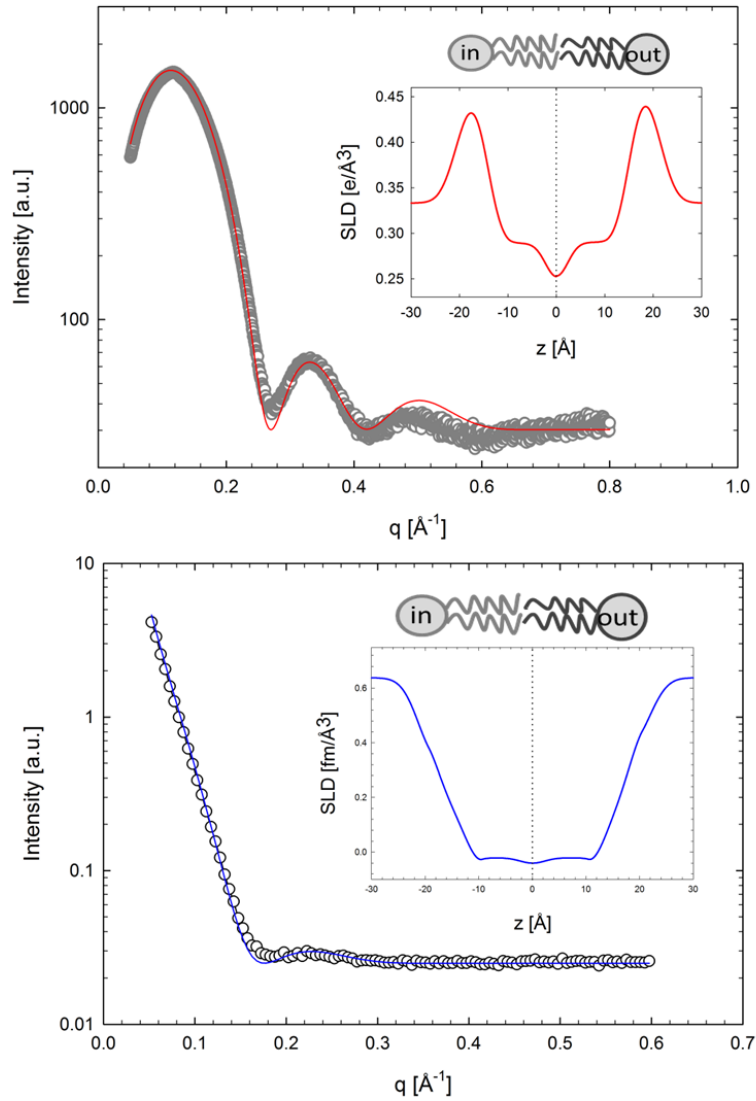
Figure S9: Joint analysis of SAXS (top panel) and SANS (lower panel) data of POPE$^{out}$/POPC$^{in}$ aLUVs at 35°C. Solid lines show best fits using the aSDP model (blue line POPE$^{out}$/POPC$^{in}$). Inserts show the corresponding scattering length density profiles.

# 3 Supplementary Tables

Table S1: Structural parameters of asymmetric and scrambles POPC$^{out}$/POPE$^{in}$ and POPE$^{out}$/POPC$^{in}$ vesicles 35 °C determined with the aSDP-model.

| | POPC$^{don}$/POPE$^{acc}$ | | | POPE$^{don}$/POPC$^{acc}$ | | |
|---|---|---|---|---|---|---|
| | asym | | scram | asym | | scram |
| | out | in | | out | in | |
| $A_L$ [Å$^2$] | 64.7 | 59.7 | 61.5 | 59.9 | 64.7 | 63.2 |
| $\sigma_{RH}$ [Å] | 2.87 | 2.79 | 2.85 | 2.84 | 2.95 | 2.85 |
| $\sigma_{CG}$ [Å] | 2.46 | 2.47 | 2.49 | 2.52 | 2.51 | 2.45 |
| $\sigma_M$ [Å] | 2.00 | 1.99 | 2.04 | 2.03 | 2.01 | 1.97 |
| $\sigma_{MN}$ [Å] | 5.01 | 5.01 | 5.01 | 5.01 | 5.01 | 4.95 |
| $|z_{RH}|$ [Å] | 19.62 | 20.04 | 19.69 | 20.13 | 18.92 | 19.36 |
| $|z_{CG}|$ [Å] | 16.35 | 17.56 | 17.12 | 17.02 | 15.88 | 16.21 |
| $|z_M|^*$ [Å] | 1.00 | 1.00 | 1.00 | 1.00 | 1.00 | 1.00 |
| $|z_{MN}|$ [Å] | 14.37 | 15.58 | 15.13 | 15.52 | 14.38 | 14.71 |

$^*$fixed parameter

# References

1. Heberle, F. A., D. Marquardt, M. Doktorova, B. Geier, R. F. Standaert, P. Heftberger, B. Kollmitzer, J. D. Nickels, R. A. Dick, G. W. Feigenson, J. Katsaras, E. London, and G. Pabst, 2016. Subnanometer Structure of an Asymmetric Model Membrane: Interleaflet Coupling Influences Domain Properties. *Langmuir : the ACS journal of surfaces and colloids* 32:5195–5200.

2. Andrews, S. B., J. Faller, J. M. Gilliam, and R. J. Barrnett, 1973. Lanthanide ion-induced isotropic shifts and broadening for nuclear magnetic resonance structural analysis of model membranes. *Proceedings of the National Academy of Sciences* 70:1814–1818.

3. Kučerka, N., M. P. Nieh, and J. Katsaras, 2011. Fluid phase lipid areas and bilayer thicknesses of commonly used phosphatidylcholines as a function of temperature. *Biochim Biophys Acta* 1808:2761–2771.

4. Kučerka, N., B. van Oosten, J. Pan, F. A. Heberle, T. A. Harroun, and J. Katsaras, 2015. Molecular structures of fluid phosphatidylethanolamine bilayers obtained from simulation-to-experiment comparisons and experimental scattering density profiles. *The Journal of Physical Chemistry B* 119:1947–1956. 25436970.

5. Marquardt, D., B. Geier, and G. Pabst, 2015. Asymmetric lipid membranes: towards more realistic model systems. *Membranes* 5:180–196.